UNIVERSITÉ DE REIMS CHAMPAGNE-ARDENNE

ÉCOLE DOCTORALE MATHEMATIQUES PHYSIQUE SCIENCES DU NUMERIQUE ET DE L'INGENIEUR n°620

THÈSE

Pour obtenir le grade de

DOCTEUR DE L'UNIVERSITÉ DE REIMS CHAMPAGNE-ARDENNE

Discipline : Physique

Spécialité : Sciences des matériaux, Surfaces et Interfaces

Présentée et soutenue publiquement par

Kevin KIM

Le 18 décembre 2025

Thèse dirigée par **Jérémy MALLET & Aurélien BRUYANT**

Synthèse et nanospectroscopie infrarouge de matériaux MXenes, application à la détection de composés siloxanes

---

JURY

Mme Laurène TETARD	Directrice de Recherche	Institut des Sciences Analytiques, FR	**Rapportrice**
M. Vincent MAUCHAMP	Professeur	Université de Poitiers, FR	**Rapporteur**
M. Yannick DE WILDE	Directeur de Recherche	Institut Langevin, FR	**Président (Examinateur)**
M. Benoit HACKENS	Professeur	Université Catholique de Louvain, BE	**Examinateur**
M. Michel KAZAN	Professeur	American University of Beirut, LB	**Examinateur**
M. Yury GOGOTSI	Professeur	Drexel University, USA	**Invité**
M. Jérémy MALLET	Maître de Conférences - HDR	Université Reims Champagne-Ardenne, FR	**Directeur de thèse**
M. Aurélien BRUYANT	Maître de Conférences - HDR	Université de Technologie de Troyes, FR	**Directeur de thèse**

"If science were not open to criticism, it would be a religion"

Résumé

Cette thèse étudie les propriétés optiques infrarouges des MXenes par le biais d'une caractérisation à plusieurs échelles, établit des relations structure-propriété fondamentales et présente des applications pratiques. Le chapitre 1 décrit les matériaux bidimensionnels, positionnant les MXenes comme de nouveaux carbures et nitrures de métaux de transition 2D avec une conductivité métallique élevée et une chimie de surface accordable. Le chapitre 2 développe les bases théoriques de la caractérisation optique multi-échelle et introduit des techniques avancées de microscopie en champ proche comme la microscopie optique en champ proche à balayage de type diffusion (s-SNOM) et la microscopie à force photo-induite (PiFM) pour l'investigation à l'échelle nanométrique au-delà des limites de la diffraction. Le chapitre 3 démontre le contrôle systématique des propriétés infrarouges par l'ingénierie de la composition, révélant que le rapport carbone/azote dans les MXenes $Ti_3C_{(2-y)}N_yT_x$ permet une modulation de la réflectance et de l'émissivité. Les compositions riches en carbone présentent des capacités exceptionnelles de blindage IR, tandis que l'incorporation d'azote augmente l'émissivité pour les applications de gestion thermique. De plus, l'étude infrarouge in-situ des intercalations ioniques dans le MXene $Ti_3C_2T_x$ montre des réponses optiques dynamiques pendant les processus électrochimiques, fournissant des informations sur les modifications structurales en temps réel et les mécanismes de transfert de charge. La PiFM est utilisée dans le chapitre 4 pour la caractérisation de la chimie des surfaces à l'échelle nanométrique, mettant en évidence des terminaisons de surface natives et une contamination par le siloxane non détectée par méthode conventionnelle. L'étude est étendue à la détection de l'oxydation du Nb_2CT_x et à la liaison préférentielle du siloxane aux plans basaux composés de terminaison hydroxyle. Dans le Chapitre 5, nous appliquons les MXenes aux plateformes de détection par Résonance Plasmonique de Surface. Le MXene $Ti_3C_2T_x$ améliore le couplage SPR et permet la détection du (3-aminopropyl)triéthoxysilane (APTES). L'approche de caractérisation optique multi-échelle développée met en lumière les performances et la versatilité de cette famille émergente de matériaux 2D.

Mots-clés: MXene - Spectroscopie infrarouge - Matériaux 2D - Nanoscopie - Chimie de surface - Contamination par les siloxanes

Abstract

This thesis investigates the infrared optical properties of MXenes through multi-scale characterization, establishes fundamental structure property relationships, and shows practical applications. Chapter 1 describes two-dimensional materials, positioning MXenes as novel 2D transition metal carbides and nitrides with high metallic conductivity and tunable surface chemistry. Chapter 2 develops theoretical foundations for multi-scale optical characterization and introduces advanced near-field microscopy techniques like scattering-type scanning near-field optical microscopy (s-SNOM) and photo-induced force microscopy (PiFM) for nanoscale investigation beyond diffraction limits. Chapter 3 demonstrates systematic control of infrared properties through compositional engineering, revealing that carbon-to-nitrogen ratio in $Ti_3C_{(2-y)}N_yT_x$ MXenes enables precise tuning of reflectance and emissivity. Carbon-rich compositions exhibit exceptional IR shielding capabilities, while nitrogen incorporation increases emissivity for thermal management applications. Additionally, infrared in-situ probing of ion intercalations in $Ti_3C_2T_x$ MXene reveals dynamic optical responses during electrochemical processes, providing insights into real-time structural modifications and charge transfer mechanisms. PiFM is employed in Chapter 4 for nanoscale surface chemistry characterization, showcasing native surface terminations and undetected siloxane contamination. Its investigation is extended to Nb_2CT_x oxidation detection and siloxane-preferential binding to hydroxyl-terminated basal planes. In Chapter 5, we apply MXene to Surface Plasmon Resonance sensing platforms. $Ti_3C_2T_x$ MXene enhances the SPR coupling and enables the detection of (3-aminopropyl)triethoxysilane (APTES). The developed multiscale optical characterization approach highlights the performance and versatility of this emerging family of 2D materials.

Keywords: MXene – Infrared spectroscopy – 2D materials - Nanoscopy – Surface chemistry – Siloxane contamination

Acknowledgments

As I reach the end of this doctoral adventure, I find myself reflecting on the paradoxical nature of achievement—the joy of completion intertwined with the melancholy of departure. These three years have been a journey of discovery, not only in the realm of science but also in the relationships that have shaped and sustained me along the way. It is with immense gratitude that I acknowledge the remarkable individuals who have made this work possible.

First and foremost, I would like to express my sincere gratitude to my thesis co-supervisors, Prof. Aurélien Bruyant and Prof. Jérémy Mallet, for their invaluable guidance, patience, and expertise throughout this research journey. Aurélien's deep knowledge in optics, infrared spectroscopy, and near-field techniques, combined with Jérémy's expertise in materials science, provided the perfect complementary supervision for this interdisciplinary work. Their insightful feedback and unwavering support have been instrumental in shaping this research and my development as a researcher. They have become great mentors and icons in the academic world. I have known Aurélien for almost a decade, since I entered UTT as a freshman back in 2016. His profound knowledge in physics has always impressed me, and his ability to explain complex concepts with clarity has been a constant source of inspiration. Throughout these years, he has not only been a supervisor but also a mentor who taught me the importance of scientific rigor and intellectual curiosity. Jérémy, whom I have known since the beginning of this journey, has been more than a scientific advisor guiding me through the intricacies of materials science and research methodology. He has been a friend with whom I shared my hobbies, long discussions about science and life, and moments of both triumph and doubt. His approachable nature and genuine interest in my personal and professional growth have made this doctoral experience truly enriching. His door was always open for questions, whether they were about experimental procedures, career advice, or simply life in general. Together, Aurélien and Jérémy created an environment where scientific excellence and personal development could flourish. Their complementary expertise and collaborative approach have shown me the true value of interdisciplinary research and the importance of building bridges between different fields of knowledge. I am deeply grateful for their mentorship and friendship, which will undoubtedly influence my future endeavors in academia and beyond.

I would like to express my sincere gratitude to the jury members for agreeing to be part of the committee despite their demanding schedules and for dedicating time to read the thesis and participate in my defense. I am especially grateful to Professors Laurene Tetard, Vincent Mauchamp, Yannick de Wilde, Michel Kazan, Benoit Hackens and Yury Gogotsi for their thorough evaluations and perceptive feedback, as well as for their thoughtful questions and observations.

I would like to extend my heartfelt appreciation to the Light Nanomaterials

Nanotechnologies laboratory at the University of Technology of Troyes, where I have had the privilege of conducting all my higher education studies over the past nine years. This institution has been my academic home, witnessing my growth from an undergraduate student to a doctoral researcher, and has provided the excellent research environment and resources that made this work possible. I am also grateful to the Grand Est Region and the EUR Nano-Phot program led by Prof. Renaud Bachelot for their financial support. I am honored to have received the Fulbright Grand Est Excellence Fellowship, which provided me with invaluable opportunities for international research collaboration.

During my first year, I was fortunate to receive guidance from postdoctoral researcher Dr. Camilo Perez de la Vega, whose expertise and mentorship were crucial during the initial stages of my research.

My sincere thanks go to Dr. Kuan-Ting Wu and Dr. Youssef El-Helou, who were PhD students at the time, for their patient training on the PiFM system. This incredibly complex instrument, which kept me awake through countless nights of troubleshooting and contemplation, became more manageable thanks to their initial guidance. I am particularly grateful to Dr. Derek Nowak, Director of Applications at Molecular Vista, for his exceptional technical support throughout my work with the PiFM system. His prompt responses to my numerous questions, whether through calls or emails, and his expertise in troubleshooting complex issues were invaluable to the success of this research.

I would like to acknowledge my enriching research stay at Drexel University's A.J. Drexel Nanomaterials Institute under the supervision of Prof. Yury Gogotsi. This international collaboration broadened my research perspective and provided access to unique facilities and expertise. Special thanks to Dr. Tetiana Parker for her collaboration and support during my time at Drexel.

I am grateful to my colleague and office mate Antoine Elie for his collaboration on the SPR aspects of this work. His expertise and collaborative spirit contributed significantly to the success of this research. Beyond our professional collaboration, I also cherish the moments of friendship and camaraderie we shared, which made the daily work environment both productive and enjoyable.

Special thanks to Antoine Dussard, who provided essential technical support in helping me fabricate substrates for my experiments. Beyond his technical expertise, Antoine offered friendship and companionship that made this journey more enjoyable and meaningful.

On a personal note, I am profoundly grateful to my family, my friends and my partner for their unconditional love, encouragement, and understanding throughout these long years of study. Their constant support and belief in me have been a source of strength and motivation during the most challenging moments of this doctoral journey.

Finally, I would like to thank all the technical and administrative staff who contributed to creating the excellent research environment that made this work possible.

Kevin KIM
Troyes, October 2025

Contents

Acknowledgments **ii**

Introduction **1**

1 State of the Art on 2D Materials and MXenes **7**
1.1 Short review of two-dimensional materials in optics 7
1.1.1 Graphene: the pioneer of 2D photonics 10
1.1.2 Transition Metal Dichalcogenides (TMDs) 11
1.1.3 Black Phosphorus (BP) 12
1.1.4 Hexagonal Boron Nitride (hBN) 13
1.2 The emergence of 2D transition metal carbides and nitrides 15
1.2.1 MAX phase precursors 17
1.2.2 MXenes synthesis 17
1.2.3 Effect of synthesis methods on the structure 19
1.2.4 MXene surface chemistry 20
1.3 Optical properties of MXenes 24
1.3.1 Plasmonic properties 24
1.3.2 MXenes for plasmonic devices 26

2 Fundamental aspects of far-field and near-field infrared methods for characterizing MXenes **31**
2.1 Introduction to the infrared spectroscopy 31
2.2 Scattering-type scanning near-field optical microscopy (s-SNOM) . . . 38
2.2.1 Interferometric Detection in s-SNOM 41
2.2.2 The Generalized Lock-In Amplifier (G-LIA) 44
2.3 Photo-induced force microscopy (PiFM) 46
2.3.1 Theoretical description of PiFM 46
2.3.2 PiFM model based on effective polarizability enhanced absorption 54
2.4 A comparative study of PiFM and s-SNOM on semi-conductors . . . 55

3 Far-field infrared characterization of MXenes: chemical composition and electrochemical interface studies **63**
3.1 The influence of the carbon-to-nitrogen ratio in $Ti_3C_yN_{(2-y)}T_x$ MXene on the infrared properties 63
3.1.1 IR reflectance 69
3.1.2 IR emission 71
3.1.3 Density functional theory calculations 76
3.1.4 Modeling of infrared reflectance: the Drude approach 78

3.2 Infrared in-situ probing of ion intercalations in $Ti_3C_2T_x$ MXene . . . 80
3.2.1 Electrochemical cell setup on FTIR-ATR crystal 81
3.2.2 Results and Discussion 83
3.2.3 Conclusions and future perspectives 86

4 Optical near-field properties of 2D MXenes using IR nanoscopy 89
4.1 Pure optical analysis of $Ti_3C_2T_x$ probed by s-SNOM 90
4.2 Surface terminations of MXenes 92
4.2.1 PiFM analysis of pristine $Ti_3C_2T_x$ and V_2CT_x MXenes 93
4.3 Oxydation and carbon defects probing on Nb_2CT_x 96
4.3.1 Raman and FTIR responses of the bulk Nb_2CT_x 97
4.3.2 PiFM response on bulk Nb_2CT_x 99
4.3.3 PiFM response of single/few-layered of Nb_2CT_x flakes 101
4.4 Nanoscale observation of siloxane compounds on titanium carbonitride MXenes 103
4.4.1 $Ti_3C_{1.5}N_{0.5}T_x$ structural characterization 105
4.4.2 Far-field vibrational spectroscopy 107
4.4.3 Local infrared properties 108
4.4.4 Spectral mapping 112

5 Application of MXene for sensing using Surface Plasmon Resonance 118
5.1 MXene thin-film deposition monitored by SPR 123
5.1.1 Current Methods for MXene Film Fabrication 123
5.1.2 Microfluidic-Assisted Deposition of MXene Films Monitored by SPR 124
5.1.3 MXene film deposition via controlled sedimentation 126
5.1.4 Determination of the dielectric constant of MXene 131
5.2 (3-Aminopropyl)triethoxysilane detection using MXene 134

General conclusion 140

Appendix A 143

Bibliography 148

Résumé français 175

Introduction

The discovery of graphene in 2004 by Novoselov and Geim [1] marked a pivotal moment in materials science, inaugurating the era of two-dimensional (2D) materials. This groundbreaking achievement, recognized with the Nobel Prize in Physics in 2010, demonstrated that atomically thin materials could not only exist in stable conditions but also exhibit extraordinary properties distinct from their bulk counterparts. Since this seminal discovery, the field of 2D materials has expanded exponentially, encompassing a diverse array of layered structures. Beyond graphene, with its remarkable electronic mobility exceeding 200,000 $cm^2/V{\cdot}s$ and exceptional mechanical strength, other 2D materials have emerged with complementary properties. Hexagonal boron nitride (h-BN), often referred to as "white graphene," exhibits excellent dielectric properties with a large bandgap of 5.9 eV and remarkable thermal conductivity, making it an ideal substrate and insulating layer for 2D heterostructures [2]. Transition metal dichalcogenides (TMDs) such as MoS_2, WS_2, and WSe_2 possess direct bandgaps in their monolayer form, enabling efficient light-matter interactions and applications in optoelectronics [3]. Black phosphorus presents highly anisotropic electronic and optical properties with a thickness-dependent bandgap ranging from 0.3 to 2.0 eV, bridging the gap between graphene and TMDs [4]. These materials collectively offer a rich palette of unique electronic, optical, mechanical, and chemical characteristics [5, 6]. More recently, MXenes have emerged as a particularly promising class of materials with exceptional potential for various technological applications. First discovered in 2011 by Naguib *et al.* at Drexel University [7], MXenes represent a family of 2D transition metal carbides, nitrides, and carbonitrides with the general formula $M_{n+1}X_nT_x$, where M denotes an early transition metal (e.g., Ti, V, Nb, Mo), X represents carbon and/or nitrogen, and T_x indicates surface terminations (e.g., -OH, -O, -F) [8].

Recent advances in computational materials science, particularly through the integration of artificial intelligence and high-throughput screening methodologies, have significantly accelerated the theoretical prediction of novel 2D materials. Current databases suggest the potential existence of over 6,000 theoretically stable 2D materials, representing an enormous untapped reservoir of materials with potentially transformative properties [9, 10]. This expanding theoretical landscape includes Xenes (silicene, germanene, stanene), which exhibit topologically non-trivial states and tunable bandgaps [11]; 2D metal oxides (e.g. V_2O_5) with exceptional electrochemical properties for energy storage applications [12]; and emerging monoelemental 2D materials like antimonene and bismuthene with promising thermoelectric performance [13]. However, the experimental realization of these theoretically predicted structures remains challenging, with approximately 100 distinct 2D materials successfully synthesized and characterized to date [14]. This stark disparity between theoretical predictions and experimental achievements underscores the

critical importance of advanced synthesis techniques and precise characterization methodologies.

The characterization of 2D materials presents unique challenges that distinguish them from conventional bulk materials. Their atomically thin nature, often comprising just a few atomic layers, necessitates characterization techniques with exceptional sensitivity and spatial resolution. Moreover, many 2D materials exhibit anisotropic properties, with dramatically different behaviors perpendicular and parallel to their basal planes. For instance, group-VI TMDs display in-plane thermal conductivities approximately 100 times greater than their cross-plane values [15], while MXenes demonstrate significant anisotropy in their electrical and optical responses due to their metal-like in-plane conductivity contrasted with semiconductor-like behavior across layers [8]. Layered double hydroxides (LDHs) exhibit unique intercalation chemistry that varies substantially between surface and interlayer regions. Even within the same family, properties can vary dramatically—borophene polymorphs display metallic, semiconducting, or superconducting behavior depending on their precise atomic arrangement [16]. These distinctive characteristics render traditional bulk characterization methods inadequate, necessitating specialized approaches capable of probing properties at the nanoscale.

Furthermore, the physics governing phenomena at the nanoscale often deviates significantly from macroscopic behaviors, with quantum confinement effects and enhanced surface-to-volume ratios fundamentally altering material properties. Consequently, the development of novel characterization techniques specifically tailored for nanoscale analysis has emerged as a critical research frontier. The evolution of techniques such as scanning electron microscopy (SEM), developed in the early 1930s by Knoll and Ruska [17], has revolutionized our ability to visualize conductive samples with nanometer resolution. This evolution has continued with the emergence of near-field microscopy techniques, which have transcended the traditional diffraction limit of optical investigations. Scanning Near-field Optical Microscopy (SNOM), pioneered by Pohl and colleagues in the 1980s [18], marked a paradigm shift by exploiting evanescent waves to achieve sub-wavelength spatial resolution. By positioning a nanoscale aperture or tip within the near-field region of a sample (typically $<$50 nm), SNOM enabled optical imaging and spectroscopy with a resolution approximately one order of magnitude beyond the diffraction limit. The subsequent development of Atomic Force Microscopy-based Infrared Spectroscopy (AFM-IR), introduced by Dazzi et al. in the early 2000s [19], further enhanced our capabilities by detecting photo-thermal expansion of samples illuminated with infrared radiation, thereby providing simultaneous topographical and chemical mapping at nanoscale resolution. This technique leverages the contact mode of AFM to transduce the infrared absorption-induced thermal expansion into cantilever deflections, offering unprecedented insights into molecular compositions at the nanoscale.

Most recently, Photo-induced Force Microscopy (PiFM), developed by Rajapaksa et al. [20] and further refined by Jahng et al. [21], has pushed the boundaries of near-field spectroscopy by directly measuring the dipole-dipole interactions between the tip and sample upon infrared illumination. Operating in non-contact mode, PiFM detects the gradient force arising from the interaction between the optically-induced dipoles in both the tip and sample, providing exceptional sensitivity to surface chemistry with spatial resolution approaching 10 nm. These advances in scanning probe microscopies, spectroscopic methods, and synchrotron-based tech-

niques have dramatically expanded our capacity to interrogate the fundamental properties of 2D materials with unprecedented spatial and chemical resolution [22], enabling detailed investigations of localized phenomena that would otherwise remain inaccessible through conventional far-field approaches.

Among the expanding family of 2D materials, recent research from Drexel University has highlighted the unprecedented global interest in MXenes, with the number of publications and patents related to these materials increasing exponentially since their discovery [23]. According to Anasori *et al.*, this surge in research activity reflects the extraordinary versatility of MXenes across multiple technological domains, with particular emphasis on their potential for next-generation energy storage devices, electromagnetic interference shielding, and advanced sensing applications.

A particularly fascinating aspect of MXenes lies in their exceptional optical properties and plasmonic behavior. Groundbreaking research by El-Demellawi *et al.* has demonstrated that $Ti_3C_2T_x$ MXene flakes exhibit tunable multipolar surface plasmons that can be systematically controlled by varying the lateral flake dimensions and thickness [24]. This discovery positions MXenes as highly promising candidates for next-generation plasmonic devices, with potential applications in biosensing, photocatalysis, and optoelectronic technologies. Furthermore, theoretical investigations by Mauchamp *et al.* have revealed that the electronic structure and dielectric properties of MXenes can be precisely modulated through compositional engineering and surface functionalization, offering unprecedented opportunities for tailoring their optical response across a broad spectral range [25].

Despite these promising findings and the rapidly growing body of research on MXenes, comprehensive optical characterization of these materials remains relatively limited, particularly concerning the correlation between their macroscopic response and nanoscale heterogeneities. While the infrared spectral region is of paramount importance because it encompasses the vibrational frequencies of most organic functional groups and provides crucial insights into the surface chemistry and structural configurations of MXenes [8]. A broader understanding of their dielectric response from the visible to the mid-infrared is essential and relevant for applications in sensing, photonics, and optoelectronics, where the interaction between electromagnetic radiation and material properties fundamentally determines device performances [26]. Understanding these optical properties is crucial as they serve as a non-destructive diagnostic tool for the material's electronic structure and carrier density.

This doctoral thesis aims to address these knowledge gaps by providing a comprehensive framework for the optical characterization of MXenes across multiple scales. The research presented herein adopts a multifaceted approach, encompassing three principal areas of investigation:

Firstly, we aim to address the synthesis of MXenes from their corresponding MAX phases, detailing the rigorous protocols established to obtain high-quality MXene sheets. It discusses the fabrication of different types of samples according to their specific applications, through different techniques. We emphasize the importance of structural characterization to ensure the reproducibility of material properties, essential for reliable optical characterization.

Secondly, we conduct comprehensive far-field optical characterization of MXene samples using conventional spectroscopic techniques, including Fourier-transform infrared spectroscopy (FTIR), Raman spectroscopy, and ultraviolet-visible spec-

troscopy. While these investigations reveal valuable insights into the collective optical response of MXene ensembles, the diffraction-limited spatial resolution of far-field techniques emerges as a significant limitation for probing localized phenomena and heterogeneities at relevant length scales.

Finally, to overcome these spatial resolution constraints, the third phase of our research employs advanced near-field nanoscopy techniques, specifically photo-induced force microscopy (PiFM). This cutting-edge approach enables simultaneous topographic and spectroscopic mapping with nanometer spatial resolution, circumventing the diffraction limit that constrains conventional optical methodologies. By implementing this technique, we achieve unprecedented insights into the localized optical properties of MXenes at the nanoscale, elucidating structure-property relationships that remain inaccessible through traditional characterization approaches.

Through this research program, we aim to bridge the gap between molecular structure and macroscopic behavior. The findings not only contribute to the fundamental understanding of MXene optical properties across the visible and infrared ranges but also provide a methodological roadmap for their integration into advanced technological applications, from electrochemical sensors to infrared shielding.

Thesis organisation

In addition to the general introduction, this thesis consists of five main chapters and it is structured as follows:

Chapter 1 provides a detailed literature review of 2D materials, with particular emphasis on the synthesis, structure, and optical properties of MXenes. Beginning with the historical development of two-dimensional materials from graphene's discovery to the present day, it traces the evolution of this rapidly expanding field. The chapter then focuses on MXenes as an emergent class of materials with significant potential for optical applications, introducing their fundamental structure as 2D transition metal carbides and nitrides. It explores in detail the MAX phase precursors from which MXenes are derived, the various synthesis methodologies employed for their production, and how these synthesis approaches directly influence structural characteristics. Special attention is given to MXene surface chemistry, highlighting the critical role of surface terminations (T_x) in determining material properties and application potential. The final section examines the current understanding of MXene optical properties, with particular focus on their plasmonic behavior, infrared response, and potential for applications in optical sensing, electromagnetic shielding, and optoelectronic devices.

Chapter 2 presents the theoretical foundations and methodological approaches for multi-scale study of MXenes, including fundamental principles of light-matter interactions and the foundations of near-field microscopy techniques. This chapter develops the conceptual framework required to understand optical phenomena in 2D materials across different length scales. It explores how electromagnetic radiation interacts with atomically thin layers, with special focus on the infrared spectral region where most organic functional groups exhibit distinctive vibrational signatures. The chapter introduces the limitations of conventional diffraction-limited techniques and delves into the theoretical underpinnings of near-field microscopy. Particular emphasis is placed on Photo-induced Force Microscopy (PiFM), eluci-

dating the dipole-dipole interaction model, the origin of photo-induced forces, and the physical mechanisms enabling nanoscale chemical mapping with this technique. Through theoretical models and experimental considerations, this chapter builds the methodological foundation for the multi-scale characterization approach employed throughout the thesis.

Chapter 3 examines the far-field infrared characteristics of MXenes by addressing two key research areas: the relationship between chemical composition and optical properties, and the real-time monitoring of electrochemical interface processes.

The first section investigates the influence of carbon-to-nitrogen ratio in $Ti_3C_{(2-y)}N_yT_x$ MXene on infrared properties through systematic experimentation with varying C/N ratios (y = 0, 0.25, 0.5, and 1). This study demonstrates that compositional tuning serves as a powerful lever for modulating optical response, revealing how nitrogen incorporation modifies crystal structure while preserving the fundamental MXene architecture. The analysis shows that higher carbon content enhances IR reflectance (ideal for shielding applications), while increased nitrogen content elevates emissivity. Experimental findings are correlated with density functional theory calculations to establish mechanisms for engineering infrared response through precise compositional control.

The second section develops infrared spectroscopy as an in-situ probe for investigating electrochemical processes in $Ti_3C_2T_x$ MXene electrodes. Using attenuated total reflection Fourier-transform infrared spectroscopy (ATR-FTIR), this work monitors Li^+ intercalation processes in real-time by tracking water molecule displacement from MXene interlayers. A custom two-electrode electrochemical cell integrated with a diamond ATR crystal enables real-time monitoring of vibrational modes during charge-discharge cycling, providing direct insights into intercalation mechanisms and structural changes within the MXene interlayer space.

Chapter 4 focuses on the recognition of chemical surface terminations and surface modification of 2D MXenes using IR nanoscopy, demonstrating the capabilities of PiFM to identify both native surface functional groups and environmental contaminants at the nanoscale. This chapter leverages the chemical specificity and spatial resolution of photo-induced force microscopy to investigate surface chemistry at unprecedented scales. It reveals the surface functional groups present on pristine Ti_3C_2Tx and $Ti_3C_{1.5}N_{0.5}T_x$ MXenes, identifying characteristic chemical bonds such as C=C, C–H, C–O, and C–F related to the terminal groups. The chapter also investigates Nb_2CT_x MXene through complementary far-field and near-field spectroscopic techniques, with particular emphasis on PiFM's capacity to detect nanoscale oxidation phenomena. This analysis reveals distinctive absorption features in the 770–1860 cm^{-1} range, notably the characteristic peaks around 950–980 cm^{-1} associated with niobium oxide formation. Remarkably, PiFM demonstrates enhanced sensitivity in detecting these oxidation signatures even in single/few-layered MXene flakes with thicknesses as low as 15 nm, highlighting the sensitivity at the nanoscale.

Additionally, the chapter demonstrates PiFM's ability to detect and map siloxane-based contamination on aged MXene flakes, specifically identifying Si–C and Si–O–Si bonds distributed uniformly across the surface, that remain undetectable by conventional spectroscopic techniques. The chapter explores the reaction mechanisms between MXene's hydroxyl terminations and siloxane compounds,

providing insights into surface modification processes and highlighting the preferential binding to surface sites rather than edges. Through comparative analysis with conventional spectroscopic methods, it establishes PiFM as an essential tool for investigating nanoscale surface chemistry in 2D materials, with profound implications for understanding environmental interactions and developing strategic approaches to surface functionalization.

Chapter 5 explores the application of MXenes for sensing using surface plasmon resonance, focusing specifically on thin-film deposition processes and molecular detection capabilities. This chapter transitions from fundamental characterization to practical applications, demonstrating the integration of MXenes into functional sensing platforms. The first section investigates the real-time monitoring of MXene thin-film deposition using the surface plasmon resonance technique, providing insights into film formation dynamics, thickness control, and surface coverage uniformity. The second section explores the detection of (3-Aminopropyl)triethoxysilane (APTES) using MXene-based SPR sensors, leveraging the surface chemistry insights gained from previous chapters, particularly the siloxane-MXene interactions identified through PiFM analysis. This investigation establishes proof-of-concept for MXene applications in chemical sensing and demonstrates how the unique surface properties of these 2D materials can be harnessed for detecting specific molecular compounds, opening pathways for developing advanced sensing technologies based on MXene platforms.

This research progression—from fundamental synthesis to far-field optical characterization and finally to near-field nanoscopic investigations—establishes a complete picture of MXene infrared properties across multiple length scales and demonstrates their potential for technological applications in sensing and beyond. The thesis advances both fundamental understanding of MXene surface chemistry and optical properties while providing practical insights for their implementation in advanced optical technologies.

Chapter 1

State of the Art on 2D Materials and MXenes

1.1 Short review of two-dimensional materials in optics . . . 7

1.1.1 Graphene: the pioneer of 2D photonics 10

1.1.2 Transition Metal Dichalcogenides (TMDs) 11

1.1.3 Black Phosphorus (BP) 12

1.1.4 Hexagonal Boron Nitride (hBN) 13

1.2 The emergence of 2D transition metal carbides and nitrides 15

1.2.1 MAX phase precursors 17

1.2.2 MXenes synthesis 17

1.2.3 Effect of synthesis methods on the structure 19

1.2.4 MXene surface chemistry 20

1.3 Optical properties of MXenes 24

1.3.1 Plasmonic properties 24

1.3.2 MXenes for plasmonic devices 26

1.1 Short review of two-dimensional materials in optics

The discovery of graphene in 2004 opened the door to a new generation of materials science called 2D materials. The field has since developed into a subdiscipline including graphene, transition metal dichalcogenides (TMDs), black phosphorus (BP), and hexagonal boron nitride (hBN) with different optical properties suitable for photonic applications [27, 28].

The transition from bulk to two-dimensional materials introduces changes in their optical and electronic properties due to quantum confinement effects and reduced dimensionality. Unlike bulk counterparts, 2D materials show layer-dependent optical bandgaps, enhanced electron-electron interactions, and modified symmetry

properties that fundamentally alter light-matter interactions [27]. The strong intralayer covalent bonding together with weak interlayer van der Waals forces allows the isolation of individual atomic layers while preserving the structural integrity and introducing new optical phenomena.

A sharp reduction in atomic-scale thickness yields sharply enhanced nonlinear optical responses compared to bulk materials. This enhancement is due to relaxed phase-matching requirements, stronger light confinement, and modified selection rules derived from 2D geometry [29]. Many TMDs switch from indirect to direct bandgap upon scaling down from bulk to monolayer form, thereby modifying their photoluminescence efficiency and opening up new optoelectronic applications [30].

Electronic properties of 2D materials extend from semimetallic graphene with linear Dirac dispersion to semiconducting behavior of TMDs with tunable bandgaps from 1-2 eV, with a moderate bandgap of black phosphorus (0.3-2 eV depending on thickness) and finally to the wide bandgap insulating properties of hBN (6 eV) [31, 32]. Such diversity constitutes a complete electronic toolkit for constructing a tailor-made optical device.

The possibility of forming van der Waals heterostructures by stacking different 2D materials without lattice matching constraints has provided unprecedented opportunities to engineer optical properties. Such heterostructures may be fabricated via direct mechanical assembly, chemical vapor deposition growth, or van der Waals epitaxy to yield materials with designer optical responses [33]. Type-I and Type-II band alignments in such heterostructures permit efficient charge separation, interlayer exciton formation and novel optical phenomena such as moire-induced superlattice effects.

The best property of 2D materials is their excellent ability to be tune under various external stimuli. Electrical gating modulates carrier density and hence optical conductivity allowing electrically tunable optical modulators and switches. Bandgap tuning and symmetry breaking can be achieved by mechanical strain engineering whereas thermal effects can induce reversible optical property changes. In addition to this, magnetic fields can induce valley polarization and magneto-optical effects in TMDs where spin-valley coupling opens up new degrees of freedom for light manipulation [27].

The following sections will provide detailed examinations of the four primary classes of 2D materials in optics: graphene, transition metal dichalcogenides, black phosphorus, and hexagonal boron nitride. This analysis will establish a reference framework of optical properties, advantages, and limitations of each material family, serving as a comparative basis for evaluating the emergence of MXenes.

A comparative study of these historical materials will reveal their respective constraints: the limited conductivity and environmental sensitivity of 2D semiconductors, the functionalization challenges of graphene, and the processing difficulties of black phosphorus. This analysis will position MXenes as a new class of 2D materials that uniquely combines the metallic conductivity of graphene, hydrophilic surfaces facilitating functionalization, and superior aqueous solution processability compared to conventional 2D materials.

This systematic comparison of physical, chemical, and processing properties will demonstrate how MXenes distinguish themselves from existing 2D materials and represent the next generation of two-dimensional materials, thus constituting the primary focus of this research work.

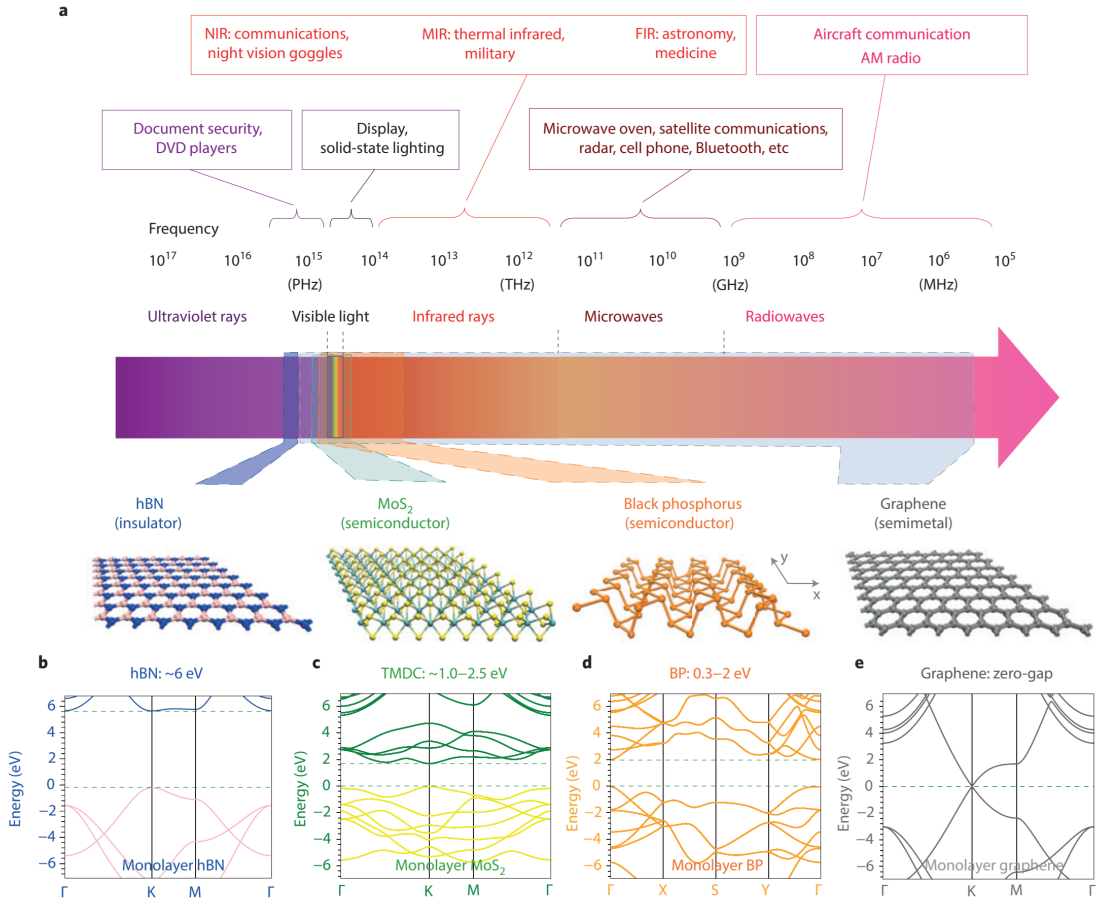

Figure 1.1: 2D materials covering a broad spectral range. (a) Electromagnetic spectrum. Applications that utilize the different spectral ranges are presented in the top portion of the panel. NIR, MIR and FIR indicate near-, mid- and far-infrared, respectively. The atomic structures of hBN, MoS_2, BP and graphene are shown in the bottom of the panel, left to right. The crystalline directions (x and y) of anisotropic BP are indicated. The possible spectral ranges covered by different materials are indicated using coloured polygons. (b–e) Bandstructures of single-layer hBN (b), MoS_2 (c), BP (d) and graphene (e). Extracted from [32].

1.1.1 Graphene: the pioneer of 2D photonics

Isolation of graphene by Novoselov and Geim at the University of Manchester in 2004 is one of the most important breakthroughs in materials science of the 21st century [34]. They isolated single-atom-thick crystallites from bulk graphite using the simple "Scotch tape" technique, demonstrating that true two-dimensional crystals can exist free-standing under ambient conditions [35]. This pioneering work, which earned them the 2010 Nobel Prize in Physics, opened an entirely new field of research and established graphene as the most typical 2D material.

Material structure and electronic properties

Graphene is made of one layer of carbon atoms in a hexagonal honeycomb lattice, with each carbon atom being sp^2-hybridized and covalently bonded to three other atoms. This structure leads to very different electronic properties than ordinary semiconductors. The electronic band structure shows linear dispersion relations forming Dirac cones at the K and K′ points of the Brillouin zone near the Fermi energy level (Figure 1.1(e)). As shown in the band diagram, the valence and conduction bands meet precisely at zero energy at these high-symmetry points, creating the characteristic zero-gap semiconductor behavior. As a consequence, charge carriers in graphene behave like massless Dirac fermions, whose extremely high mobility exceeds 10,000 $cm^2V^{-1}s^{-1}$ at room temperature [34].

The linear energy-momentum relationship near the Dirac points, evident from the conical band structure, gives rise to a constant Fermi velocity $v_F \approx 10^6$ m/s, approximately 1/300 of the speed of light. Because graphene has a zero bandgap nature and this linear dispersion, it produces an ambipolar electric field effect where both electrons and holes can be induced in concentrations up to 10^{13} cm^{-2} with gate voltages. The Fermi level, indicated by the dashed line at zero energy, can be electrostatically shifted above or below the Dirac point, enabling precise control of carrier type and concentration. This unique electronic structure makes graphene an ideal platform for electrically tunable optical devices.

Optical properties, light-matter interaction and electrical tunability

Despite being only 1 atom thick, graphene has excellent optical properties. It absorbs approximately 2.3% of the incident light in a broad spectral range from ultraviolet to terahertz frequencies and is one of the most optically active 2D materials [36]. Such universal optical absorption is obtained from linear band structure and constant optical conductivity, with $\sigma_0 = \frac{e^2}{4\hbar} \approx 6.08 \times 10^{-5}$ S in the optical regime.

In the infrared range, graphene supports surface plasmon polaritons with strong confinement and long propagation lengths. These graphene plasmons are excited and controlled electrically providing unprecedented opportunities for active plasmonic devices. Plasmonic resonance frequency scales as $\sqrt{n}$, where n is the carrier density allowing wide tunability by electrical gating [37].

The most remarkable property of graphene is the electrical tuning of its optical properties via Fermi level modulation. Applying gate voltages can shift the Fermi energy from the Dirac point to either conduction or valence bands, thereby changing the optical response [38].

Key optical applications

Broadband optical response coupled with electrical tunability makes graphene an attractive platform for many photonic applications. Graphene-based electro-absorption modulators operate at visible to terahertz wavelengths with modulation depths of 0.1 dB/mm at operation speeds exceeding 10 GHz for telecommunications [39]. As saturated absorbers, graphene has provided the basis for ultrafast laser technology, mode-locking, and Q-switching over broad wavelengths to give rise to femtosecond and picosecond pulses with excellent stability [40]. Despite its zero bandgap, graphene photodetectors show outstanding performance in photoconductivity, photovoltaic, and bolometric modes from ultraviolet to terahertz with sub-picosecond response times [41]. Electrically tunable graphene plasmons also provide opportunities for reconfigurable metamaterials and perfect absorbers, and its high optical transparency (97.7%) and good electrical conductivity make it attractive for next-generation transparent electrodes [42].

Graphene success in photonics demonstrated the potential of 2D materials and established key principles and device architectures for future 2D material platforms. Its pioneering role has opened up other specialized 2D materials with adapted optical properties for specific applications.

1.1.2 Transition Metal Dichalcogenides (TMDs)

Transition metal dichalcogenides (TMDs) represent a fascinating class of layered 2D materials with the general chemical formula MX_2, where M denotes a transition metal atom (Mo, W, Ti, etc.) and X represents a chalcogen atom (S, Se, or Te) [30]. These materials consist of a hexagonally packed transition metal layer sandwiched between two chalcogen layers, forming a three-atomic-plane structure with a typical thickness of 6-7 Å per monolayer [43]. The individual layers are held together by weak van der Waals forces, while strong covalent bonds exist within each layer.

Crystal Structure and Polymorphism

TMDs show three principal polymorphs: trigonal (1T), hexagonal (2H), and rhombohedral (3R) characterized by stacking sequences [43]. The 2H phase is the most stable thermodynamically among these. Crystal structure influences the electronic properties: 2H-MoS_2 is semiconducting while 1T polymorph is metallic [44]. The four electrons that the metal atoms provide fill the bonding states, giving oxidation states of +4 for the metal and -2 for the chalcogen atoms.

Layer-Dependent Electronic Properties

One of the most remarkable features of TMDs is the modification of their electronic band structure with layer thickness [45]. Bulk TMDs have a typical indirect bandgap, whereas monolayer TMDs have a direct bandgap at the K points of the hexagonal Brillouin zone (Figure 1.1(c)). This change from indirect to direct bandgap behavior fundamentally alters the optical and electronic properties of these materials.

For monolayer TMDs such as MoS_2, WS_2, $MoSe_2$, and WSe_2, the direct bandgap ranges from 1.57 to 2.0 eV [46]. This layer-dependent behavior is due to quantum

confinement effects and altered interlayer coupling. This indirect-to-direct transition may occur at different layer numbers based on the specific TMD: at the bilayer for 2H-WSe_2 and at the tetralayer for 2H-WTe_2 [47].

Optical Properties and Tunability

Due to reduced dielectric screening and quantum confinement in the 2D limit, TMDs exhibit extremely strong excitonic effects with exciton binding energies several hundred meV higher than those of conventional 3D semiconductors [48]. Two prominent excitonic transitions (A and B) from spin-orbit splitting of the valence band are reflected in the optical spectra, while a single monolayer absorbs up to 20% of incident light [49].

Monolayer TMDs possess broken inversion symmetry, leading to valley-dependent optical selection rules: right circularly polarized photons (σ^+) couple to the K^+ valley, while left circularly polarized photons (σ^-) couple to the K^- valley [50]. Combining spin-valley coupling and optical selection rules provides a basis for valleytronic applications directly addressing valley states [51].

TMDs' optical properties are tuned by external parameters. Mechanical strain engineering allows for bandgap modulation and can induce direct-to-indirect bandgap transitions [52]. The dielectric environment influences excitonic properties via screening effects [53], whereas electrostatic gating controls carrier density and optical response [54]. Additionally, van der Waals heterostructures allow the formation of interlayer excitons with spatially separated electrons and holes, having long recombination lifetimes and tunable properties via external influences such as electric fields, temperature, and twist angles [55].

The tunability, together with the deep physics of TMDs including layer-dependent bandgap engineering, strong excitonic effects, valley physics, and heterostructure formation make these materials ideal platforms for next-generation optoelectronic devices and fundamental studies of 2D quantum materials [56].

1.1.3 Black Phosphorus (BP)

Structure and Electronic Properties

Black phosphorus (BP), also known as phosphorene is one of the most promising 2D materials for tunable photonic applications. Unlike graphene and most TMDs, BP has a puckered honeycomb crystal structure with three neighboring phosphorus atoms covalently bonded to each other [57]. Its unique structure results in strongly anisotropic properties along the armchair (x-direction on Figure 1.1(d)) and in zigzag (y-direction on Figure 1.1(d)) crystallographic directions. The direct bandgap of BP is layer-dependent, which can be tuned continuously from 0.3 eV in bulk form to 2.0 eV in monolayer phosphorene [57]. BP's thickness-dependent bandgap makes it attractive for mid-infrared applications since few-layer BP operates in the technologically important 3-5 mm atmospheric window. In addition, BP shows a carrier mobility greater than 1000 $cm^2V^{-1}s^{-1}$.

Optical Properties and Tunability

This anisotropic crystal structure of BP leads directly to highly anisotropic optical properties. The material shows polarization-dependent absorption and photolumi-

nescence with different responses along the armchair and in zigzag directions [58]. This intrinsic anisotropy allows special photonic applications like polarization-sensitive photodetectors and integrated polarizers. BP has a strong optical absorption in the mid-infrared region due to its moderate direct bandgap, and the absorption spectrum is highly dependent on the number of layers and the incident light polarization, thus allowing for the engineering of the optical response by controlling the material thickness and the orientation [59]. BP optical properties can be tuned by several mechanisms. Electrical gating permits the modulation of carrier density and thus the optical absorption via the Pauli-blocking effect. The Quantum-confined Stark effect and Franz-Keldysh effect are particularly prominent under out-of-plane electric fields, enabling voltage-controlled bandgap tuning [60]. The high mechanical flexibility of the material allows for another powerful approach for BP tunability - strain engineering.

Applications in Tunable Photonics

BP has demonstrated exceptional performance in mid-infrared photodetection applications. High-responsivity photodetectors with external responsivity up to 82 AW^{-1} at 3.39 μm wavelength have been achieved [61]. The polarization-sensitive response enables development of integrated polarization analyzers and anisotropic photodetectors. In the field of ultrafast photonics, BP serves as an excellent saturable absorber for mode-locked fiber lasers operating at 2-3.5 μm wavelengths [62, 63]. Broadband absorption and fast carrier dynamics make this material suitable for ultrashort pulse generation in the mid-infrared region. However, the practical implementation of BP-based devices faces significant challenges due to the material's degradation in ambient conditions. Efforts to develop effective passivation strategies like encapsulation with hexagonal boron nitride or integration with chalcogenide glasses are still required to exploit the full potential of BP in tunable photonic applications [64].

1.1.4 Hexagonal Boron Nitride (hBN)

Structure and Electronic Properties

Hexagonal boron nitride (hBN) has the honeycomb crystal structure of graphene but has alternating boron and nitrogen atoms in a polar lattice. This structural similarity, with differing atomic compositions, leads to dramatically different electronic properties. In contrast to the semimetallic graphene, hBN is a broad-bandgap insulator with a direct bandgap of about 6 eV [65]. The ionic character of B-N bonds, resulting from the electronegativity difference between boron and nitrogen atoms, gives hBN polar optical property while maintaining good thermal and chemical stability.

Because hBN is polar, it exhibits strong ionic bonding characteristics unlike other 2D materials. This polarity is the basis of its outstanding properties, allowing unique light-matter interactions in the mid-infrared spectral region. High-quality crystalline structure and a wide bandgap make hBN suitable for polaritonic applications where low losses and high field confinement are required.

Phonon Polaritons and Hyperbolic Properties

The polar optical phonons in hBN couple strongly with electromagnetic radiation, yielding phonon polaritons with excellent confinement and propagation properties. In the mid-infrared region, BN shows hyperbolic dispersion behavior with two distinct Reststrahlen bands where permittivity becomes negative along different crystallographic directions [66]. This naturally occurring hyperbolic behavior permits sub-diffractional confinement of electromagnetic fields exceeding the performance of artificially engineered hyperbolic metamaterials.

The hyperbolic dispersion in hBN is represented by Type I hyperbolic behavior (about 1370-1610 cm^{-1}) with a negative in-plane permittivity, while the positive out-of-plane component and Type II behavior (about 780-830 cm^{-1}) with an opposite sign configuration. These regions allow extraordinary wave propagation with large wave vectors for sub-wavelength imaging, enhanced spontaneous emission and thermal radiation control applications. The excited polariton modes in bN can be excited and manipulated near the field, thus providing unprecedented control over nanoscale light-matter interactions.

Tunability of Polaritonic Properties

Though its large bandgap limits electronic tunability, hBN provides several mechanisms to control its polaritonic response. The thickness dependence of polariton dispersion allows for easy engineering of the electromagnetic field distribution and resonance frequencies. The electrical gating of graphene in hBN/graphene heterostructures permits a dynamic control of coupled plasmon-phonon polariton modes [67].

Strain engineering is another approach for tuning hBN's polaritonic properties, since mechanical deformation can shift the phonon frequencies and change the hyperbolic dispersion characteristics. Temperature-dependent studies reveal that polariton properties can be thermally controlled by changes in the phonon population. Additionally, the twist angle of hBN heterostructures affords a new degree of freedom for engineering polaritonic band structures similar to electronic band structures in twisted bilayer graphene [68].

Applications in Tunable Photonics

Polariton-based nanoantennas and resonators constructed from hBN nanostructures demonstrate superior performance compared to metallic counterparts due to reduced ohmic losses [69]. The integration of hBN with other 2D materials creates hybrid polaritonic systems where the optical response can be dynamically controlled through electrical, optical, or mechanical means. Furthermore, hBN's thermal emission properties can be engineered through nanostructuring, enabling applications in thermal management and radiative cooling technologies.

The polaritonic properties of bN allow many applications in nanophotonics and infrared optics. Subwavelength focusing and super-resolution imaging are possible with the high-k modes facilitated by hyperbolic dispersion. The strong field confinement increases spontaneous emission rates via the Purcell effect, making hBN an attractive platform for designing infrared emitters and detectors.

Polariton-based nanoantennas and resonators made of hBN nanostructures show better performance than their metallic counterparts due to lower ohmic losses [69]. In combination with other 2D materials, hBN forms hybrid polaritonic systems that can be controlled dynamically either electrically or optically. Furthermore, the hBN thermal emission properties can be engineered through nanostructuring for thermal management and radiative cooling applications.

The combination of low losses, strong field confinement, and multiple tunability mechanisms positions hBN as a key material for next-generation infrared photonic devices, in addition to the electronic tunability of graphene, TMDs, and black phosphorus in integrated 2D material platforms.

While graphene, TMDs, black phosphorus, and hBN represent the most extensively studied 2D materials with demonstrated tunable optical properties, the rapidly expanding family of 2D materials offers additional opportunities for advanced photonic applications. Among these emerging materials, MXenes—a large family of 2D transition metal carbides, nitrides, and carbonitrides—have recently attracted significant attention due to their unique combination of metallic conductivity and surface chemistry tunability. Their distinctive properties position MXenes as promising candidates for next-generation tunable photonic devices, complementing and extending beyond the capabilities of conventional 2D materials. In the following section, we explore in detail the structure, synthesis, and properties of MXenes, with particular emphasis on their emerging optical and photonic characteristics that make them attractive for tunable applications.

1.2 The emergence of 2D transition metal carbides and nitrides

The first two-dimensional (2D) transition metal carbides and nitrides have been discovered in 2011, namely $Ti_3C_2T_x$, composed of 3 layers of titanium and 2 layers of carbon. Since then, a plethora of other 2D materials have been discovered which become a large family of new materials named MXenes (pronounced "maxines") [7]. MXenes are represented by the formula $M_{n+1}X_nT_x$, where M represents an early transition metal (Sc, Y, Ti, Zr, Hf, V, Nb, Ta, Cr, Mo, or W) X denotes carbon or nitrogen, and $n = 1 - 4$. T indicates surface terminations such as =O, -F, and -OH and x represents the number of surface functionalities.

Most of the MXenes are produced by selective etching of aluminum layers from MAX phases. MAX phases, which were first reported in the 1930s to the 1960s, refer to layered ternary carbides and nitrides where $M_{n+1}X_n$ layers are interleaved with layers of an A element. MAX phases material have a metallic bonding between M-A layers, which are usually weaker than the M-X bonds, making selective etching possible. Adopting a top-down approach, the chemical etching of MAX phases is generally performed using an acid mixture containing hydrofluoric acid (HF) and hydrochloric acid (HCl) [8, 70]. More recently, fluoride-free etching methods, including molten salts and electrochemical techniques, have shown the ability to etch A-layers. MXenes can also be synthesized via chemical vapor deposition (CVD), a bottom-up method that produces surface termination-free MXenes. This approach provides a promising alternative for fabricating MXenes with precise control over their composition and structure.

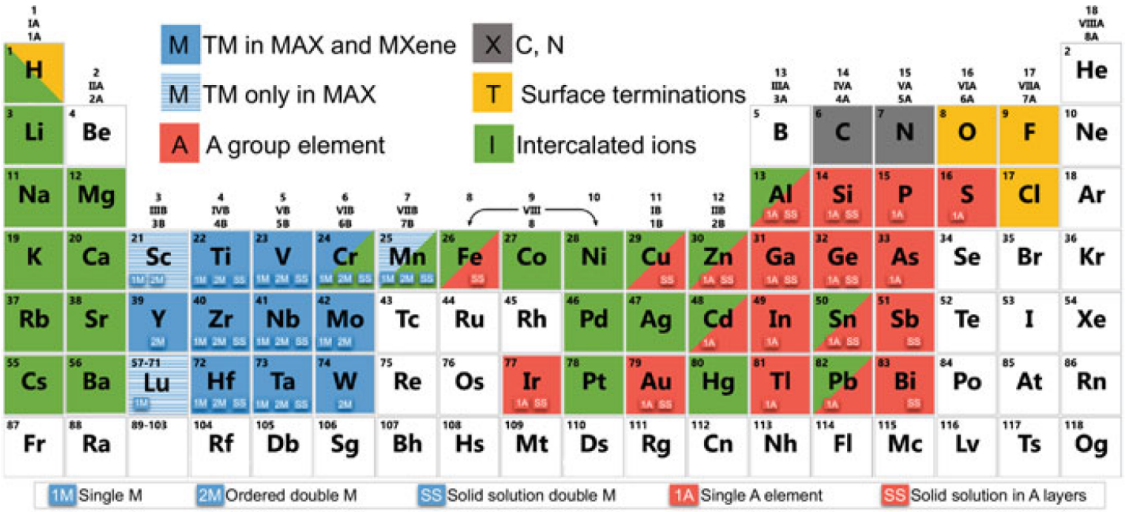

Figure 1.2: Periodic table representing the elements in MAX phases and MXenes, and surface terminations [8]

The MXene family is subdivided into four families, depending on the number of transition metal layers in the MAX phase precursor (M_5AX_4, M_4AX_3, M_3AX_2, and M_2AX).

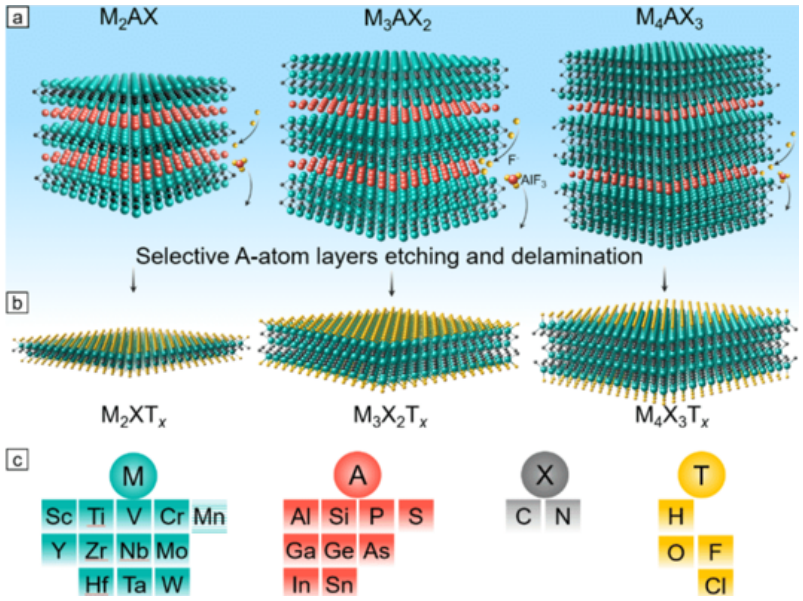

Figure 1.3: Top-down synthesis of MXenes from MAX phase precursors [8]

With more than 50 experimental combinations possible, MXenes have a large range of different properties, making them suitable for many applications. They can be hydrophilic, dispersible in water and other organic solvents, exhibit plasmonic resonances [24], and have high electrical conductivity [71]. These characteristics make MXenes highly attractive for various applications such as energy storage [72], electromagnetic interference shielding [73, 74], sensors [75], optoelectronics [76], optics, and biomedical fields [8]. Furthermore, MXenes can be designed into different types of samples and patterns, going from inks to thin films, and even mixed with polymers to make composite structures. Their versatility and multifunctionality are

key factors driving ongoing research and development in this area.

1.2.1 MAX phase precursors

MXenes 2D materials are produced from MAX phase. This section introduces the MXene's precursor, giving information about its synthesis, crystal structure, and definitions.
Defined by Pr. Barsoum [77], the MAX phases have the general formula $M_{n+1}AX_n$ with $n = 1 - 4$. The M elements correspond to transition metals, mainly from groups 3 to 6 (Sc, Y, Ti, Zr, Hf, V, Nb, Ta, Cr, Mo, or W). The A element is from group 13 to 16 of the periodic table (Al, Ga, In, etc), and the X element is C and/or N. New subfamilies of MAX phases have been discovered, namely, in-plane and out-of-plane ordered double transition metal carbides (usually a heavy transition metal with a light one). For instance, in the out-of-plane ordered structure, two layers of a transition metal are sandwiching one or two layers of another M in the carbide structure (e.g. Mo_2TiAlC_2, $Mo_2Ti_2AlC_3$). The in-plane structure has been discovered for M_2AC MAX phase in which the basal planes consist of two distinct rows of two types of M elements (e.g. $Mo_{2/3}Sc_{1/3})_2AlC$).

In conventional two-dimensional materials, such as graphene and transition metal dichalcogenides, adjacent layers are primarily held together by weak van der Waals forces, enabling mechanical exfoliation methods [1, 78–80]. However, the three-dimensional precursors of MXenes, particularly the MAX phases (where M represents an early transition metal, A is a group 13-16 element, and X is carbon or nitrogen), exhibit fundamentally different interlayer interactions. These precursors are characterized by strong chemical bonds between layers, either through direct A-element bonding or through more complex A_mC_{m-1} interlayer structures, where strong metallic, ionic, or covalent bonds dominate. Due to these robust interlayer chemical bonds, traditional mechanical exfoliation techniques prove ineffective for MXene synthesis. Instead, selective chemical etching methods have been exclusively employed to synthesize MXenes, typically involving the removal of the A-layer atoms while preserving the integrity of the M-X bonds. This chemical exfoliation process, commonly utilizing fluoride-containing acidic solutions (such as HF or a mixture of LiF and HCl), is essential for achieving successful delamination of the layered structure into individual MXene sheets while maintaining their characteristic 2D morphology and chemical composition.

1.2.2 MXenes synthesis

Selective etching, a top-down method

The synthesis of MXenes via selective etching consists of etching A elements from MAX phases selectively. This process typically involves wet chemical etching, using acidic solutions containing fluoride ions, such as hydrofluoric acid (HF) or a mixture of lithium fluoride (LiF) and hydrochloric acid (HCl).

The first and most commonly used MXene, the titanium carbide (Ti_3C_2), was produced by a selective etching of the A layer made of Al, from Ti_3AlC_2 MAX phase using a HF [7]. Since 2011, many groups have been working on this MXene and optimized the chemical etching. Nowadays, to synthesize Ti_3C_2, a mixture of HF and HCl is used, showing a better yield [8]. Upon that, alternative synthesis

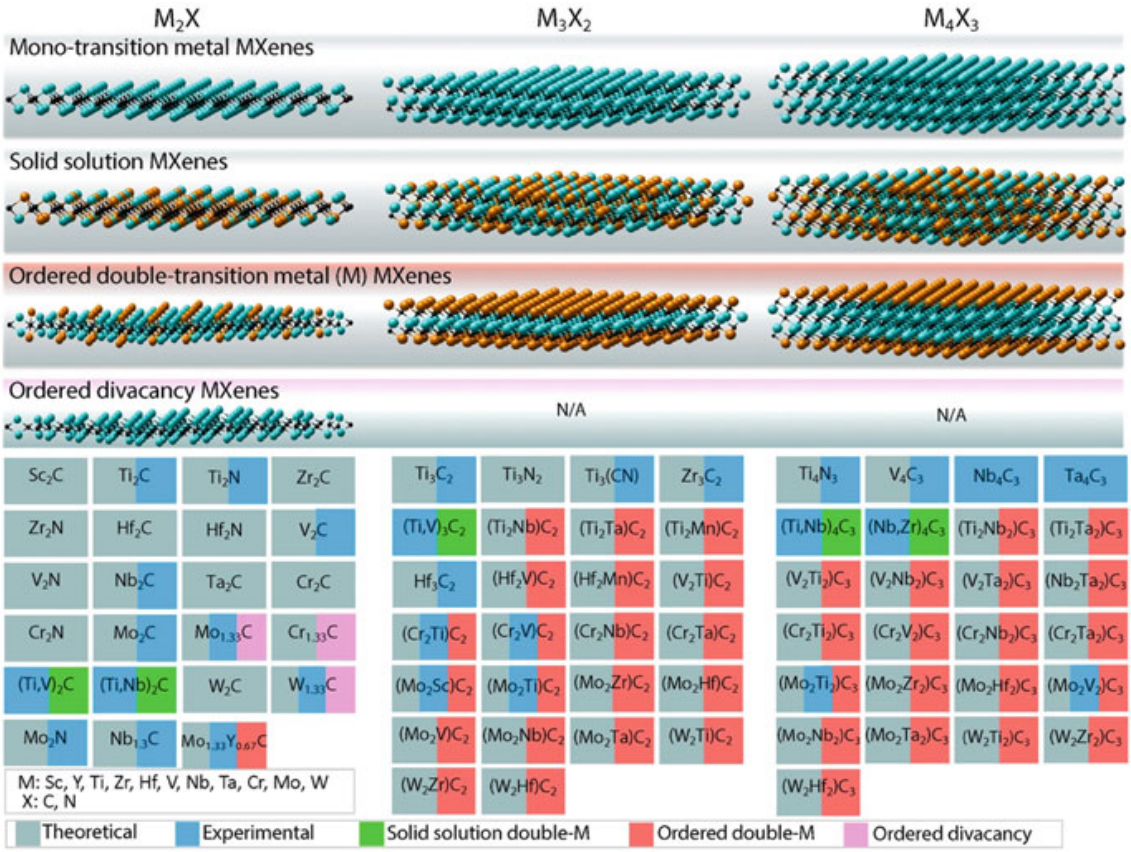

Figure 1.4: MXene compositions reported in 2019. The top row of the structures shows mono-M MXenes (marked as 1M in Fig. 1.1); the second row shows double-M solid solutions (SS). The double-M SS compositions are marked in green. The third row shows ordered double-M MXenes, and their compositions are marked in red. The fourth row shows ordered divacancy MXenes which is only reported for the M2C MXenes, making an $M_{1.33}C$ composition due to 33 at.% vacancy in the M layers, and their compositions are marked in pink. This table includes both experimentally (marked in blue) and theoretically (marked in gray) explored compositions of MXenes. Surface terminations are not shown [72].

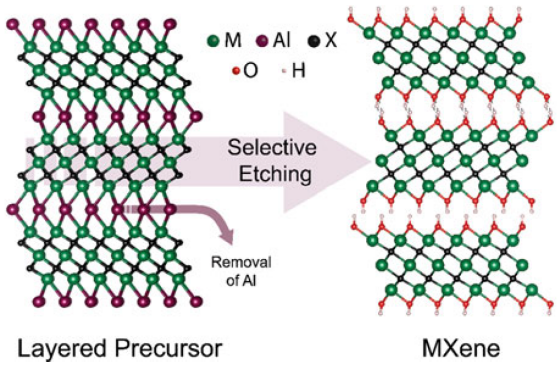

Figure 1.5: Schematic of the selective etching of a M_3AlX_2 layered precursor.[8]

methods acid-free have been reported, using molten salts, alkaline solutions, and/or hydrothermal treatments, bringing new material specificities. Depending on the synthesis' method, the MXene will have different surface terminations, such as hydroxyl (OH), fluorine (F), and oxygen (O) functional groups. It has been shown that these functional groups are randomly distributed on the surface of the MXene and the ratio between each functional group depends on the synthesis' method [81].

Example of the synthesis of Ti_3C_2. As mentioned before, the most common MXene, namely Ti_3C_2 can be produced by wet etching involving an acidic mixture of HF, HCl, and H_2O:

$$Ti_3AlC_2 + 3HCl + 3HF \rightarrow Ti_3C_2 + AlCl_3 + 3H_2 + 3F^-[7] \quad (1.1)$$

Commonly, aqueous hydrofluoric acid solution at 50% and aqueous hydrochloric acid solution at 37% are used, giving a volumic ratio of HF:HCl:H_2O 1:6:3. The etching is set for 24h at 35°C. During this reaction, the aluminum layers are removed from the MAX phase, leading to Ti_3C_2 layers. The etching time, temperature, and etchant concentration are factors that play an important role in the final material.

At this point, Ti_3C_2 material is a multi-layered MXenes. A delamination process is needed to obtain single flakes MXenes. Delamination refers to the process of separating stacked layers into individual or few-layer sheets. This process involves intercalating molecules or ions. The intercalated species weaken the van der Waals forces between the layers, allowing them to be separated more easily, often using mechanical agitation. Lithium chloride ions are commonly used for Ti_3C_2, but other species can be used, such as dimethyl sulfoxide (DMSO), tetramethylammonium hydroxide (TMAOH) or tetrabutylammonium hydroxide (TBAOH).

1.2.3 Effect of synthesis methods on the structure

2D MXenes are commonly synthesized through the selective etching of the A-layer if its MAX phase precursor using etchants based on acidic fluoride solution [7, 82]. The synthesis of MXenes is intricately dependent on the chemical etching process, where multiple experimental parameters can significantly modulate the final material's structural and chemical characteristics. Crucial factors such as etchant composition, concentration, and chemical nature, alongside processing conditions like etching temperature and initial MAX phase precursor particle dimensions, play pivotal roles in determining the etching kinetics and material transformation. These parameters directly impact the micro- and atomic-scale architectures of the resulting two-dimensional materials, necessitating a comprehensive and nuanced approach to understanding the complex interactions between synthesis conditions and MXene properties.

The etching process for MXene synthesis is a critical procedure that requires precise control to selectively remove the "A" element atoms while preserving the structural integrity of the two-dimensional material. This process fundamentally alters the material's crystal structure through the formation of surface functional groups and enables ion and water intercalation, which can be systematically tracked by analyzing changes in the c-lattice constant via X-ray diffraction (XRD) [83, 84]. Experimental studies have demonstrated that etching parameters such as hydrofluoric acid concentration, etching time, and temperature significantly influence the

interlayer spacing and surface chemistry [83]. Notably, the lattice constant exhibits high sensitivity to various factors including drying conditions, ion intercalation, and water molecule interactions. For instance, different cation intercalations (K^+ versus Mg^2+) can dramatically modify the d-spacing between MXene layers, with hydration states further complicating these structural transformations [84].

Beyond the selective removal of "A" atom layers (such as Al or Ga), chemical etching processes can inadvertently trigger complex chemical reactions that compromise the structural integrity of the carbide layers in MXene materials. These interactions potentially introduce structural defects, with nanopores [85, 86] emerging as a particularly prevalent consequence of chemical etching techniques. Such nanoscale porosity is not merely a structural artifact but can significantly modulate the material's functional characteristics, particularly in applications requiring sophisticated ion transport mechanisms, such as advanced water desalination technologies [87, 88].

Recent advancements in MXene research have significantly enhanced our understanding of synthesis-induced structural characteristics through a multidisciplinary approach combining advanced characterization techniques such as X-ray diffraction [8], atomic-resolution scanning/transmission electron microscopy, neutron diffraction [84], and computational methods including density functional theory (DFT) [89] and molecular dynamics (MD) [90] simulations. Despite these technological breakthroughs, significant challenges remain in precisely designing MXenes with targeted crystal structures, controlled defect levels, and specific surface functionalities. The current knowledge predominantly relies on empirical observations, with substantial limitations in theoretically predicting atomic-scale phenomena, particularly during complex chemical etching processes. The intricate mechanisms governing atomic defect formation, nanopore generation, and surface functional group distribution remain incompletely understood, necessitating sophisticated in situ experimental investigations coupled with comprehensive ab initio computational analyses.

1.2.4 MXene surface chemistry

MXene surfaces naturally undergo termination with species that differ from those present in the parent MAX phase. Surface termination dramatically stabilizes MXenes by reducing their formation energy (the energy required to form a compound from its constituent elements), which demonstrates that terminating groups (-O, -OH, -F) establish strong covalent bonds with the exposed metal (M) atoms on the surface [91, 92]. This energetic stabilization explains why MXenes naturally undergo surface termination during the etching process, as the formation of these bonds is thermodynamically favorable [89]. Consequently, the general chemical formula for MXenes can be expressed as $M_{n+1}X_nT_x$, where T represents the terminating species, and the subscript x denotes their coverage on the MXene surface. This termination occurs concurrently with the etching of the A layer from the MAX phase. As the original bonds between the MX slabs and the A-layer atoms are broken, new bonds form with the etchant molecules. Although the specifics of the etching process depend on the chemicals used, theoretical studies have demonstrated the termination mechanism, as shown in Figure 1.6 [91]. This simulation illustrates the interaction of hydrofluoric acid (HF) with a Ti_3AlC_2 MAX phase edge, targeting the A-layer atoms while also interacting with neighboring M elements. During this process, HF dissociates, with fluoride ions binding preferentially to both A and M atoms, while

hydrogen atoms exhibit weaker interactions and tend to recombine into H_2 gas. At higher HF concentrations, the M-A bonds are fully cleaved, leading to the formation of AlF_3 and the subsequent removal of the A element. Following this removal, the exposed M-element surfaces are predominantly terminated by fluoride ions, with hydrogen forming as a secondary by-product, as depicted in Figure 1.6c.

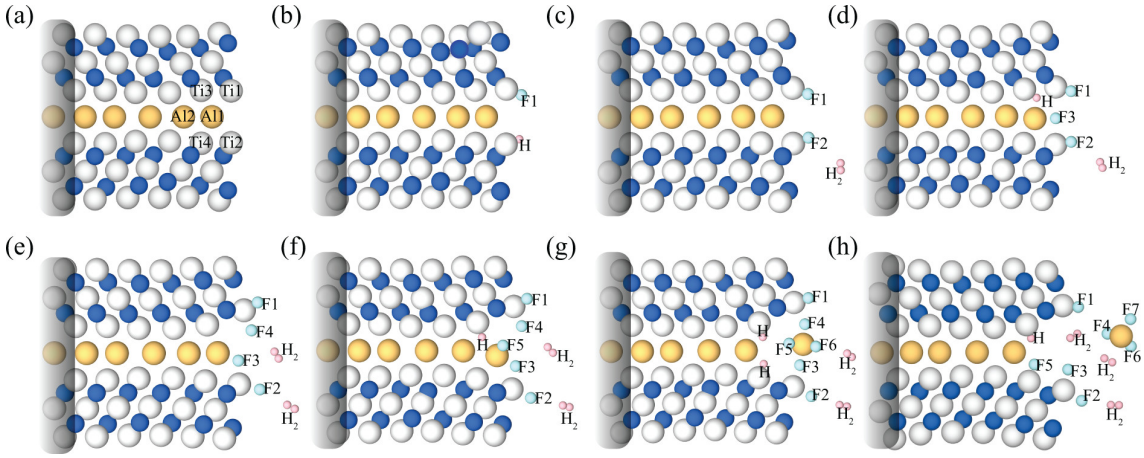

Figure 1.6: Schematic representation of the chemical exfoliation of Ti_3AlC_2 phase in the presence of HF. (a) pristine and (b) one, (c) two, (d) three, (e) four, (f) five, (g) six, and (h) seven HF-intercalated MAX complexes. Atoms at the left edge are fixed and shown here by a shaded region. Silver, blue, orange, cyan, and pink balls represent Ti, C, Al, F, and H atoms, respectively [91]

Based on this model, simplified reaction equations have been proposed:

$$Ti_3AlC_2 + 3HF \rightarrow AlF_3 + \frac{3}{2}H_2 + Ti_3C_2 \tag{1.2}$$

$$Ti_3C_2 + 2H_2O \rightarrow Ti_3C_2(OH)_2 + H_2 \tag{1.3}$$

$$Ti_3C_2 + 2HF \rightarrow Ti_3C_2F_2 + H_2 \tag{1.4}$$

$$Ti_3C_2(OH)_2 \rightarrow Ti_3C_2O + H_2O \tag{1.5}$$

The surface chemistry of MXene materials emerges through a sequential chemical transformation involving multiple reaction pathways, where etchant-derived species interact with the newly exposed transition metal surfaces [83, 91]. Advanced characterization techniques, including X-ray diffraction [93] and density functional theory calculations [89], have revealed a nuanced understanding of surface termination mechanisms. Initially, hydroxyl groups were identified as the primary surface-modifying species (1.3), with fluorine terminations presenting as a potential alternative [94]. Subsequent investigations have demonstrated that the surface chemistry is substantially more intricate, encompassing not only hydroxyl and fluorine groups but also incorporating oxygen species (1.5) [95, 96]. The proposed mechanism suggests that surface-bound hydroxyl groups can undergo spontaneous recombination, generating water molecules and atomic oxygen through an equilibrium-driven process [92].

In vacuum environments, typically encountered during analytical characterization, the reduced water vapor pressure can create transient surface conditions characterized by termination vacancies or bare surface sites. While these exposed surfaces can be momentarily sustained depending on the specific vacuum parameters, any exposure to ambient atmospheric conditions immediately triggers spontaneous oxidation processes [97]. This rapid surface modification underscores the inherent reactivity of MXene materials and highlights the critical importance of controlled environmental conditions in preserving their pristine structural and chemical characteristics.

Advanced analytical techniques have emerged to investigate the surface chemistry and electronic structure of MXene materials, revealing nuanced termination mechanisms that fundamentally influence their physicochemical properties. Nuclear magnetic resonance (NMR) spectroscopy has been used in the identification of the interactions of the terminating species, conclusively demonstrating that oxygen and fluorine predominantly constitute surface-bound species, with hydroxyl groups occupying a minimal fraction—less than 5%—of available surface sites [81]. A multimodal characterization approach integrates complementary analytical methods to provide comprehensive insights. Energy-dispersive X-ray spectroscopy (EDX) offers elemental mapping capabilities, particularly effective for transition metal elements, though inherently limited in detecting light elements [92, 93, 98]. In contrast, electron energy loss spectroscopy (EELS) in (scanning) transmission electron microscopy ((S)TEM) exhibits remarkable sensitivity, capable of distinguishing terminating species and their precise spatial configurations through fine structural analysis [95, 97].

Quantum mechanical theoretical calculations suggest a dynamic surface chemistry where multiple termination configurations exist, but structural relaxation processes typically converge towards energetically stable Face-Centered Cubic (Fcc) and Hexagonal Close-Packed (Hcp) sites. Intriguingly, the potential for mixed configuration surfaces—such as Hcp-coordinated species on one surface layer concurrent with Fcc-coordinated species on the opposing layer—introduces additional complexity to understanding MXene surface interactions [96, 99].

The comprehensive convergence of advanced analytical methodologies, including spectroscopy, microscopy, and computational techniques, has given a deep understanding of MXene surface chemistry at the atomic scale. This multidisciplinary research approach reveals the extraordinary structural flexibility of MXenes, demonstrating how minute surface modifications can profoundly alter fundamental electronic, mechanical, and chemical characteristics.

Table 1.1: Comparative analysis of techniques for studying the surface chemistry of MXenes.

Technique	**Principle**	**Advantages**	**Disadvantages**
NMR [94]	Analysis of nuclear interactions with external magnetic field	Precise identification of terminal groups (OH, F). Sensitive to local environments. Non-destructive.	Limited sensitivity for light elements. High-purity samples required. Time-consuming.
EDX [97]	Analysis of X-rays emitted during electron-sample interaction	Efficient O and F detection. Rapid analysis.	Cannot distinguish O/OH. Lower sensitivity to light elements. Poor spatial resolution.
EELS [97]	Analysis of energy losses of transmitted electrons	High sensitivity to terminal species. Identifies binding sites. Atomic resolution capability.	Complex spectral interpretation. Sample thickness limitations.
XPS [95]	Analysis of photoelectron binding energies from X-ray irradiation	Quantitative surface composition. Chemical state identification. Wide elemental range detection.	Surface-sensitive (few nm depth). Requires ultra-high vacuum. Potential beam damage.
Raman [100]	Analysis of inelastic scattering of monochromatic light	Structural fingerprinting. Sensitive to Ti–C and Ti–O/F vibrations. Fast and non-destructive.	Potential local heating damage. Fluorescence background. Weak signal for monolayers.
SIMS [101]	Mass analysis of secondary ions ejected by ion bombardment	Extreme sensitivity to trace elements. Detects light elements (H, Li). Depth profiling capability.	Destructive technique. Matrix effects complicate quantification. High vacuum required.
PDF [93]	Analysis of interatomic distances via neutron/X-ray scattering	Reveals local structure and interlayer interactions. Models random terminations. Bulk analysis.	Requires advanced facilities. Complex interpretation. Limited time resolution.
(S)TEM [97]	Direct visualization of atomic structure	Direct terminal species observation. Atomic resolution imaging. Precise elemental mapping.	Complex sample preparation. Surface-limited. Potential beam damage.
PiFM [102]	Detection of photothermal expansion and electromagnetic forces via AFM	Nanoscale chemical sensitivity. Non-destructive functional group mapping. 5 nm spatial, 1 cm^{-1} spectral resolution.	Surface/near-surface limited. Complex signal interpretation.

In this thesis, we extend these investigative approaches by introducing local probe nanoscopy, specifically photo-induced force microscopy (PiFM), as an innovative technique to explore the surface chemistry of MXenes. Local probe microscopy offers unprecedented spatial resolution and direct interaction capabilities, providing unique insights into nanoscale structural and chemical characteristics that previous methodologies could not access. Table 2.1 presents a brief comparison between PiFM and conventional techniques, with detailed investigations presented in subsequent sections.

1.3 Optical properties of MXenes

Since their discovery, two-dimensional MXenes have gained significant attention across various fields due to their exceptional properties. These include high electrical conductivity [71], a large active surface area [8], and outstanding mechanical properties [103]. Beyond these characteristics, MXenes have also demonstrated immense potential in optical and optoelectronic applications, as highlighted by numerous studies.

MXenes exhibit a remarkable combination of properties that make them highly versatile for a wide range of applications. Their tunable plasmonic behavior, arising from metallic-like free electron density, positions them as promising candidates for photonics and energy harvesting. Additionally, their ability to support nonlinear optical phenomena, such as saturable absorption and second-harmonic generation, further expands their utility in ultrafast optics and quantum photonics. These unique features are enhanced by their chemical versatility, which allows for fine-tuning of optical properties through surface functionalization with groups like -O, -OH, and -F.

In this section, we aim to provide a comprehensive overview of the optical properties of MXenes, including their plasmonic behavior, ultrafast carrier dynamics, and nonlinear optical responses. We will also discuss their various applications in optoelectronics, biosensing, surface-enhanced Raman spectroscopy (SERS), tip-enhanced Raman spectroscopy (TERS), and electromagnetic shielding. This exploration not only highlights the current state of knowledge but also underscores the potential of MXenes to address challenges in advanced photonic technologies.

1.3.1 Plasmonic properties

MXenes offer a variety of colors which depend on the composition. In the Figure 1.7, extracted from [104], various colloïdal solutions of MXenes and free-stranding films have been prepared, showing various colors. For all MXenes, the X-element is carbon, and transition metal M differs. The number of M-layer influences the absorption, even with the same nature. Maleski et al. [104] showcased in the Figure 1.8 the UV-VIS-NIR optical extinction properties of the various MXenes presented in the optical images.

When the light interacts with a metal, it generates plasmons which is defined as a type of collective oscillation of free charge carriers in a material that propagates as electromagnetic waves. Two-dimensional $Ti_3C_2T_x$, the most studied MXene, shows intense surface plasmons but it strongly depends on the flake morphology. El Demellawi et al. [24] have studied this MXene using electron energy loss

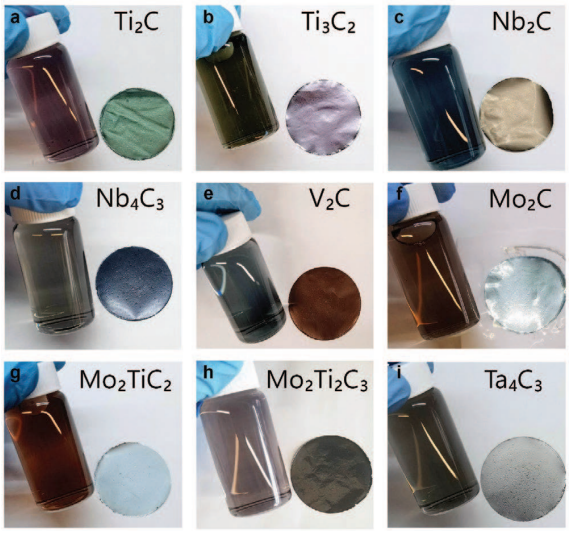

Figure 1.7: Optical properties of representative MXenes in the UV-Vis-NIR range. (a-i) Digital photographs of MXene colloidal dispersions (20 mL) and corresponding free-standing films fabricated by vacuum filtration for (a) Ti_2C, (b) Ti_3C_2, (c) Nb_2C, (d) Nb_4C_3, (e) V_2C, (f) Mo_2C, (g) Mo_2TiC_2, (h) $Mo_2Ti_2C_3$, and (i) Ta_4C_3 [104].

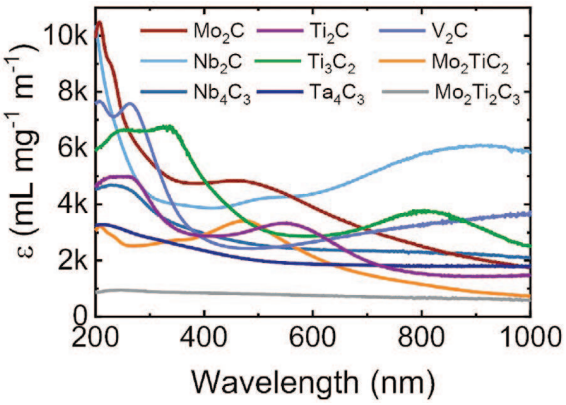

Figure 1.8: UV-VIS-NIR optical extinction properties of 2D transition metal carbides [104].

spectroscopy (EELS), allowing to investigate the spatial and energy distribution of surface plasmons. $Ti_3C_2T_x$ exhibits surface plasmons down to 0.1 eV in the mid-infrared region. Figure 1.9a, the zero-loss-peak (ZLP) subtracted EELS has been measured on a triangular flake and six distinct modes has been identified from 0.44 to 3.5 eV.

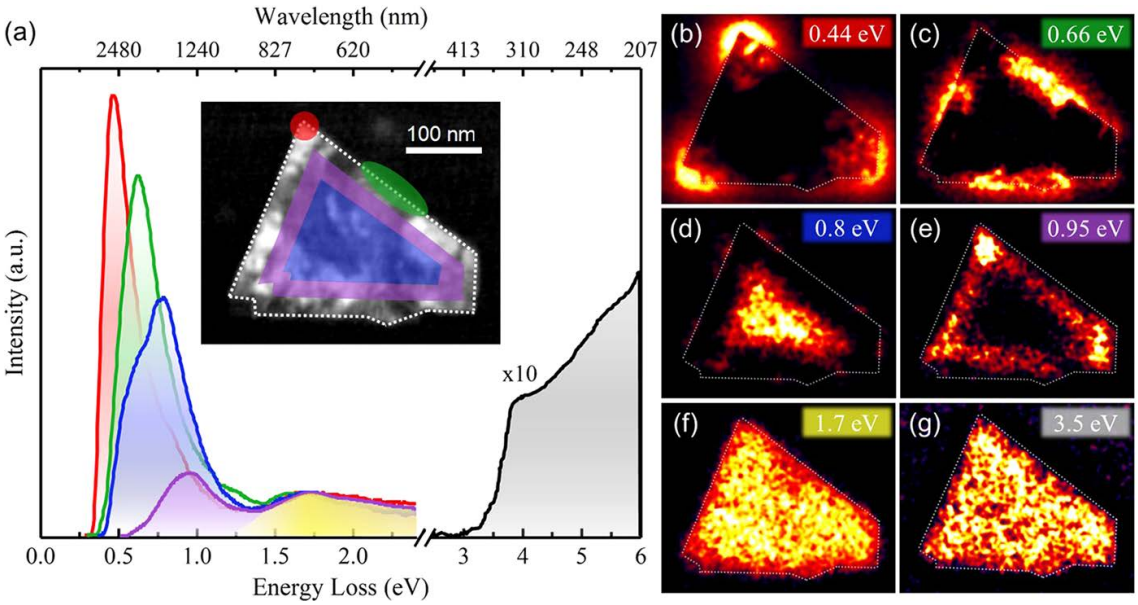

Figure 1.9: (a) Electron energy loss spectroscopy (EELS) acquired on $Ti_3C_2T_x$ flake. (b-g) EELS fitted intensity maps of the corresponding SP modes and IBT sustained by the flake at the energy losses plotted in (a). The dotted lines are added to define the boundaries of the flake [24]

.

1.3.2 MXenes for plasmonic devices

Recent work by Chaudhuri et al. [105] demonstrates the development of a broadband plasmonic absorber utilizing nanostructured $Ti_3C_2T_x$ MXene. It exhibits high light absorption capabilities attributed to its intrinsic optical losses and localized surface plasmon resonances. The engineered system achieves 85-90% absorption efficiency across the 400-1550 nm spectral range. The researchers fabricated $Ti_3C_2T_x$ nanodisk arrays on Au/Al_2O_3 substrates, implementing a metal-insulator-metal architecture that yields absorption efficiencies approaching 99%, demonstrating significant advancement in optical absorption engineering.

The exceptional plasmonic characteristics of $Ti_3C_2T_x$ MXene, particularly its strong localized surface plasmon resonances and extensive optical absorption range, make it highly suitable for advanced photonic implementations. Surface-Enhanced Raman Scattering (SERS) represents one of its most promising applications, where MXenes function as detection substrates. Research by Sarycheva et al. [106] has revealed that $Ti_3C_2T_x$ significantly amplifies Raman signals through enhanced electromagnetic field concentration at its surface. The combination of a two-dimensional structure, metallic conductivity, and adjustable plasmonic properties enables MXenes to effectively enhance the Raman response of target molecules. This enhancement facilitates highly sensitive detection in environmental, biomedical, and foren-

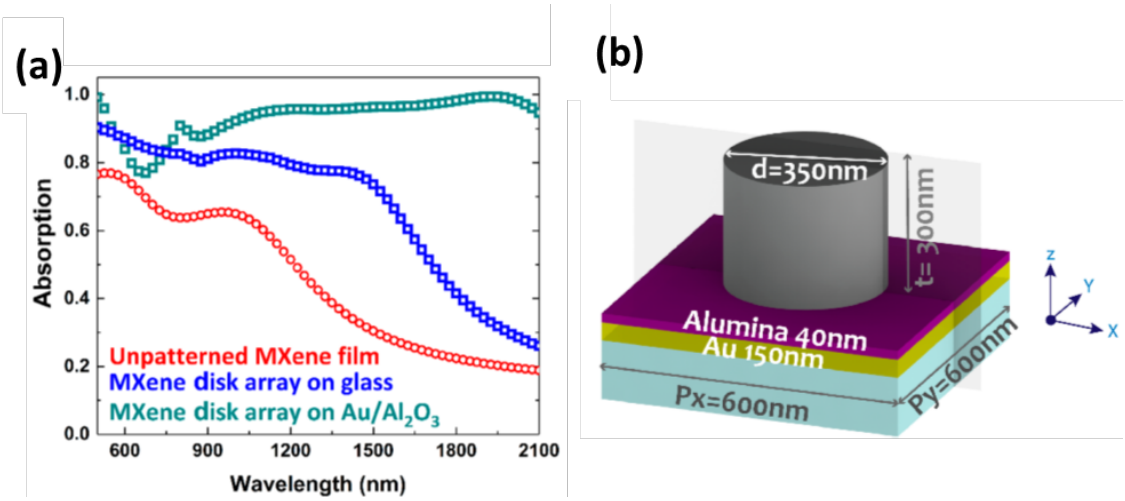

Figure 1.10: (a) Simulated absorption spectra comparison of unpatterned MXene film, MXene disk array on glass, and MXene disk array on Au/Al_2O_3 using Finite Element Method (FEM). (b) Schematic of a unit cell.

sic applications. MXenes present several advantages over conventional noble metal SERS substrates, including large active surface, simple to functionalize, and cost-effectiveness.

In the field of Surface Plasmon Resonance (SPR) biosensing, MXenes demonstrate significant potential for label-free molecular detection. Their capacity to maintain controllable plasmonic resonances and robust light-matter interactions enhances SPR sensor performance. Recent papers demonstrate that incorporating $Ti_3C_2T_x$ MXene layers into SPR systems substantially improves resonance sensitivity during biomolecular binding events [107, 108]. This advancement enables precise, real-time monitoring of various biomolecules, supporting applications in medical diagnostics, pharmaceutical research, and environmental analysis. The biocompatible nature and chemical adaptability of MXenes further support their integration into advanced biosensing platforms.

MXenes have also demonstrated exceptional performance in electromagnetic interference (EMI) shielding applications, crucial for modern electronics and telecommunications. Their distinctive electrical properties and layered structure enable effective electromagnetic wave attenuation. Research by Rakmanov et al. [74] demonstrates that $Ti_3C_2T_x$-based materials achieve superior EMI shielding compared to traditional carbon and metal-based materials. The ability to incorporate MXenes into flexible, lightweight structures expands their potential applications in portable electronics, aerospace systems, and advanced communication networks.

The versatility of MXenes across plasmonic applications, biosensing platforms, and EMI shielding technologies underscores their technological significance. Their unique combination of plasmonic properties and excellent electrical characteristics positions them as crucial materials for future sensing, energy conversion, and electronic protection systems. Continued research into surface modification and material optimization will likely reveal additional applications in optoelectronics, security systems, and high-frequency communication technologies.

The MXenes overview presented in this chapter highlights their exceptional potential as 2D materials with unique optical and plasmonic properties. To better

understand how MXenes position themselves within the broader landscape of two-dimensional materials, Table 1.2 provides a comparative analysis between conventional 2D materials (graphene, TMDs, black phosphorus, and h-BN) and MXenes. This comparison demonstrates how MXenes uniquely combine the metallic conductivity of graphene with hydrophilic surfaces and superior aqueous solution processability, addressing many of the processing limitations encountered with traditional 2D materials.

Table 1.2: Comparative analysis of 2D materials: positioning MXenes among conventional 2D materials.

Material	Key Properties	Main Advantages	Primary Limitations	Synthesis/Processing
Graphene	Semimetal, zero bandgap. Exceptional conductivity ($> 10^4$ S/cm). Broadband optical absorption [37].	Outstanding electrical/thermal conductivity. Excellent mechanical properties. Well-established research base.	Zero bandgap limits electronics. Poor functionalization. Hydrophobic, difficult processing [109].	CVD, mechanical exfoliation. Challenging large-scale production. Limited aqueous processability.
TMDs	Semiconducting, tunable bandgap. Valley polarization. Moderate mobility [45, 51].	Direct bandgap in monolayers. Good optoelectronic properties. Valley physics applications [50].	Complex synthesis conditions. Limited conductivity. Substrate-dependent properties.	CVD growth, hydrothermal methods. Quality control challenges. Requires surfactants for processing.
Black Phosphorus	Direct bandgap (0.3-1.5 eV). High mobility (> 1000 $cm^2/V{\cdot}s$). Anisotropic properties [57, 58].	Excellent MIR photodetection. High carrier mobility. Tunable bandgap with thickness [60].	Rapid air degradation. Poor ambient stability. Challenging processing and storage.	Mechanical exfoliation, liquid-phase methods. Stability issues limit scalability.
h-BN	Wide bandgap insulator (5.9 eV). Excellent thermal stability. Chemically inert [65].	Outstanding insulating properties. High thermal conductivity. Chemical/thermal stability [66].	Limited electronic applications. Poor solution processability. Challenging functionalization.	CVD growth, mechanical exfoliation. Similar challenges to graphene production.
MXenes	Metallic conductivity (up to 20,000 S/cm). Hydrophilic surfaces. Rich surface chemistry (-O, -OH, -F) [71, 94].	**Metallic conductivity, hydrophilic surfaces, excellent aqueous processability, tunable surface chemistry** [110].	Oxidation sensitivity at high temperatures. HF-based synthesis safety concerns [7].	**Solution-based processing from MAX phases. Excellent scalability potential via aqueous routes** [111].

To understand and optimize these distinctive characteristics that set MXenes apart from their conventional counterparts, a thorough understanding of their infrared optical behavior is essential. Since surface terminations (-O, -OH, -F) directly control both the electronic structure and optical properties of MXenes, infrared spectroscopy becomes a critical characterization tool for understanding how these surface functionalities affect material performance. Given that most organic vibrations and surface functional group modes occur within the infrared spectral range, infrared characterization is indispensable for optimizing MXenes for specific applications.

In this thesis work, we aim to elucidate the optical properties of MXenes, with specific focus on their infrared spectral response. Chapter 2 will first establish the fundamental aspects of infrared spectroscopy applied to MXene characterization, providing the theoretical framework necessary for understanding light-matter interactions in these complex 2D systems. We will then explore advanced near-field microscopy techniques that enable nanoscale optical investigation beyond the diffraction limit, setting the stage for the comprehensive characterization studies presented in subsequent chapters.

Chapter 2

Fundamental aspects of far-field and near-field infrared methods for characterizing MXenes

2.1 Introduction to the infrared spectroscopy 31

2.2 Scattering-type scanning near-field optical microscopy (s-SNOM) 38

2.2.1 Interferometric Detection in s-SNOM 41

2.2.2 The Generalized Lock-In Amplifier (G-LIA) 44

2.3 Photo-induced force microscopy (PiFM) 46

2.3.1 Theoretical description of PiFM 46

2.3.2 PiFM model based on effective polarizability enhanced absorption 54

2.4 A comparative study of PiFM and s-SNOM on semiconductors 55

2.1 Introduction to the infrared spectroscopy[1]

Spectroscopy defines the study of the interaction between light and other radiation and matter. This branch of science is based on the study of electromagnetic radiation as a function of its wavelength or frequency, allowing to obtain information on the analyzed matter. Spectroscopic analysis has played a major role in the development of the foundational theories of physics, and the principle has been applied in different fields such as quantum mechanics, general theories of relativity, or quantum electrodynamics. Depending on the type of radiation, spectroscopy can be classified into different methods: electromagnetic radiation, particles, acoustic waves, and dynamic mechanical analysis. In this work, we focus our attention only on the interaction between electromagnetic radiation and matter, and more specifically, infrared electromagnetic waves.

[1]The theoretical foundations of infrared spectroscopy presented in this chapter are primarily based on the comprehensive introduction provided by Günzler and Gremlich [112] in their seminal work *IR Spectroscopy: An Introduction* (Weinheim: Wiley-VCH, 1994).

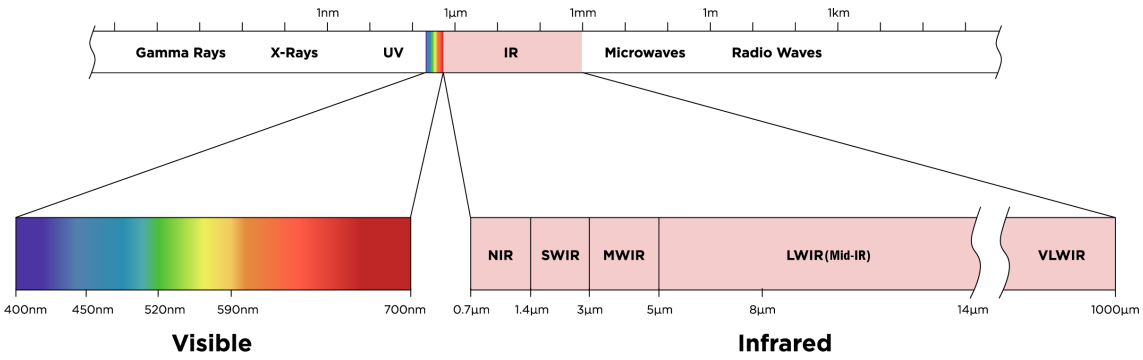

Figure 2.1: Electromagnetic spectrum combining all frequencies of electromagnetic radiation. In this work, we mainly focused our attention in the long wave infrared (LWIR), also called mid-infrared (Mid-IR) region.

Electromagnetic radiation is characterized by its energy and therefore, by its wavelength with the base unit m. The electromagnetic spectrum is divided into different spectral regions, going from radio waves to γ-rays.

In the infrared region, the micrometer (μm) is typically used. The frequency ν is another typical parameter used to describe the wave motion and is defined as the number of oscillations of the electric (or magnetic) radiation vector per unit of time. The frequency is often expressed in Hertz (Hz). The frequency is proportional to the wavelength λ and the speed of light c

$$\nu = \frac{c}{v} \tag{2.1}$$

The wavenumber $\overline{\nu}$ is another magnitude that has gained acceptance, especially in IR spectroscopy because it is proportional to the frequency and thus to the energy of the electromagnetic alternating field. Usually expressed in cm^{-1}, it describes the number of waves in a 1 cm-long wavetrain.

$$\overline{\nu} = \frac{\nu}{c} \quad cm^{-1} \tag{2.2}$$

$$\overline{\nu} = \frac{1}{\lambda[cm]} = \frac{1.10^4}{\lambda[\mu m]} \tag{2.3}$$

In IR spectroscopy, both units are used.
The radiation energy related to an electromagnetic field is expressed in Joule and depends on the frequency, the Plank constant h ($h = 6.626.10^{-34}$ Js), and the speed of light c.

$$E = h.\nu = h.\frac{c}{\nu} \tag{2.4}$$

The frequency of the electromagnetic field and the energy are directly proportional. Therefore, infrared radiations have lower energies compared to visible radiations.

Interest in infrared spectroscopy in materials science

The infrared region is particularly interesting because it gives a lot of information on the chemical composition and structure. It offers a variety of possibilities for sample measurement and sample preparation. IR spectroscopy is an important analytical

method for analytical chemistry. This technique is used as much as nuclear magnetic resonance (NMR) spectroscopy, mass spectroscopy (MS) and ultraviolet-visible (UV-Vis) spectroscopy. Both qualitative and quantitative analysis can be performed with IR spectroscopy. Indeed, the position and intensity of the absorption band of a substance are specific to that substance. It can be compared to a fingerprint of a person. The best-suited bands for chemical identification are classified to the carbon back-bone of the molecule and this is usually found in the spectral range of 1500 to 650 cm^{-1}, called the "fingerprint region". Quantitative analysis can be performed by IR spectroscopy by evaluating the radiant power (I_0) and the intensity transmitted through the sample (I). The ratio I/I_0 is called the transmittance of the sample labeled T. When light interacts with a material, the incident radiation can undergo three fundamental processes: transmission, reflection, and absorption. The energy conservation principle dictates that the sum of these three components equals unity:

$$T + R + A = 1 \tag{2.5}$$

where T is the transmittance, R is the reflectance, and A is the absorption. The reflectance represents the fraction of incident light that is reflected from the sample surface, while absorption quantifies the fraction of light energy converted into other forms of energy (typically heat or molecular excitation).

Theoretical foundations of infrared spectroscopy

As mentioned in the last section, IR spectroscopy is a useful technique for molecular species identification. Indeed, the absorption peak in an IR spectrum refers to a specific bonding vibration and rotation. In this section, we will develop the different types of molecular vibrations and rotations and explain the origin of these peaks.

Light-matter interaction.

Atomic model. The light-matter interaction can be described at different scales, using different models. According to Bohr model, an atom is composed of a positively charged nucleus encircled by negatively charged electrons following elliptical orbits. Each of these electron orbits has a specific energy content E. The electron's energy is quantized, and can only be half or whole numbers. An electron can jump from one orbit to another with a specific energy uptake or release, according to the energy difference existing between the two levels:

$$\Delta E = E_1 - E_2$$

E_1 and E_2 refer respectively to the electron's energy in orbits 1 and 2. If the electromagnetic wave's energy strictly equals ΔE, the electron will jump from orbital 1 to orbital 2. The return of an electron from orbital 2 to orbital 1 results in the emission of radiation. This description is based on the Bohr model (quantum mechanics). The Schrödinger model (wave mechanics) can also describe the phenomenon. In this case, electron orbitals are replaced by wave functions which represent the probability of finding an electron in this particular region.

Molecular vibration. A molecule is composed of two or more atoms, linked by interactions, with a certain distance between them. When a molecule is irradiated by light, atoms can be excited and vibrate around their state of equilibrium. As for electronic transition, the vibrational energy is also quantized.
To describe molecular motions, atoms are usually simplified as points of mass kept together by elastic springs. With the simplest model considering 2 atoms, Hooke's law is applied, considering vibrating masses m_1 and m_2 separated from a distance r and an elastic force constant k.

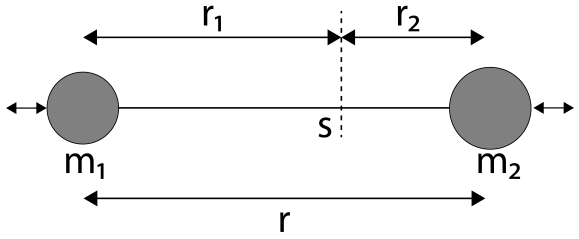

Figure 2.2: Diatomic mechanical model

Based on the harmonic oscillator model (in 1D), it is possible to determine a differential equation that describes the system's motion. By defining the reduced mass $\mu = \frac{m_1 m_2}{m_1+m_2}$ and the distance r between the atoms, the differential equation for vibration is:

$$\mu \frac{d^2 r}{dt^2} + k\Delta r = 0$$

The solution $r(t) = r_{\max} \cos(2\pi\nu t)$ gives the vibration frequency:

$$\nu = \frac{1}{2\pi}\sqrt{\frac{k}{\mu}}$$

Both atoms vibrate around the shared center of mass s in opposite phases, and if they have different masses $m_1 \neq m_2$, the amplitude will change.

Classical mechanics alone does not adequately describe molecular motion. Therefore, the description must be extended to quantum mechanics. In this transition, mechanical parameters are assigned in quantum mechanics to operators. The Hamiltonian operator is used $H = T + V$. For a one-dimensional single particle system, the Schrödinger equation is given by:

$$-\frac{\hbar^2}{2m}\frac{d^2\psi}{dx^2} + V(x)\psi = E\psi$$

where ψ is the wave function and E is the energy, describe the system. The functions are normalized such that the total probability is one: $\int \psi\psi^* dx = 1$.

The energy eigenfunctions for a one-dimensional harmonic oscillator are given by:

$$E_v = h\nu\left(v + \frac{1}{2}\right) \quad \text{with} \quad v = 0, 1, 2, \ldots$$

Here, ν is the oscillator frequency from classical mechanics, and n is the vibrational quantum number, which can be any non-negative integer. Only transitions

where $\Delta v = \pm 1$ are allowed, based on selection rules derived from the Schrödinger equation. The vibrational frequency depends on the atomic masses and the binding forces between them, represented by the elastic force constant k.

Crystalline vibrations. Atomic and molecular vibration models are important but in the case of two-dimensional MXene materials, the matter is organized in a crystal. In a crystal, atoms are arranged in a period lattice. Even if atoms can be treated as discrete particles, they usually vibrate collectively due to interatomic interactions. These collective vibrations are described through the concept of phonons. Those phonons are considered as quasiparticles representing quantized vibrations modes of the crystal. A phonon corresponds to a quantized mode of vibrations, much like a photon is a quantum of the electromagnetic field. The study of phonons is important as they play a major role in various physical properties of solids such as thermal conduction, optical properties and electronic properties.

Two-dimensional MXene materials are classified as crystalline structures due to their well-defined atomic arrangement between the transition metal (M) and carbon/nitrogen (X) layers within a specific crystal lattice. For example, Ti_3C_2, the most extensively studied MXene, exhibits a hexagonal crystal structure with three titanium layers interleaved with two carbon layers. The vibrational properties of these materials are governed by phonons, which are quantized lattice vibrations that play a crucial role in determining their thermal, optical, and mechanical properties.

MXenes belong to the point group D_{3d}, and their vibrations can be described using Mulliken symbols as: 2(N-2)E_g + (N-2)A_{1g} + 2(N-2)E_u + (N-2)A_{2u}. E_g and E_u are doubly degenerate modes [113–116]. E_g and A_{1g} are Raman-active vibrations, where E_g corresponds to in-plane vibrations, and A_{1g} corresponds to out-of-plane vibrations. The number of active Raman modes depends on the MXene structure: M_2XT_x members have two active Raman modes (E_g + A_{1g}), while $M_3X_2T_x$ structures exhibit four active Raman modes corresponding to in-plane and out-of-plane vibrations of both M and X atoms. For $M_4X_3T_x$ structures, six active Raman modes are predicted: three out-of-plane and three in-plane vibrations. According to group theory, the middle layer of atoms (C layer in Ti_2CT_x, middle Ti layer in $Ti_3C_2T_x$, middle carbon layer in $Nb_4C_3T_x$) remains silent and does not contribute to the Raman spectrum under normal circumstances.

In the case of MXenes, crystal lattice vibrations occur at low frequencies, typically below 300 cm^{-1} as presented in Chapter 4 [100, 113–117]. Raman spectroscopy is particularly well-suited for probing these low-frequency vibrations and serves as the primary technique for characterizing MXene phononic properties. The vibrations involving all MXene atoms except the middle layer are usually the most intense and are located at lower frequencies. Carbon layer vibrations (in $M_3X_2T_x$ and $M_4X_3T_x$ MXenes) appear at higher frequencies, starting from 500 cm^{-1}.

The surface chemistry of MXenes is characterized by the presence of functional groups (–O, –OH, –F) that are covalently bonded to the outer transition metal layers. These surface terminations exhibit distinct molecular vibrational modes at frequencies typically above 300 cm^{-1}, which can be distinguished from the phononic behavior of the bulk crystal structure. These higher-frequency surface vibrations are detectable by PiFM spectroscopy (coupled with a mid-infrared laser), providing complementary information to Raman spectroscopy.

Fundamental aspects of infrared nanoscopy

Scanning probe microscopy (SPM) has revolutionized the study of materials at the nanoscale by enabling high-resolution imaging and analysis of surface properties. Among the most prominent SPM techniques are atomic force microscopy (AFM), scattering-type scanning near-field optical microscopy (s-SNOM), and photo-induced force microscopy (PiFM). Each technique leverages the interaction between a sharp probe and the sample surface, but their unique modes of operation allow them to extract complementary information for nanoscale characterization.

These advanced techniques have emerged in response to the growing demand for high-resolution characterization methods, driven in part by the needs of the microelectronics industry and the limitations of conventional optical microscopy. Optical microscopy is constrained by the diffraction limit, which restricts spatial resolution to approximately half the wavelength of the incident light, as described by:

$$d = \frac{\lambda}{2n \sin \theta} \tag{2.6}$$

where d is the diffraction-limited resolution, λ is the wavelength of light, n is the refractive index of the medium, and θ is the half-angle of light collection. For visible and infrared light, this limit typically lies in the range of hundreds of nanometers, far exceeding the characteristic dimensions of nanostructures and devices.

To overcome this limitation, techniques like s-SNOM and PiFM integrate the capabilities of AFM with optical and mechanical detection schemes, enabling resolutions far beyond the diffraction limit. AFM, as the foundational technique, provides precise topographic and mechanical information through the interaction of a sharp probe with the sample surface. Building upon this, the role of the AFM tip becomes crucial in s-SNOM and PiFM, where it acts as a *nanoantenna* for light. In s-SNOM, the metallic-coated tip enhances and confines light to subwavelength dimensions, enabling nanoscale optical imaging. Similarly, in PiFM, the AFM tip mediates the detection of localized optical forces generated by light-matter interactions, allowing the mapping of chemical and optical properties with extraordinary sensitivity.

Together, these techniques address the demand for high-resolution characterization methods in microelectronics, nanophotonics, and materials science, forming a comprehensive framework for the nanoscale investigation of structural, optical, and chemical properties.

Principle of atomic force microscopy

Atomic force microscopy (AFM) serves as the cornerstone of scanning probe microscopy, enabling the precise mapping of surface topography and mechanical properties through the interaction of a sharp probe with the sample. By detecting forces between the tip and the surface, AFM provides high-resolution images and quantitative data.

Scattering-type SNOM (s-SNOM) builds directly on AFM by integrating optical excitation into the setup. The metallic AFM tip acts as an optical nanoantenna, confining light to subwavelength dimensions and enabling optical imaging with nanometer resolution. In addition, to enhance and localize the electromagnetic field, the tip scatters the near-field interaction into far-field radiation, which is subsequently

detected by an external detector. This process enables s-SNOM to access local dielectric properties, making it a powerful tool for studying optical responses, such as phonon polaritons and plasmonic resonances.

PiFM further advances these capabilities by coupling AFM's mechanical sensitivity with localized optical forces induced by light-matter interactions. This hybrid approach enables the direct mapping of chemical signatures and optical properties with spatial resolution comparable to AFM, while retaining the molecular specificity of infrared and Raman spectroscopy.

Together, these techniques highlight the evolution of scanning probe methodologies, moving from purely mechanical characterization in AFM to advanced optical and chemical imaging in s-SNOM and PiFM. Their complementary nature makes them invaluable for comprehensive nanoscale analysis. In the following sections, I will first describe the functioning of conventional AFM, followed by s-SNOM, and finally PiFM.

A typical Atomic Force Microscopy system can operate in three different modes: contact mode, non-contact mode, and taping mode.

Contact AFM mode is the simplest approach in AFM. The tip, acting as a probe, is brought to a sample surface and is placed in contact with that surface. The probe scans the surface and by attractive and repulsive force between the tip and the surface sample, the cantilever will bend. The cantilever deformation is detected through a feedback laser displacement which is reflected from the cantilever to a photodetector. This technique offers a high resolution and the ability to measure mechanical properties. Nevertheless, constant contact can damage soft samples due to frictional forces [118].

Non-contact AFM mode usually offers high spatial resolution and avoids damage of both the sample and the tip. The tip scans the surface at a certain distance, while it's oscillating at its resonance frequency. Variations in the oscillation amplitude or frequency due to the interaction with the sample are monitored. This technique is ideal for imaging soft and delicate samples. Nevertheless, the resolution is usually lower than in contact or tapping mode and measurements can be affected by environmental conditions, such as humidity [119].

Tapping AFM mode, also referred as intermittent mode, involves oscillating the AFM tip at its resonant frequency, same as the non-contact mode. In this mode, the AFM cantilever is oscillated at or near its resonant frequency (typically in the range of 50-500 kHz) with amplitudes ranging from a few nanometers to several hundred nanometers. The tip intermittently touches the surface sample during each oscillation cycle, which allows for high-resolution imaging while significantly reducing the lateral forces and contact forces between the tip and the sample surface . This reduction in contact force can be as significant as an order of magnitude, with forces estimated to be as low as a tenth of a nanonewton, even under ambient conditions.

The intermittent nature of the tip-sample interaction offers several key advantages over traditional contact mode AFM. Since the tip is no longer continuously in contact with the surface, both tip wear and sample degradation are minimized , making this technique particularly suitable for imaging soft, fragile, or easily deformable materials such as polymers, biological samples, and organic thin films. The oscillating motion with amplitudes up to approximately 100 nm effectively eliminates capture of the tip by surface fluid layers , which is often problematic

in ambient conditions. Additionally, tapping mode enables simultaneous acquisition of both topographic and phase information, where the phase shift between the driving signal and cantilever response provides valuable insights into local material properties [120].

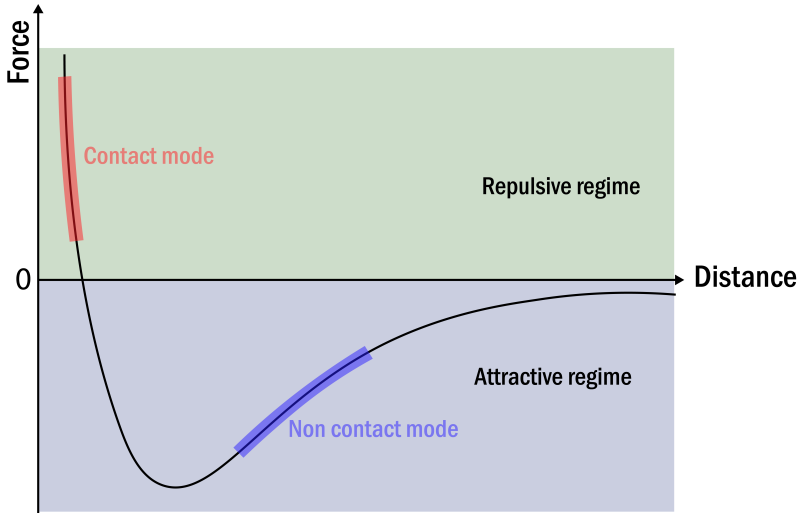

Figure 2.3: Force-distance curve of atomic force microscopy with the 3 different regimes. The force is typically in the order of 100 pN and the distance in the order of nm.

2.2 Scattering-type scanning near-field optical microscopy (s-SNOM)

The scattering-type scanning near-field optical microscopy (s-SNOM) has emerged as a powerful technique to overcome the diffraction limit inherent to conventional optical microscopy. Based on concepts proposed by Edward Synge in 1928 [121], near-field optics has seen significant advancements with the advent of scanning probe techniques in the late 20th century.

The initial concepts of near-field optical microscopy were centered around aperture-based techniques, where a subwavelength aperture was used to achieve resolution beyond the diffraction limit. While aperture-based SNOM has been instrumental in advancing near-field optics, the advent of scattering-type SNOM (s-SNOM) has provided significant advantages. s-SNOM eliminates the need for a physical aperture, enabling higher spatial resolution, stronger near-field enhancement, and compatibility with a broader spectral range. This development has made s-SNOM an indispensable tool for nanoscale optical imaging and spectroscopy, particularly for studying complex material systems.

S-SNOM, pioneered by Knoll, Hillenbrand, and Keilmann in the late 1990s, has established itself as a versatile method for nanoscale optical characterization. By coupling a sharp metallic probe with laser excitation, s-SNOM enables the mapping of optical properties with spatial resolutions typically below 10 nm [122–124].

Principle of operation

S-SNOM relies on the interaction between a focused laser beam and a sharp metallic or metalized tip oscillating in close proximity to the sample surface. The metallic tip acts as a nanoantenna, confining the incident electromagnetic field to a subwavelength region. This confinement generates a near-field interaction localized at the tip apex, which contains information about the material's optical properties, such as its complex dielectric function $\varepsilon(\omega)$.

The near-field interaction can be described using the dipole approximation, where the tip-sample system is modeled as coupled dipoles through the dipole image model. In this model, the presence of the sample creates an image dipole that interacts with the tip, effectively modifying its polarizability. The scattered electric field is given by:

$$E_{\text{scattered}} \propto \alpha_{\text{eff}} E_{\text{incident}} \tag{2.7}$$

where α_{eff} is the effective polarizability of the tip-sample system. According to the dipole image model, the effective polarizability can be expressed as:

$$\alpha_{eff}^{PD} = \frac{\alpha}{1 - \frac{\alpha\beta}{16\pi(R+H)^3}} \tag{2.8}$$

where α is the polarizability of the tip in free space, H is the tip-sample distance, R is the tip radius and the term β is the reflection coefficient or optical response function of the material, which determines the strength of the near-field coupling between the tip and sample [122–125]:

$$\beta = \frac{\varepsilon(\omega) - 1}{\varepsilon(\omega) + 1} \tag{2.9}$$

The tip oscillates vertically at a frequency Ω, typically at or near its mechanical resonance frequency. This oscillation modulates the near-field interaction, allowing the separation of near-field and far-field contributions. The scattered light, which contains both near-field and far-field components, is demodulated at higher harmonics of the oscillation frequency (e.g., $2\Omega, 3\Omega$) to isolate the near-field signal, as near-field contributions decay nonlinearly with tip-sample distance [123].

The scattered light is detected by a photodetector (usually Mercury-Cadmium-Tellurium in mid-IR), converting the optical signal into an electrical signal. This electrical signal is then processed using a lock-in amplifier, which demodulates the signal at the selected harmonics of the tip oscillation frequency Ω_0.

For each harmonic $n\Omega_0$, the lock-in amplifier provides two primary output channels through dual-phase demodulation:

$$s_{n\Omega_0} = R_{n\Omega_0} e^{i\theta_{n\Omega_0}} \tag{2.10}$$

The lock-in amplifier measures the signal amplitude at the reference frequency V_{sig} and determines the phase difference θ between the signal and the reference. Through dual-phase demodulation, two orthogonal components are extracted:

$$X = V_{\text{sig}} \cos\theta \tag{2.11}$$

$$Y = V_{\text{sig}} \sin\theta \tag{2.12}$$

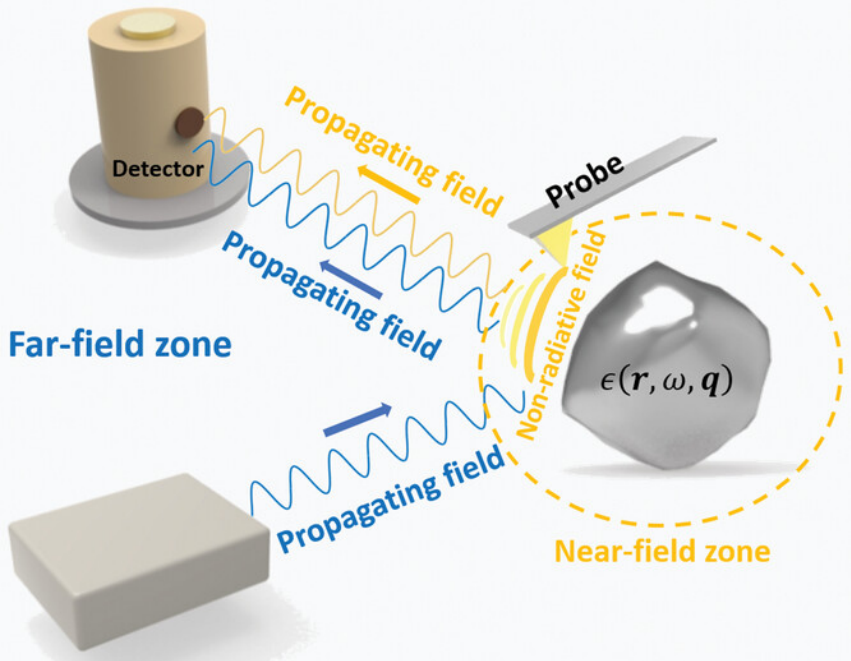

Figure 2.4: S-SNOM basic principle. Far-field (blue) and near-field (yellow) measurements, accessing the propagating field and the evanescent field, respectively. Illustration extracted from [125].

From these components, the amplitude and phase of the demodulated signal are calculated as:

$$R_{n\Omega_0} = \sqrt{X^2 + Y^2} \tag{2.13}$$

$$\theta_{n\Omega_0} = \arctan\left(\frac{Y}{X}\right) \tag{2.14}$$

where:

- $R_{n\Omega_0}$ is the amplitude of the demodulated signal, which represents the strength of the near-field interaction.
- $\theta_{n\Omega_0}$ is the phase of the demodulated signal, which carries information about the resonant behavior of the material.

The amplitude $R_{n\Omega_0}$ is particularly sensitive to the magnitude of the local optical response, while the phase $\theta_{n\Omega_0}$ provides complementary information related to the material's resonant characteristics. Figure 2.5 illustrates the principle: the lock-in amplifier requires the input signal $V_s(t)$ and the reference signal $V_t(t)$. After processing, amplitude and phase are extracted. The amplitude and phase at different harmonics exhibit varying sensitivities to different aspects of the tip-sample interaction, with higher harmonics generally providing better background suppression but potentially lower signal-to-noise ratios. Indeed, near-field signals decay as $1/z^3$ (where z is the tip-sample distance), while far-field contributions decay as $1/z$. By demodulating the signal at higher harmonics (e.g., $2\Omega_0$, $3\Omega_0$), the far-field background is effectively suppressed. The demodulated signal at the n-th harmonic is expressed as:

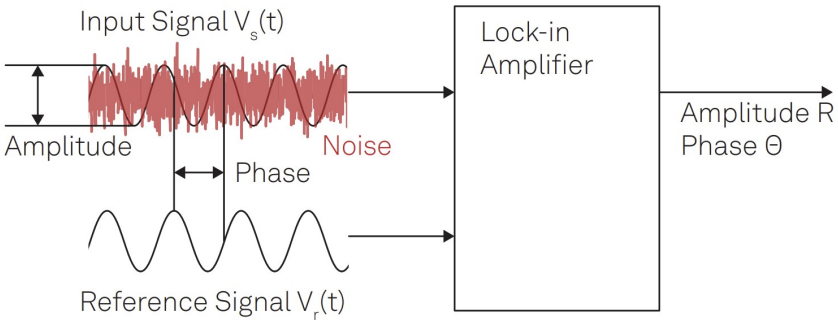

Figure 2.5: Lock-in amplifier working principle capable of measuring the amplitude and the phase of a signal (V_s) relative to a defined reference signal (V_r). Illustration extracted from Zurich Instruments [126].

$$S_n \propto \int_0^T E_{\text{scattered}}(t) \sin(n\Omega t)\, dt \tag{2.15}$$

where T is the oscillation period, and Ω is the oscillation frequency.

Higher harmonics enhance the sensitivity to local optical properties, enabling nanoscale imaging of phonon polaritons, plasmonic resonances, and molecular vibrations. For instance, in polar materials like 4H-SiC, s-SNOM has been used to resolve surface phonon polaritons and their propagation characteristics [123, 125].

2.2.1 Interferometric Detection in s-SNOM

To enhance the sensitivity and separate amplitude and phase information, s-SNOM often employs interferometric detection. Without such methods, the scattered light intensity is dominated by background noise, limiting the detection of near-field contributions.

In interferometric setups, the scattered field E_{sc} can be expressed as:

$$E_{\text{sc}} = E_{\text{near-field}} + E_{\text{background}} \tag{2.16}$$

While the near-field contribution carries the desired local optical information, the far-field background arises from reflections at the tip, cantilever, and sample surface.

Self-homodyne detection. Early implementations of s-SNOM often used *self-homodyne detection* (SHD) for its simplicity, as depicted in Figure 2.6(a). In this approach, the detector measures the total intensity, which is the square of the sum of the near-field and background electric fields:

$$I = (\tilde{E}_n + \tilde{E}_b)(\tilde{E}_n + \tilde{E}_b)^* \tag{2.17}$$

where $\tilde{E}_n$ represents the complex near-field scattered electric field, $\tilde{E}_b$ denotes the complex background field, and the superscript * indicates complex conjugation. By expanding this product, we obtain:

$$I = \tilde{E}_n\tilde{E}_n^* + \tilde{E}_b\tilde{E}_b^* + \tilde{E}_n\tilde{E}_b^* + \tilde{E}_b\tilde{E}_n^* \tag{2.18}$$

Expressing the fields in terms of their magnitudes and phases gives:

$$I = |\tilde{E}_n|^2 + |\tilde{E}_b|^2 + 2\,|\tilde{E}_n|\,|\tilde{E}_b|\cos\big(\varphi_n - \varphi_b\big) \tag{2.19}$$

where φ_n and φ_b are the phases of the near-field and background fields, respectively.

A lock-in amplifier subsequently demodulates the signal at higher harmonics of the tip-tapping frequency. Because $|\tilde{E}_b|$ remains relatively constant with respect to the tip-sample distance, the term $|\tilde{E}_b|^2$ is mostly removed by the demodulation filter. As a result, the primary contribution after filtering can be written as:

$$I \approx |\tilde{E}_n|^2 + 2\,|\tilde{E}_n|\,|\tilde{E}_b|\cos\big(\varphi_n - \varphi_b\big) \tag{2.20}$$

In practice, $|\tilde{E}_b|$ is usually much larger than $|\tilde{E}_n|$, effectively boosting the near-field signal in the measured intensity. However, a key limitation of SHD is that only intensity information is retrieved: the phase of the near-field cannot be extracted, since φ_b is not actively controlled.

Homodyne Detection. While self-homodyne detection is barely used in modern s-SNOM systems, the more widely used approach is *homodyne detection* (HD). As depicted in Figure 2.6(b), HD employs a symmetric Michelson interferometer, where the scattered light is combined with a separate reference beam of the same frequency. This setup enables the measurement of both the near-field amplitude and phase.

In the presence of three fields—the near-field $\tilde{E}_n$, the background $\tilde{E}_b$, and the reference $\tilde{E}_r$—the total electric field is $\tilde{E}_n + \tilde{E}_b + \tilde{E}_r$. Hence, the measured intensity I at the detector can be written as:

$$I = \big(\tilde{E}_n + \tilde{E}_b + \tilde{E}_r\big)\,\big(\tilde{E}_n + \tilde{E}_b + \tilde{E}_r\big)^* \tag{2.21}$$

By expanding this expression in terms of field magnitudes and phases, one obtains:

$$\begin{aligned} I \;&= |\tilde{E}_n|^2 + |\tilde{E}_b|^2 + |\tilde{E}_r|^2 \;+\; 2\,|\tilde{E}_n|\,|\tilde{E}_b|\,\cos(\varphi_n - \varphi_b) \\ &\quad +\; 2\,|\tilde{E}_n|\,|\tilde{E}_r|\,\cos(\varphi_n - \varphi_r) \;+\; 2\,|\tilde{E}_b|\,|\tilde{E}_r|\,\cos(\varphi_b - \varphi_r) \end{aligned} \tag{2.22}$$

where φ_n, φ_b, and φ_r are the respective phases of the near-field, background, and reference.

During the experiment, a lock-in amplifier demodulates the signal at higher harmonics of the tip-tapping frequency. Because neither $|\tilde{E}_b|$ nor $|\tilde{E}_r|$ is modulated by the tip motion, the terms $|\tilde{E}_b|^2$, $|\tilde{E}_r|^2$, and $2\,|\tilde{E}_b|\,|\tilde{E}_r|\cos(\varphi_b - \varphi_r)$ are largely filtered out. Thus, after demodulation, the dominant contribution reduces to:

$$I_{\text{demod}} \;\approx\; |\tilde{E}_n|^2 \;+\; 2\,|\tilde{E}_n|\,|\tilde{E}_b|\cos(\varphi_n - \varphi_b) \;+\; 2\,|\tilde{E}_n|\,|\tilde{E}_r|\cos(\varphi_n - \varphi_r) \tag{2.23}$$

A key strategy in HD is to make the reference field much stronger than the near-field or the background field. This condition ensures that the last term of Eq. (2.23), proportional to $|\tilde{E}_n|\,|\tilde{E}_r|$, dominates the detected signal. As the reference beam's optical path length (and hence φ_r) can be finely tuned, one can retrieve both the amplitude and phase of the near-field by varying the reference path and measuring the corresponding intensity changes.

In highly reflective samples, $|\tilde{E}_b|$ can be large, and the middle term of Eq. (2.23) may not be entirely negligible. One widely used strategy to mitigate background artifacts is to normalize the measured data by a reference measurement. For instance, placing a metal padding near the sample and dividing the sample signal by the reference signal significantly reduces unwanted variations from $\tilde{E}_b$[127, 128].

Heterodyne Detection (HTD). Heterodyne detection (HTD) is able to completely suppress the signal background [129, 130]. The main difference between heterodyne and homodyne detection schemes is that, in HTD, the reference beam is frequency-shifted by $\Delta\omega$, whereas in homodyne detection, both the reference and the near-field beams share the same frequency. Typically, this frequency shift is achieved using an acousto-optic modulator (AOM) or piezo-driven mirrors, as illustrated in Figure 2.6(c).

Similar to the homodyne case, the total electric field in HTD consists of the near-field $\tilde{E}_n$, the background $\tilde{E}_b$, and the frequency-shifted reference $\tilde{E}_r$.

Thus, the intensity I measured by the detector is:

$$I \;=\; \big(\tilde{E}_n + \tilde{E}_b + \tilde{E}_r\big)\,\big(\tilde{E}_n + \tilde{E}_b + \tilde{E}_r\big)^* \tag{2.24}$$

where $\tilde{E}_r$ now represents a beam at frequency $\omega + \Delta\omega$. Expanding this expression yields:

$$\begin{aligned} I \;&= |\tilde{E}_n|^2 + |\tilde{E}_b|^2 + |\tilde{E}_r|^2 \;+\; 2\,|\tilde{E}_n|\,|\tilde{E}_b|\cos(\varphi_n - \varphi_b) \\ &\quad +\; 2\,|\tilde{E}_n|\,|\tilde{E}_r|\cos\big(\Delta\omega\,t + \varphi_n - \varphi_r\big) \;+\; 2\,|\tilde{E}_b|\,|\tilde{E}_r|\cos\big(\Delta\omega\,t + \varphi_b - \varphi_r\big) \end{aligned} \tag{2.25}$$

where φ_n, φ_b, and φ_r denote the phases of the near-field, background, and reference fields, respectively, and t is time.

Similar to homodyne detection, a lock-in amplifier is used to demodulate the signal at harmonics of the tip-tapping frequency Ω. However, in HTD the reference beam's additional frequency shift $\Delta\omega$ plays a crucial role. The terms $|\tilde{E}_b|^2$ and $|\tilde{E}_r|^2$ remain constant in time and are removed by the lock-in filtering. The mixed terms involving $|\tilde{E}_b|\,|\tilde{E}_r|$ and $|\tilde{E}_n|\,|\tilde{E}_b|$ appear at frequencies $\Delta\omega$ and Ω, respectively, and can also be separated from the near-field term by choosing the appropriate demodulation frequency.

The near-field signal of interest is primarily contained in

$$2\,|\tilde{E}_n|\,|\tilde{E}_r|\cos\big(\Delta\omega\,t + \varphi_n - \varphi_r\big) \tag{2.26}$$

which is modulated at frequencies near $n\,\Omega \pm \Delta\omega$ (where n is the harmonic index). By selecting $n\,\Omega \pm \Delta\omega$ as the demodulation frequency, one effectively isolates the term proportional to $|\tilde{E}_n||\tilde{E}_r|$, thus enhancing the near-field signal while suppressing $\tilde{E}_b$.

Because $\Delta\omega$ is defined by the experimenter (for instance, through the AOM driver), its phase and amplitude are fully controllable. This makes the detected phase information purely related to the near-field, free from any unpredictable background phase contributions. One practical benefit of HTD is the convenient reference provided by the beat frequency $\Delta\omega$, which can be used to stabilize and align the interferometer.

Pseudo-Heterodyne Detection (PHD). A limitation of the heterodyne detection (HTD) scheme is that the reference beam frequency shift is typically introduced by an acousto-optic modulator (AOM), which operates only within a restricted spectral range. To overcome this issue, a technique called *pseudo-heterodyne detection* (PHD) has been proposed and is now widely used [131–133]. As illustrated in Figure 2.6(d), the PHD setup closely resembles the standard homodyne configuration, with the important difference that the reference mirror is made to oscillate at a low frequency ω_m (much smaller than the tip's tapping frequency Ω) and with a small spatial amplitude a. This mechanical motion changes the optical path of the reference arm, thus *phase modulating* the reference beam.

The reference electric field can be expressed as a Fourier series:

$$\tilde{E}_r \;=\; \sum_{k=-\infty}^{+\infty} A_k \, e^{\,ik\,\omega_m\,t} \tag{2.27}$$

where the coefficients A_k are given by

$$A_k \;=\; J_k\big(\kappa\big)\, e^{\,i\,k\,\Delta\varphi} \tag{2.28}$$

J_k is the kth-order Bessel function of the first kind, and κ depends on the oscillation amplitude of the mirror. The term $\Delta\varphi$ represents the phase offset between the reference and the near-field beams.

Because the reference is phase-modulated, sidebands arise around the harmonics of the tip-tapping frequency $n\Omega$ at frequencies $n\Omega \pm m\,\omega_m$ (where n and m are integers). Each sideband carries a specific combination of the *real* or *imaginary* part of the complex near-field signal. By choosing an appropriate amplitude a for the mirror oscillation, one can ensure that these sidebands encode both the real and imaginary components of the near-field response with comparable magnitudes.

2.2.2 The Generalized Lock-In Amplifier (G-LIA)

The Generalized Lock-In Amplifier (G-LIA) [134] extends the capabilities of traditional lock-in amplifiers by accommodating non-linear phase modulations and improving signal-to-noise ratio (SNR). While standard lock-in amplifiers demodulate signals based on sinusoidal reference waveforms, G-LIA generalizes the approach to handle arbitrary periodic modulation functions. The scattered intensity $I(t)$ in the interferometer is expressed as:

$$I(t) \propto P\,[1 + s\cos(\Delta\phi(t))] \tag{2.29}$$

where P is the optical power, s is proportional to the scattered field amplitude E_s, and $\Delta\phi(t) = \phi_r(t) - \phi_s$ represents the phase difference between the reference beam ($\phi_r(t)$) and the scattered beam (ϕ_s).

Unlike traditional approaches, G-LIA uses orthogonal reference signals, defined as:

$$C(t) = \cos[\phi_r(t)] \tag{2.30}$$

$$S(t) = \sin[\phi_r(t)] \tag{2.31}$$

to demodulate the detected signal. The outputs of the G-LIA are then calculated as:

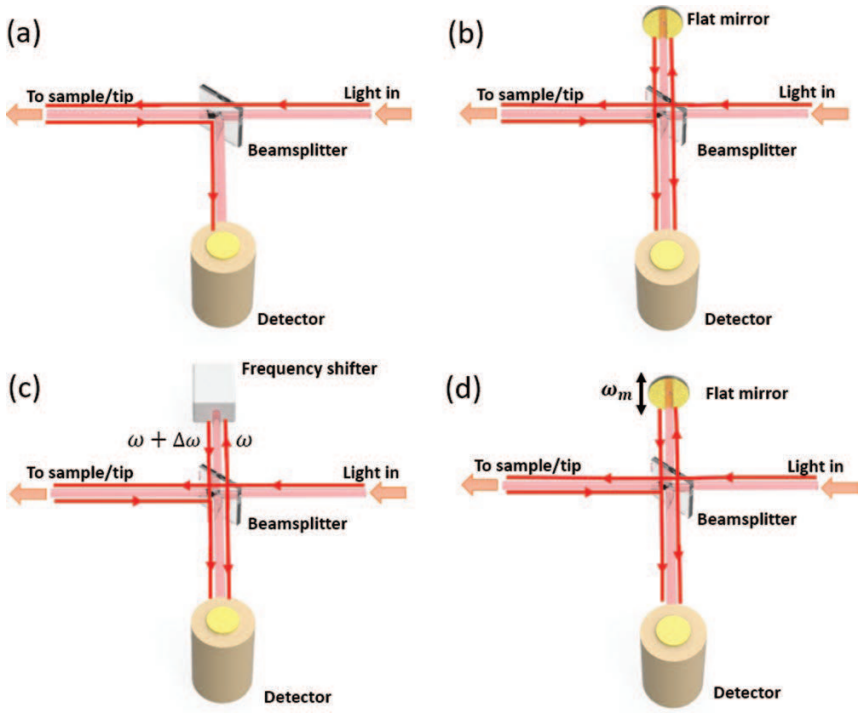

Figure 2.6: S-SNOM detection schemes. (a) Self-homodyne detection, (b) homodyne detection, (c) heterodyne detection and (d) pseudo-heterodyne detection [125].

$$X(I) = \frac{1}{t_{\text{int}}} \int_0^{t_{\text{int}}} I \cos(\Omega t)\, dt \propto s \cos(\phi_s) \tag{2.32}$$

$$Y(I) = \frac{1}{t_{\text{int}}} \int_0^{t_{\text{int}}} I \sin(\Omega t)\, dt \propto s \sin(\phi_s) \tag{2.33}$$

averaged over a time t_{int}. From these outputs, the amplitude s and phase ϕ_s of the scattered signal can be reconstructed as:

$$s \propto \sqrt{X^2 + Y^2} \tag{2.34}$$

$$\phi_s = \tan^{-1}\left(\frac{Y}{X}\right) \tag{2.35}$$

Advantages of G-LIA in s-SNOM

The introduction of G-LIA into s-SNOM systems offers several key advantages over traditional lock-in amplifiers. G-LIA is capable of handling non-linear phase modulations, such as sinusoidal or triangular modulations, which often arise in experimental setups. This flexibility ensures robust demodulation even under complex modulation schemes. The generalized lock-in amplifier (G-LIA) improves the signal-to-noise ratio by integrating information from multiple harmonics of the modulation frequency, enabling the detection of weak near-field signals even in the presence of strong background noise. In systems with sinusoidal phase modulation, the near-field signal is distributed across multiple sidebands, which G-LIA efficiently combines to recover the amplitude and phase response. For example, if we set $\omega_0 = f_0$, the modulation frequency of the piezo in the reference arm (typically sinusoidal at a few hundred

hertz) interacts with the scattered light modulation at the cantilever's tapping frequency (f_0) or its higher harmonics (e.g., $2f_0$). This interaction produces sidebands around the cantilever frequencies due to the mixing process. G-LIA integrates these sidebands and uses two orthogonal reference signals synchronized to the modulation frequency of the reference arm, enabling precise determination of the scattered light's phase. This capability makes G-LIA particularly powerful for isolating weak near-field signals in complex systems.

2.3 Photo-induced force microscopy (PiFM)

2.3.1 Theoretical description of PiFM

The photo-induced force microscopy is a scanning probe microscopy (SPM) nanoscopy based on atomic force microscopy. This technique combines topographic information at the nanoscale by measuring the interaction force between a nanoscopic tip and the surface of a sample but also spectroscopic information using an excitation laser which induces an optical interaction between the tip and the surface sample [135]. PiFM is part of a large family of nano-spectroscopic SPM, including scanning near-field optical microscopy (s-SNOM) and tip-enhanced Raman spectroscopy. PiFM detects the light-matter interaction through the mechanical vibration of the cantilever while s-SNOM detects the light scattered from the tip apex in the far-field, as previously described.

The PiFM operates in tapping mode, where the tip is externally driven by a piezoelectric element to create oscillation of the cantilever beam with a small amplitude (typically 1 to 2 nm). The oscillation frequency is carefully chosen to match the mechanical resonance of the cantilever. For topography measurements, the cantilever oscillates at the second mechanical resonance ($f_2 \simeq 1.6$ MHz), while for the photo-induced force signal, the cantilever is tuned to its first mechanical resonance ($f_1 \simeq 250$ kHz). In this work, f_1 is referred to as the PiFM channel, and f_2 as the topography channel.

In addition to PiFM, the Vista One system from Molecular Vista, used in this work, also includes an s-SNOM module. Rather than detecting the mechanical oscillation of the cantilever induced by the infrared laser, the scattered light from the tip apex is collected by a parabolic mirror and sent to a detector. Typically, this detector is a mercury-cadmium-telluride (MCT) detector cooled by liquid nitrogen. A two-arm interferometric module is also present, enabling both homodyne and heterodyne detection schemes. A detailed description of s-SNOM is available in the section 2.2.

Homodyne and heterodyne detection modes

PiFM detects photo-induced forces between the tip and the sample. The origin of these forces is complex and will be described in more detail in the paragraphs below. Two detection modes are employed: homodyne detection and heterodyne detection, also referred to as direct drive detection and *sideband* detection, respectively. The incident laser is power-modulated at the frequency f_m which can take two different values depending on the detection mode:

$$f_m = f_1$$

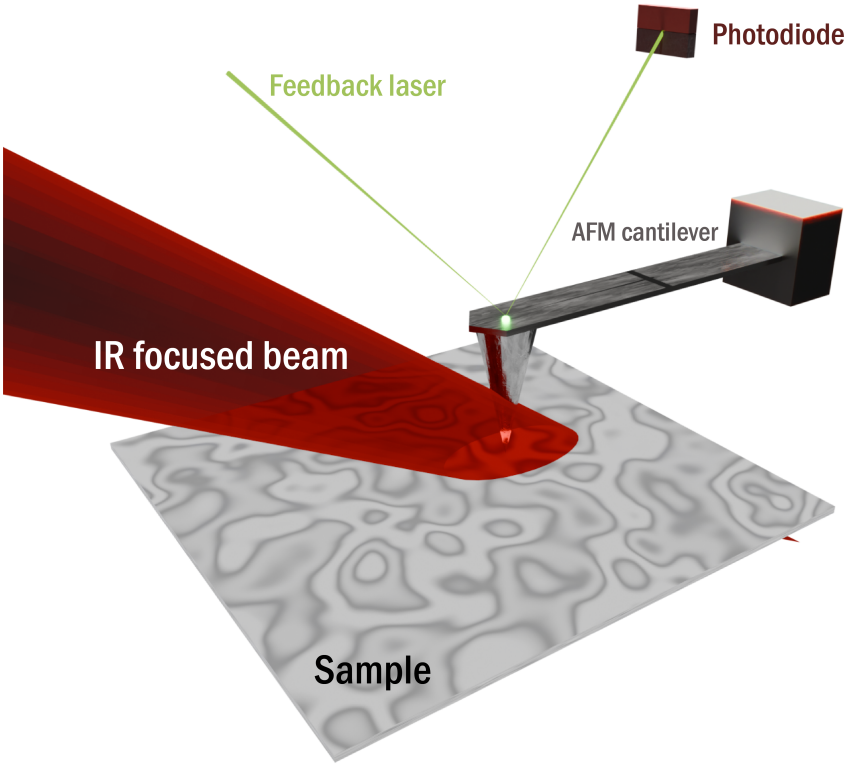

Figure 2.7: PiFM system scheme and detection modes. In *direct* detection mode, the topography is acquired at the second mechanical resonance of the cantilever f_2 and the photo-induced force is measured at the first mechanical resonance f_1. However, in *sideband* detection mode, the photo-induced force is detected through $f_m = |f_2 \pm f_1|$.

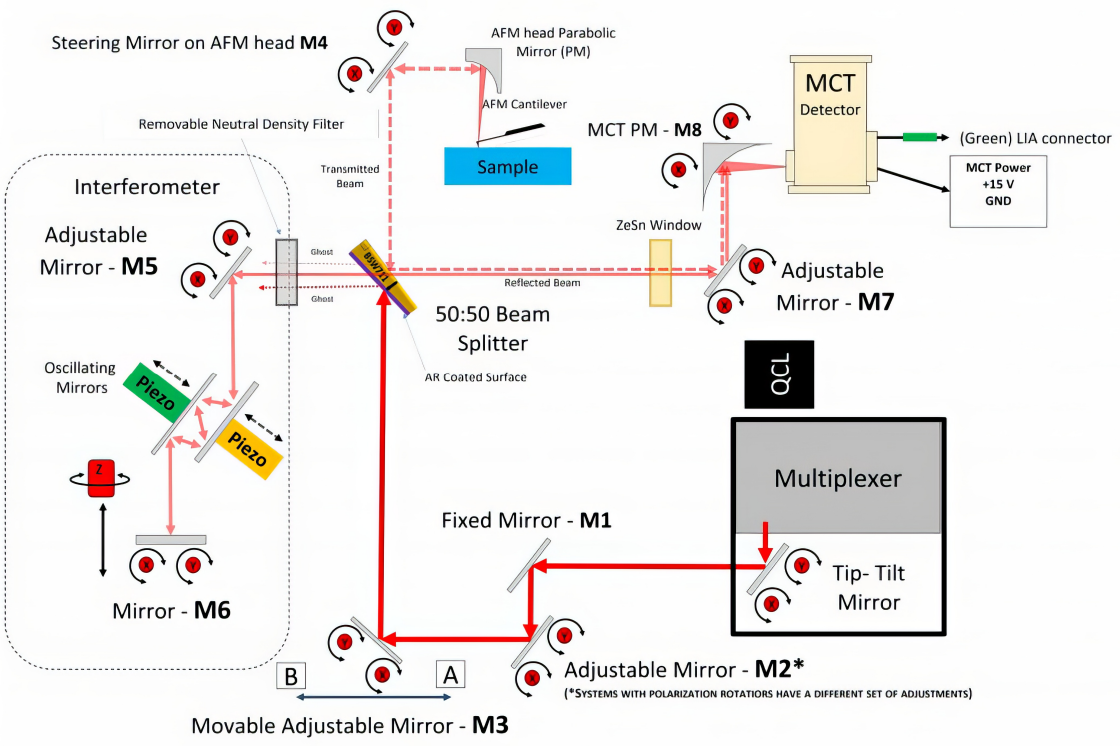

Figure 2.8: Optical pathways of the Vista One system from Molecular Vista Inc., highlighting the PiFM setup, the s-SNOM module, and the interferometric module. The infrared laser, shown in red, originates from the QCL source and is focused onto the tip apex. In a conventional s-SNOM configuration, the scattered light is collected by an MCT detector. In the interferometric s-SNOM mode, the incident laser beam is split: 50% is directed to the interferometer, while the remaining 50% is focused onto the tip apex. Illustration provided by Molecular Vista Inc.

or

$$f_m = |f_2 \pm f_1|$$

. The photo-induced forces are detected through the demodulation (typically with a lock-in amplifier) of the cantilever's oscillation amplitude near f_1. Frequency modulation is showcased on the Figure 2.7.

Homodyne (direct) detection mode. In homodyne detection mode, the cantilever is driven at its first mechanical resonance frequency (f_1) and the incident laser at $f_m = f_1$. The oscillation amplitude demodulation of the cantilever at f_1 allows to retrieve both scattering and gradient forces.

Heterodyne (sideband) detection mode Also referred as *sideband* mode, the heterodyne mode aims to provide a background-free signal. This mode is optimized to isolate the gradient forces which are highly localized at the tip-sample interface. The cantilever is driven at f_2 while the incident laser is power-modulated at f_m which satisfies the condition $f_1 = f_2 - f_m$. Once again, the signal is demodulated near mechanical resonance frequency f_1. This mode is far more sensitive to small variations due to a nonlinear dependence of the forces at the tip-sample junction. This method is widely favored for high-resolution optical imaging where background-free signals are crucial [136].

It is worth noting that the detection mode directly influences the probing volume. In *direct* mode, the probing volume is large, more than 100 nm depth and in-plane direction. This mode is convenient for homogeneous materials, also called bulk materials. In contrast, the *sideband* mode has a higher spatial resolution, with a penetration depth less than 20 nm. The in-plane resolution usually goes down to 5 nm.

Table 2.1: Comparison of Homodyne and Heterodyne Detection Techniques for PiFM.

Feature	**Homodyne Detection**	**Heterodyne Detection**
Detection Principle	Laser modulated at first resonance frequency (f_1), detecting both scattering and gradient forces.	Laser modulated at frequency f_m, generating a sideband at $f_2 - f_m = f_1$, isolating gradient forces.
Signal Composition	Includes both scattering and gradient forces, leading to noise.	Isolates gradient forces, suppressing scattering forces for a cleaner signal.
Resolution	Lower spatial resolution due to scattering forces.	Higher resolution with sensitivity to localized gradient forces.
Background Signal	Contains background from scattering light.	Near-background-free signal by removing scattering forces.
Complexity of Setup	Simpler setup with single frequency modulation.	More complex setup requiring frequency mixing for sideband detection.
Speed of Acquisition	Faster, suitable for rapid imaging.	Slower due to the complexity of modulation.

Physical origin of the photo-induced force

The AFM tip plays a major role in the PiFM system. The tip is positioned near the sample surface and externally driven at f_m using a dithering piezoelectric. The tip, polarized by the incident infrared light, strongly confines evanescent fields at the tip apex. The polarizability is mainly in the vertical direction and those evanescent waves are mostly p-polarized.
The physics behind the interaction between the light and the tip-sample junction is complex and still under debate. In this section, we will discuss the various contributors of the photo-induced force. Originally, the PiFM was developed to probe the electromagnetic force between the tip and the sample, but it has been discovered that there are other contributions. Most important contributors derive from light absorption by the sample or the tip, and the thermal expansion of the sample at the tip-sample junction [135].

Photo-induced Electromagnetic Force

When light illuminates the cantilever tip, it induces charge oscillations, resulting in polarization at the optical driving frequency. This polarization can be modeled as an oscillating dipole: $p_t = \alpha_t E$, where $\alpha_t = \alpha_t' + i\alpha_t''$ is the tip's polarizability, and E represents the electric field. Assuming scalar polarizability, the time-averaged electromagnetic force acting on the tip is given by the following expression:

$$\langle F \rangle = \frac{\alpha_t'}{2} \sum_i \Re \left(E_i \nabla E_i \right) + \frac{\alpha_t''}{2} \sum_i \Im \left(E_i \nabla E_i \right) \tag{2.36}$$

where $i = \{x, y, z\}$ corresponds to the Cartesian directions. The first term, proportional to the real part of the polarizability, describes a non-dissipative, conservative force related to the optical gradient. The second term, linked to the imaginary part of the polarizability, is a dissipative force arising from momentum transfer through light scattering.

The magnitude of the gradient force depends on the steepness of the local optical field gradient near the tip, which is enhanced near surfaces supporting localized electromagnetic resonances, such as surface plasmons or phonon polaritons. This principle underlies PiFM contrast in areas with strong field variations, like plasmonic structures or materials with collective vibrational modes.

When the tip approaches a dielectric surface, the local field and resulting photo-induced force change due to proximity effects. Using image dipole theory, where the image dipole has polarizability α_t', the distance-dependent force in the z-direction is:

$$\langle F_g \rangle_z \approx \frac{3\Re(\alpha_t \alpha_t')}{4\pi\epsilon_0\epsilon_m z^4} |E_z|^2 \tag{2.37}$$

Here, ϵ_m is the permittivity of the medium around the tip. The force scales as z^{-4}, meaning it becomes stronger as the tip approaches the sample, and the force is attractive. The magnitude of the induced force is also sensitive to the material's permittivity underneath the tip.

Dipole-dipole interaction force. The incident IR light, focused at the tip apex, induces a polarization of the tip and the sample. The sample's polarization is

$p_s = \alpha_s E$, where $\alpha_s = \alpha_s^{'} + i\alpha_s^{"}$ is the polarization of the sample, with the real part $\alpha_s^{'}$ relating to the dispersive properties and the imaginary part $\alpha_s^{"}$ relating to absorption. The presence of these dipoles affects the local field at the tip, leading to a gradient force described by:

$$\langle F_g \rangle_z \propto \frac{3\,\mathrm{Re}\{\alpha_t \alpha_s\}}{4\pi\epsilon_0 z^4} |E_z|^2 \tag{2.38}$$

where z is the separation between the tip and the sample. The interaction exhibits a characteristic dispersive lineshape near an optical resonance of the sample, where the dipole-dipole forces significantly contribute to the PiFM signal. These forces, although in the range of piconewtons (pN), can be detected with high precision [137].

As mentioned in the beginning of the section, the PiFM signal can be attributed to different mechanisms, primarily the dipole-dipole interaction or photothermal effects. The dipole-dipole force, which dominates in many cases, follows a dispersive spectral response tied to the real part of the sample's polarizability. This dispersive behavior contrasts with the Lorentzian lineshape associated with photothermal effects, which relate to heat exchange between light and matter.

Both effects contribute to the overall signal and heterodyne detection techniques are used to isolate the sample-dependent components from undesired scattering forces. The dipole-dipole interaction is described mathematically by the following expression for the photo-induced force:

$$F_{\mathrm{pif}} = \frac{2\pi\alpha_t''}{\lambda}|E_x|^2 - \frac{3\alpha_t''\alpha_s''}{2\pi^2 z^4}|E_z|^2 \tag{2.39}$$

where α_t'' and α_s'' are the imaginary parts of the polarizabilities of the tip and sample. The force is modulated at the frequency of the incident light.

Model for tip-sample interaction: Several models have been proposed to describe the interaction between the AFM tip and the sample in PiFM, with two prominent ones being the Point Dipole (PD) model and the Finite Dipole (FD) model.

Point Dipole Model. In this model, the AFM tip is approximated as a small polarizable sphere of radius R. When polarized by the incident field E_i, the induced dipole moment is:

$$p = \alpha E_i \tag{2.40}$$

α, the tip's polarizability is:

$$\alpha = 4\pi R^3 \frac{\varepsilon_t - \varepsilon_m}{\varepsilon_t + 2\varepsilon_m} = 4\pi R^3 \frac{\varepsilon_t - 1}{\varepsilon_t + 2} \tag{2.41}$$

with R the apex radius, ε_t the tip dielectric constant and ε_m the surrounding medium dielectric constant. For a metallic tip (Au/Pt) in air ($\varepsilon_m = 1$), α is practically constant in the infrared since $|\varepsilon_t| \gg 1$.

According to image charges theory, the tip dipole considered at a distance of $R + H$, induces a mirror image dipole in the sample at a distance $-(R + H)$. This

image dipole has moment defined as $p_{im} = \beta p$. β is the sample response reflection coefficient. This virtual source is responsible for self-field reflected back on the primary source dipole. The field of the image dipole is given by $E_{im}(r_{tip}) = S^{nf}(r_{tip}, r_{im})p_{im}$, where S^{nf} is the near field contribution of the dyadic Green's propagator that links E and p ($S^{\mathrm{nf}} = \frac{1}{16\pi(R+H)^3}$ when only the term perpendicular to the sample surface is considered). Therefore, the dipole moment of the tip is affected by the presence of the induced dipole $p = \alpha(E_i + E_{im})$ (the local field $E_L = E_i + E_{im}$)[122, 138]. By replacing E_{im}, the relation between E_i and E_L is derived:

$$E_L = \frac{E_i}{(1 - \alpha\beta S^{nf})} \tag{2.42}$$

Finally, the effective polarizability becomes:

$$\alpha_{eff}^{PD} = \frac{\alpha}{1 - \alpha\beta S^{nf}} = \frac{\alpha}{1 - \frac{\alpha\beta}{16\pi(R+H)^3}} \tag{2.43}$$

Finite Dipole Model. The FD model treats the tip as an elongated spheroid, better suited for explaining field enhancement effects. The elongated dipole consists of two charges $\pm Q_0$, which, when near the sample, induce a second dipole with charges $\pm Q_i$. The effective polarizability in this case is:

$$\alpha_{\mathrm{eff}}^{\mathrm{FD}} = \alpha^{\mathrm{FD}} \left(1 + \frac{f_0\beta}{1 - f\beta}\right) \tag{2.44}$$

where f_0 and f are functions of the tip geometry and distance from the sample surface. This model provides a more detailed representation of the tip-sample interaction, particularly in cases where the AFM tip induces strong near-field effects that shift the resonance frequency.

Both models aim to describe the near-field interactions between the AFM tip and the sample, which result in measurable forces or scattered fields in techniques like PiFM or Scanning Near-field Optical Microscopy (SNOM). While the Point Dipole model is simpler and often sufficient, the Finite Dipole model captures more complex interactions.

Photo-thermal expansion force

When a sample absorbs light, expansion can occur due to increased local temperature. The infrared laser induces a local heat at the surface sample and the electromagnetic field is also confined by the tip apex. The thermal expansion ΔL is proportional to the thermal expansion coefficient σ, the effective distance d_{eff}, and ΔT. ΔT is the temperature rise over d_{eff}.

$$\Delta L = \sigma . d_{eff} . \Delta T \tag{2.45}$$

The temperature variation ΔT depends on the absorbed power P_{abs}, the modulation frequency f_{mod}, and the heat capacity C:

$$\Delta T = \frac{P_{\mathrm{abs}}}{2 f_{\mathrm{mod}} C}$$

The diffusion length expression involves the thermal diffusivity α and the angular frequency of the heating modulation ω:

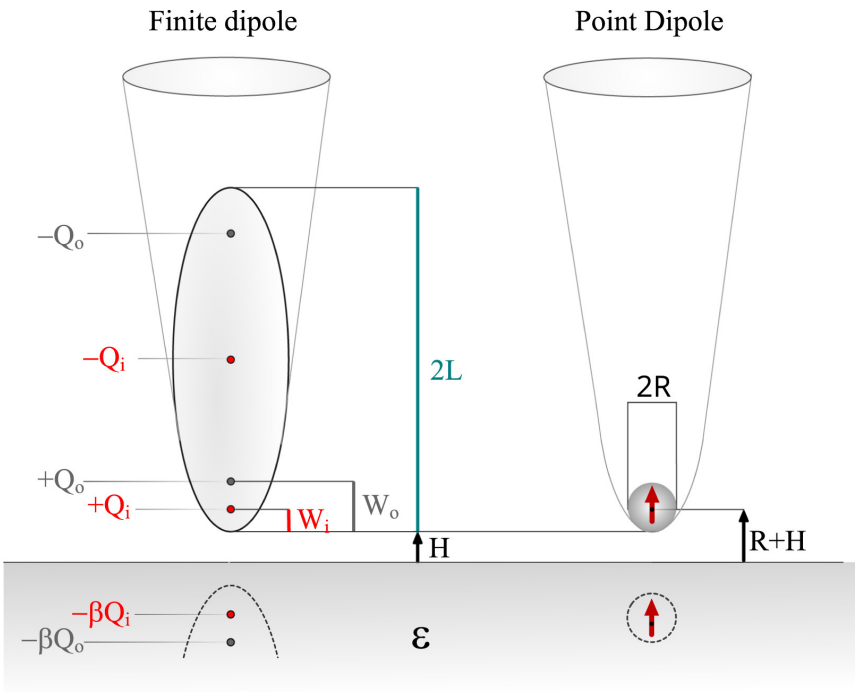

Figure 2.9: Schematic comparison of the Finite Dipole Model and the Point Dipole model, providing the different scales involved. Far from a surface only the charges and are present. The effective charges induced by the surface are mostly in the center and lower spheroid focus [139, 140]

$$\omega = 2\pi f_{\text{mod}}$$

The heat diffusion equation is given by:

$$\frac{\partial T}{\partial t} = \alpha \nabla^2 T$$

The temperature distribution in a medium can be expressed as:

$$T = \exp\left(\frac{-z}{\sqrt{\frac{2\alpha}{\omega}}}\right)$$

Where the diffusion length $D(\omega)$ is:

$$D(\omega) = \sqrt{\frac{2\alpha}{\omega}}$$

For organic materials, d_{eff} is usually 1-100 nm range and ΔL 1-100 pm. Even if these variations are very small, they can still be detected through changes in the force between the tip and the sample.

Even in the absence of illumination, the tip experiences a force due to its proximity to the sample. This interaction between the tip and sample, denoted as $F_{ts}(z)$, can be modeled as a combination of conservative and non-conservative forces, expressed as:

$$F_{ts}(z) = F_c(z) - G(z)\dot{z}$$

Here, $F_c(z)$ represents the conservative component, while $G(z)$ is an effective damping coefficient associated with a dissipative mechanism [135]. The force F_{ts} highly depends on the tip-sample distance, z, and includes attractive and repulsive components.

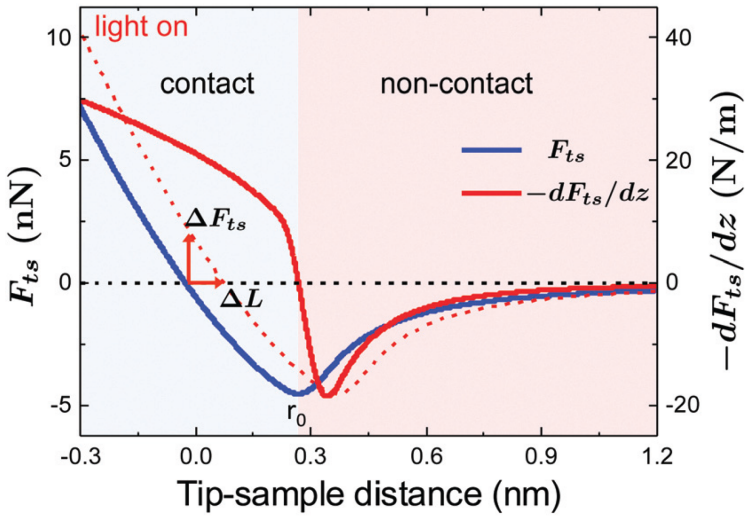

Figure 2.10: Effect of the thermal expansion ΔL on the tip-sample interaction force F_{ts}. Blue curve shows F_{ts} when the light is off, while red dashed curve shows F_{ts} when the light is on. The red solid curve shows $-\partial F_{\mathrm{ts}}/\partial z$, which is proportional to the magnitude of the thermal expansion force [135].

Figure 2.10 illustrates the behavior of F_{ts} as a function of z. In the region where the tip does not come into contact with the sample, F_{ts} is governed primarily by attractive forces, such as van der Waals (VdW) interactions. As the tip approaches the sample and enters the contact region, repulsive forces dominate. When $z = 0$ or less, the tip is in full contact with the surface, and F_{ts} becomes exclusively repulsive. These repulsive forces can be described using the Derjaguin–Muller–Toporov (DMT) model. Both the VdW and DMT forces depend on the distance z. Variations in sample size affect the tip-sample distance, leading to changes in the interaction force.

2.3.2 PiFM model based on effective polarizability enhanced absorption

Recent publications [139, 141, 142] have shown that the induced dipole force is more intense on materials with strong phonon oscillators, which have stronger polarizability with a negative real part of the dielectric function ε'. In contrast, the magnitude of the induced thermal forces is directly influenced by photo-absorption near the material surface. Jahng et al. [143] proposed an analytical model based on the evaluation of an effective absorption coefficient which assumes a low absorption regime.

Theoretically, it could be possible to predict the dipole-dipole force and the photothermal response of 2D materials such as MXenes, but this requires knowledge of the material's dielectric function $\varepsilon(\omega)$. Since MXene is a complex material composed of different layers of transition metals and has a non-homogeneous surface, it is difficult to measure or simulate its dielectric function.

The total optical absorption power in a given volume is:

$$P = A \int Q(z)\, dz \tag{2.46}$$

where A is a small cross-sectional area below the tip apex, $Q(z) = \frac{1}{2}\omega|\mathcal{E}(z)|^2\varepsilon_0\varepsilon''$, and $\mathcal{E}(z)$ is the evanescent electric field below the surface, generated by the tip. It is worth noting that the power P is only dependent on the z-axis because the PiFM tip detects only the force along the z direction.

By considering illumination of the tip directly and through reflection, where the incident light is mostly p-polarized, we have:

$$Q(z) \propto \frac{1}{2}\omega|1 + r_p|^2|\alpha_{\text{eff}}E(z)|^2\varepsilon_0\varepsilon'' \tag{2.47}$$

where r_p is the sample reflectivity derived from Fresnel equations, ε_0 is the vacuum permittivity, and the loss term reduces to the imaginary part of the complex dielectric function of the sample.

This theoretical framework will be validated experimentally in Chapter 5, where we will demonstrate that PiFM spectra on MXenes show remarkable similarity to FTIR spectra. This similarity provides important insights into the optical interaction mechanism, as FTIR spectroscopy directly probes ε'' in the far-field regime without significant local field amplification. This also confirms the close similarity between those two techniques for non-resonant materials such as organic materials [144–147]. Spectral matching will indicate that the effective polarizability α_{eff} remains approximately constant across the investigated frequency range, suggesting the absence of significant localized plasmonic resonances or tip-enhanced effects. Additionally, our far-field measurements presented in Chapter 3 will show that the reflectivity term $|1 + r_p|^2$ exhibits quasi-homogeneous behavior across different MXene samples.

Under these theoretical conditions, all prefactors in the complete expression become frequency-independent multiplicative constants. In the case of MXene, the absorption power density can therefore be simplified to:

$$Q(z) \propto \varepsilon'' \tag{2.48}$$

This simplification predicts that the PiFM signal should directly reflect the imaginary part of the dielectric function, making it particularly suitable for direct chemical identification of MXene materials where the spectroscopic contrast directly correlates with the material's intrinsic vibrational modes. The experimental validation of this model will be presented in Chapter 5.

2.4 A comparative study of PiFM and s-SNOM on semi-conductors

Previously, we described that Photo-induced Force Microscopy (PiFM) and scattering-type Scanning Near-field Optical Microscopy (s-SNOM) are two related nanoscale characterization techniques that both exploit the electromagnetic coupling between a sharp metallic tip and the sample surface. Despite their conceptual

similarity in tip-sample interaction and near-field enhancement mechanisms, these techniques differ fundamentally in signal detection principles and data acquisition strategies.

In PiFM, the focused laser illumination at the tip apex generates localized electromagnetic fields that interact with the sample's optical properties. This interaction manifests as measurable modifications in the dynamic behavior of the AFM cantilever oscillation through various mechanisms as discussed previously. The technique thus converts optical information into mechanical signals that are detected through the modification of the oscillation of the AFM cantilever.

In the opposite, s-SNOM operates through elastic light scattering, where the incident laser beam focused at the tip-sample junction undergoes scattering processes that encode information about the local dielectric properties of the sample. The backscattered light is then collected and analyzed by interferometric detection schemes to obtain both amplitude and phase information about the near-field optical response.

Given these distinct signal detection principles, a fundamental question emerges: for a given sample, which technique should be preferred and what specific material properties can each method uniquely reveal? The dual photomechanical nature of PiFM, involving both photothermal effects and electromagnetic dipole-dipole interactions, may provide enhanced sensitivity to thermomechanical responses and absorption-based contrasts, while s-SNOM's direct scattering detection could offer superior access to complex dielectric functions and plasmonic behaviors. Understanding whether these techniques yield complementary insights or redundant information is crucial for optimizing experimental strategies and maximizing the information content extracted from nanoscale measurements.

To address these questions, we conducted a comparative analysis using two type of materials: bulk silicon carbide and pattern silicon oxide. These materials were selected to provide a diverse range of optical and mechanical properties, enabling a comprehensive evaluation of each technique's capabilities and limitations across different material classes.

Silicon carbide

Semiconductor materials such as silicon carbide (SiC) serve as excellent benchmark systems for near-field microscopy due to their well-characterized phononic properties and established theoretical models. 4H-SiC, a wide-bandgap semiconductor with hexagonal crystal structure, exhibits distinct infrared-active phonon modes that provide clear spectroscopic signatures for technique validation. In this section, we compare PiFM and s-SNOM spectroscopic capabilities on 4H-SiC as a precursor to investigating more complex two-dimensional materials.

4H-SiC corresponds to a specific stacking sequence of silicon and carbon atoms in a hexagonal configuration. This material finds extensive applications in high-power electronics, including JFET transistors and power conversion devices, due to its superior thermal conductivity, high breakdown field, and chemical stability [139]. The thermal management properties of SiC devices are intimately linked to their phononic behavior, making spectroscopic characterization of phonon modes crucial for device optimization and thermal modeling [148].

The infrared response of SiC is dominated by polar optical phonon modes that

couple strongly to electromagnetic radiation. The primary phonon modes of interest are the transverse optical (TO) and longitudinal optical (LO) phonons, which in polar semiconductors give rise to surface phonon polaritons (SPhPs) - hybrid excitations coupling photons with surface phonons. Theoretical models developed by Hillenbrand for s-SNOM and the finite/point dipole model [139] for PiFM provide frameworks for interpreting the spectroscopic response of these systems.

Spectroscopic comparison. Figure 2.11 presents a direct comparison of spectroscopic data acquired using two different approaches: PiFM and conventional s-SNOM. Since 4H-SiC presents a homogeneous, unstructured surface, spectroscopic measurements rather than spatial imaging were performed to evaluate the spectral resolution and sensitivity of each technique.

The acquisition of GLIA spectroscopic data presents significant experimental challenges compared to conventional s-SNOM or PiFM measurements. The GLIA technique requires precise control of the Michelson interferometer's reference mirror amplitude for each wavelength point across the spectrum. This wavelength-dependent optimization is necessary because the interferometric balance between the reference and sample arms must be carefully maintained to achieve optimal background suppression and signal enhancement. The reference mirror oscillation amplitude must be individually adjusted to match the specific scattering characteristics at each frequency, making spectroscopic acquisition considerably more time-consuming and technically demanding than single-wavelength imaging. At that time, the GLIA spectrum could not be acquired. Nevertheless, fixed-wavelength imaging was achievable and is demonstrated on the following material (silicon nano-array).

PiFM spectroscopic response. The PiFM spectrum (yellow curve) reveals two distinct peaks at approximately 800 cm^{-1} and 920 cm^{-1}, corresponding to the transverse optical (TO) and surface phonon polariton (SPhP) modes, respectively. As described by El-Helou et al. [148], the SPhP mode observed in PiFM measurements corresponds to the longitudinal optical (LO) phonon mode in the bulk material. The slight frequency shift compared to far-field LO measurements can be attributed to the strong near-field interaction between the AFM tip and the sample surface, which modifies the local electromagnetic environment and the effective phonon dispersion.

The PiFM spectrum exhibits excellent signal-to-noise ratio and well-defined peak structures, demonstrating the technique's capability for high-resolution vibrational spectroscopy. The photomechanical detection mechanism in PiFM provides direct access to absorption-related processes, making it particularly sensitive to phonon modes with strong oscillator strength.

s-SNOM spectroscopic analysis. Both conventional s-SNOM (FM2R) and GLIA-enhanced s-SNOM (GLIAR) show spectroscopic features in the same frequency range, but with notable differences in peak positions, intensities, and spectral profiles compared to PiFM. The s-SNOM techniques probe the local dielectric function through elastic light scattering, providing access to both real and imaginary parts of the complex permittivity.

The conventional s-SNOM measurement (FM2R, orange curve) shows spectroscopic features in the same frequency range but significant differences in peak po-

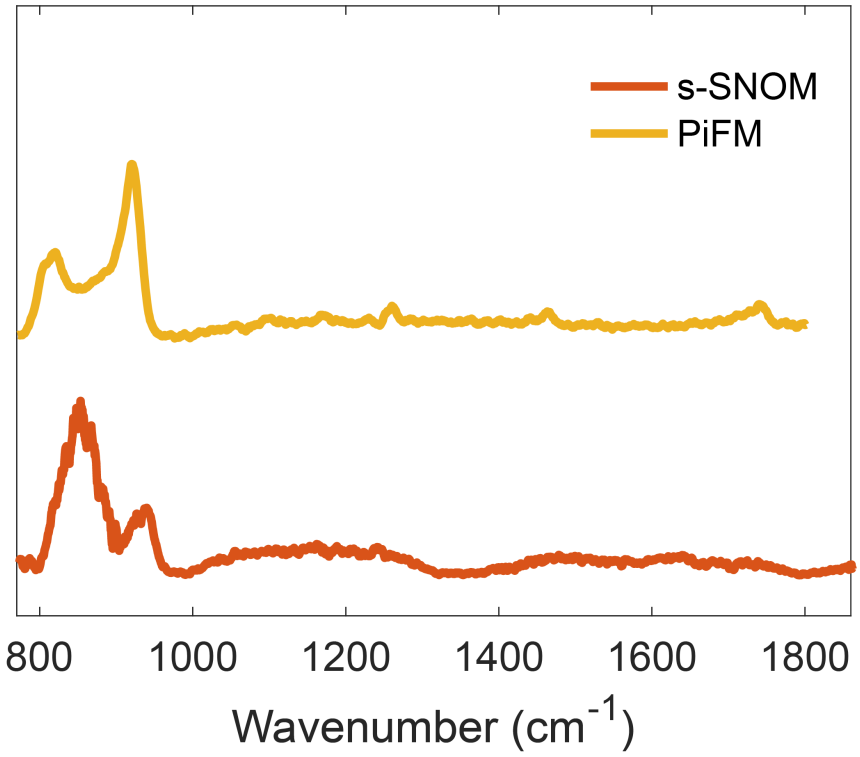

Figure 2.11: 4H-SiC spectra acquired using PiFM and s-SNOM. PiFM signal (yellow curve) was acquired in *sideband* mode with a dither amplitude of 1 nm. Conventional s-SNOM (orange curve) was recorded at ω_O with a dither amplitude of 50 nm.

sitions compared to the PiFM spectrum. The s-SNOM peak positions are shifted compared with those obtained with PiFM, suggesting that the two techniques are probing different aspects of the same phononic system or having different tip-sample interaction mechanisms.

Many factors may explain these spectral differences. The basic detection mechanisms vary considerably between techniques: PiFM uses photo-induced forces from local absorption processes and dipole-dipole interactions between the tip and sample, while s-SNOM detects elastic light scattering related to the complex dielectric function. In PiFM, the dominant mechanism is dipole-dipole coupling between polarized tip apex and the sample, which produces measurable forces that modulate cantilever dynamics. That distinction could cause different sensitivities to the real and imaginary parts of the material's optical response. Also, the tip-sample interaction volume spatial extent and geometry may differ between techniques affecting the phonon dispersion. The coupling mechanisms with surface phonon polaritons could also differ.

Note that the definitive assignment of these spectral differences requires additional investigation, including theoretical modeling of the respective tip-sample interaction mechanisms and systematic study of the wavelength-dependent response.

Silicon nano-array

The silicon oxide nanoarray sample consists of cylindrical nano-holes etched into native silicon oxide, with the surrounding surface covered by thermally deposited silicon dioxide. This calibration standard, also used for AFM validation due to its

precise geometry, presents a test case for evaluating optical contrast mechanisms in near-field microscopy. Since native and thermally grown oxides have different structural properties, their infrared response is unique, making this sample suitable for benchmarking PiFM and s-SNOM techniques.

The topographical characterization (Figure 2.12(a)) showcases a regular array of cylindrical holes with a diameter of approximately 1 μm and a depth of 50 nm, consistent with the manufacturer specifications. The cross-sectional schematic illustrates the two distinct oxide regions: the exposed native SiO_2 at the bottom of the etched holes and the thermally deposited SiO_2 layer on the top surface.

Conventional s-SNOM Detection. The s-SNOM measurements performed at 1666 cm^{-1} using conventional homodyne detection reveal distinct behavioral differences between the fundamental (ω_0) and second harmonic ($2\omega_0$) demodulation approaches. At ω_0 (Figure 2.12(b)), the magnitude signal exhibits weak optical contrast between the two oxide types, with signal levels ranging from 38 μV to 964 μV. However, the image quality is significantly compromised by prominent interference fringes that obscure the underlying material contrast. These fringes arise from the interference between the near-field signal scattered by the tip-sample system and residual far-field background contributions.

Higher harmonic demodulation at $2\omega_0$ (Figure 2.12(c)) demonstrates the expected reduction in far-field artifacts, with notably diminished interference fringe intensity. However, this improvement comes at the cost of reduced signal amplitude (0.3 μV to 60.1 μV) and correspondingly lower signal-to-noise ratio, resulting in an image that is challenging to interpret quantitatively. This trade-off between background suppression and signal strength represents a fundamental limitation of conventional harmonic detection schemes.

Generalized Lock-in Amplifier (GLIA) approach. Compared to bulk silicon carbide, the nano-array was imaged at a fixed frequency, facilitating the use of the GLIA approach. The implementation of the GLIA detection scheme (Figure 2.12(d)) demonstrates remarkable improvement in measurement performance. The magnitude image shows dramatically enhanced contrast between the native and thermally grown oxides, with maximum signal levels reaching 1.68 mV—nearly double the peak signal obtained with conventional ω_0 detection. More importantly, the GLIA approach completely eliminates the interference fringes that plagued the conventional measurements, producing a clean spectroscopic image without requiring post-processing or background subtraction.

This superior performance can be attributed to GLIA's ability to selectively extract the near-field component while inherently suppressing far-field contributions through its advanced demodulation algorithm. The result is both enhanced sensitivity and improved image fidelity, making GLIA particularly valuable for samples with subtle optical contrasts.

Phase Analysis. The phase information (Figure 2.12(e)) provides complementary insights into the dielectric properties of the two oxide regions. The phase contrast reveals distinct values between the hole regions (native oxide) and the surrounding surface (thermal oxide). This phase contrast reflects differences in the complex refractive index between the two oxide types, potentially arising from variations in

density, stoichiometry, or structural ordering introduced by the different formation processes. The phase data, when combined with the amplitude information, enables a more complete characterization of the local dielectric response and can be used to extract quantitative optical constants through appropriate modeling approaches.

The absence of phase artifacts in the GLIA measurement further demonstrates the technique's superiority for quantitative near-field optical analysis, providing both enhanced contrast and artifact-free phase information essential for rigorous material characterization.

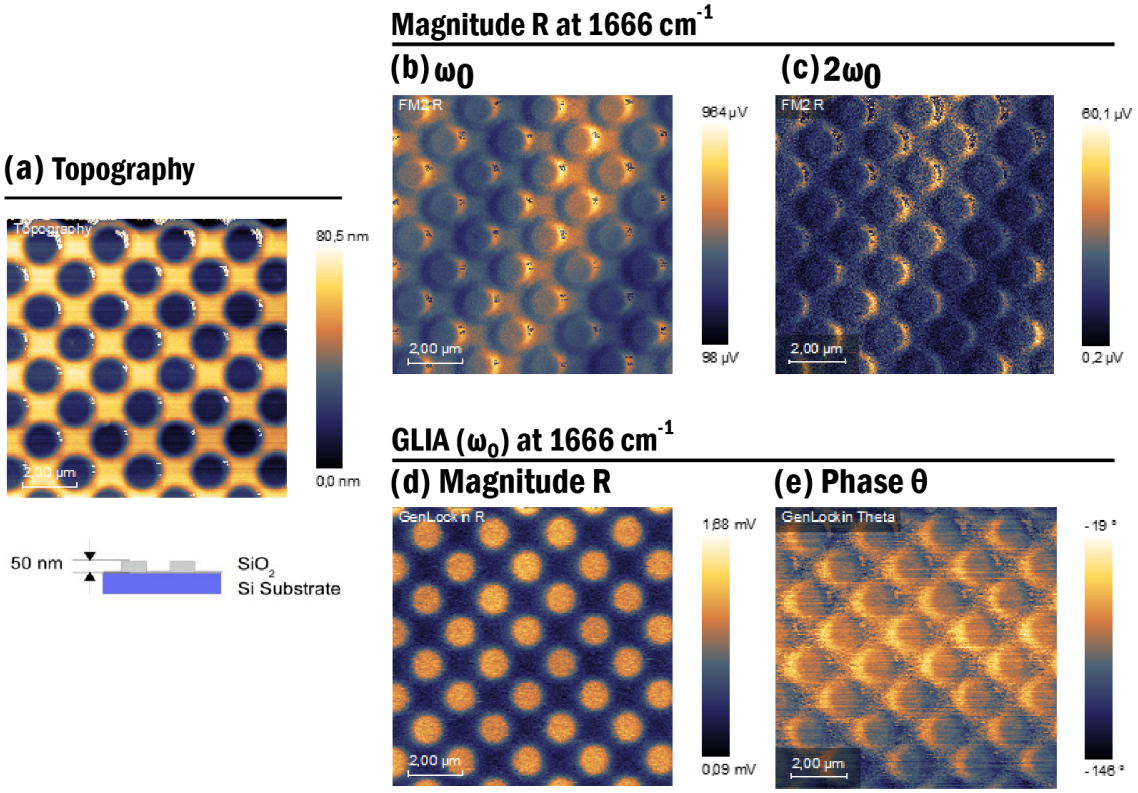

Figure 2.12: Silicon calibration grid. The higher locations on the grid are thermally deposited oxide. The lower locations are native SiOx.

PiFM characterization. PiFM measurements on the same silicon oxide nanoarray samples were performed in addition to s-SNOM analysis. The spectroscopic abilities of PiFM enable wavelength-dependent characterization of the photo-induced response of the various oxide regions over the infrared spectrum.

Spectroscopic analysis. The PiFM spectroscopic data (Figure 2.13(b)) reveals distinct spectral signatures for the two oxide types across the 800-1900 cm^{-1} range. Two prominent absorption peaks are identified: a strong resonance at 1095 cm^{-1} and a secondary peak at 1263 cm^{-1}. These feature typical Si–O stretching vibrations in silicon dioxide with peak positions and relative intensities, revealing local bonding environments and structural differences between native and thermally grown oxides.

The spectral contrast between the two oxide regions (red and blue curves) indicates that PiFM can distinguish between materials having slight differences in vibrational properties. Native oxide (red curve) and thermal oxide (blue curve)

show different peak intensities with minor frequency shifts reflecting local chemical environments, density, and structural ordering variations due to the different formation processes.

Based on the spectroscopic analysis, PiFM imaging was performed at two strategically selected wavelengths to maximize material contrast:

Imaging at 1094 cm^{-1} (Figure 2.13(c)) shows high spatial contrast between the hole regions and the surrounding surface. The PiFM signal ranges from 0.72 mV to 1.84 mV, with the holes appearing as dark regions against a bright background. This contrast pattern indicates that the thermal oxide exhibits a stronger response at this wavelength, consistent with its position near the main Si-O stretching resonance. The image quality is remarkably clean, with no interference fringes or background artifacts, demonstrating PiFM's inherent immunity to far-field interference effects.

Imaging at 1262 cm^{-1} (Figure 2.13(d)) presents a complementary view with inverted contrast compared to the 1094 cm^{-1} measurement. Here, the signal ranges from 74 μV to 684 μV, with the holes now appearing as bright features against a darker background. This contrast inversion suggests that at 1262 cm^{-1}, the native oxide in the holes exhibits a stronger photo-induced response than the thermal oxide on the surface.

This wavelength-dependent contrast capability represents a significant advantage of PiFM, as it allows for chemically selective imaging based on vibrational resonances. The ability to tune the excitation wavelength and observe contrast changes provides a powerful tool for material identification and characterization at the nanoscale.

The PiFM measurements demonstrate several key advantages compared to the s-SNOM results on the same sample. First, the PiFM images are completely free from interference artifacts, eliminating the need for higher harmonic detection or advanced demodulation schemes. Second, the spectroscopic capability allows for wavelength-selective imaging, providing additional chemical specificity. Finally, the contrast mechanisms in PiFM are fundamentally different from s-SNOM, potentially providing complementary information about the sample's properties. Data were extracted from Molecular Vista Inc User guide.

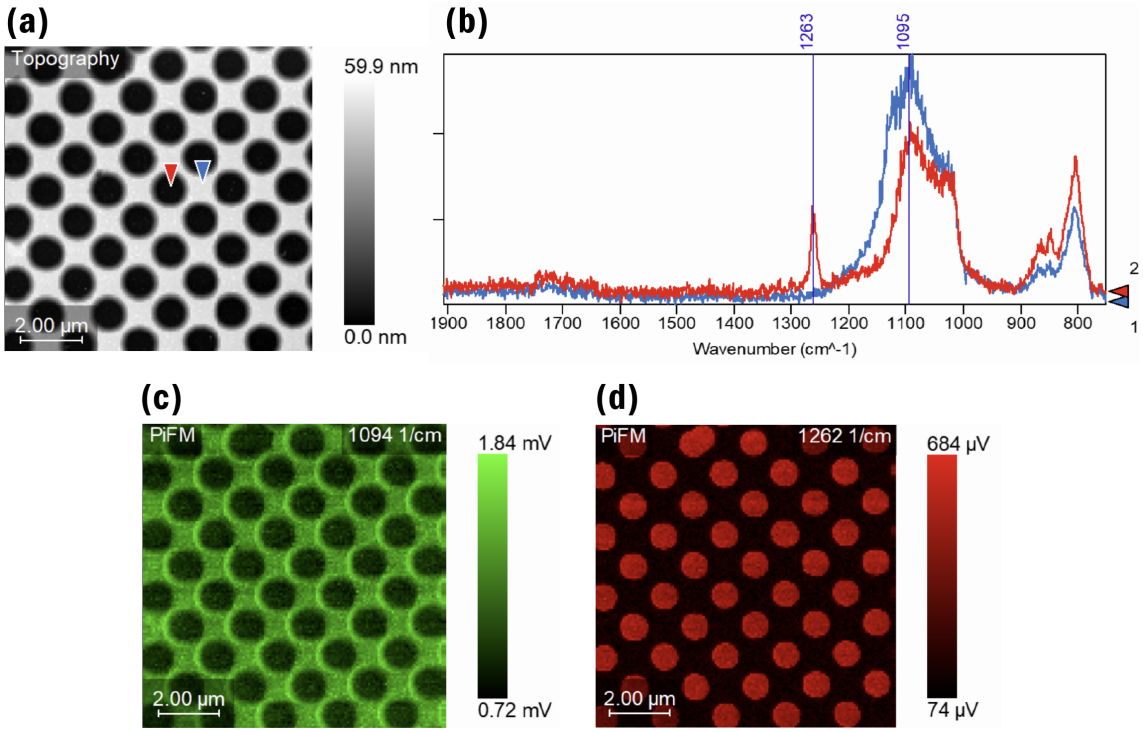

Figure 2.13: PiFM anaylsis of the silicon nano-array: (a) topography showing the two acquisition locations. (b) PiFM spectra of the native (red curve) and thermally deposited (blue curve) oxides. PiFM spectral images at 1094 cm-1 (c) and at 1262 cm-1 (d) highlighting the different materials spatially. Data were extracted from Molecular Vista Inc User guide.

Chapter 3

Far-field infrared characterization of MXenes: chemical composition and electrochemical interface studies

3.1 The influence of the carbon-to-nitrogen ratio in $Ti_3C_yN_{(2-y)}T_x$ MXene on the infrared properties 63

3.1.1 IR reflectance 69

3.1.2 IR emission 71

3.1.3 Density functional theory calculations 76

3.1.4 Modeling of infrared reflectance: the Drude approach . . . 78

3.2 Infrared in-situ probing of ion intercalations in $Ti_3C_2T_x$ MXene 80

3.2.1 Electrochemical cell setup on FTIR-ATR crystal 81

3.2.2 Results and Discussion 83

3.2.3 Conclusions and future perspectives 86

3.1 The influence of the carbon-to-nitrogen ratio in $Ti_3C_yN_{(2-y)}T_x$ MXene on the infrared properties[1]

Within the plethora of MXenes explored, titanium carbonitrides $Ti_3C_{(2-y)}N_yT_x$ have attracted much attention due to their outstanding and tunable properties. The higher electronegativity of nitrogen compared to carbon results in stronger Ti-N bonds, which modify the material's structural, electronic, and optical properties [149, 150]. Previous studies have demonstrated that nitrogen-containing MXenes exhibit higher electronic conductivity and catalytic activity compared to their pure carbide counterparts, primarily attributed to a higher density of states at the Fermi

[1]An abridged version of this chapter has been published in *Materials Today Physics*, The C/N ratio as a lever for infrared properties tuning in carbonitride MXenes, Materials Today Physics, Volume 58, October 2025, 101860, https://doi.org/10.1016/j.mtphys.2025.101860

level [151]. Despite their promising characteristics, optical studies of titanium carbonitride MXenes remain limited, particularly in the infrared region. Han et al. demonstrated that Ti_3CNT_x has greater thermal emissivity than $Ti_3C_2T_x$ at room temperature, suggesting applications in thermal management for electronic components [152]. This property is valuable for developing heat-dissipative coatings that can effectively extract heat from electronic devices, preventing performance degradation due to thermal issues [109]. Furthermore, Ti_3CNT_x MXene has shown excellent electromagnetic interference (EMI) shielding capabilities despite its moderate electrical conductivity, providing greater shielding effectiveness than the more conductive $Ti_3C_2T_x$ variant and even for metal films of the same thickness [153].

The results from this work have significant implications for the development of advanced IR-responsive materials for electronics and related technologies. Materials with tunable IR reflectance and emissivity are increasingly critical in modern electronic devices where thermal management presents a significant challenge, particularly in miniaturized and high-performance computing systems [26]. The ability to precisely control the IR properties of titanium carbonitride MXenes through carbon-to-nitrogen ratio adjustment offers promising solutions for heat dissipation in integrated circuits, thermal interface materials, and electronic packaging. Furthermore, these materials could find applications in IR sensing components, thermal signature management for security applications, and next-generation optoelectronic devices operating in the infrared spectrum. This work investigates the infrared optical properties of titanium carbonitride MXenes with systematically varied carbon-to-nitrogen ratios across the 1-25 μm wavelength range. We present comprehensive characterization of their structural and optical properties through X-ray diffraction (XRD), Raman spectroscopy, and Fourier-transform infrared spectroscopy (FTIR), along with detailed analysis of their IR reflectance behavior and thermal emissivity at elevated temperatures. The structural evolution and chemical bonding characteristics resulting from varying C/N ratios are systematically correlated with the observed optical and thermal properties. Additionally, theoretical calculations using density functional theory were performed to elucidate the fundamental mechanisms underlying the observed IR property variations and predict behavior under different conditions. The selection of the four specific carbon-to-nitrogen ratios (y=0,0.25,0.5 and 1) in this study was strategically designed to span the complete compositional range from pure carbide to equal carbon-nitrogen content. This systematic variation allows for a comprehensive evaluation of composition-property relationships and identification of potential threshold values where significant property transitions occur. These ratios correspond to the compositions commonly observed in MAX phase precursors used for MXene synthesis, ensuring practical relevance for scalable production.

In the following sections, we present our results, and detailed analysis of how carbon-to-nitrogen ratio variation enables precise control over the IR properties of these versatile 2D materials for advanced electronic applications. Details on fabrication and characterization methods are available in the Appendix.

Results and discussion

MXene samples were prepared using two distinct methods: spray coating and blade coating. Figure 3.1(a) shows a molecular three-dimensional model with the different

carbon-to-nitrogen ratios represented by the faded arrow. Notably, the stoichiometric C/N ratios were verified via X-ray photoelectron spectroscopy in a preliminary study by Zhang et al. [154]. Spray-coated samples (Figure 3.1(b)) entail the deposition of a thin layer of MXene aqueous solutions onto microscopic glass slides (Fisher Scientific) substrate using an airbrush [155]. Prior to deposition, substrates were cleaned with DI water/isopropanol sonication, followed by O_2 plasma treated to increase hydrophilicity. Thicknesses are typically hundreds of nanometers. Blade-coated samples (Figure 3.1(c)) were generated by manually spreading MXene slurry (highly concentrated aqueous dispersion) onto microscopic glass slides using a doctor blade, yielding thicker films (few microns thick).

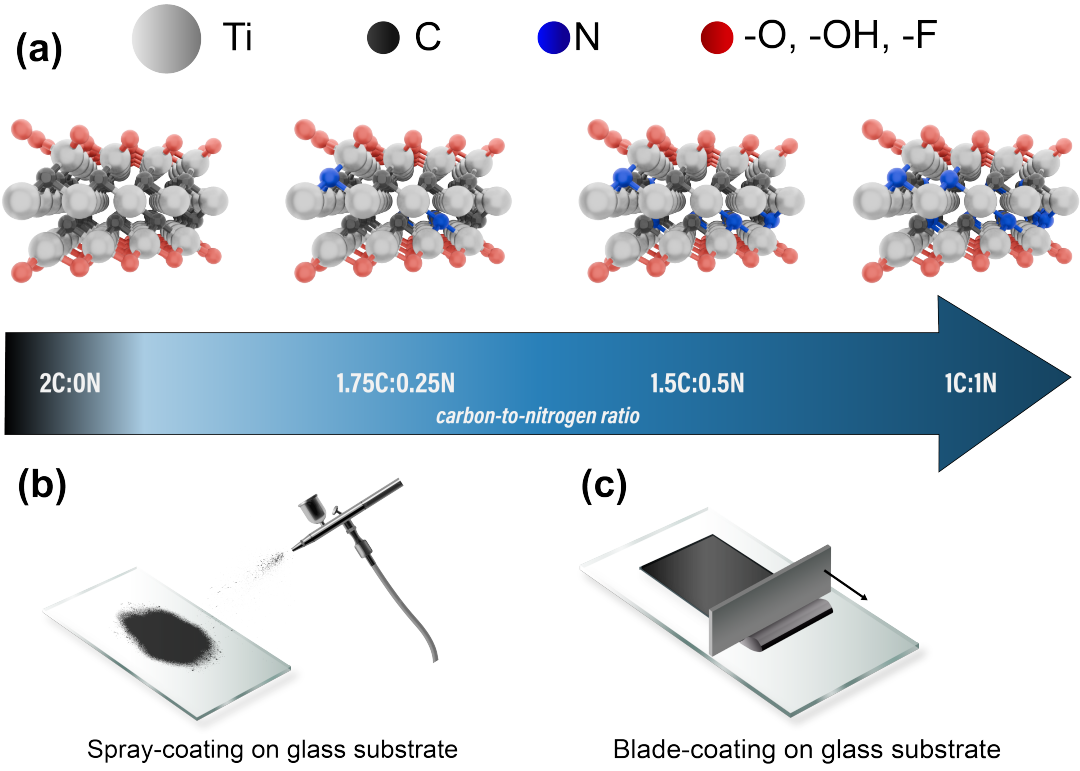

Figure 3.1: (a) Titanium carbonitride 3D models showing the systematic variation of carbon-to-nitrogen ratios from 2C:0N to 1C:1N. (b) Spray-coating technique for MXene deposition onto glass substrates, yielding thin films with thickness ranging from 148 to 450 nm. (c) Blade-coating technique using doctor blade for MXene slurry deposition, producing thicker films ranging from 1.5 to 9.6 μm.

The XRD analysis of $Ti_3C_{(2-y)}N_yT_x$ with varying C/N ratios revealed notable structural modifications in both the MAX phases and their derived MXenes (Figure 2). A characteristic shift at $2\theta = 60.5°$ was observed in the MAX precursors, indicating lattice perturbations due to nitrogen incorporation. With increasing nitrogen content, we observed systematic variations in the crystal structure, particularly evident in the (110) plane reflections. In all $Ti_3C_{(2-y)}N_yT_x$ systems investigated, the MAX structure progressively deformed to accommodate the smaller atomic radius and higher electronegativity [156, 157] of nitrogen compared to carbon.

The c-lattice parameter (Figure 3.2(e)), which represents the out-of-plane length of the unit cell [154, 158], was calculated from X-ray diffraction data using Bragg's law. The c-parameter was determined from the (002) reflection peak position using

the relationship:

$$c = \frac{2\lambda}{2\sin\theta_{002}} \tag{3.1}$$

where λ is the X-ray wavelength (Cu Kα_1 = 1.5406 Å) and θ_{002} is the Bragg angle of the (002) reflection. Our calculations revealed that the c-lattice parameter decreases linearly with increasing nitrogen content, following Vegard's law [159]. The c-parameter ranged from 18.72 Å for Ti_3AlC_2 ($y = 0$) to 18.44 Å for Ti_3AlCN ($y = 1$), with intermediate values of 18.60 Å and 18.55 Å for $Ti_3AlC_{1.75}N_{0.25}$ and $Ti_3AlC_{1.5}N_{0.5}$, respectively. This linear decrease in the c-parameter with nitrogen substitution is consistent with Vegard's law, as the relative change in lattice parameter (1.5%) falls well within the acceptable range for ideal solid solutions. The systematic contraction of the unit cell along the c-axis can be attributed to the smaller covalent radius of nitrogen (0.71 Å) compared to carbon (0.76 Å), leading to a progressive compression of the MAX phase structure as carbon atoms are replaced by nitrogen atoms.

To gain deeper insight into the fundamental mechanisms responsible for these structural modifications, density functional theory (DFT) modeling would be required. Such computational approaches could provide atomistic insights into how varying C/N ratios affect the electronic structure, bonding characteristics, and resultant lattice parameters of both MAX phases and their derived MXenes. To complement our experimental findings, we conducted DFT simulations to model these materials' optical response (dielectric function and reflectance) with varying C/N ratios. These calculations provide theoretical validation of the observed structural trends and their impact on electromagnetic properties. Further details regarding the computational methodology and simulated optical responses are available in subsequent sections of this thesis.

Figure 3.3(a) presents the Fourier Transform Infrared (FTIR) transmission spectra revealing significant insights into the structural modifications induced by nitrogen substitution in the MXene lattice.

The spectra exhibit characteristic absorption bands associated with terminal functional groups (T_x) and metal-carbon/nitrogen bonds. Prominent vibration modes are identified and labeled, including C–O (∼1800 cm^{-1}), O–H (∼1400 cm^{-1}), C–F (∼1100 cm^{-1}), Ti–O (∼600 cm^{-1}), and Ti–F (∼700 cm^{-1}) [113]. Additionally, a C–N vibration band is observed, particularly in nitrogen-containing compositions.

The pristine $Ti_3C_2T_x$ spectrum exhibits the most pronounced absorption features, with particularly strong bands corresponding to C–O and Ti–O vibrations. As nitrogen content increases progressively through the series, several systematic spectral changes are observed such as a general diminution in absorption band intensity, a gradual flattening of the spectral profile, and an alteration in relative intensity and shape of the C–O, O–H, and C–F bands.

The region between 600–700 cm^{-1}, corresponding primarily to Ti–O interactions [113], shows marked differences between compositions, indicating substantial changes in metal–oxide bonding characteristics with increasing nitrogen content. These spectroscopic observations provide valuable insights into how nitrogen substitution influences the MXene basal plane composition, surface chemistry, and functional group distribution, with potential implications for their electrochemical and catalytic properties.

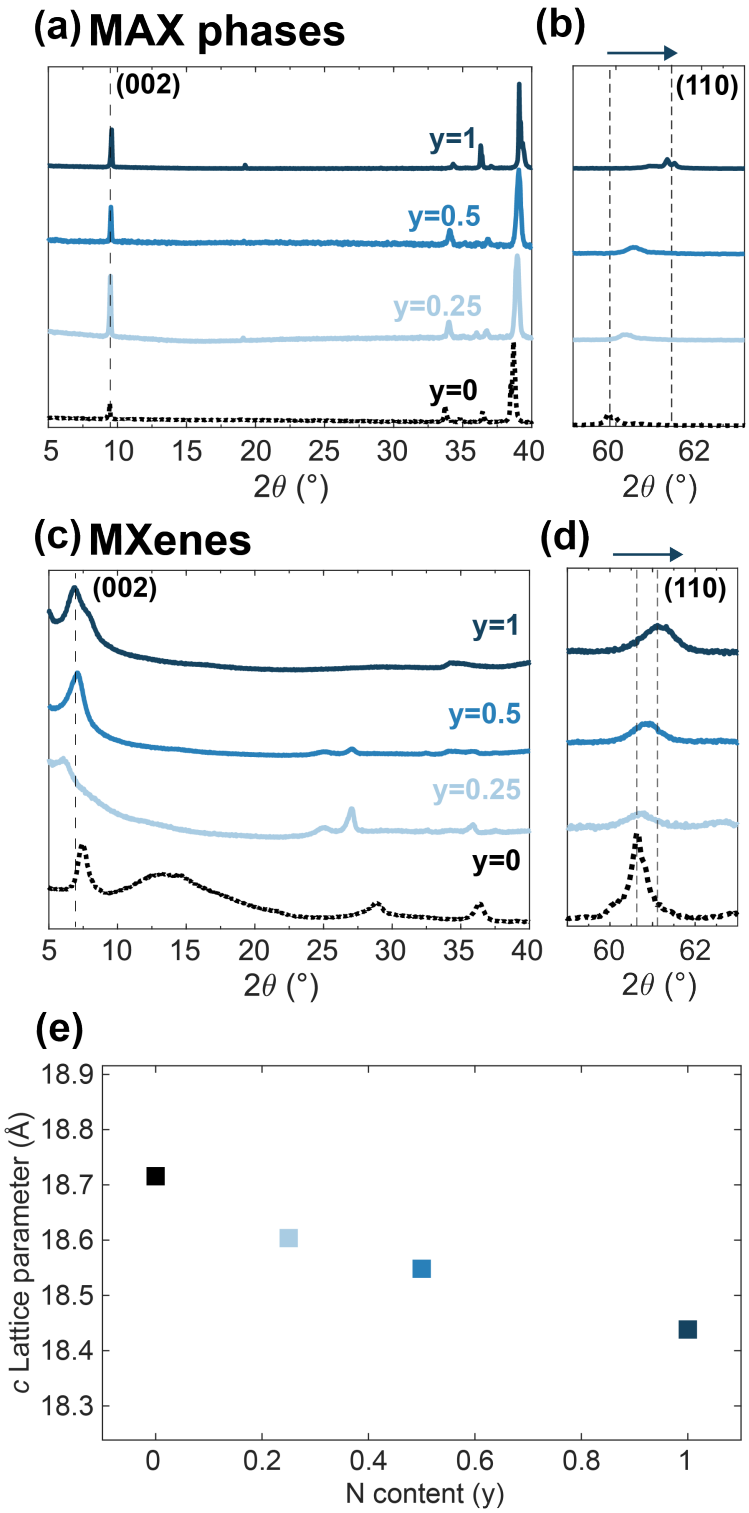

Figure 3.2: : (a) XRD patterns of titanium carbonitride MAX phases with four different ratios measured on freeze-dried powders. (b) Bragg angle shift depending on the C/N ratio. (c) XRD patterns of the corresponding MXenes. (d) Bragg angle shift depending on the C/N ratio. (e) c-Lattice parameters of MAX phases plotted as a function of the N content, calculated from Bragg's law.

Figure 3.3(b) presents the Raman spectra of the four MXene compositions. These spectra provide complementary structural information to the FTIR analysis, offering valuable insights into the vibrational modes of the MXene lattice as nitrogen content increases.

The Raman spectrum of pristine $Ti_3C_2T_x$ displays several characteristic peaks, notably a sharp, well-defined peak at approximately 200 cm^{-1}, which can be attributed to A_{1g} Ti-C symmetric vibration [114]. Additional bands are observed at approximately 380 cm^{-1} corresponding to E_gO vibrations of termination groups and at approximately 620 cm^{-1} corresponding to E_g in-plane carbon vibrations in OH-terminated MXene [100, 114, 160].

As nitrogen content increases across the series, several systematic changes in the Raman signatures become evident: the sharp peak at 200 cm^{-1} becomes progressively broader and less intense, and the overall spectral features become less defined. The broadening and weakening of Raman features with increasing nitrogen content suggests a higher degree of structural disorder within the lattice. This phenomenon can be attributed to the substitution of carbon atoms by nitrogen, which introduces compositional heterogeneity and creates a distribution of bond strengths (Ti–C vs. Ti–N) at the nanoscale. According to the phonon confinement model, such structural disorder leads to a breakdown of Raman selection rules, allowing non-zone-center phonons to participate in scattering and resulting in asymmetric peak broadening [161]. Additionally, the variability in local bonding environments—arising from the random distribution of C and N atoms—causes inhomogeneous broadening, as different regions of the material exhibit slightly different vibrational frequencies that integrate into a broadened ensemble spectrum [161].

These Raman spectroscopic findings corroborate our XRD and FTIR analyses, providing additional evidence that nitrogen incorporation induces systematic structural modifications throughout the MXene lattice, affecting not only long-range order but also local bonding environments and vibrational modes.

To investigate the elemental distribution and compositional homogeneity across different C/N ratios, Energy Dispersive X-ray Spectroscopy (EDS) analysis was performed on MXene spray-coated films showcased on Figure 3.3(c). The EDS spectra, normalized by the Ti Lα peak intensity, show no systematic variation in the nitrogen Kα peak intensity that correlates with the nominal C/N ratios. This lack of correlation can be attributed to the inherent limitations of EDS for quantitative analysis of light elements, particularly nitrogen, which exhibits low X-ray fluorescence yield and overlapping spectral features that compromise detection sensitivity and accuracy. A variation in the oxygen K_α peak is also observed depending on the ratio, stemming from the inherent oxidation of the MXene, which is enhanced by the presence of nitrogen.

Despite the limitations of EDS in detecting compositional variations, the influence of C/N ratio on material properties is clearly evidenced through multiple complementary characterization techniques. Raman spectroscopy reveals systematic peak broadening and intensity changes with increasing nitrogen content, while XRD analysis demonstrates progressive lattice parameter variations following Vegard's law. These consistent structure-property relationships across multiple analytical techniques confirm successful compositional control during synthesis, despite the challenges in direct elemental quantification of light elements through EDS.

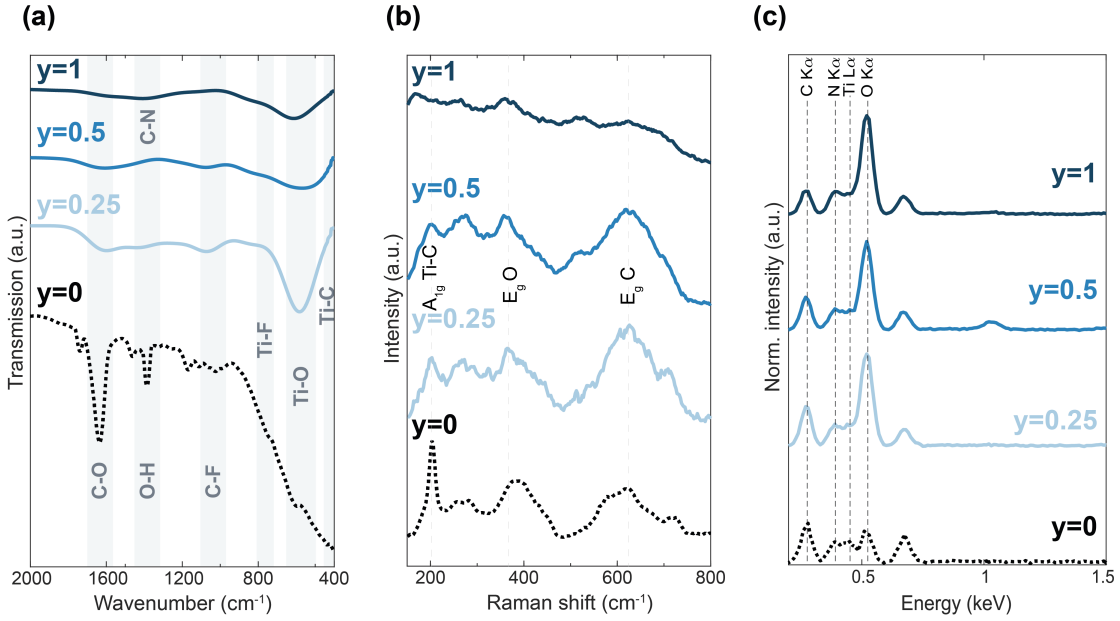

Figure 3.3: Vibrational spectroscopy and elemental analysis of $Ti_3C_{(2-y)}N_yT_x$ MXenes with varying nitrogen content measured on re-stacked flakes on alumina substrate. (a) FTIR transmission spectra revealing absorption bands characteristic of terminal functional groups (T_x) and metal-carbon/nitrogen bonds. (b) Raman spectra showing a progressive broadening and intensity reduction as nitrogen content increases. (c) EDS spectra normalized by Ti Lα peak intensity, demonstrating the limitations of EDS for quantitative analysis of light elements despite successful compositional control evidenced by structural and optical property variations.

3.1.1 IR reflectance

IR reflectance measurements were conducted on the four MXene samples, covering different C/N ratios, prepared as thin films (Figure 3.4). Fresnel reflectance, defined as the proportion of electromagnetic radiation reflected at the interface between the sample and the ambient air [162–164], was determined for MXene samples at a near-normal angle of incidence. The reflectance is governed by the complex refractive index:

$$\hat{n}(\omega) = n(\omega) + ik(\omega) \tag{3.2}$$

where $n(\omega)$ is the refractive index and $k(\omega)$ is the extinction coefficient (absorption index), both correlated through the Kramers-Kronig transformation. From the Fresnel equations, the degree of reflection at normal incidence can be determined using the following equation [165]:

$$R(\omega) = \frac{(n_2(\omega) - n_1(\omega))^2 + k_2^2(\omega)}{(n_2(\omega) + n_1(\omega))^2 + k_2^2(\omega)} \tag{3.3}$$

where n_1 represents the refractive index of the first non-absorbing medium (air) and n_2 and k_2 represent the sample's refractive index and extinction coefficient, respectively.

The polarization of electromagnetic radiation plays a crucial role in reflection measurements, particularly at non-normal angles of incidence. The dependence

of the reflection coefficient on the angle of incidence is especially significant for p-polarized electromagnetic waves [165]. To minimize polarization effects, the incident beam is collimated at a ten-degree angle, which minimize distortion (Figure 3.4(c)).

We measured reflectance spectra of MXene coatings from 1 to 25 μm at room temperature using an FTIR spectrometer. To maximize collection efficiency, parabolic mirrors were employed to capture both specular and a portion of the diffuse reflection components. Our measurements revealed that the overall reflectance increased systematically with increasing carbon content in the MXene structure. To quantitatively compare the reflectance performance of each C/N ratio, we calculated the integrated reflectance over the entire spectral range using the trapezoidal rule:

$$\bar{R} = \int_{\lambda_1}^{\lambda_2} R(\lambda)\, d\lambda \approx \sum_{i=1}^{n-1} \frac{R(\lambda_i) + R(\lambda_{i+1})}{2} \cdot (\lambda_{i+1} - \lambda_i) \tag{3.4}$$

The $Ti_3C_2T_x$ ($y = 0$) exhibited the highest integrated reflectance ($\bar{R} = 23.45$) corresponding to 93.8% of the theoretical maximum, compared to 15.85 (63.4%) for the Ti_3CNT_x ($y = 1$). The intermediate compositions ($Ti_3C_{1.75}N_{0.25}T_x$ and $Ti_3C_{1.5}N_{0.5}T_x$) show $\bar{R}$ values between these extremes (Figure 3.4(a-b)), with $y = 0$ and $y = 0.25$ yielding similar profiles. Across all compositions, the reflectance exhibited a significant decrease below 4 μm. These results demonstrate that MXenes exhibit excellent reflectance properties that can be systematically tuned through compositional modifications and preparation methods.

To better understand the relationship between composition and infrared properties, electrical conductivity measurements were performed using a four-point probe method. The results reveal a dramatic decrease in electrical conductivity with increasing nitrogen content (Table 3.1). $Ti_3C_2T_x$ ($y = 0$) exhibits the highest conductivity of 5533.7 S/cm, which drops significantly to 0.99 S/cm for Ti_3CNT_x ($y = 1$). This trend directly correlates with the observed infrared reflectance behavior, where higher electrical conductivity corresponds to enhanced metallic character and superior IR reflectance performance. The substantial conductivity reduction upon nitrogen incorporation can be attributed to increased electron scattering due to compositional disorder and the formation of more localized Ti-N bonds compared to the more delocalized Ti-C bonding network [151, 166].

Table 3.1: Electrical conductivity of $Ti_3C_{(2-y)}N_yT_x$ MXenes as a function of nitrogen content

Nitrogen content (y)	Conductivity (S/cm)
0	5533.7
0.25	50.9
0.5	49.0
1	0.99

In the near-infrared (NIR) region, the observed low reflectance can be attributed to energy absorption by free electrons, characteristic behavior of metallic materials [167]. The absorbance A, defined as:

$$A = 1 - R - T \tag{3.5}$$

represents the energy absorbed by the material (R: reflection and T: transmission), which induces molecular vibrations in the mid-infrared (MIR) range [162]. The intrinsic properties of carbon and nitrogen atoms significantly influence this behavior. The incorporation of nitrogen modifies the vibrational properties of the crystal lattice through several mechanisms. Ti-N bonding introduces higher atomic mass (m_N = 14.007 u vs m_C = 12.011 u) and greater electronegativity [157, 168], leading to stronger electron-phonon coupling, new phonon modes, and increased adsorption. Furthermore, the higher electronegativity of nitrogen (3.04) compared to carbon (2.55) induces greater charge transfer and modifies the electronic density of states near the Fermi level, altering the material's optical response. These combined vibrational and electronic effects result in enhanced absorbance and reduced reflectance with increasing nitrogen content. Notably, the IR shielding performance favors carbon rich compositions, where $Ti_3C_2T_x$ shows superior reflectance. This trend is consistent across different preparation methods, though we observed that the reflectance values for blade-coated (Figure 3.4(b)) MXene samples were lower than those for spray-coated samples (Figure 3.4(a)). For example, the integrated reflectance of $Ti_3C_{1.5}N_{0.5}T_x$ is 17.67 (70.7%) for blade-coated samples compared to 19.06 (76.2%) for spray-coated.

Film thickness and surface roughness significantly influence the optical behavior of MXene coatings. Greater thickness increases the probability of internal scattering within the material, potentially reducing the intensity of reflected light [169, 170]. Surface roughness, characterized by height variations at the interface, can cause diffuse scattering in multiple directions, thereby reducing specular reflection. Our analysis revealed that blade-coated samples (Figure 3.4(b)) exhibit higher roughness ($\sim$ 300 nm) and greater thickness compared to spray-coated films (Figure 3.4(a)) ($\sim$ 100 nm roughness), which led to increased internal scattering and diffuse reflection at the rougher interface.

3.1.2 IR emission

All materials above absolute 0 K emit thermal radiation [171], a process whose efficiency is characterized by emissivity — a dimensionless property ranging from 0 (perfect reflector) to 1 (perfect blackbody emitter) [172]. To investigate this property in our MXene samples, we measured the spectral emissivity from 5 to 25 μm for four spray-coated MXenes at 200°C (Figure 3.5(a)) and specifically tracked the temperature-dependent behavior of spray-coated $Ti_3C_{1.75}N_{0.25}T_x$ across temperatures ranging from 100 to 300°C (Figure 3.5(b)). These measurements were performed using a Bruker Invenio R temperature chamber, with IR emissions collected via a parabolic mirror and collimated onto the detector.

Figure 3.5(a) reveals that the overall emissivity increases systematically with increasing nitrogen content. The results demonstrate a direct relationship between nitrogen content and emissivity, with values systematically increasing as nitrogen content rises. The pure carbide composition ($y = 0$) exhibits the lowest emissivity (0.05), while the highest nitrogen content ($y = 1$) shows the highest emissivity (0.65). Notably, the $y = 1$ sample's spectrum features a distinctive peak in the 7.9-9.9 μm range, which can be attributed to partial oxidation when exposed to air at elevated

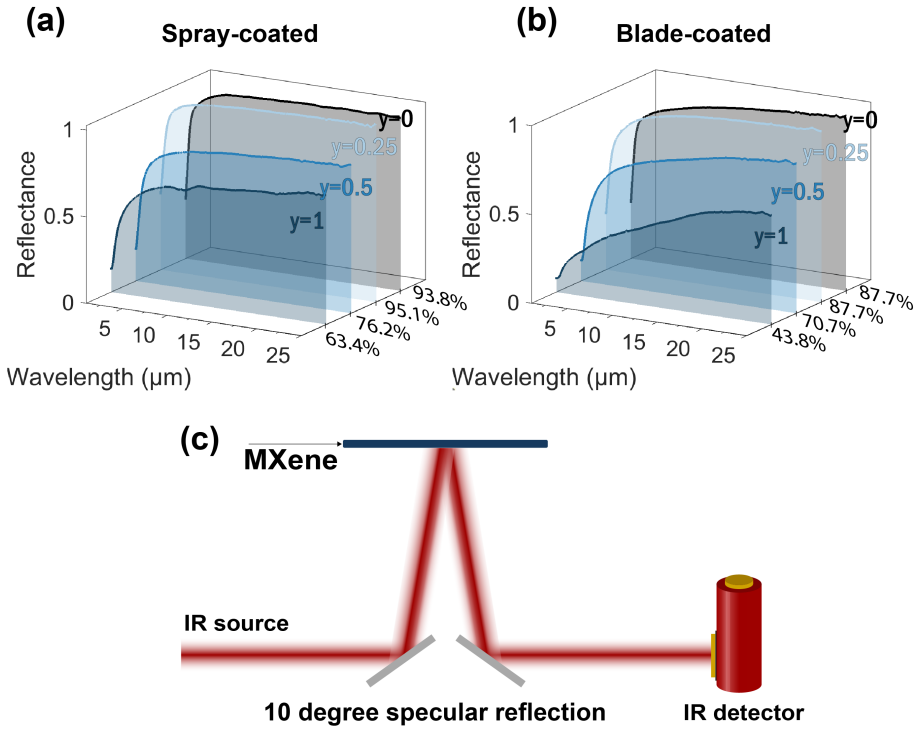

Figure 3.4: Infrared reflectance properties of $Ti_3C_{(2-y)}N_yT_x$ MXenes. (a) 3D reflectance spectra of spray-coated samples showing systematic increase in reflectance with increasing carbon content. (b) Reflectance spectra of blade-coated samples displaying similar trends but with overall lower reflectance values due to increased thickness and surface roughness. (c) Schematic diagram of the FTIR reflectance measurement setup using 10-degree specular reflection geometry.

temperatures, as previously reported. This observation indicates varying degrees of thermal stability across compositions, with nitrogen-rich MXenes demonstrating lower oxidation resistance and generally decreasing phase stability with increasing nitrogen content due to lower cohesive energy (defined as the energy required to break all bonds in the crystal structure)[173–175].

This trend inversely correlates with the reflectance behavior observed at room temperature, consistent with Kirchhoff's law of thermal radiation, which states that for an opaque material [171]:

$$\varepsilon(\lambda) = 1 - R(\lambda) \tag{3.6}$$

These emissivity measurements demonstrate that selective infrared emission characteristics can be achieved by controlling the carbon-to-nitrogen ratio in titanium carbonitride MXenes.

The $Ti_3C_{1.75}N_{0.25}T_x$ exhibited a nearly linear increase in emissivity with temperature, as illustrated in Figure 3.5(b-c). To account for potential systematic effects in absolute emissivity calibration, we analyzed the temperature dependence using relative changes with respect to the reference temperature (100°C):

$$\frac{\Delta\varepsilon(T)}{\varepsilon(T_0)} = \beta_{rel}(T - T_0) \tag{3.7}$$

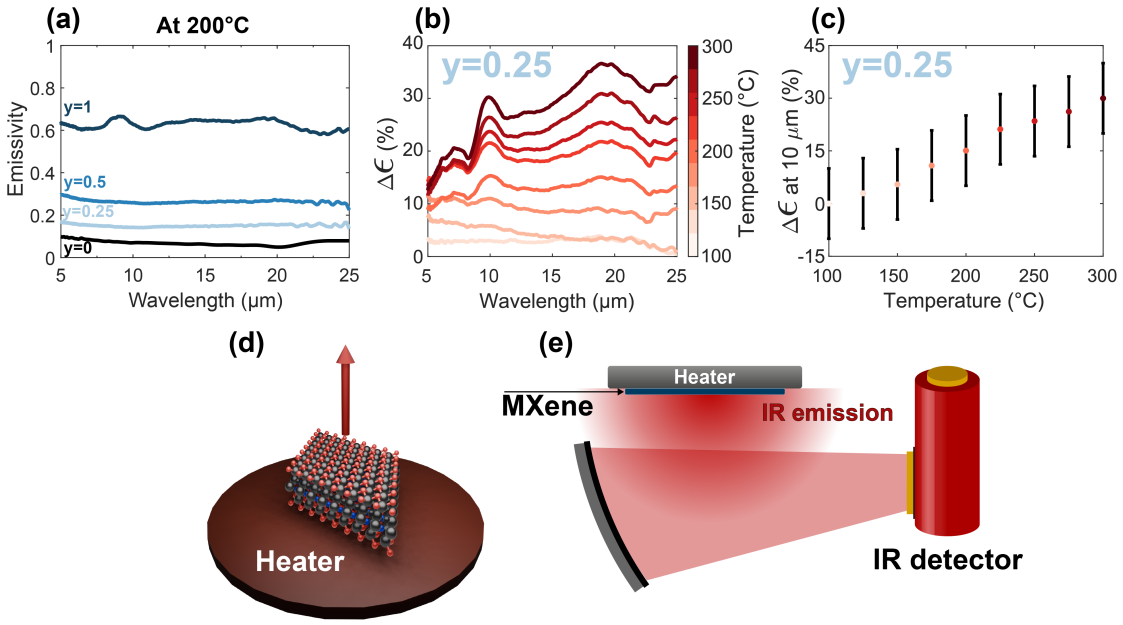

Figure 3.5: Thermal emissivity assessment of $Ti_3C_{(2-y)}N_yT_x$ MXenes. (a) Emissivity at 200°C for spray-coated $Ti_3C_{(2-y)}N_yT_x$ films showing $Ti_3C_2T_x$ (y = 0) with lowest emissivity (0.05) and Ti_3CNT_x (y = 1) with highest (0.65). (b) Temperature-dependent emissivity spectra of $Ti_3C_{1.75}N_{0.25}T_x$ from 100 to 300°C demonstrating systematic increase with temperature. (c) relationship between emissivity and temperature at 10 μm wavelength with error bars showing measurement uncertainty. (d) Schematic representation of heated MXene film for thermal emission analysis. (e) FTIR thermal emission measurement setup with heated sample chamber and parabolic mirror collection system.

where β_{rel} is the relative temperature coefficient of emissivity and $T_0 = 100$°C. Linear regression of experimental data at 10 μm wavelength over the 100–300°C range yields $\beta_{rel} = (1.57 \pm 0.03) \times 10^{-3}$ K^{-1} with an excellent correlation coefficient $R^2 = 0.990$. This corresponds to a 1.57‰ increase per Kelvin, resulting in a total 31.5% enhancement over the 200°C measurement range. For comparison, polished stainless steel exhibits a relative temperature coefficient of approximately $\beta_{rel} \approx 6.3 \times 10^{-3}$ K^{-1} over the same temperature range [176], approximately four times larger than our MXene.

This substantial temperature sensitivity can be attributed to three primary mechanisms operating in carbonitride MXenes:

Enhanced electron-phonon coupling: The mixed Ti–C/Ti–N bonding network in $Ti_3C_{1.75}N_{0.25}T_x$ creates additional scattering channels as temperature increases. Unlike pure carbide MXenes, the presence of nitrogen introduces stronger ionic character [166, 177], enhancing the temperature dependence of electrical conductivity and, consequently, infrared emissivity through the Hagen–Rubens relation, which correlates emissivity with electrical resistivity for metallic conductors at long wavelengths.

Progressive phonon activation: Higher temperatures activate vibrational modes associated with both the carbide/nitride lattice and surface terminations (–O, –OH, –F). The carbonitride composition provides a richer phonon spectrum compared to pure $Ti_3C_2T_x$, contributing to enhanced infrared absorption with in-

creasing temperature.

Electronic structure modulation: Temperature-induced changes in carrier concentration and mobility alter the optical response. The moderate nitrogen content (y = 0.25) creates an optimal balance between metallic conductivity and phonon-mediated absorption, maximizing temperature sensitivity.

As temperature increases, several concurrent mechanisms contribute to enhanced emissivity: increased phonon population and electron-phonon scattering reduce electrical conductivity; thermal expansion modifies interatomic spacing and band structure; and surface terminations (–O, –OH, –F) may undergo subtle chemical or structural changes. These combined effects collectively alter the material's electronic properties and optical response in the infrared region. For $Ti_3C_{1.75}N_{0.25}T_x$, the moderate nitrogen content creates a balance between metallic (from Ti–C) and ionic character (from Ti–N) [166, 178]. This compositional balance results in an optimal sensitivity to temperature changes, manifested as the near-linear emissivity increase observed in Figure 3.5(c). The excellent linearity ($R^2 = 0.990$) and temperature coefficient ($\beta_{rel} = 1.57 \times 10^{-3}$ K^{-1}) demonstrate that carbonitride MXenes exhibit predictable and substantial thermal responsiveness. The compositional tunability demonstrated across the C/N series further enables optimization of thermal sensitivity for specific operating temperature ranges. This fundamental understanding guides the rational design of MXenes for tailored thermal radiation properties in sensing, energy and optoelectronic applications [179, 180].

To address potential structural changes during thermal measurements, we conducted comparative reflectance analysis before and after high-temperature emissivity measurements (300°C in air). Figure 3.8 shows the reflectance spectra of all four compositions before (pristine MXene, solid lines) and after thermal treatment (dashed lines). The results reveal systematic changes that provide insights into the thermal stability and oxidation behavior of titanium carbonitride MXenes.

All compositions exhibit a systematic decrease in reflectance after thermal treatment, with the magnitude of reduction increasing with nitrogen content. $Ti_3C_2T_x$ shows the smallest change, maintaining relatively stable reflectance values, while nitrogen-rich compositions (y = 0.5 and y = 1) demonstrate more pronounced degradation. This trend suggests that Ti-N bonds are less thermally stable than Ti-C bonds under oxidative conditions, consistent with the lower formation energy of nitride phases compared to carbides.

The appearance of distinct absorption features (peaks and valleys) in the post-treatment spectra, particularly evident in the 5-15 μm range, can be attributed to partial oxidation of the MXene surface and bulk. The formation of titanium oxides [181, 182] introduces new vibrational modes and electronic transitions, creating characteristic absorption bands that manifest as reduced reflectance in specific wavelength regions. Additionally, the systematic reflectance reduction across the entire spectral range indicates a transition from metallic to more semiconducting behavior, resulting from decreased free carrier density due to oxidation-induced structural modifications.

These findings are corroborated by empirical visual observations over time. We observed that samples with higher nitrogen content progressively develop a whitish appearance, both after post-emissivity measurements and under ambient conditions after approximately one week of exposure (Figure 3.6). This visual degradation

becomes more pronounced with increasing nitrogen content and is also observed when MXenes are stored in aqueous solutions, further confirming that nitrogen-rich compositions exhibit inherently lower stability due to enhanced oxidation susceptibility.

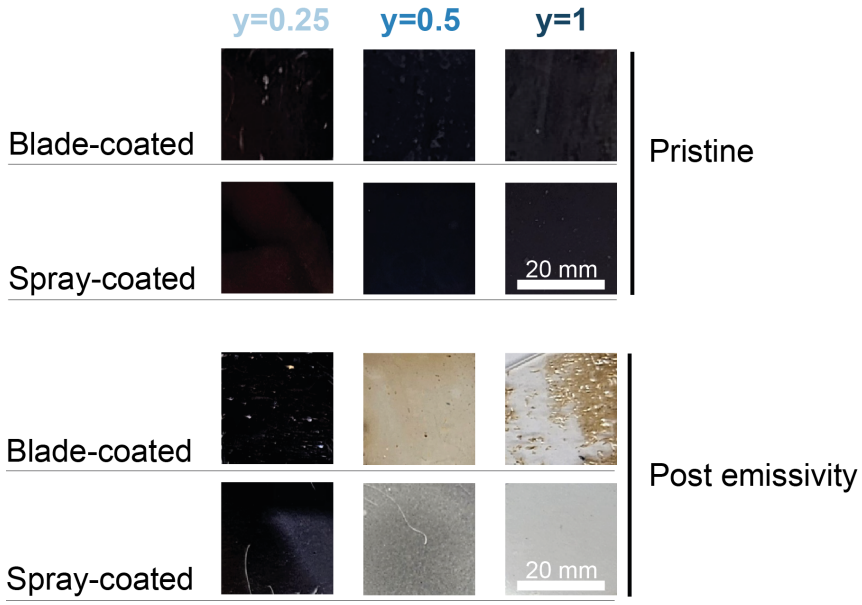

Figure 3.6: Optical images of blade/spray-coated $Ti_3C_{(2-y)}N_yT_x$ MXenes before (pristine) and after emissivity measurements (post emissivity) across different C/N ratios (y = 0.25, 0.5, 1).

The compositional dependence of thermal radiation properties is further illustrated through infrared thermal imaging of MXene films on a heated substrate (100°C), which visually demonstrates the differential IR emission behavior across C/N ratios (Figure 3.7). The thermal images show distinct temperature signatures for each composition, confirming the systematic variation in IR properties observed in our spectroscopic measurements.

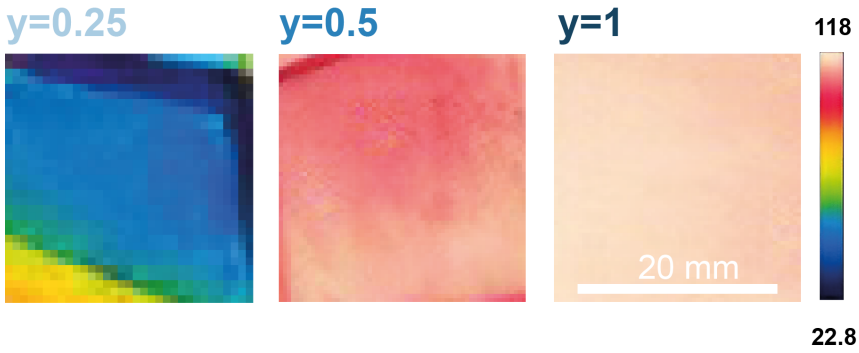

Figure 3.7: IR thermal imaging of spray-coated $Ti_3C_{(2-y)}N_yT_x$ MXenes on a 100°C hot plate demonstrating composition-dependent thermal radiation and IR shielding performance across different C/N ratios (y = 0.25, 0.5, 1).

These findings demonstrate that while titanium carbonitride MXenes exhibit excellent IR properties at moderate temperatures, their long-term thermal stability decreases with increasing nitrogen content. The observed changes validate our

temperature-dependent emissivity measurements and confirm that the C/N ratio not only controls initial IR properties but also influences thermal stability under oxidative conditions.

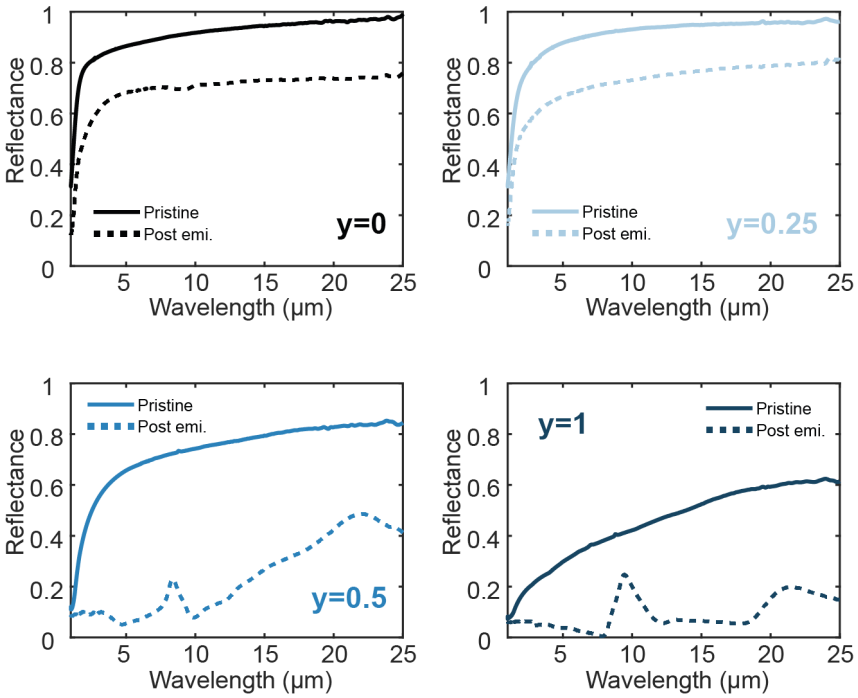

Figure 3.8: Reflectance spectra comparison before (pristine MXene, solid lines) and after post-emissivity measurements (dashed lines) for $Ti_3C_{(2-y)}N_yT_x$ MXenes. Post-emissivity measurements were conducted following thermal ramping up to 300°C in air during emissivity characterization. The systematic decrease in reflectance and appearance of new absorption features indicate oxidation-induced structural modifications occurring during high-temperature exposure.

3.1.3 Density functional theory calculations[2]

The effects of carbon-to-nitrogen ratio on the optical properties of $Ti_3C_{(2-y)}N_yT_x$ MXenes were investigated theoretically using density functional theory (DFT). This *ab initio* computational approach enabled us to calculate both the real (ε_1) and imaginary (ε_2) components of the dielectric function as a function of photon energy across the electromagnetic spectrum corresponding to wavelengths from the ultraviolet to approximately 7 μm in the mid-infrared region.

The calculations were performed using the Vienna *Ab initio* Simulation Package (VASP) with the generalized gradient approximation (GGA) parameterized by Perdew-Burke-Ernzerhof (PBE) for the exchange-correlation functional. A plane-wave basis set with a cutoff energy of 520 eV was employed, and Brillouin zone integration was performed using a Γ-centered k-point grid of $12 \times 12 \times 1$ for structural optimizations and a denser $24 \times 24 \times 1$ mesh for electronic and optical property calculations. All structures were fully relaxed until the forces on each atom were less than 0.01 eV/Å.

[2]DFT calculations have been performed by B. Moses Abraham, Drexel University.

The computed reflectance spectra at normal incidence for different C:N ratios are presented as a function of wavelength in Figure 6(d). The reflectance values were calculated using the following equation:

$$R = \left(\frac{n_{\text{air}} \cos(\theta) - \sqrt{n_s^2 - \sin^2(\theta)}}{n_{\text{air}} \cos(\theta) + \sqrt{n_s^2 - \sin^2(\theta)}} \right)^2 \tag{3.8}$$

with

$$n = \frac{1}{\sqrt{2}} \sqrt{\sqrt{\epsilon_1^2 + \epsilon_2^2} + \epsilon_1}$$

$$k = \frac{1}{\sqrt{2}} \sqrt{\sqrt{\epsilon_1^2 + \epsilon_2^2} - \epsilon_1}$$

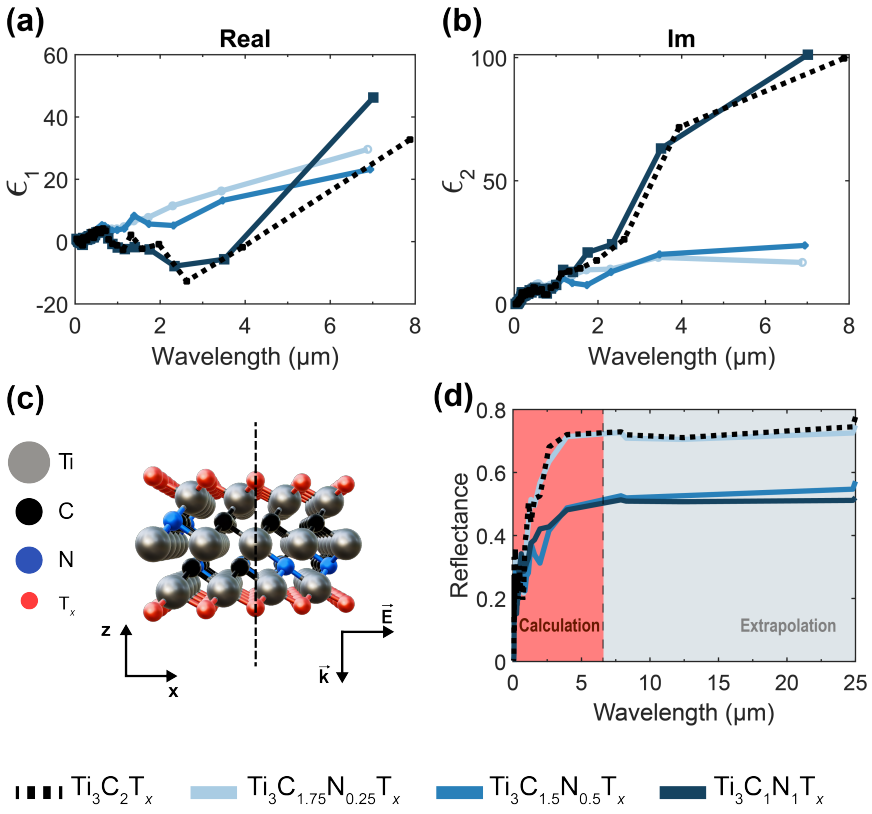

Figure 3.9: Real (a) and imaginary (b) part of the calculated dielectric function. (c) 2D layer structure schematic of $Ti_3C_{(2-y)}N_yT_x$, showing the direction of wave vector k along the z direction and the electric component of light oriented in the x-y plane. (d) Calculated reflectance spectra of $Ti_3C_{(2-y)}N_yT_x$. The dashed line separates the calculated and extrapolated data.

To further understand the impact of nitrogen substitution on the optical behavior of $Ti_3C_{(2-y)}N_yT_x$ MXenes, we performed DFT calculations to evaluate their dielectric and reflectance properties. The computed real (ε_1) and imaginary (ε_2) parts of the dielectric function are presented in Figures 6(a) and 6(b). In the mid-infrared region (2–4 μm), $Ti_3C_2T_x$ exhibits strongly negative ε_1 values, reflecting its metallic character and significant free carrier concentration. As the nitrogen content increases, ε_1 shifts toward positive values in the longer wavelength region,

indicating a transition to dielectric behavior. On the other hand, ε_2 exhibits a non-linear trend with increasing nitrogen substitution, suggesting that the dielectric response is governed by the nature of chemical bonding. These variations arise from structural changes introduced by nitrogen, where the formation of shorter and more ionic Ti–N bonds promotes electron localization and modifies the carrier distribution near the Fermi level, thereby influencing the overall dielectric behavior. This composition-dependent modulation in dielectric response directly influences the reflectance spectra. Figure 3.9(d) shows that $Ti_3C_2T_x$ has the highest IR reflectance due to its metallic behavior, while Ti_3CNT_x has the lowest reflectance, which is consistent with the experimental results. The decline in reflectance with increasing nitrogen content is attributed to the reduction in free-electron density, which weakens the Drude response. Overall, the variations in carbon-to-nitrogen ratio enable tunable infrared optical properties in MXenes, allowing for the design of materials with tailored reflectance and emissivity suitable for thermal management, infrared shielding and photonics applications.

3.1.4 Modeling of infrared reflectance: the Drude approach

To further correlate the macroscopic optical response of the $Ti_3C_{(2-y)}N_yT_x$ series with their fundamental electronic transport properties, the experimental infrared reflectance spectra were modeled using a classical Drude framework [183]. This approach provides a direct estimation of parameters such as free carrier density and electronic scattering rates, bridging the gap between chemical composition and optical behavior.

The complex dielectric function $\varepsilon(\omega)$ is expressed as:

$$\varepsilon(\omega) = \varepsilon_\infty - \frac{\omega_p^2}{\omega^2 + i\omega\gamma} \tag{3.9}$$

Where ε_∞ is the high-frequency background dielectric constant, ω_p is the plasma frequency (directly related to the free electron density), and γ represents the carrier collision rate or damping factor, which is inversely proportional to the relaxation time.

The parameters obtained from the best fit of the experimental reflectance data for the different stoichiometries are summarized in Table 3.2.

Table 3.2: Fitted Drude model parameters for $Ti_3C_{(2-y)}N_yT_x$ samples with varying Nitrogen concentrations.

Parameters	**0N**	**0.25N**	**0.5N**	**1N**
ε_∞	1.00	1.00	8.28	1.95
ω_p (rad/s)	1.59×10^{15}	1.66×10^{15}	5.00×10^{15}	2.46×10^{15}
γ (rad/s)	5.00×10^{13}	5.00×10^{13}	8.00×10^{14}	8.00×10^{14}

As illustrated by the experimental data, all investigated MXene stoichiometries exhibit a distinct metallic behavior characterized by high reflectance in the mid-infrared range. However, the incorporation of nitrogen significantly modulates this response:

- **Transition of Metallic Character:** A clear trend is observed where increasing the nitrogen content leads to a decrease in the overall metallic character.

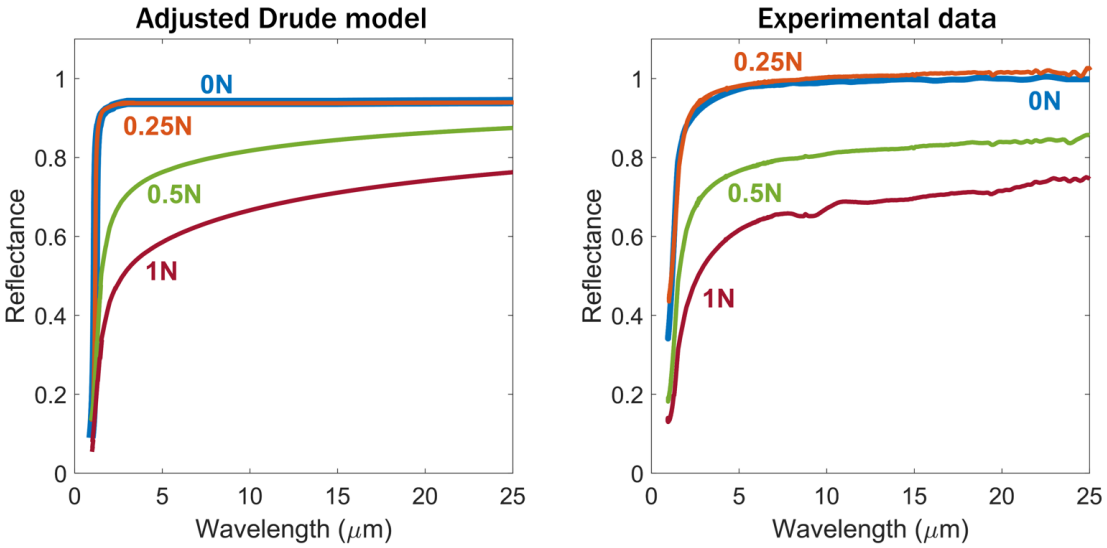

Figure 3.10: Comparison between (left) simulated and (right) experimental infrared reflectance spectra of $Ti_3C_{(2-y)}N_yT_x$ spray-coated films. The simulations were performed using an adjusted Drude model to correlate the macroscopic optical response with electronic transport parameters. The different curves highlight the modulation of the metallic character as a function of the nitrogen concentration.

This is reflected in the experimental reflectance curves by a lower "plateau" and a change in the plasma edge slope as N concentration rises.

- **Collision Rate and Resistivity:** A critical observation is the order-of-magnitude increase in the collision rate γ, jumping from 5.00×10^{13} rad/s (for 0N and 0.25N) to 8.00×10^{14} rad/s for higher nitrogen concentrations. This evolution points toward higher intrinsic resistivity, likely driven by increased electronic disorder and electronegativity differences introduced by nitrogen substitution within the carbide lattice.

- **Carrier Density:** While ω_p shows variations across the series, the overall reduction in reflectance at high N content is dominated by the increased damping (γ).

While the Drude model successfully captures the primary metallic response and follows the general experimental trends, it does not account for localized phenomena such as interband transitions and specific phonon modes. This is particularly evident in the deviations observed at shorter wavelengths and the anomalous increase of ε_∞ for the 0.5N sample (8.28), which suggests additional contributions to the dielectric response not captured by free-carrier models.

These localized discrepancies and the macroscopic nature of these measurements justify the need for high-resolution techniques. Consequently, the following chapters will employ near-field nanoscopy (PiFM) to investigate these chemical heterogeneities and localized optical properties at the nanometer scale, which remain unresolved by conventional far-field spectroscopy.

Conclusion

This study demonstrates the successful tuning of infrared (IR) properties in titanium carbonitride MXenes $Ti_3C_{(2-y)}N_yT_x$ through precise control of their carbon-to-nitrogen ratio. By synthesizing MXenes with varying C/N ratios and conducting a comprehensive suite of experimental and theoretical analyses, we reveal a strong correlation between composition and IR performance. Our structural characterization through X-ray diffraction (XRD) confirms systematic variations in lattice parameters with increasing nitrogen content, particularly evident in the (110) plane reflections, while preserving the fundamental MXene structure. Complementary Raman spectroscopy demonstrates progressive peak shifts and intensity changes across the series, providing direct evidence of modified vibrational modes and bonding characteristics with varying C/N ratios. Furthermore, FTIR analysis reveals distinctive absorption bands associated with surface termination groups and metal–carbon/nitrogen bonds, offering valuable insights into surface chemistry evolution across compositions. Specifically, higher carbon content enhances IR reflectance, making these compositions promising candidates for IR shielding and reflective coatings, with $Ti_3C_2T_x$ exhibiting an exceptionally low emissivity of 0.06. In contrast, increasing the nitrogen content leads to higher emissivity and distinct modifications in phonon-related absorption features, with Ti_3CNT_x reaching an emissivity of 0.65, which can be exploited in thermal management and IR sensing applications. The temperature-dependent emissivity behavior, particularly the near-linear increase observed in compositions with moderate nitrogen content, aligns well with our extended Hagen–Rubens model that accounts for electron–phonon interactions and changes in electrical conductivity. These results establish a clear strategy for engineering the IR response of titanium carbonitride MXenes, highlighting their potential as tunable, multifunctional materials for next-generation optoelectronic and optical technologies.

While this section has focused primarily on the impact of the C/N ratio on the infrared properties of titanium carbonitride MXenes, infrared spectroscopy offers far broader capabilities for MXene characterization beyond static compositional analysis. The vibrational signatures revealed by FTIR can also serve as sensitive probes for monitoring dynamic electrochemical processes, particularly ion intercalation mechanisms in energy storage applications. In the next section, we aim to demonstrate how attenuated total reflection FTIR (ATR-FTIR) can be employed as an operando technique to investigate the real-time electrochemical behavior of $Ti_3C_2T_x$ MXene electrodes.

3.2 Infrared in-situ probing of ion intercalations in $Ti_3C_2T_x$ MXene

Introduction

MXenes have emerged as promising candidates for energy storage applications due to their unique two-dimensional layered structure, high electrical conductivity, and tunable surface chemistry[184, 185]. Among these materials, $Ti_3C_2T_x$ has demonstrated outstanding performance as an electrode material for supercapacitors and batteries because of the wide interlayer spacing can accommodate different ions

[186, 187].

For optimizing MXene-based energy storage devices, it is important to understand the capacitive, electrochemical behavior during charge and discharge cycles [188]. During operation, multiple phenomena occur simultaneously, including ion intercalation/deintercalation, structural changes, and electrolyte interactions. Currently, various ex-situ characterization techniques including X-ray diffraction, scanning electron microscopy, and X-ray photoelectron spectroscopy allow insight into post-mortem analysis of electrode materials [189]. However, these techniques cannot capture the dynamic processes occurring during real-time operation.

The number of in-situ characterization techniques is limited for understanding the basic mechanisms of ion transport and storage in MXene electrodes [190, 191], although X-ray tomography has emerged as a powerful tool for probing structural evolution and ionic dynamics in electrochemical systems [192]. However, such techniques can induce beam damage to sensitive materials and require access to large-scale facilities such as synchrotrons, limiting their widespread application. Real-time monitoring of electrochemical processes is required to close the gap between static structural analysis and dynamic electrochemical performance. Several in-situ characterization methods, including X-ray diffraction (XRD) and X-ray absorption spectroscopy (XAS), although applied to battery material, are limited to MXene electrodes. Although operando XRD has proven valuable for monitoring phase transformations and structural changes during electrochemical cycling and in-situ XAS provides element-specific insights into oxidation state changes [193], these techniques offer limited information about the real-time dynamics of ion intercalation mechanisms in MXene interlayers. A recent study has demonstrated that FTIR spectroscopy can effectively probe the intercalation of water molecules between MXene layers. The diffusion of Li^+ ions was examined under various humidity levels, and XRD results revealed that the interlayer spacing increases due to the insertion of Li^+ cations solvated by multiple water molecules (as shown in Figure 3.11(c)) [194].

This work proposes to apply infrared spectroscopy as an in-situ probe to investigate the electrochemical behavior of $Ti_3C_2T_x$ MXene electrodes. We employ attenuated total reflection Fourier-transform infrared spectroscopy (ATR-FTIR) to monitor Li^+ intercalation processes in real-time [195]. Based on the principle that Li^+ intercalation is accompanied by the displacement of water molecules from the MXene interlayer space [94, 196]. Following the evolution of water-related vibrational bands as a function of applied potential reveals direct information about the intercalation mechanisms and electrochemical processes underlying MXene-based energy storage systems. The experimental setup, consisting of a designed two-electrode electrochemical cell integrated with a diamond ATR crystal allows real-time monitoring of vibrational modes during galvanostatic charge-discharge cycling. In this way, lithium intercalation, water molecule reorganization, and structural changes in the MXene interlayer space are described.

3.2.1 Electrochemical cell setup on FTIR-ATR crystal

Figure 3.11(a) illustrates the custom-designed electrochemical cell employed for in situ ATR-FTIR measurements. The cell is designed for in situ measurements with a $Ti_3C_2T_x$ MXene working electrode with a thickness of 15 μm deposited directly onto a diamond ATR crystal substrate, paired with a graphite counter electrode

in a two-electrode configuration. The electrodes are in contact by a cellguard soaked by a 1 M LiCl aqueous electrolyte, chosen for its high ionic conductivity and compatibility with the MXene surface chemistry. While simplifying the cell design with the two-electrode configuration, applied potentials must be read carefully because they represent the difference between working and counter electrode potentials, and not absolute values versus a reference. A constant voltage (potentiostatic charge/discharge cycle) is applied between the graphite counter electrode and the MXene working electrode, driving the lithium intercalation/deintercalation process. Figure 3.11(c), extracted from [197], shows the intercalation of water molecules between MXene sheets. In this study the solvation of water molecules induced by lithium ion increases the d-spacing [197].

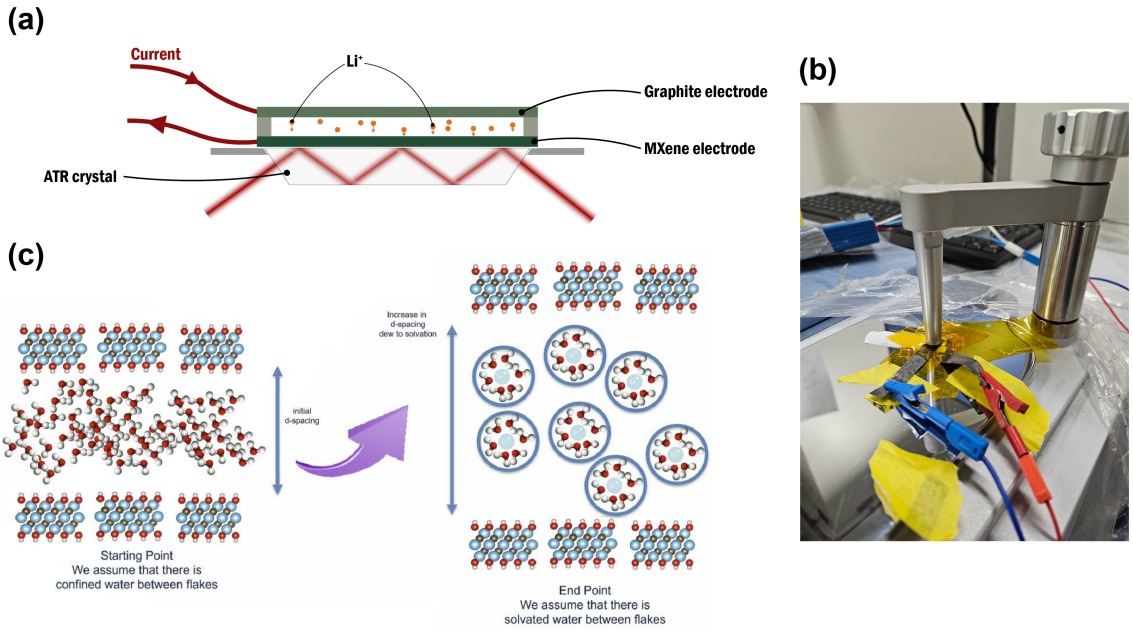

Figure 3.11: Concept of MXene electrochemical monitoring. (a) Schematic representation of the electrochemical cell used for in situ ATR-FTIR spectroscopy. The cell consists of a $Ti_3C_2T_x$ MXene working electrode (approximately 15 μm thick) deposited onto an ATR crystal, and a graphite counter electrode. Li^+ ions (orange spheres) shown intercalating into the MXene structure during electrochemical cycling. (b) ATR-FTIR cell setup. (c) Comparison of OH-confined vs OH-solvated for $Ti_3C_2T_x$ in LiCl, schematic extracted from [197].

FTIR spectra were collected between 400-4000 cm^{-1} with a resolution of 4 cm^{-1} using a Bruker Invenio R FTIR spectrometer. Each spectrum is averaged over 16 scans to obtain a good signal-to-noise ratio, and acquisition takes about 30 seconds per spectrum. Spectra were recorded at 0.2 V discrete potential intervals with a holding time of 2 min during potentiostatic cycling between 0 V and -1.2 V vs Ag wire. The choice of this potential window was based on preliminary cyclic voltammetry experiments that identified the optimal range for lithium intercalation without significant water electrolysis or electrode degradation. This protocol allowed for a systematic investigation of the aqueous solution confined between MXene nanosheets. The ATR crystal enables real-time monitoring of structural and chemical changes in the MXene electrode through multiple internal reflections of the infrared beam (shown in red), allowing for operando FTIR spectroscopic analy-

sis during electrochemical reactions. This configuration provides direct insight into the ion storage mechanisms and structural evolution of the MXene electrode during charge/discharge cycles.

3.2.2 Results and Discussion

Figure 3.12 presents the evolution of ATR-FTIR spectra as a function of applied potential during the cathodic polarization from 0 V to -1.2 V, corresponding to the lithium intercalation process. Several peaks appear: at low frequency (below 700 cm^{-1}), Ti–O vibrations occur [197], while between 1500 and 2000 cm^{-1}, the signal is due to C–O stretching [113]. Between 2000 and 3000 cm^{-1}, the ATR diamond crystal absorbs [198]. Here, we focus on the region above 3000 cm^{-1}, where the vibrational frequencies of water molecules are located. The spectra exhibit significant and systematic modifications across the entire measured range, reflecting the complex structural and chemical changes occurring during Li^+ intercalation into the MXene structure.

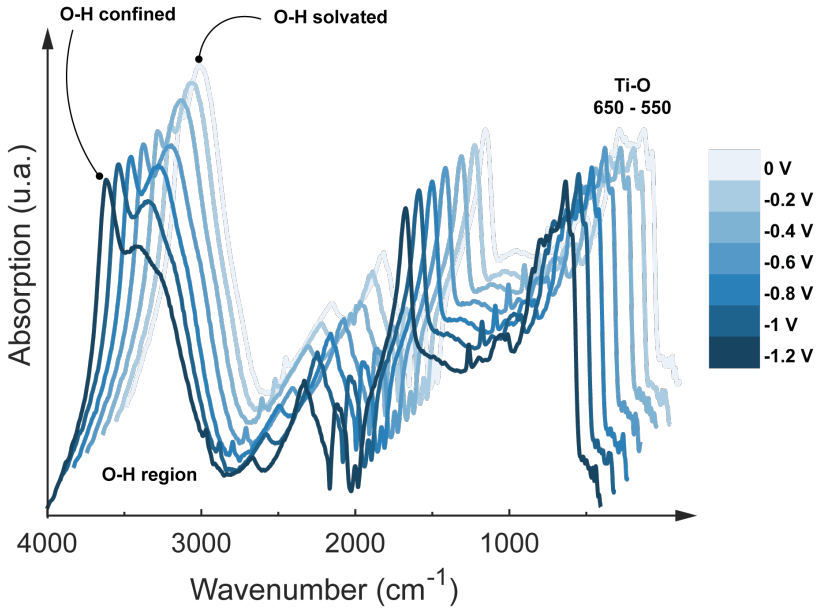

Figure 3.12: Evolution of ATR-FTIR spectra of $Ti_3C_2T_x$ MXene electrode as a function of applied potential from 0 V to -1.2 V during Li^+ intercalation in 1 M LiCl aqueous electrolyte.

The most informative changes occur in the O–H stretching region (2500-4000 cm^{-1}) during electrochemical cycling. This spectral region contains contributions from both solvated and confined water populations within the MXene structure. Solvated O-H groups correspond to hydroxyl groups in a bulk-like aqueous environment. Confined O-H groups, resulting from water molecules trapped in the nanoscale interlayer space (1-2 nm) between MXene sheets, exhibit narrower, better-resolved peaks: a low-frequency component at 3160 cm^{-1} (strongly hydrogen-bonded to surface termination groups, Table 3.3) and a high-frequency component at 3500-3600 cm^{-1} (weakly bonded or "free" O-H groups in the center of the interlayer gallery)[194, 197, 199, 200]. A three-dimensional representation of this spectral region during a full charge-discharge cycle is shown in Figure 3.13, revealing both

the magnitude of these changes and their reversibility, which reflects the dynamic evolution of water organization and hydrogen-bonding environments during ion intercalation and de-intercalation processes.

Charging Process (0 V → -1.2 V): Decreased O-H stretching intensity systematically throughout the charging process correlates with the "displacement of water molecules by incoming Li^+ ions" as described in the mechanistic framework [196]. The progressive modification of the -OH peak region provides quantitative information for the ion-exchange mechanism where Li^+ intercalation is accompanied by water molecule expulsion from the interlayer space.

Discharge Process (-1.2 V → 0 V): Complete recovery of initial spectral features during the discharge process shows that intercalation mechanism is fundamentally reversible. This behavior confirms that the "redistribution of water molecules within the MXene confinement" is fully reversible on the experimental timescale, indicating good structural stability and cyclability of the electrode material. Reversibility is an important feature for practical applications and has been considered an advantage of MXene-based electrodes over conventional materials [185, 187].

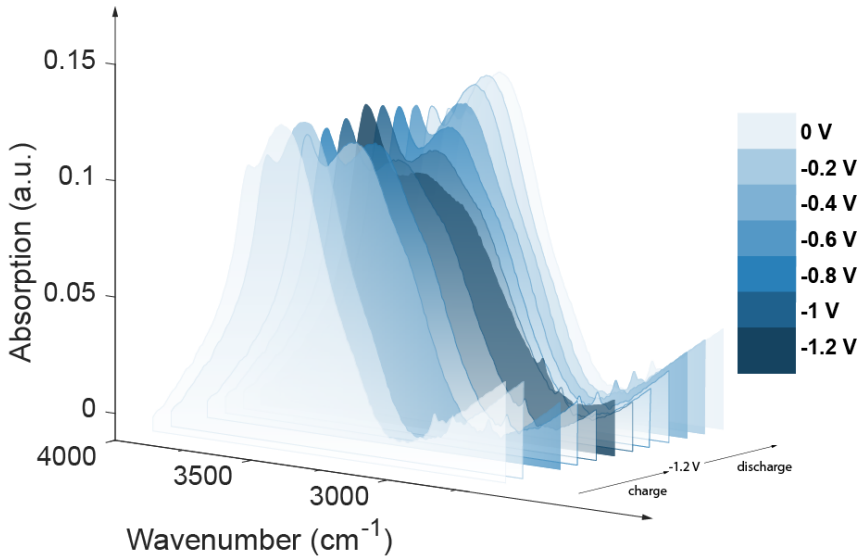

Figure 3.13: Three-dimensional representation of the O-H stretching region evolution during a complete charge-discharge cycle. The surface plot shows the absorption intensity as a function of both wavenumber and applied potential, demonstrating the reversible changes in water and hydroxyl group populations. The charging process (0 V to -1.2 V) shows systematic intensity decrease, while the discharge process (-1.2 V to 0 V) exhibits complete recovery of the initial spectral features.

To understand molecular-level changes in the O-H stretching region, a Gauss function spectral deconvolution was performed (Figure 3.14). This complex shape reflects the heterogeneous hydrogen bonding environments of the MXene interlayer space, which required a multi-component analysis to derive information about individual water populations.

The optimal fit was achieved using four distinct Gaussian components, each representing different hydrogen-bonding environments within the MXene structure. The deconvolution parameters obtained at -1.2 V (Table 3.3) demonstrate excellent statistical quality with minimal fitting errors, indicating robust identification of the individual water populations.

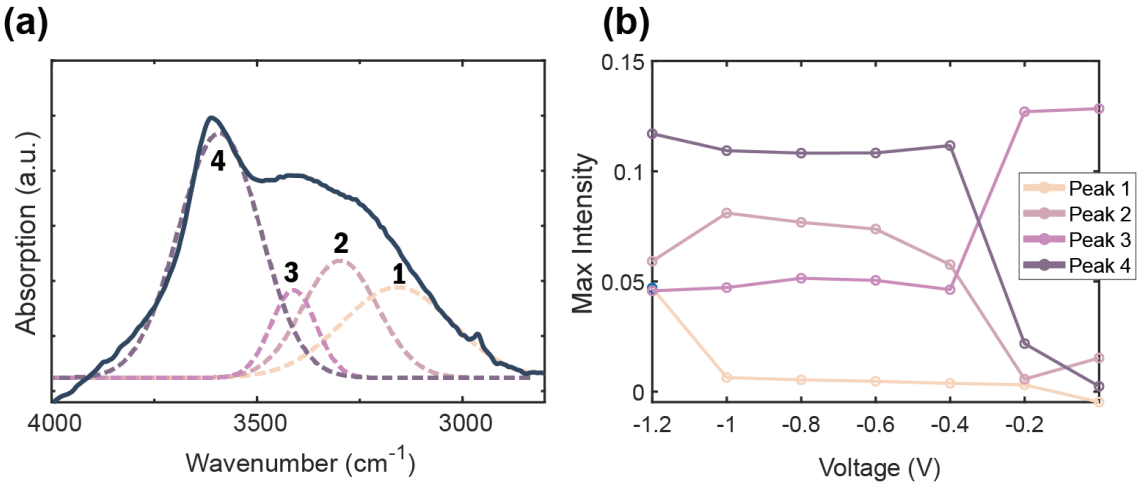

Figure 3.14: (a) Deconvolution of the O-H stretching band into four components representing different hydrogen-bonding environments within the MXene structure. The optimal fit was achieved using a Gauss function. (b) Potential-dependent evolution of the integrated intensities for each deconvoluted peak during the charging process, revealing distinct behaviors for different water populations.

Table 3.3: Deconvolution parameters for the O-H stretching region at -1.2 V vs. counter electrode [194, 197, 199–201]

Peak	Center (cm^{-1})	Width (cm^{-1})	Height	Area	Assignment
1	3159 ± 118	270 ± 78	0.041	13.9	Strongly bound H_2O
2	3298 ± 20	183 ± 75	0.053	12.2	Moderately bound H_2O
3	3411 ± 6	110 ± 16	0.040	5.5	Weakly bound H_2O
4	3591 ± 2	200 ± 3	0.111	27.8	Free OH groups

The deconvolution analysis (Figure 3.14(a)) successfully resolves four distinct water populations, each characterized by specific hydrogen bonding environments within the MXene interlayer structure:

- **Peak 1 (3159 cm^{-1})**: Strongly bound water molecules confined within narrow interlayer spaces, exhibiting the lowest vibrational frequency due to strong hydrogen bonding interactions with MXene surface terminations.
- **Peak 2 (3298 cm^{-1})**: Moderately bound water molecules representing the transition zone between strongly confined and mobile populations, with intermediate hydrogen bonding strength.
- **Peak 3 (3411 cm^{-1})**: Weakly bound water molecules with enhanced mobility and reduced surface interactions, likely located near the electrode-electrolyte interface.
- **Peak 4 (3591 cm^{-1})**: Free hydroxyl groups including both MXene surface terminations (-OH) and isolated water molecules with minimal hydrogen bonding.

This assignment aligns with the mechanistic understanding described in the literature, where the "dynamic interplay between weak charge-induced O-H stretch-

ing (water attracted by MXene surface oxygen terminations) and stronger cation-induced O-H stretching (water molecules surrounding the cations)" governs the spectroscopic response [197]. The frequency-structure correlations are consistent with established hydrogen bonding theory [199] and previous vibrational studies of confined water systems [200].

3.2.3 Conclusions and future perspectives

The preliminary investigations presented in this work have been subsequently extended and validated through comprehensive studies conducted by the Drexel University research group [197]. Building upon our foundational ATR-FTIR methodology, their extensive research program has explored the electrochemical behavior of both $Ti_3C_2T_x$ and $Ti_3C_2Cl_2$ MXenes across multiple electrolyte systems, including acidic (0.5 M H_2SO_4), neutral (1 M LiCl), and basic (6 M KOH) environments. This systematic investigation has revealed electrolyte-dependent intercalation mechanisms and provided deeper insights into the role of surface terminations on electrochemical performance.

The advanced spectroscopic analysis performed by Parker et al. has validated our initial observations regarding water molecule displacement during lithium intercalation and has extended the understanding to include the behavior of different cation species (H^+, Li^+, K^+) and their interactions with varying MXene surface chemistries. Their work has demonstrated that the fundamental principles identified in our preliminary LiCl studies are applicable across a broad range of aqueous electrolyte systems, establishing ATR-FTIR as a powerful and versatile tool for understanding ion storage mechanisms in 2D materials.

Moreover, their integration of complementary techniques, including in situ Raman spectroscopy and ab initio molecular dynamics simulations, has provided comprehensive validation of the ion-exchange mechanisms and water reorganization processes initially identified through our ATR-FTIR approach. This multi-technique validation underscores the reliability and broader applicability of the molecular-level insights obtained from infrared spectroscopic analysis of MXene electrodes.

The molecular-level insights obtained from this ATR-FTIR investigation open exciting possibilities for advanced characterization of electrochemical cells using near-field spectroscopic techniques, particularly through Photo-Induced Force Microscopy (PiFM). This emerging technique represents a paradigm shift in operando electrochemical characterization by combining the spatial resolution of atomic force microscopy with the chemical specificity of infrared spectroscopy.

Atomic force microscopy has already demonstrated significant value in the in situ characterization of electrochemical cells by analyzing the mechanical deformation of electrodes during charge-discharge cycling [202]. Come et al. have shown that nanoscale elastic changes (Figure 3.15) in $Ti_3C_2T_x$ MXene electrodes can be directly correlated with ion intercalation processes, providing insights into the mechanical response of 2D materials during pseudocapacitive charge storage. Their work revealed heterogeneous mechanical behavior at the nanoscale, with localized regions showing different degrees of elastic modulus change depending on the local intercalation state.

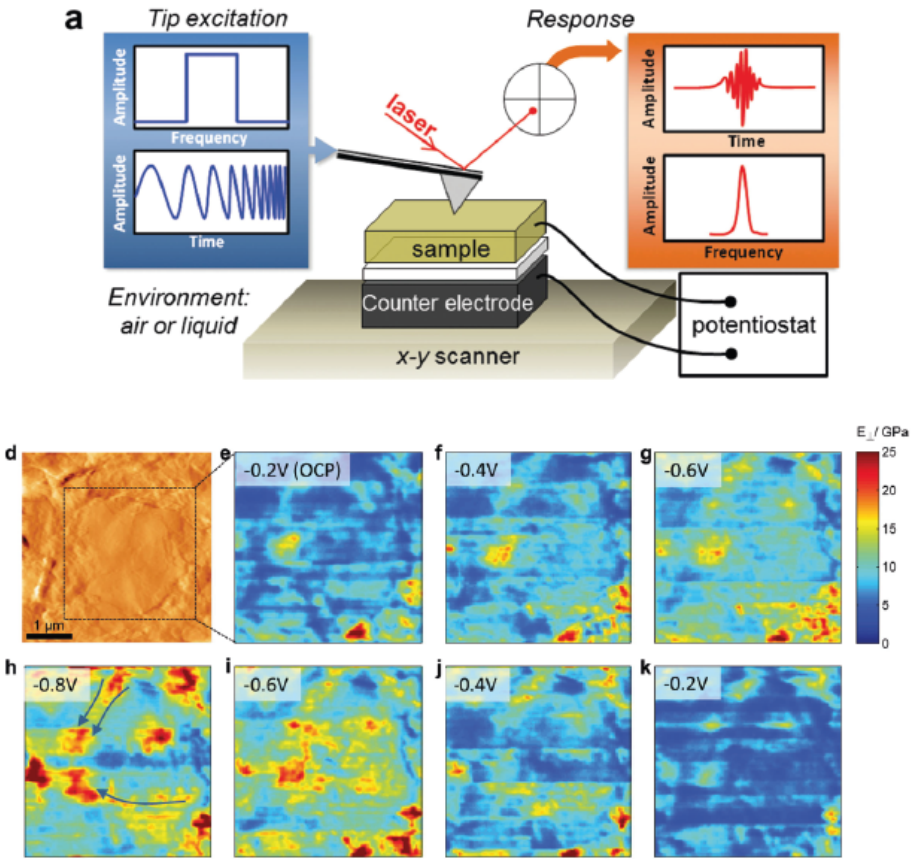

Figure 3.15: In situ contact resonance AFM measurements during electrochemical cycling. (a) Schematic representation of the experimental setup, where the AFM tip is vibrated in contact with the sample's surface with a band excitation waveform. Elastic changes of $Ti_3C_2T_x$ in Li_2SO_4 electrolyte, (d) Contact AFM topography image of a multilayer MXene flake at the surface of the electrode. (e–k) Elastic modulus images taken at potentials between -0.2 V and -0.8 V versus Pt during Li^+ charge (e–h) and discharge (h–k). Extracted from [202].

By coupling AFM with photo-induced force spectroscopy, unprecedented opportunities emerge for correlating spectroscopic signatures with mechanical properties at the nanoscale. Specifically, the ability to spatially map the O-H vibrational signal identified in our ATR-FTIR studies while simultaneously monitoring mechanical deformation would provide direct visualization of the relationship between local water content and structural changes within individual MXene flakes.

Conclusion

This chapter has demonstrated the power of Fourier Transform Infrared (FTIR) spectroscopy to characterize MXenes through two complementary approaches: compositional engineering and in situ electrochemical monitoring.

The first part established that modulating the carbon-to-nitrogen ratio in $Ti_3C_{(2-y)}N_yT_x$ MXenes enables precise control over their infrared optical properties. Systematic analysis reveals a direct correlation between composition and IR response, with emissivities ranging from 0.06 for $Ti_3C_2T_x$ to 0.65 for Ti_3CNT_x. This compositional engineering strategy opens promising perspectives for IR shielding applications, reflective coatings, and thermal management systems.

The second part validated the effectiveness of the ATR-FTIR approach for real-time probing of ionic intercalation mechanisms. Preliminary investigations on lithium intercalation in $Ti_3C_2T_x$ were extended and confirmed by comprehensive studies conducted by the Drexel University research group [197], demonstrating the applicability of this methodology across different electrolyte systems (acidic, neutral, basic) and cation types (H^+, Li^+, K^+). These works established that interactions between confined water molecules and surface terminations play a crucial role in charge storage mechanisms.

The integration of these two approaches reveals that the functional properties of MXenes result from the complex interplay between their intrinsic composition (C/N ratio) and surface chemistry (T_x terminations). While far-field FTIR spectroscopy provides ensemble-averaged information across the sample, spatial resolution remains limited for characterizing nanoscale heterogeneity in surface terminations.

This limitation underscores the necessity for higher spatial resolution characterization techniques, thus motivating the approach developed in the following chapter (Chapter 4). Photo-induced Force Microscopy (PiFM) will enable exploration of the nanometric distribution of surface functional groups, thereby complementing the global understanding of structure-property relationships in MXenes and offering a more complete vision of these promising 2D materials.

Chapter 4

Optical near-field properties of 2D MXenes using IR nanoscopy

4.1 Pure optical analysis of $Ti_3C_2T_x$ probed by s-SNOM . . 90

4.2 Surface terminations of MXenes 92

4.2.1 PiFM analysis of pristine $Ti_3C_2T_x$ and V_2CT_x MXenes . 93

4.3 Oxydation and carbon defects probing on Nb_2CT_x . . . 96

4.3.1 Raman and FTIR responses of the bulk Nb_2CT_x 97

4.3.2 PiFM response on bulk Nb_2CT_x 99

4.3.3 PiFM response of single/few-layered of Nb_2CT_x flakes . . 101

4.4 Nanoscale observation of siloxane compounds on titanium carbonitride MXenes 103

4.4.1 $Ti_3C_{1.5}N_{0.5}T_x$ structural characterization 105

4.4.2 Far-field vibrational spectroscopy 107

4.4.3 Local infrared properties 108

4.4.4 Spectral mapping 112

Introduction

The previous chapter explored how systematically varying the carbon-to-nitrogen ratio in titanium carbonitride MXenes ($Ti_3C_{(2-y)}N_yT_x$) significantly impacts their infrared properties. Composition tuning at the atomic level is one way to engineer MXene properties; however, surface chemistry plays an important role in the engineering process: the type and distribution of terminal functional groups (T_x). These etching-induced surface terminations usually contain oxygen, hydroxyl, and fluoride groups, which are critical for the electronic, optical, and chemical behaviors of MXenes.

Conventional spectroscopic methods such as Fourier Transform Infrared (FTIR) and Raman spectroscopy provide information about MXene surface chemistry but are spatially limited. Such techniques combine average information over relatively large sample areas, which may hide nanoscale differences in surface termination

distribution that may affect material properties and performance. Also, the highly reactive nature of MXene surfaces makes them easily contaminated and chemically modified at ambient conditions, complicating their characterization and application.

This chapter addresses those challenges using advanced near-field infrared nanoscopy techniques for chemical mapping with nanometer-scale spatial resolution. We begin with the characterization of $Ti_3C_2T_x$ using scattering-type Scanning Near-field Optical Microscopy (s-SNOM). While this approach offers valuable insights, the interpretation of s-SNOM results proves challenging due to the complex electromagnetic interactions with the metallic nature of MXenes. This limitation motivates our subsequent transition to Photo-induced Force Microscopy (PiFM), which offers complementary benefits for nanoscale chemical analysis.

The chapter then progresses through a series of interconnected investigations. First, we examine the surface terminations of various MXenes ($Ti_3C_2T_x$, V_2CT_x), giving information about their native surface chemistry. Next, we focus specifically on Nb_2CT_x MXene, demonstrating how PiFM can detect oxidation and carbon defects resulting from synthesis conditions. This provides critical insight into how processing parameters affect the chemical integrity of MXene surfaces at the nanoscale. We also examine the distribution of siloxane-based contaminants on pristine and aged MXene surfaces - information useful for surface control applications.

4.1 Pure optical analysis of $Ti_3C_2T_x$ probed by s-SNOM

Optics and plasmonics behavior of MXenes have attracted increasing attention recently due to their application potential in nanophotonics and optoelectronics. Several pioneering studies have explored surface plasmon polaritons in $Ti_3C_2T_x$, including the electron energy loss spectroscopy (EELS) investigation by El-Demellawi et al. in 2018 [203], and more recently, the work by Rieger et al. in 2025, who employed multiphoton photoemission electron microscopy (nP-PEEM) to directly image the plasmonic near fields of multilayered $Ti_3C_2T_x$ structures [204]. The plasmonic characteristics of MXenes have been revealed through these studies, which may enable localized surface plasmon resonances in the near-infrared as well as mid infrared spectral regions.

Even though all of these advances have been achieved, scattering-type scanning near-field optical microscopy (s-SNOM) has been underutilized for characterizing the optical properties of other two-dimensional materials such as graphene compared to Raman spectroscopy for instance [205, 206]. s-SNOM offers several unique advantages for studying 2D materials: it provides simultaneous topographical and optical information with nanoscale spatial resolution (10-20 nm), allowing nanoscale spectroscopic analysis and direct probing of near-field optical responses that are unavailable with far-field techniques.

Here we report an attempt to investigate $Ti_3C_2T_x$ single flakes by s-SNOM in the mid-infrared (MIR) region. Our results show interesting optical contrast and spectral features but are difficult to interpret because the dielectric function of $Ti_3C_2T_x$ is not well known in the MIR spectral range. This complex interaction between intrinsic optical properties, surface terminations and possible oxidation or contamination effects makes quantitative analysis very demanding. Still, s-SNOM imaging

reveals strong optical contrast in agreement with sample morphology and reveals interesting near-field optical behavior of this MXene.

Materials and methods

$Ti_3C_2T_x$ MXene flakes were synthesized according to the standard HF/HCl etching protocol described in Chapter 1 and spin-coated onto aluminum oxide (Al_2O_3) substrate. This substrate was selected because of its optical properties in the mid-infrared range. In contrast to silicon dioxide (SiO_2), which shows strong phonon absorption bands around 1000-1200 cm^{-1}, interfering with MXene spectral features, Al_2O_3, shows a flat and featureless optical response in our spectral range of interest (770-1860 cm^{-1}). This ensures that observed optical contrast is due to MXene flakes and not substrate-related artifacts.

Near-field optical measurements were carried out using a Vista One system from Molecular Vista Inc., which combines photo-induced force microscopy (PiFM) with scattering-type scanning near-field optical microscopy (s-SNOM) capabilities. The instrument operates by focusing a power-modulated quantum cascade laser (spectral range: 5.3–13 μm, corresponding to 770–1860 cm^{-1}) at the apex of a platinum-coated silicon atomic force microscope (AFM) tip using a parabolic mirror with numerical aperture (NA) = 0.9. The system operates in "direct" (homodyne) detection mode and the amplitude dither varies from 30 to 50 nm.

Results and discussion

Figure 4.1 presents topographic and near-field optical images of $Ti_3C_2T_x$ MXene flakes deposited on an Al_2O_3 substrate. The topography (Figure 4.1(a)) reveals two single-flakes overlapping at the center of the scanned area. The s-SNOM images acquired at 1460 cm^{-1} (Figure 4.1(b)) show clear contrast between the MXene flakes and the Al_2O_3 substrate. The flakes appear brighter, indicating enhanced scattering compared to the dielectric substrate. This enhanced optical signal from the MXene material may be expected due to its metallic character, which leads to stronger near-field coupling compared to the dielectric Al_2O_3 substrate. According to the effective polarizability model presented in Chapter 2 (point dipole model), the tip-sample system can be described by the effective polarizability:

$$\alpha_{eff}^{PD} = \frac{\alpha}{1 - \alpha\beta S^{nf}} = \frac{\alpha}{1 - \frac{\alpha\beta}{16\pi(R+H)^3}} \tag{4.1}$$

For metallic or semi-metallic materials like MXenes, the sample response β tends toward one, significantly enhancing α_{eff} and thus the scattered field intensity. This may explain the strong contrast observed between the MXene flakes and the dielectric substrate.

The s-SNOM image is the significantly brighter signal in the central region where the two flakes overlap. This enhanced signal in the overlap region can be attributed to the geometric sensitivity of s-SNOM to sample thickness. The s-SNOM technique operates with a relatively large dither amplitude (typically 50 nm) [207], which results in a larger probe volume compared to PiFM (typically 1-2 nm) [135] and makes the measurement more sensitive to geometric effects. The thicker bilayer region provides a larger effective interaction volume with the MXene, leading to

enhanced near-field scattering. This geometric sensitivity is a characteristic feature of s-SNOM measurements, where the signal depends not only on the material's intrinsic optical properties but also on its structural dimensions [208].

It is worth noting that the spatial resolution in s-SNOM, while sufficient to resolve individual flakes, is limited by the relatively large tapping amplitude. The tip-sample distance modulation of 50 nm results in a less confined near-field interaction compared to non-contact technique. This makes s-SNOM particularly well-suited for detecting plasmonic resonances, phonon polaritons, and antenna effects, but less ideal for probing surface chemistry variations. In contrast, as we will demonstrate in Section 4.2.1, PiFM operates at much smaller tip-sample distances in non-contact mode, providing significantly enhanced surface sensitivity and spatial confinement at the surface. Notably, PiFM measurements do not show enhanced signal in the bilayer overlap region (see Figure 4.18), suggesting that PiFM is less sensitive to thickness variations and more directly probes the surface chemical composition through localized photo-absorption.

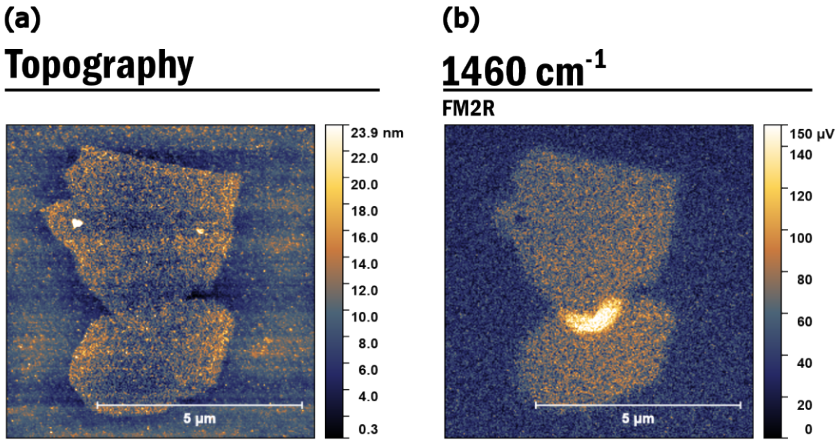

Figure 4.1: S-SNOM analysis of $Ti_3C_2T_x$ MXene: (a) Topography of 2 single-flakes overlapping at the center of the image. (b) s-SNOM image of $Ti_3C_2T_x$ MXene flakes at 1460 cm^{-1}.

4.2 Surface terminations of MXenes

The surface chemistry of MXenes is of particular interest as it is shown to affect the properties in several domains, including electrical conductivity, chemical reactivity, and optical behavior [8]. The type and distribution of surface terminations (–OH,–O,–F,–Cl) influence the electronic structure, work function, and chemical stability of these two-dimensional materials [209]. Thus advanced characterization methods to identify and map these surface functional groups are sought.

Several spectroscopic techniques are traditionally used to characterize MXene surface chemistry. Fourier transform infrared spectroscopy (FTIR) is widely used to identify surface termination groups characterized by characteristic absorption bands at 1800cm^{-1} for C-O, 1400 cm^{-1} for O-H, 1100 cm^{-1} for C-F, 600 cm^{-1} for Ti-O, and 700 cm^{-1} for Ti-F bonds [113]. Raman spectroscopy provides complementary

structural information, revealing vibrational modes such as the A_{1g} Ti-C symmetric vibration at 200 cm^{-1}, E_g O vibrations at 350 cm^{-1}, and E_g in-plane carbon vibrations at ∼620 cm^{-1} [114, 115]. X-ray photoelectron spectroscopy (XPS) has also been extensively utilized to quantify surface termination ratios and oxidation states [210].

However such conventional characterization techniques have low spatial resolution. In this work, we employ PiFM to investigate the surface terminations of pristine $Ti_3C_2T_x$ and V_2CT_x MXenes, providing insights into their nanoscale surface chemistry and demonstrating the sensitivity of this technique for MXene characterization.

4.2.1 PiFM analysis of pristine $Ti_3C_2T_x$ and V_2CT_x MXenes

Figure 4.2 shows a detailed PiFM analysis of pristine $Ti_3C_2T_x$ MXene flakes with surface terminations to demonstrate nanoscale detection of surface terminations. Topography image (Figure 4.2(a)) shows several MXene flakes of different thicknesses with a height scale from 0 to 20 nm due to flake overlapping. A red mask overlay denotes regions where topographical outliers or artifacts have been excluded for data quality assurance.

In the raw PiFM signal (Figure 4.2(b)), the contrast is weak across the sample and the signal intensities reach up to 136 mV. To enhance the signal-to-noise ratio and visualization enhancement, 2D Fast Fourier Transform (FFT) filtering was applied to obtain the processed image in Figure 4.2 (c) with filtered signal intensities up to 60 mV. In the FFT residual image shown in Figure 1d, high-frequency noise components have been removed during the filtering to validate the data processing approach.

In the filtered PiFM image, the MXene flakes contrast with the Al_2O_3 substrate. The MXene regions show strong chemical signals whereas the substrate is signal-free, indicating that the detected vibrational modes are intrinsic to the MXene surface chemistry. Spectral imaging was performed with absorption frequencies of 1067 cm^{-1} for C-O and C-F stretching vibrations from surface termination groups.

The PiFM spectrum was extracted from the sample center, i.e., from the region marked by the white triangle on the topography image (Figure 4.3(e)). The spectrum shows a typical broad absorption band around 1000-1200 cm^{-1} in the green shaded region due to C-O and C-F stretching vibrations from the surface termination groups (-OH,-O,-F) characteristic of $Ti_3C_2T_x$ MXenes.

The PiFM characterization of pristine V_2CT_x MXene, with its surface chemistry detection capabilities, is shown in Figure 4.3. The topography (Figure 2(a)) shows a single, well-defined triangular MXene flake with a thickness of approximately 5 nm, indicating a few-layer structure. The flakes are smooth with sharp edges typical of good MXene synthesis.

The raw PiFM signal (Figure 4.3(b)) follows the same processing methodology and shows signal intensities up to 234 μV. A processed image after 2D FFT filtering (Figure 4.3(c)) shows uniform chemical contrast across the entire MXene flake at 88 μV signal intensities. The FFT residual (Figure 4.3(d)) shows that the noise filtering worked well.

A clear contrast is visible between the V_2CT_x flake and the Al_2O_3 substrate, with strong PiFM signals localized exclusively on the MXene regions. The spectral

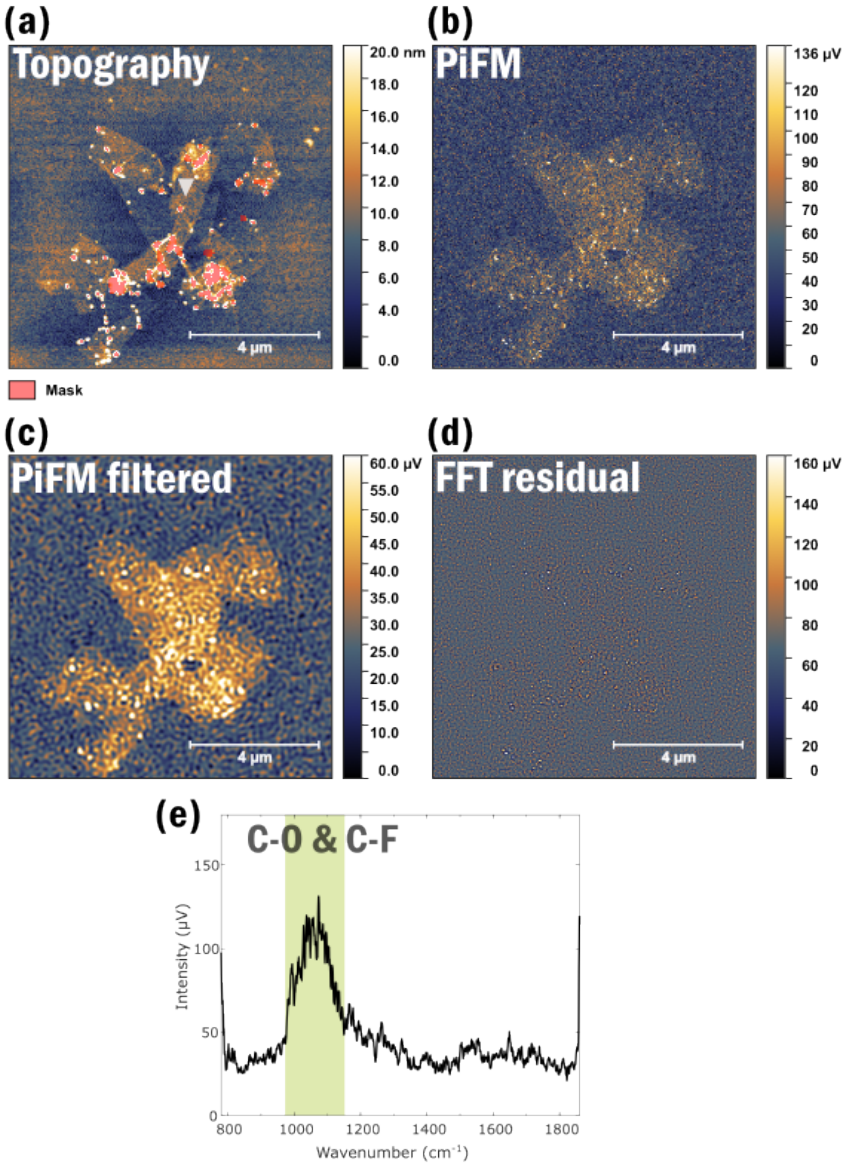

Figure 4.2: Pristine $Ti_3C_2T_x$ single flake probed by PiFM showing the surface terminations related bonds. (a) is the topography of the MXene. (b) is the raw PiFM spectra image at 1067 cm^{-1}. (c) is the 2D FFT filtered PiFM image at 1067 cm^{-1}. (d) is the residual image after the filtering. (e) is the averaged PiFM spectrum acquired at the white spot showcased on the topography.

imaging was performed at 1085 cm^{-1}, corresponding to the C-O and C-F absorption frequencies for this composition. Unlike the $Ti_3C_2T_x$ analysis, the PiFM spectrum for V_2CT_x (Figure 4.3(e)) represents an averaged spectrum acquired from all regions marked by red triangles on the topography image.

This extracted spectrum also shows a similar broad absorption band around 1000-1200 cm^{-1} region, which is again attributable to C-O and C-F stretching vibrations from surface terminations. A similar spectral profile is obtained for $Ti_3C_2T_x$, which indicates the presence of similar oxygen- and fluorine-containing surface termination groups.

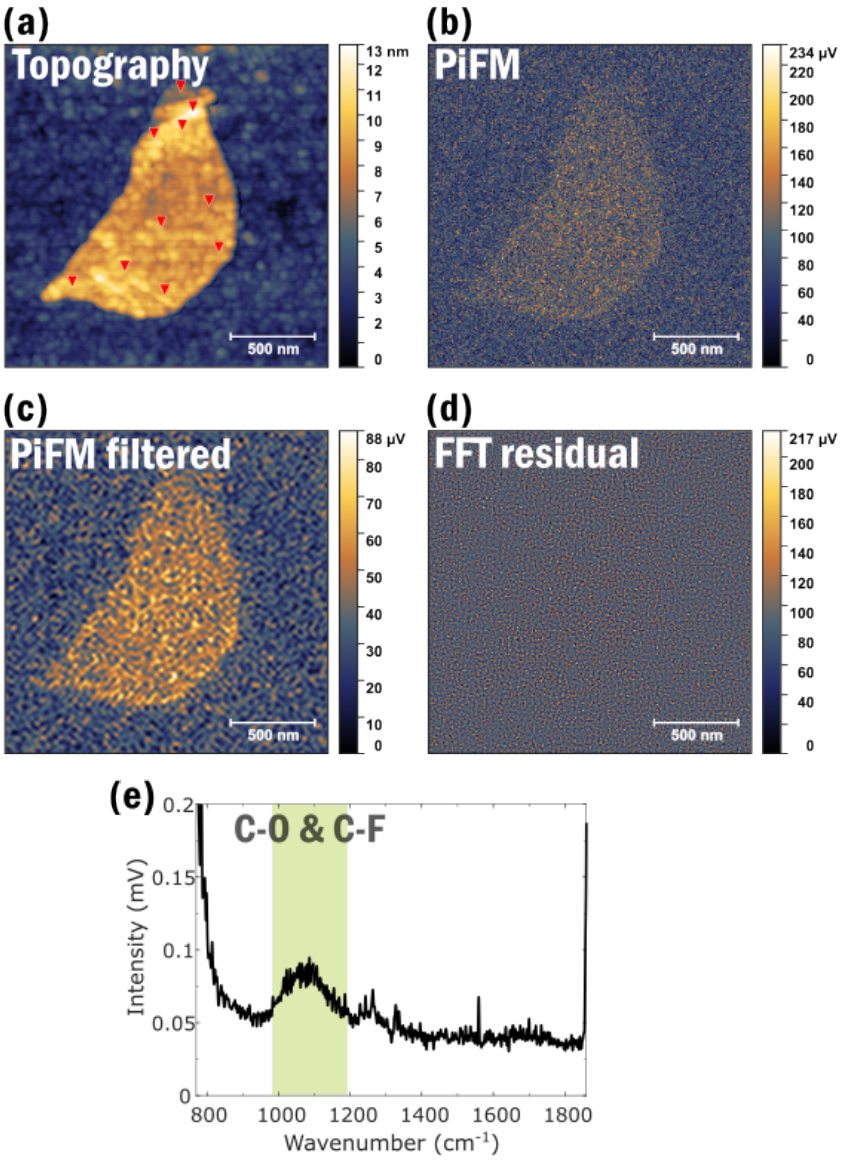

Figure 4.3: Pristine V_2CT_x single flake probed by PiFM showing the surface terminations related bonds. (a) is the topography of the MXene. (b) is the raw PiFM spectra image at 1085 cm^{-1}. (c) is the 2D FFT filtered PiFM image at 1085 cm^{-1}. (d) is the residual image after the filtering. (e) is the averaged PiFM spectrum acquired at the red spot showcased on the topography.

Both pristine MXene compositions have clear PiFM signatures around the 1000-1200 cm^{-1} region for oxygen- and fluorine-containing surface terminations. The

spatial uniformity of the PiFM signals across individual flakes indicates homogeneous surface chemistry, consistent with the uniform etching conditions used during synthesis. The distinct contrast between the MXene flakes and the Al_2O_3 substrate in both cases validates the selectivity of the technique for detecting MXene-specific surface chemistry.

The difference in signal intensities between $Ti_3C_2T_x$ and V_2CT_x, is probably related to instrumental variations due to the PiFM setup, such as laser alignment, tip quality, and measurement conditions rather than fundamental differences in surface chemistry. These results demonstrate that PiFM can characterize surface terminations across different MXene compositions with high spatial resolution and provide chemical insights not possible with classical far-field spectroscopy.

4.3 Oxydation and carbon defects probing on Nb_2CT_x

In this section, we investigate niobium carbide MXene (Nb_2CT_x), a member of the M_2X_x family of MXenes with two transition metal layers and one carbon layer. This family of MXenes is of particular interest because of the documented tendency to oxidize in ambient conditions [211, 212]. The oxidation behavior of niobium makes it an ideal target to study surface chemistry modifications and oxide formation mechanisms in two-dimensional materials. Additionally, niobium oxide has spectral signatures in the spectral range of the PiFM system. The formation process of niobium oxide can be illustrated by the schematic shown in Figure 4.4, adapted from Su *et al.* publication [213].

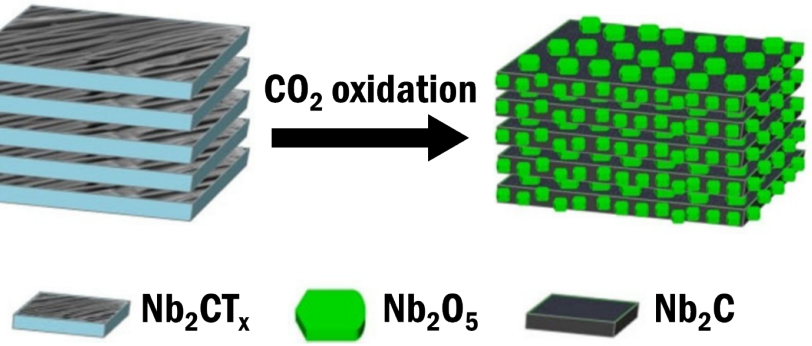

Figure 4.4: Schematic illustration for the formation of the $Nb_2O_5/C/Nb_2C$ composite through CO_2 oxidation at 850°C. The layered Nb_2CT_x MXene structure (left) transforms into a composite material where Nb_2O_5 nanoparticles (green hexagons) are homogeneously distributed on the surface of the remaining Nb_2C layers (dark gray), with amorphous carbon acting as an interfacial bridge. Adapted from Su *et al.* [213]

In this example, the formation steps are characterized by a controlled oxidation mechanism where the pristine layered Nb_2CT_x MXene structure undergoes selective transformation under CO_2 atmosphere at elevated temperature. The process involves the elimination of surface termination groups, followed by the preferential oxidation of the outer MXene layers to form Nb_2O_5 nanoparticles, while simultaneously generating amorphous carbon species as interfacial bridges between the oxide

and the preserved carbide core. The elimination of surface termination groups would imply that, in such a case, their observation would not be expected.

The objective of this study is to characterize the distribution of niobium oxide species derived from Nb_2CT_x by multi-scale spectroscopic approach. Knowing both the oxidation process and the resulting oxide phases is important for fundamental research and practical applications, since surface oxidation can change the electronic, optical and catalytic properties of MXenes. Our experimental methodology involves two-tiered characterization to probe the material at different scales. First, we characterize bulk quantities of niobium by conventional far-field spectroscopy techniques like Fourier Transform Infrared (FTIR) and Raman spectroscopy. Such techniques yield ensemble-averaged information about the chemical composition and vibrational modes of the material, which allows for the identification of the oxide phases with their characteristic spectral signatures. Afterward, we analyze individual Nb_2CT_x flakes deposited on silicon substrates by PiFM. This allows nanoscale spatial resolution and chemical mapping of the local distribution of oxide species not detectable by conventional far-field methods. Comparing far-field and near-field measurements enables correlations between bulk material properties and local surface chemistry variations. This dual-scale characterization is particularly relevant to the heterogeneous nature of oxidation processes in MXenes, where local environmental conditions and defect sites can induce spatially varying oxide formation.

Materials and Methods

Nb_2CT_x MXene was synthesized by selective etching of Nb_2AlC phase powder, similar to what was described in Chapter 1. The delamination process, allowing the obtention of monolayers, was performed using tetramethylammonium hydroxide (compared to LiCl for titanium carbide). Three types of samples were prepared: "bulk" MXene (3 μm of MXene on Si substrate), single/few-layered MXene flakes on Si substrate, and freeze-dried MXene powder.

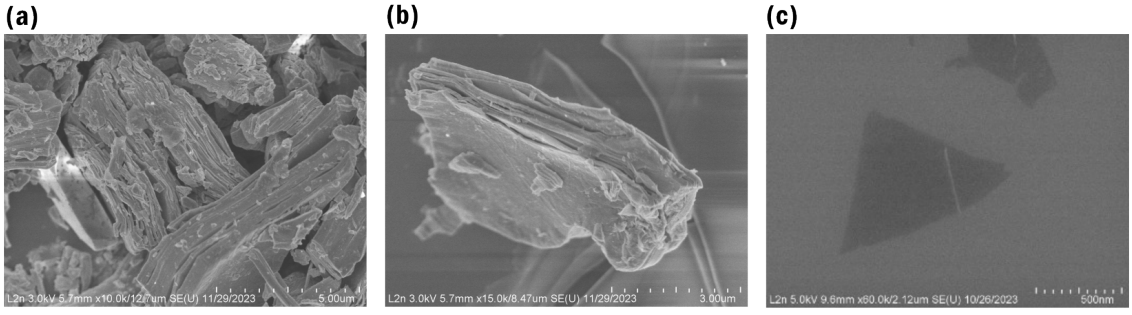

Figure 4.5: SEM images of Nb_2CT_x MXene, (a-b) multilayered flakes before the delamination process and (c) single flake after the exfoliation, deposited on a silicon substrate.

4.3.1 Raman and FTIR responses of the bulk Nb_2CT_x

Figure 4.6 shows FTIR spectra of the Nb_2CT_x powder in Attenuated Total Reflectance (ATR) and transmission mode. In both modes, a dip at 950 cm^{-1} is

distinguishable, suggesting an absorption peak at this IR which has not been reported so far. More information can be extracted in ATR mode where two dips at 1490 cm^{-1} and 1640 cm^{-1} can be attributed to a C–H bonding and C=C stretching respectively [113]. The existence of these carbon linkages may be attributed to organic contamination, but also to the degradation of MXenes induced by over-etching during wet chemical etching.

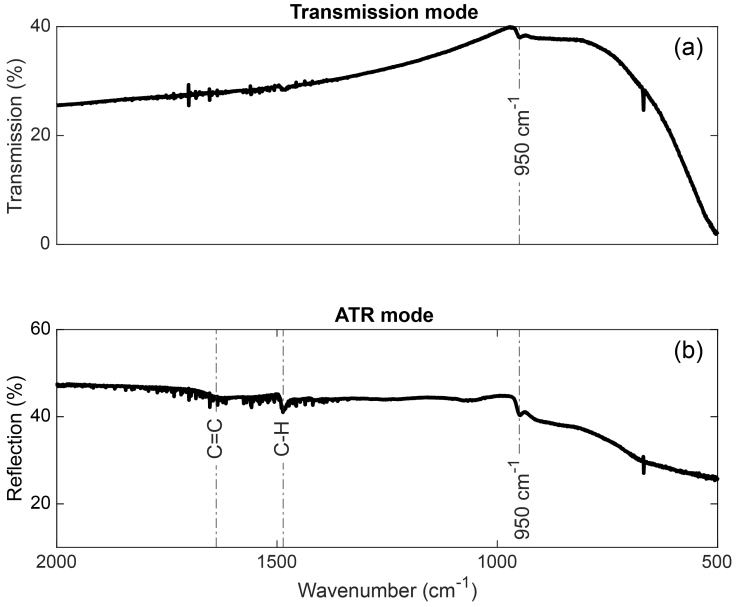

Figure 4.6: Nb_2CT_x powder FTIR spectra in (a) transmission mode and (b) attenuated total reflectance.

The Raman spectroscopy analysis shown in Figure 4.7 provides additional insights into the bulk Nb_2CT_x. The bands observed at 258 cm^{-1} (associated with the bending modes of Nb–O–Nb linkages [214]) and 638 cm^{-1} (attributed to the Nb–O stretching mode [214]) are indicative of Nb_2O_5 [215]. Furthermore, the bands at 1350 and 1590 cm^{-1} are denoted as the D band and G band, respectively, in carbon bonding. The D band points to the presence of defects within the carbon-based structure, while the G band is linked to the in-plane vibration of sp2 carbon atoms. Moreover, a noticeable peak at 980 cm^{-1} is observed in the Raman spectrum. The spectral analysis carried out in the same work showed that the intensity of this specific Raman peak increases with the degree of oxidation. Accordingly, the relative intensity of this peak can be considered as an indicator of the oxidation level of the MXene. Additionally, the presence of peaks associated with Nb and O bonds confirms the presence of oxide in our sample as also observed in [214]. Recently, Su et al. [215] demonstrated the occurrence of the oxyde peak in Nb_2CT_x MXene mixed with Nb_2O_5. Collectively, these findings allow us to affirm the presence of oxidized niobium. The oxidation of niobium results in the generation of carbon monolayers. This transformation is distinctly revealed through Raman spectroscopy, where the G and D bands (mute in direct infrared spectroscopy) confirm these carbon layers' presence. In contrast to what was presented in the previous section on surface terminations, here we do not detect vibrations related to surface terminations despite a similar synthesis method because the surface chemistry has been modified by oxide formation [213].

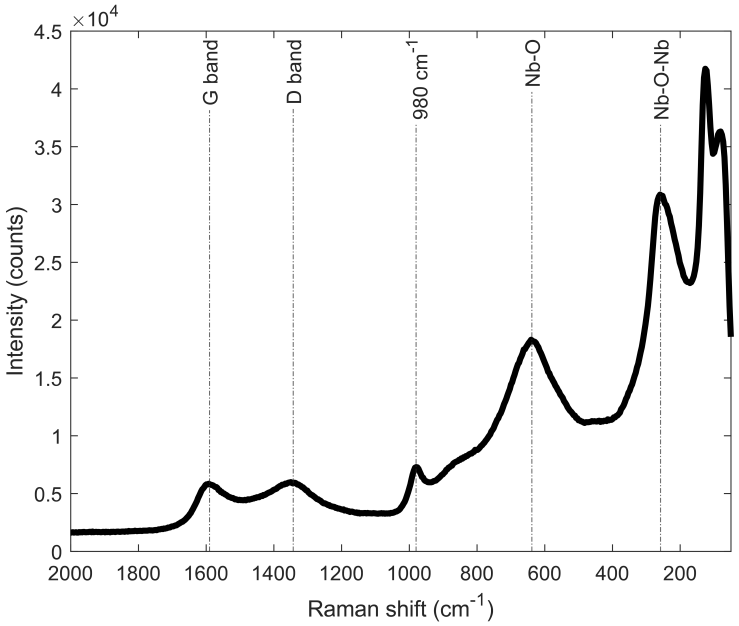

Figure 4.7: Nb_2CT_x Raman spectrum showcasing the present of oxides.

4.3.2 PiFM response on bulk Nb_2CT_x

Figure 4.8 displays the normalized PiFM spectrum of the synthesized material (a), compared with the substrate response (b). Several peaks and an absorption band are visible. Based on our previous results and the model explaining the nature of the PiFM signal presented in Chapter 2, we can attribute the peak at 1640 cm^{-1} to C=C bond in the MXene structure [216], which is barely visible on the FTIR spectra (Figure 4.6). Similarly, the other sharp peak at 1490 cm^{-1} can be associated with organic contamination (carbon contaminant) or Nb_2CT_x flake degradation. It is worth noting that for some degraded tips, the observed silica-related band at 1100 cm^{-1} may originate from the tip itself rather than the sample, due to deterioration of the tip coating. [1] We observed that this broad peak tends to intensify progressively during measurements. This is explained by the degradation of the platinum coating on the AFM tip, exposing the silicon core of the tip. Finally, below 1000 cm^{-1}, a substantial absorption band is noticeable. Based on the previous far-field spectra (FTIR and Raman), this band is related to oxidation.

[1] Tip contamination and coating degradation can introduce unwanted signals in PiFM measurements. Previous measurements on various sample types revealed characteristic polydimethylsiloxane (PDMS) spectral features originating from gel pack storage containers rather than the samples themselves. Since this observation, AFM tips are now purchased in metallic containers to avoid polymer contamination. Another source of artifacts arises from degradation of the metallic coating (typically Au or Pt) on silicon-based tips, which can expose the underlying silicon/silicon oxide layer and introduce silica-related spectral features around 1000-1200 cm^{-1}. Tests conducted by former PhD students in our laboratory, as well as our own observations, indicate that platinum-coated tips exhibit superior durability and provide more reproducible spectra over time compared to gold-coated tips, likely due to the enhanced chemical stability of platinum.

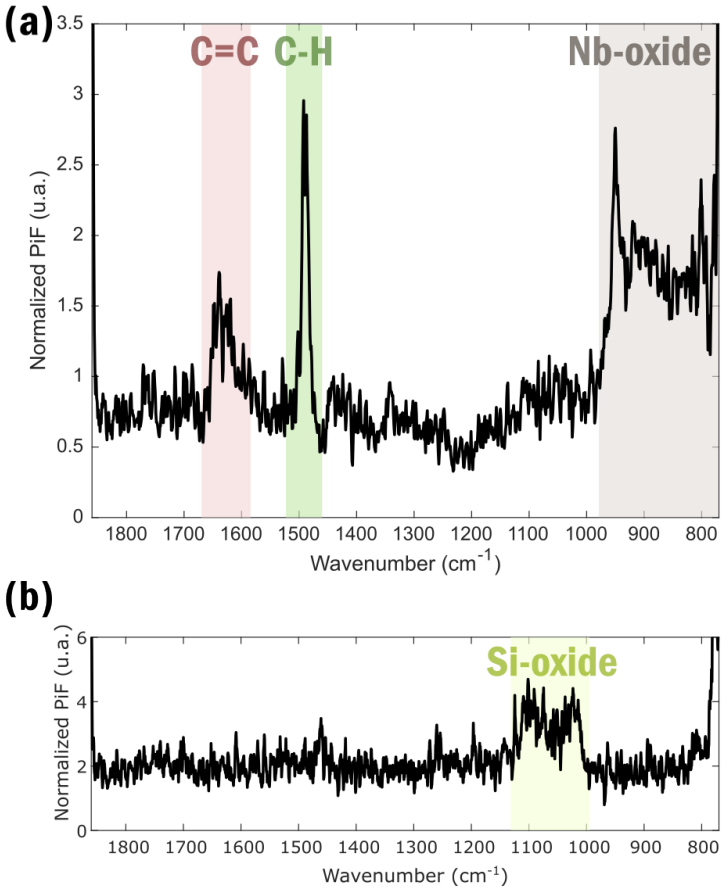

Figure 4.8: PiFM spectrum of (a) bulk Nb_2CT_x (b) undoped silicon wafer (substrate) with peak identification.

4.3.3 PiFM response of single/few-layered of Nb_2CT_x flakes

A similar experiment was conducted on a single/few-layered Nb_2CT_x flakes deposited on an undoped silicon substrate. The morphology of the flakes is observed by AFM and SEM characterization methods (Figure 4.5). We observe that we obtain either single flakes or stacks of a few layers depending on location. Figure 4.9 presents the PiFM characterization of an individual Nb_2CT_x flake on a silicon substrate. The topography (Figure 4.9(b)) shows flakes with a thickness of approximately 6 nm, which corresponds to a stack of 2-3 single flakes. The PiFM image acquired at 900 cm^{-1} (Figure 4.9(a)) shows clear optical contrast between the flake and the substrate. This spatial correlation between topography and optical response confirms that the detected signal originates from the MXene flake rather than substrate artifacts. The PiFM spectrum extracted from the center of the flake (red triangle marker, Figure 4.9(c)) exhibits several distinct features across the mid-infrared range. Despite the relatively small sample thickness, a discernible spectral signature is observed. The spectrum shows increased intensity in the region above 1000 cm^{-1}, with particularly strong signal around 800-900 cm^{-1}. Importantly, the spectral features observed on this few-layer flake are consistent with those measured on bulk Nb_2CT_x samples (Section 4.8), confirming that the chemical composition and surface terminations are still detectable. The observed bands can be attributed to vibrations of surface termination groups (–O, –OH, –F) and Nb–C bonds, characteristic of the Nb_2CT_x MXene structure. The relatively high noise level in the spectrum, particularly in the 1200-1800 cm^{-1} region, can be attributed to the weak absorption of these few-layer flakes and the inherently lower signal-to-noise ratio when probing such thin samples. The Nb–O vibration signal increase suggests dominant contributions from phononic modes of the MXene lattice.

PiFM of the spatial distribution of oxidation products in Nb-based double-layer stacks was investigated to understand the oxidation mechanism at the nanoscale. Figure 4.10 shows topographical analysis of Nb_2CT_x multilayer stack together with PiFM spectra at two locations: The center of the stack is a red triangle and the edge of a flake is a black triangle. A comparative analysis of PiFM spectra shows minor differences between the spectral response of the edge and center regions of a multilayer stack. Stronger signal intensities are notably detected near the edge in two of the key spectral regions depicted in red and green: 1550–1750 cm^{-1} and 1400–1550 cm^{-1}. Established vibrational assignments indicate that these spectral bands correspond to carbon-related vibrations, namely C-C stretching modes and C-H bonding interactions [117, 217, 218]. The preferential enhancement of carbon-related signals at the edge regions supports spatial heterogeneity in the oxidation process. This observation is in agreement with the oxidation mechanism proposed by Su *et al.* [213], where CO_2 oxidation of Nb_2CT_x produces $Nb_2O_5/C/Nb_2C$ composites by controlled surface oxidation. As an intermediate product, amorphous carbon is formed, serving as an electron-transport bridge between the oxide and carbide phases. However, near-field analysis of sample edges can be affected by artifacts due to variations in morphology. The tip-sample interaction is more complex.

The discrepancy in the PiFM signal between the two measurement points is caused by this intrinsic inhomogeneity between the basal plane surface of the flake and the edges, where amorphous carbon exposure occurs. This spatial heterogeneity reflects the selective nature of oxidation: edge sites with higher reactivity are

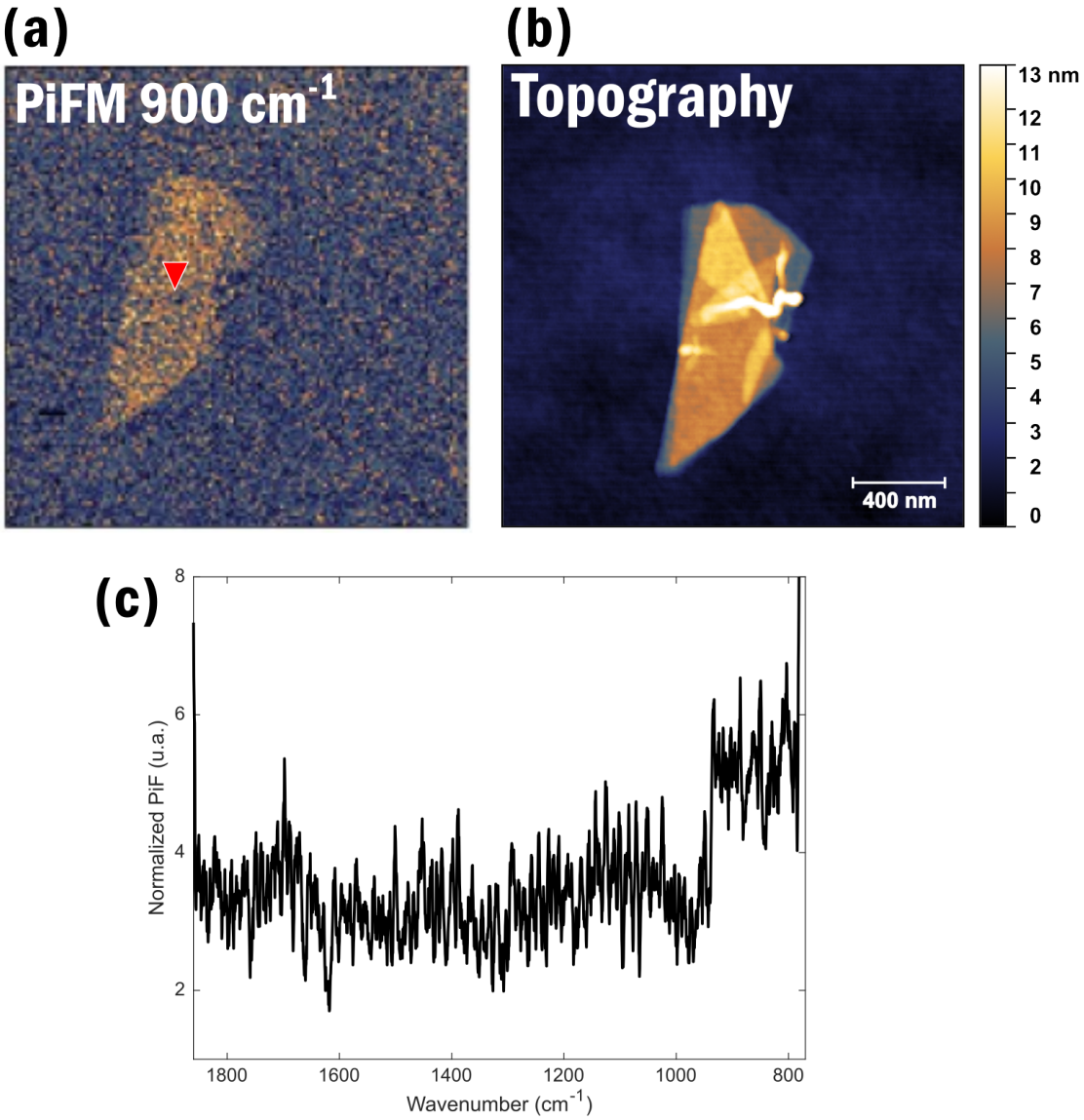

Figure 4.9: PiFM characterization of Nb_2CT_x: (a) Spectral image at 900 cm^{-1} showing signal on the MXene flake compared to the substrate. (b) Corresponding topography revealing a flake thickness of approximately 6 nm, indicating a stack of 2-3 monolayers. (c) PiFM spectrum acquired at the position marked by the red triangle on the topography.

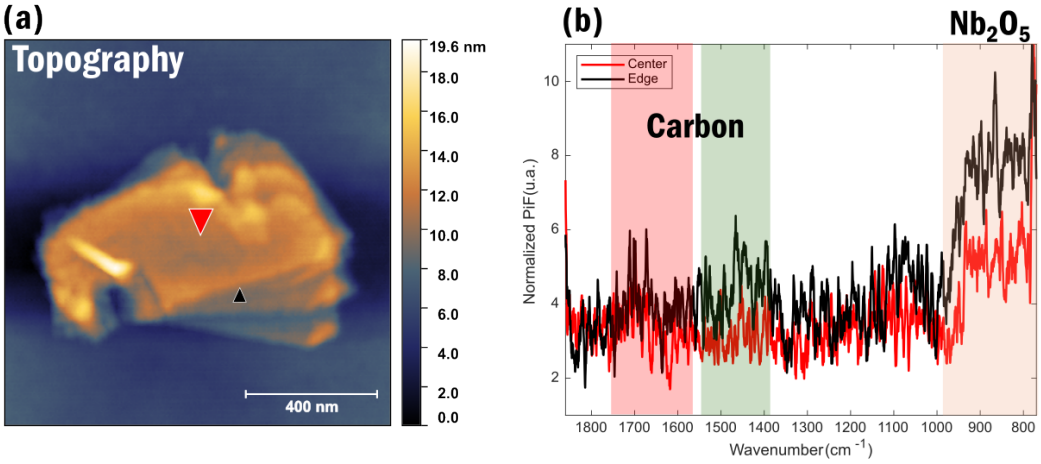

Figure 4.10: (a) Nb_2CT_x stack of 4 flakes with a thickness of 5 nm. (b) PiFM spectra acquired at the basal plane of MXene (red triangle) and at the edge (black triangle).

preferentially transformed, resulting in stronger carbon-related signatures in these regions than in more protected basal plane areas.

4.4 Nanoscale observation of siloxane compounds on titanium carbonitride MXenes

A key factor influencing the optical, electrical, and chemical properties of MXenes is their surface chemistry, which is largely dictated by the nature of their surface terminations. These terminations affect not only the intrinsic performance of MXenes but also play a crucial role in their interactions with other materials and their stability in different environments. Recent theoretical and experimental studies show that controlling MXene surface terminations [219] can lead to exceptional properties such as tuning the Fermi level [220], ferromagnetic behavior [221], and superconductivity [222].

MXenes require careful handling in a controlled laboratory environment due to the presence of surface functional groups that are inherent to their synthesis method. These surface terminations make them highly reactive to volatile chemical compounds in their environment, necessitating precise control of storage and handling conditions. Additionally, depending on the MXene type, they can exhibit varying degrees of susceptibility to oxidation. For instance, while $Ti_3C_2T_x$ demonstrates remarkable stability against oxidation under ambient conditions, other MXene compositions such as Ti_3CNT_x are significantly more prone to oxidative degradation, requiring stricter storage protocols and inert atmosphere handling [223]. The surface functional groups fundamentally determine the ability of MXenes to bind with chemical compounds such as the siloxane family, whether this interaction is intentional or unintentional. This binding capacity represents both an opportunity for controlled functionalization and a challenge for contamination control. In the case of siloxanes, MXenes are particularly promising candidates for binding with this family of compounds due to the presence of hydroxyl groups on their surface resulting from the selective etching synthesis method.

Siloxanes represent an excellent example of this environmental reactivity challenge. These organosilicon compounds are characterized by repeating silicon–oxygen (Si–O–Si) bonds and are found in industrial and consumer products due to their chemical stability, low surface tension, thermal resistance and volatility. Their volatility makes them applicable to quick-drying formulations as well as surface treatments in industrial and laboratory applications. Such compounds are ubiquitous in laboratory equipment, cleaning agents, cosmetic products, and ambient conditions, creating both functionalization opportunities and contamination risks [224–226]. Volatile methylsiloxanes (VMS), in particular the cyclic forms (cVMS), have attracted much attention due to their wide application and environmental persistence. These compounds are widely found in outdoor air and have concentrations up to thousands ng/m^3. In addition, elevated levels of cVMS in indoor air and biosolids have been reported, and toxicological studies showed low acute risks to aquatic life but mixed evidence of chronic toxicity to mammals [227].

Paradoxically, siloxane compounds can also be intentionally used to modify surface properties and enhance material performance. For example, silane treatments have been used to increase the stability of MXene against structural degradation due to oxidation [228], change the hydrophilicity of MXene to bind to the organic matrix/polymers for membrane preparation for enhanced water purification [229], and modify the surface potential of MXene flakes at neutral pH for advanced applications such as in situ self-assembled films [230]. This dual nature of siloxanes—as both contaminants and functional modifiers—underscores the critical importance of understanding and controlling their presence on MXene surfaces.

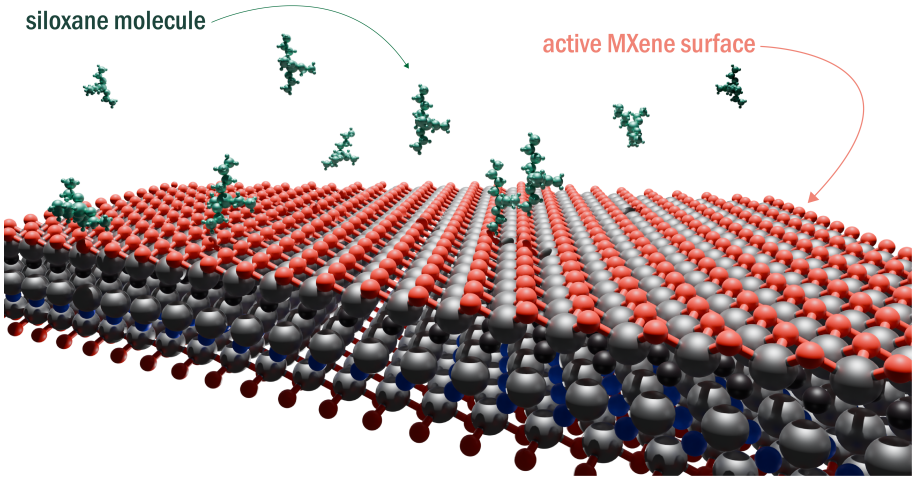

Figure 4.11: Schematic illustration of a mono-layer MXene with its active surface and siloxane compounds. The MXene structure shows the characteristic layered arrangement with surface terminations (red spheres representing oxygen atoms), while siloxane molecules (green structures) are depicted interacting with the active MXene surface sites.

In this context, characterizing surface chemistry is essential for advancing MXene research, including both the material's intrinsic surface terminations and compounds that can adsorb onto it, such as siloxanes. To address this challenge, high-resolution techniques capable of detecting and mapping surface chemistry at the nanoscale

are essential. Infrared photo-induced force microscopy (PiFM) [102, 135], a recent near-field infrared spectroscopy method combining impressive spatial resolution and chemical specificity [146], appears as a possible method to investigate the chemistry of the 2D MXene surfaces. This experimental approach was notably used in a previous communication [231], to map oxides and carbon defects in MXenes with nanoscale precision. Herein, we employ PiFM to identify and spatially map surface functional groups on two types of pristine carbonitride MXenes from the M_3X_2 family, namely: $Ti_3C_2T_x$ and $Ti_3C_{1.5}N_{0.5}T_x$. Besides their expected affinity with siloxanes, these two types exhibit complementary aspects: the carbonitride presents multilayer flakes, allowing us to study the influence of topography on surface chemistry, while the pure carbide is studied in monolayer form. Additionally, we characterize exposed MXene flakes which were stored in a closed chamber containing (3-Aminopropyl)triethoxysilane (APTES, 99%, Sigma-Aldrich) in liquid phase at atmospheric pressure and ambient air for several days (a schematic is available in the Appendix).

Results and discussion

4.4.1 $Ti_3C_{1.5}N_{0.5}T_x$ structural characterization

Morphological and structural analysis of $Ti_3C_{1.5}N_{0.5}T_x$ are shown in Figure 4.12. Figure 4.12(a) shows the electron beam image of this sample, while Figure 4.12(b) highlights the freeze-dried $Ti_3C_{1.5}N_{0.5}T_x$. Figure 4.12(c) presents the sample's topography, indicating overlapping flakes that form a stack with a total thickness of approximately 300 nm and (d) is a schematic representation of a $Ti_3C_{1.5}N_{0.5}T_x$ flake.

The corresponding XRD pattern is presented in Figure 4.13(a). The energy dispersive X-ray (EDS) (Figure 4.13(b)) spectrum confirms the presence of titanium with Kα at 4.51 eV and Kβ_1 at 4.93 keV, carbon with Kα_1 at 0.28 keV, and nitrogen with Kα_1 at 0.39 keV, while the signal at 1.49 keV arises from the aluminum contained in the substrate. These pristine MXene flakes, analyzed immediately after synthesis, serve as a baseline to characterize the native surface terminations of $Ti_3C_{1.5}N_{0.5}T_x$.

The corresponding X-ray diffraction patterns are presented in Figure 4.13(a), comparing the parent $Ti_3AlC_{1.5}N_{0.5}$ MAX phase (upper pattern) with the etched $Ti_3C_{1.5}N_{0.5}T_x$ MXene (lower pattern). The XRD analysis demonstrates successful Al layer removal and characteristic peak shifts indicating MXene formation, with the disappearance of the MAX phase peaks and the emergence of MXene-specific reflections at lower 2θ angles due to increased interlayer spacing. The energy dispersive X-ray (EDS) spectrum (Figure 4.13(b)) confirms the presence of titanium with Kα at 4.51 eV and Kβ_1 at 4.93 keV, carbon with Kα_1 at 0.28 keV, and nitrogen with Kα_1 at 0.39 keV, while the signal at 1.49 keV arises from the aluminum contained in the sample holder.

In addition to pristine MXene, aged MXene samples were prepared by exposing the same $Ti_3C_2T_x$ and $Ti_3C_{1.5}N_{0.5}T_x$ material to ambient laboratory conditions. This exposure led to surface contamination, primarily by siloxane species, as revealed by the presence of Si–C and Si–O–Si bonds in the PiFM analysis discussed later. The aged MXene provides a unique opportunity to study the influence of environmental siloxane adsorption on the surface chemistry of MXene. By comparing

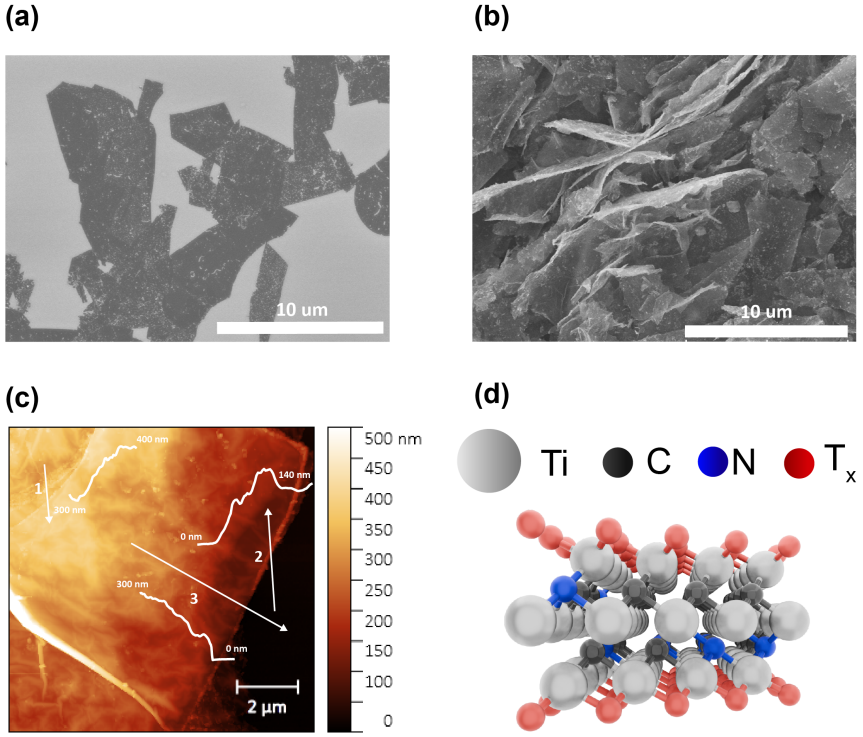

Figure 4.12: (a) Scanning electron microscopy (SEM) image of individual $Ti_3C_{1.5}N_{0.5}T_x$ flakes deposited on Al_2O_3 substrate. (b) SEM image of freeze-dried $Ti_3C_{1.5}N_{0.5}T_x$ powder displaying stacked flake structures. Image (c) corresponds to the atomic force microscopy (AFM) topography of aged $Ti_3C_{1.5}N_{0.5}T_x$ flakes. (d) Schematic of $Ti_3C_{1.5}N_{0.5}T_x$.

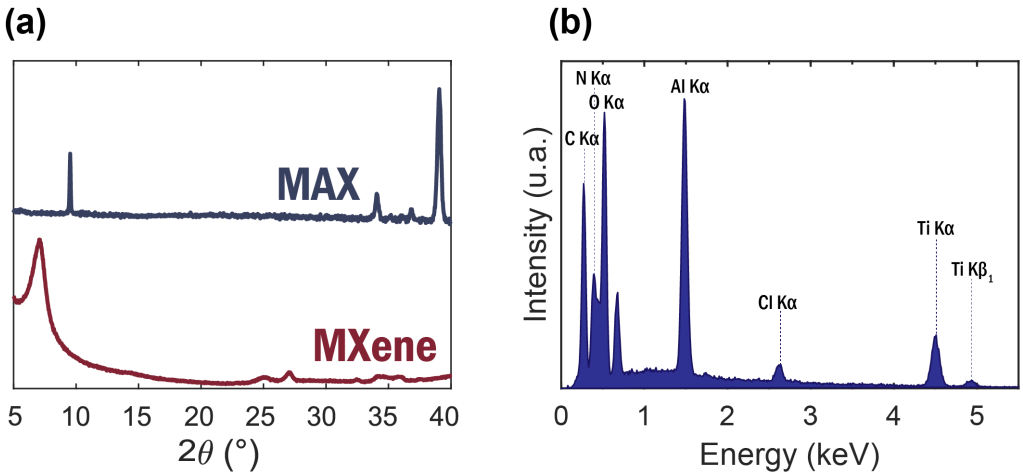

Figure 4.13: Structural analysis of $Ti_3C_{1.5}N_{0.5}T_x$ MXene flakes: (a) X-ray diffraction (XRD) patterns of $Ti_3AlC_{1.5}N_{0.5}$ MAX phase (upper pattern) with the etched $Ti_3C_{1.5}N_{0.5}T_x$ MXene (lower pattern). (b) Energy dispersive X-ray spectroscopy (EDS) spectrum of exposed $Ti_3C_{1.5}N_{0.5}T_x$.

the pristine and aged samples, we aim to elucidate the significant role of surface contaminants in modifying MXene properties and their potential implications for practical applications.

4.4.2 Far-field vibrational spectroscopy

The optical properties of MXenes probed by Raman spectroscopy have been extensively investigated in recent years, with comprehensive studies by Shevchuk et al. [114, 116] and Sarycheva et al. [100] establishing fundamental spectroscopic signatures for various MXene compositions and surface terminations. These investigations have revealed that Raman spectroscopy provides information into both the structural integrity of the MXene lattice and the nature of surface functional groups, making it an invaluable characterization tool for confirming material identity and assessing surface chemistry modifications. In our analysis, Raman spectroscopy serves as a complementary technique to validate the structural characteristics of our synthesized $Ti_3C_{1.5}N_{0.5}T_x$ and to investigate the potential presence of siloxane species on the MXene surface.

Raman analysis. The Raman spectrum can be deconvoluted into three distinct vibrational regions [100, 114] that reflect different structural components of the MXene: (i) very low frequencies below 200 cm^{-1} dominated by skeletal lattice modes governing the fundamental Ti–C–N framework dynamics, (ii) intermediate frequencies (200–600 cm^{-1}) characteristic of surface termination groups (-O, -OH, -F) that dictate surface chemistry and reactivity, and (iii) high frequencies above 600 cm^{-1} primarily associated with carbon-based vibrations and potential carbonaceous contaminants or structural defects within the MXene structure. Figure 4.14(a) reveals the characteristic vibrational fingerprint of the synthesized $Ti_3C_{1.5}N_{0.5}T_x$ across distinct spectral regions. Peak 1 at 200 cm^{-1} corresponds to the A_{1g} Ti–C symmetric vibration mode, representing the fundamental breathing motion of the titanium-carbon framework [100]. Surface termination groups manifest in the intermediate frequency domain through peaks 3 and 4: the E_g(O) vibration at 350 cm^{-1} and the A_{1g}(OH) vibration at 520 cm^{-1}, respectively, confirming the presence of oxygen and hydroxyl surface functionalities typical of solution-processed MXenes [114]. The higher frequency region exhibits carbon-related vibrational signatures, including the E_g in-plane carbon vibration at 620 cm^{-1} (peak 5) and the characteristic D and G carbon bands (peaks 7 and 8), indicative of both intrinsic MXene carbon atoms and potential carbonaceous impurities or structural disorder [232]. Peak 6 at 706 cm^{-1} corresponds to carbon vibrations [116]. Peak 7 at 875 cm^{-1} likely originates from titanium oxidation processes, as this feature intensifies with progressive MXene degradation [100].

FTIR analysis. Fourier Transform Infrared (FTIR) spectroscopy (Figure 4.14(b)) was performed on exposed $Ti_3C_{1.5}N_{0.5}T_x$ samples deposited on Al_2O_3 substrate using reflectance mode acquisition. The spectral data are presented as (1 − Reflectance) versus wavenumber to optimize visualization of the vibrational resonances. Despite relatively low signal intensity, three distinct absorption features were identified: Peak A, centered at 1000 cm^{-1}, is attributed to C–O and C–F stretching vibrations [113, 233, 234]. In titanium-based MXenes, $-O$ and $-F$ surface terminations are typically

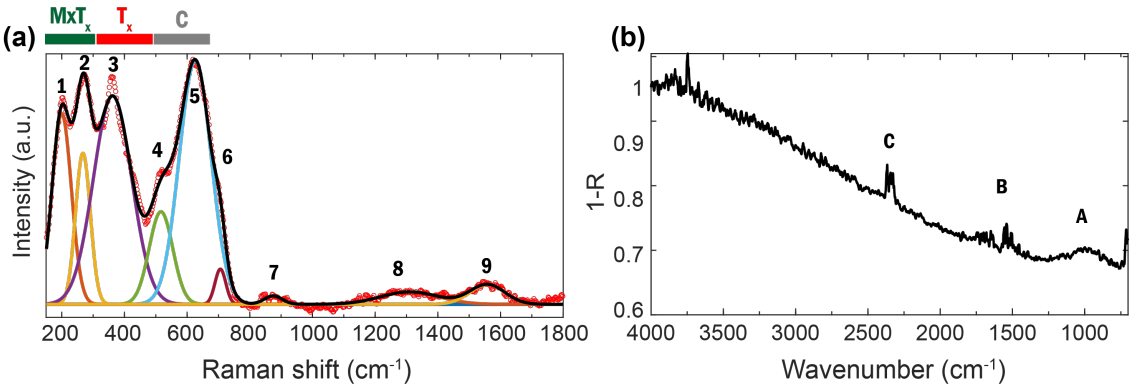

Figure 4.14: Vibrational spectroscopy of exposed $Ti_3C_{1.5}N_{0.5}T_x$ MXene flakes (stack of ∼100 nm thickness) on Al_2O_3 substrate, showing surface termination groups and structural characteristics. (a) Raman spectrum. Data points (circles) are fitted with multi-Gaussian peaks (black line) and deconvoluted into individual components (colored curves). (b) FTIR spectrum in reflexion normalized against the Al_2O_3 background, presented as (1 – Reflectance) versus wavenumber. The thick substrate (400 μm) results in zero transmission, necessitating reflectance measurements.

coordinated with the transition metal (Ti); however, infrared vibrational modes suggest that these species are bound to carbon. This observation can be explained by the degradation of the MXene structure. Specifically, over-etching may induce Ti vacancies, while oxidation processes can expose carbon layers, allowing them to react with oxygen and fluorine. Furthermore, residual MAX phase precursors could also be responsible for this signal. To validate these hypotheses, a detailed X-ray photoelectron spectroscopy (XPS) investigation is required. Peak B, observed at 1535 cm^{-1}, corresponds to N–O stretching modes, while Peak C at 2345 cm^{-1} is characteristic of C=O bonding vibrations [235]. The Raman and FTIR results obtained are characteristic of $Ti_3C_{1.5}N_{0.5}T_x$ flakes obtained by this synthesis process. These far-field measurements (Raman and FTIR) clearly highlight the presence of high-quality MXenes and show no evidence of other elements even on exposed MXenes to siloxane-compounds. To probe our materials at a finer scale, we employed photo-induced force microscopy (PiFM), described hereafter.

4.4.3 Local infrared properties

Near-field infrared microscopy, specifically photo-induced force microscopy (PiFM), was employed to investigate the surface chemistry of single- and few-layered MXene flakes. Due to the strong electromagnetic field confinement by the sharp tip, the probing volume extends to depths of approximately 10 nm [102, 146]. This high-resolution spectroscopic technique is particularly suitable for analyzing the complex surface chemistry of MXene materials. A power-modulated quantum cascade laser (770 - 1860 cm^{-1}) is focused at the sharp AFM tip apex using a parabolic mirror (NA = 0.9), creating a highly confined electromagnetic field. The intense near-field interaction between the tip and sample induces photomechanical forces [135], which modify the tip-sample interaction. The resulting mechanical oscillations of the platinum-coated silicon cantilever are detected by the feedback laser through a quadrant photodetector and lock-in amplifier system operating in sideband (hetero-

dyne) mode [102, 135].

Surface termination of pristine MXenes. For pristine $Ti_3C_{1.5}N_{0.5}T_x$, the PiFM spectrum represented by the black line on Figure 4.15(b), exhibits a characteristic band from 1000 to 1100 cm^{-1}, associated with C–O and C–F bonds [113, 236]. This PiFM peak was consistently observed across various MXene types investigated in this study. The peak is attributed to surface terminations (T_x) characteristic of MXene chemistry. Other PiFM spectra of pristine MXenes ($Ti_3C_2T_x$, V_2CT_x) can be found in the Section 4.2.

Siloxane detection on MXenes. Photo-induced force microscopy (PiFM) analysis revealing siloxane contamination on exposed $Ti_3C_{1.5}N_{0.5}T_x$ MXene surfaces. Considering the similarities between PiFM signals on organic materials and FTIR absorption spectra [144, 237], PiFM peaks can be attributed to molecular vibrations, analogous to FTIR. A discussion of the interpretation of the PiFM signal is provided in the following paragraph. The pristine $Ti_3C_{1.5}N_{0.5}T_x$ spectrum (black curve) exhibits a characteristic band from 1000–1100 cm^{-1} attributed to native MXene surface terminations (C–O and C–F bonds) [113, 233, 234]. Exposed $Ti_3C_{1.5}N_{0.5}T_x$ flakes, shown on Figure 4.15(b) exhibit a markedly different spectral signature, with four distinct peaks distributed uniformly across the flake surface. The peaks at 820 cm^{-1} and 1260 cm^{-1} are attributed to Si–C stretching vibrations, while those at 1020 cm^{-1} and 1100 cm^{-1} correspond to Si–O–Si stretching vibrations [238, 239]. Although silicon is not intrinsically present in this MXene, the detection of silicon- and oxygen-containing chemical species strongly indicates siloxane contamination [240]. Measurement locations were strategically selected across different areas of the sample, as indicated by the four squares (1–4) in Figure 4.15(a). While the point spectra exhibit high consistency in peak positions and intensities, the corresponding PiFM maps reveal subtle contrasts that appear to correlate with topographic variations. This observation suggests that the chemical composition in "curved" or highly morphological regions may deviate slightly from that of the flat terraces, possibly due to localized accumulation or strain-induced surface chemistry changes. The substrate spectrum (green, acquired on bare Al_2O_3 without MXene) shows no siloxane-related features, confirming selective binding to MXene surfaces.

This spectral pattern is well-established in the literature as being characteristic of siloxane compounds [238]. The infrared spectrum of the dimethoxydimethylsilane oligomer, shown in Figure 4.16(c), exhibits strong similarities to the PiFM spectrum of exposed $Ti_3C_{1.5}N_{0.5}T_x$ MXene (orange line, extracted from Figure 4.15). The black line corresponds to a FTIR reference spectrum of dimethoxydimethylsilane oligomer from [238]. The excellent correspondence provides definitive spectroscopic evidence for siloxane contamination, with peak assignments detailed in Table 4.1. This Table 4.1 provides a detailed analysis of the peak assignments, summarizing the correspondence of the various peaks related to siloxane, their origins, and specifying whether they correspond to silane or siloxane species [238, 239].

MXenes, featuring highly reactive surface terminations (–OH groups), are particularly susceptible to interactions with the Si–OH groups present in siloxane species.The proposed mechanism is consistent with what is proposed by Riazi et al. [230], which involves the reaction between MXene's –OH groups and silicon atoms in siloxane compounds, resulting in stable bond formation. The signals as-

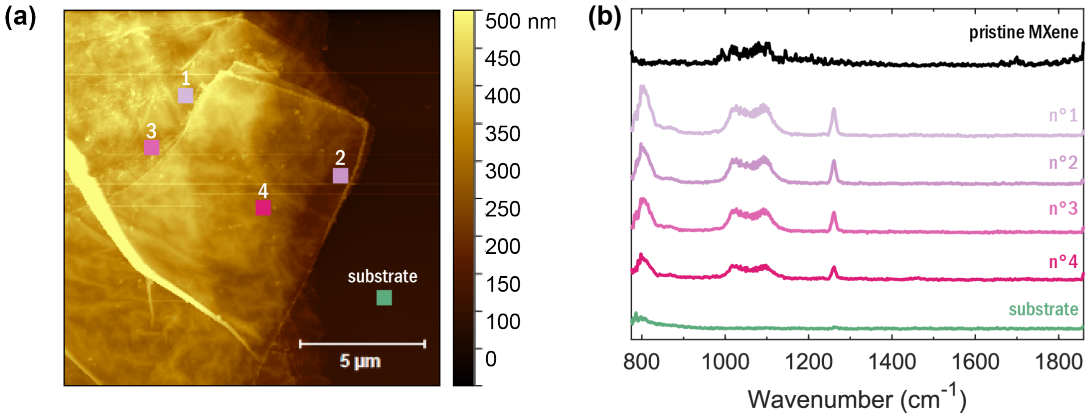

Figure 4.15: Photo-induced force microscopy (PiFM) analysis revealing siloxane contamination on exposed $Ti_3C_{1.5}N_{0.5}T_x$ MXene surfaces. (a) AFM topography of exposed $Ti_3C_{1.5}N_{0.5}T_x$ flakes showing the measurement locations.(b) Comparative PiFM spectra acquired at 1 cm^{-1} steps with 30 s acquisition time per point. The pristine $Ti_3C_{1.5}N_{0.5}T_x$ spectrum (black curve) exhibits a characteristic band from 1000–1100 cm^{-1} attributed to native MXene surface terminations (C-O and C–F bonds). Exposed $Ti_3C_{1.5}N_{0.5}T_x$ spectra acquired at four different locations (colored squares 1–4) across the flake surface show consistent spectral signatures with four distinct siloxane-related peaks.

sociated with Si–O–Si and Si–C bonds are notably absent at the green acquisition point/spectrum (Figure 4.15(b)), which corresponds to the substrate (Al_2O_3). This observation highlights the reactivity of the MXene due to its surface chemistry, as no grafting occurs on the substrate.

Siloxane compounds (Figure 4.16), characterized by the presence of silanol group (Si–OH), exhibit high reactivity toward the hydroxyl functionalities (–OH) that terminate the basal planes of MXene structures. The covalent attachment [230] occurs via a dehydration condensation mechanism, wherein the nucleophilic oxygen of the MXene's hydroxyl termination attacks the electrophilic silicon center of the silanol group. This reaction proceeds with the concomitant elimination of a water molecule, yielding a Ti-O-Si linkage at the MXene-siloxane interface.

The condensation reaction between siloxanes and MXene surface hydroxyl groups proceeds through a nucleophilic substitution mechanism [241]. In this process, the oxygen atom in the MXene surface hydroxyl group (Ti–OH) acts as a nucleophile, attacking the silicon atom in the silanol group (Si-OH). This nucleophilic attack forms a pentacoordinate silicon intermediate state. The reaction proceeds with the elimination of a water molecule, resulting in the formation of a Ti-O-Si covalent bond.

The general reaction is:

$$\text{Ti-OH} + \text{HO-Si(R)}_3 \rightarrow \text{Ti-O-Si(R)}_3 + \text{H}_2\text{O} \tag{4.2}$$

where R represents organic substituents on the siloxane molecule [241]. This type of condensation reaction is thermodynamically favorable under ambient conditions, which explains the spontaneous binding of siloxanes to MXene surfaces upon exposure to environments containing siloxane compounds. The reaction is particularly favorable when catalyzed by trace amounts of acids [242], which can be present as

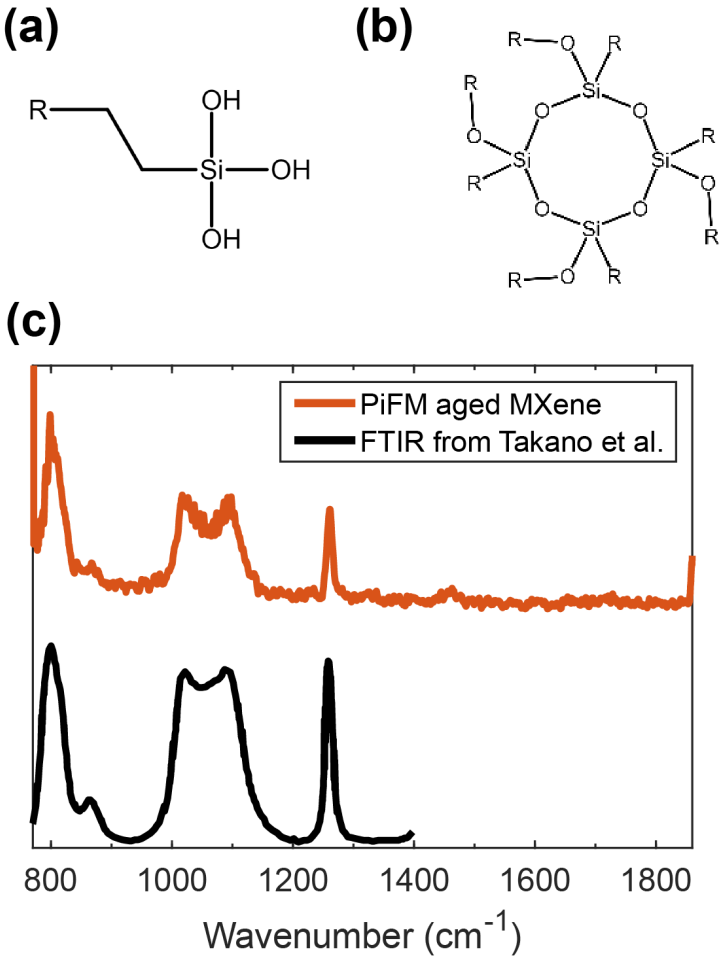

Figure 4.16: Lewis structures of (a) linear Si–O–Si configuration and (b) cyclic Si–O–Si arrangement. (c) Comparative infrared spectroscopy validating siloxane identification. The reference FTIR spectrum of dimethoxydimethylsilane oligomer (black line, re-digitized from Takano et al. [238]) exhibits four characteristic absorption peaks at 800, 1020, 1090, and 1260 cm^{-1} corresponding to different siloxane vibrations.

Table 4.1: Peak analysis based on wavenumbers and corresponding vibrational assignments. [238, 239]

Wavenumber (cm^{-1})	**Assignment / Vibration**
800 – 850	Dimethylsilane: Si – C stretching vibration
1020 – 1050	Linear siloxane: Si – O – Si stretching vibration (linear chain)
1050 – 1080	4-membered siloxane: Si – O – Si stretching vibration (4-membered chain)
1080 – 1090	Macro-cyclic siloxane: Si – O – Si stretching vibration (large ring)
1250 – 1260	Methylsilane: Si – C stretching vibration

residual species from the MXene synthesis process. The resulting Ti-O-Si linkages create a robust interface that can significantly alter the surface properties of MXenes, including their wettability, chemical reactivity, and electronic characteristics [228, 229]. This binding mechanism is similar to silane coupling reactions widely utilized in surface modification of metal oxides and plays a crucial role in the aging behavior observed in MXene materials exposed to siloxane-containing environments.

4.4.4 Spectral mapping

The PiFM spectral images on Figure 4.17 were acquired at four distinct wavenumbers (820, 1020, 1100 and, 1260 cm^{-1}) providing insight into the spatial distribution of specific chemical bonds across the exposed $Ti_3C_{1.5}N_{0.5}T_x$ flakes. These spectral maps reveal the presence of siloxane-related chemical bonds distributed across the MXene surface, reflecting its surface chemistry and reactivity. The spectral map at 820 cm^{-1} (Figure 4.17(a)) highlights regions with pronounced Si–C bonds, distributed predominantly along the surface of the MXene flake. This uniform presence on the flake suggests that Si–C bonds are formed primarily due to siloxane contamination adhering to the MXene surface. The 1260 cm^{-1} (Figure 4.17(d)) map corresponds to Si–C stretching vibrations and displays an intensity profile consistent with the 820 cm^{-1} map. This spectral match suggests that Si–C bonds are similarly distributed across the flake, with no significant variation in intensity across the surface. The 1020 cm^{-1} map (Figure 4.17(b)) indicates a similar spatial pattern, corresponding to Si–O–Si vibrations. The signal is distributed across the MXene flake, further confirming the presence of siloxane species.

The consistency of this signal across the surface, but its absence at the substrate, reinforces the chemical interaction between the reactive –OH terminations of MXene and the siloxane contaminants. The spectral map at 1100 cm^{-1} (Figure 4.17(c)), also attributed to Si–O–Si bonds, demonstrates a comparable distribution to the 1020 cm^{-1} map. The overlap between the 1020 cm^{-1} and 1100 cm^{-1} maps strengthens the evidence for siloxane contamination. The signal's distribution across the flake indicates that siloxane species are likely adsorbed or chemically bonded to the MXene surface through a reaction involving –OH groups, although signal variations may result from the formation of siloxane compound agglomerates, as described by Sypabekova et al. [243].

The siloxane compound signal is detected in addition to C–O and C–F vibrations,

as shown in the previous section. Control measurement at 1330 cm^{-1} presented on Figure 4.17(e) shows a negligible signal across the entire scan area. This frequency was set as it does not correspond to any siloxane absorption peak. Notably, dark regions in all spectral maps correspond to the Al_2O_3 substrate areas where no siloxane signals are detected, demonstrating selective binding of siloxane species to MXene surfaces rather than the substrate. The consistent spatial correlation between all four siloxane vibrational modes, combined with the absence of signal at non-resonant frequencies, provides strong evidence for uniform environmental siloxane adsorption across the entire MXene basal plane surface.

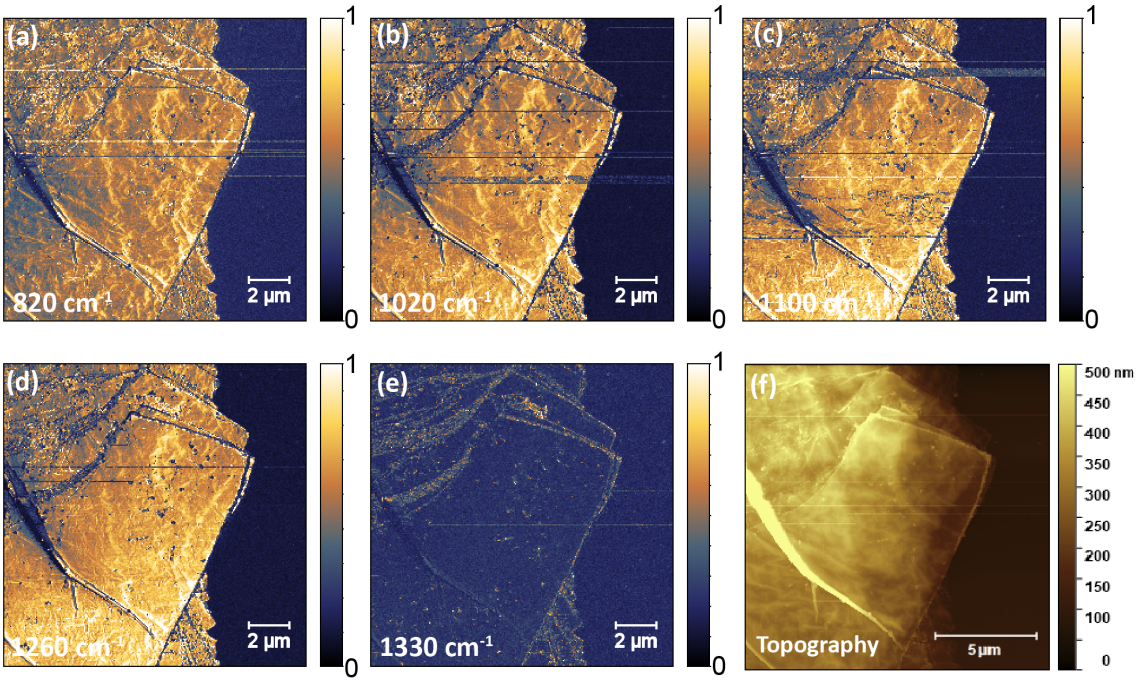

Figure 4.17: Spatial distribution mapping of siloxane contamination on exposed $Ti_3C_{1.5}N_{0.5}T_x$ MXene flakes using PiFM spectral imaging. PiFM images acquired over a 10×10 μm scan area at 256×256 pixel resolution with a scan rate of 0.7 lines/sec, showing the spatial distribution of siloxane-related vibrational modes: (a) 820 cm^{-1} (Si–C stretching), (b) 1020 cm^{-1} (Si–O–Si stretching), (c) 1100 cm^{-1} (Si–O–Si stretching), and (d) 1260 cm^{-1} (Si–C stretching). (e) Control measurement at 1330 cm^{-1}, a frequency that does not correspond to any siloxane absorption peak. The color scale has been optimized to highlight the signal distribution. (f) Simultaneously acquired AFM topography showing the flake morphology and thickness variations.

Siloxane detection on mono-layers. Concerning the exposed single flake $Ti_3C_2T_x$ shown in Figure 4.18, the results consistently revealed the presence of siloxane-related chemical bonds uniformly distributed across the MXene surfaces (Figure 4.18(a-d)), with no significant variation in signal intensity or spatial distribution. Even when a mono-layer was probed, the siloxane was still detectable, which highlights the technique sensitivity.

The acquisition of spectrum n°3 presented in Figure 4.18(g) was performed on a slightly thicker region that indicates a restacked area of 2-3 layers (Figure 4.18(e)).

Remarkably, the signal intensity remains identical to the spectra acquired at locations 1 and 2 on monolayer regions. This observation allows us to hypothesize that the siloxane contamination deposits only on the surface and not between the layers, otherwise we would observe a significantly higher signal for the multilayer stack. This finding suggests an interesting strategy for MXene storage to avoid contamination: maintaining them in multilayer form (without delamination) could provide natural protection against environmental contaminants by minimizing the exposed surface area.

Furthermore, by comparing results from stacked and single flake MXenes, no siloxane response was detected on MXene stack edges. Indeed, siloxane binds with -OH terminations, which are present mainly on the MXene surface rather than at the edges. Results are similar to $Ti_3C_{1.5}N_{0.5}T_x$ MXene flakes shown in Figure 4.17. Additionally, a reference spectral image (Figure 4.18(f)) has been acquired at 981 cm^{-1}, a frequency that does not correspond to any known siloxane vibrational mode, showing negligible signal across the entire flake surface. This control measurement confirms the chemical specificity of the siloxane detection.

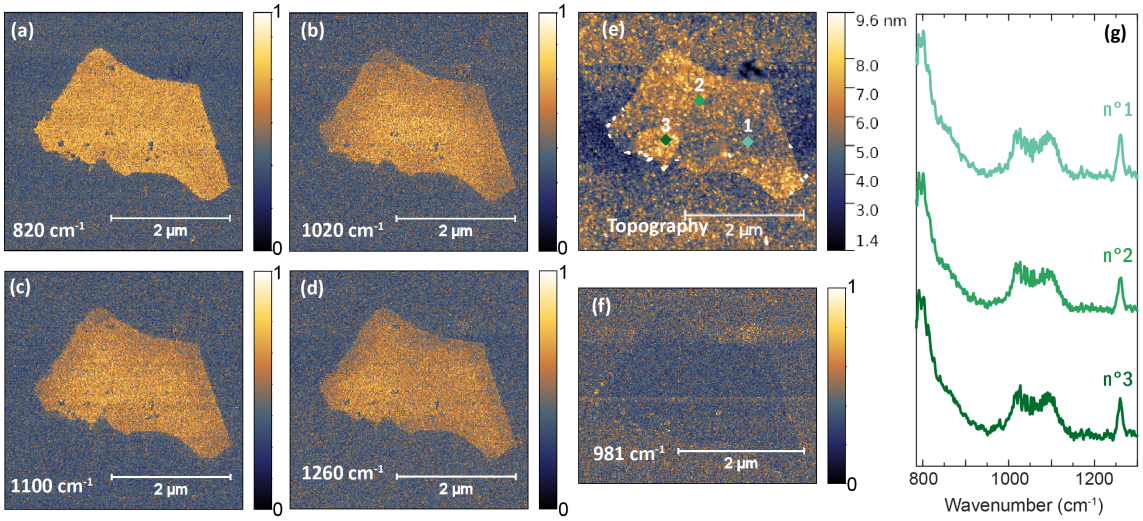

Figure 4.18: PiFM spectral imaging of siloxane contamination on exposed $Ti_3C_2T_x$ monolayer. PiFM images acquired over a 10×10 μm scan area at 256×256 pixel resolution showing the spatial distribution of siloxane-related vibrational modes on a single $Ti_3C_2T_x$ flake: (a) 820 cm^{-1} (Si–C stretching), (b) 1020 cm^{-1} (Si–O–Si stretching), (c) 1100 cm^{-1} (Si–O–Si stretching), and (d) 1260 cm^{-1} (Si–C stretching). (e) Simultaneously acquired AFM topography highlighting the monolayer thickness (∼1.4 nm) characteristic of single $Ti_3C_2T_x$ flakes. (f) Control measurement at 981 cm^{-1}, a frequency between siloxane absorption peaks. The color scale has been optimized to highlight the signal distribution. (g) Representative PiFM spectra acquired at three different locations (numbered 1, 2, and 3 on image e) across the MXene surface.

Specific adhesion to the basal plane. Figure 4.19 corresponds to a closer view of the edge of the exposed $Ti_3C_{1.5}N_{0.5}Tx$ flakes, showing that the intensity at 820 cm^{-1} is significantly lower at the edges (red region), approximately 250 μV compared

to the surface (green region) where it measures approximately 350 μV. Similarly, at 1020, 1100, and 1260 cm^{-1}, the intensity at the edges is roughly 250 μV while at the surface it reaches 450 μV. This substantial intensity difference (∼40% reduction at edges) suggests for the preferential binding of siloxane compounds to surface hydroxyl (-OH) terminations located on the basal planes rather than at the flake edges.

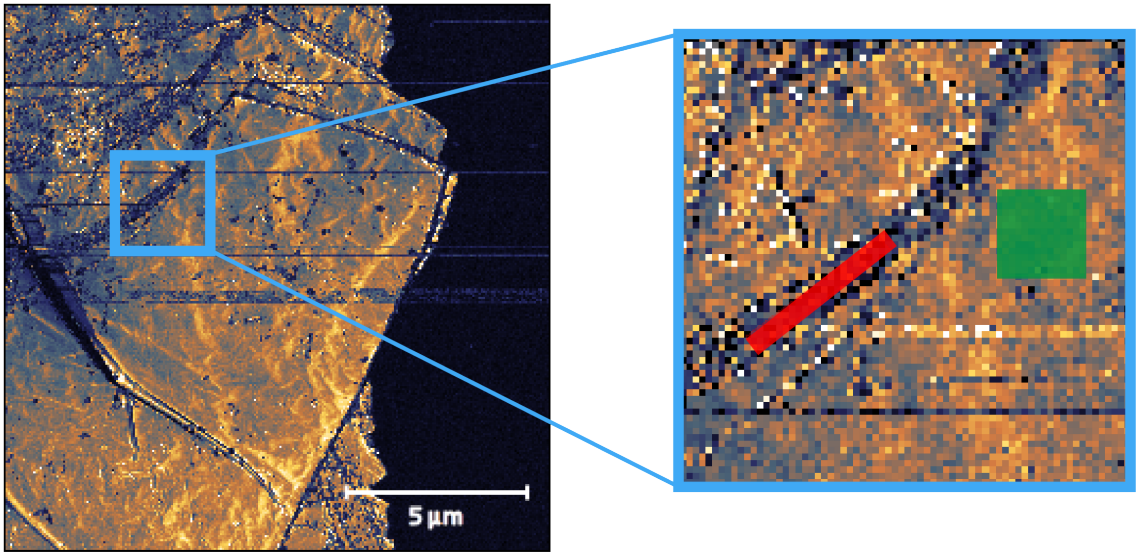

Figure 4.19: Analysis of siloxane distribution at MXene flake edges revealing preferential surface binding. Left image shows the combined PiFM signal (sum of all four siloxane-related frequencies: 820, 1020, 1100, and 1260 cm^{-1}) over the full 10×10 μm scan area (256×256 pixels) from Figure 4.17. The blue box indicates the region selected for detailed edge analysis. Right image presents a zoomed-in view of the MXene stack edge extracted from the initial image, showing the spatial distribution of siloxane contamination. The step height measured from the topography indicates a stack thickness of approximately 100 nm. Color-coded regions highlight the significant difference in siloxane signal intensity: the red region represents the flake edges with lower average signal intensity, while the green region corresponds to the basal plane surface with higher average signal intensity.

The preferential binding to -OH terminated surfaces rather than edges can be attributed to several factors. First, the density of -OH terminations is typically higher on the basal planes of MXene flakes due to the etching process used during synthesis, which preferentially removes A-layer atoms and creates vacancy sites that are subsequently terminated with -OH groups [8, 81]. The absence of siloxane signals at the edges suggests that these regions may either possess different terminal groups (such as -F or -O) or have a lower density of active sites for siloxane binding. The uniform distribution of siloxane across the surface of single flakes, including mono-layers, suggests that environmental exposure leads to consistent surface modification regardless of flake thickness. The high sensitivity of PiFM in detecting siloxane even on mono-layers demonstrates the technique's utility for studying surface modifications of 2D materials at the nanoscale. This capability is particularly valuable for understanding aging mechanisms and environmental interactions of MXenes, which are known to impact their performance in various applications significantly.

To further validate the APTES spectral signature, we performed controlled functionalization experiments on pristine silicon wafer using PiFM analysis. Freshly cleaned Si wafers exhibited no detectable spectral features within the investigated frequency range. Following APTES functionalization via vapor-phase deposition under vacuum conditions, the treated wafer displayed characteristic vibrational peaks consistent with those observed on exposed MXene samples. This control experiment confirms that the detected signals originate from APTES molecules. Detailed experimental procedures and comparative spectra are provided in the Appendix.

Interpretation of the PiFM signal. The spectroscopic contrast in our PiFM measurements reflects the photo-absorption properties of MXene materials at the nanoscale. The close correspondence between our PiFM spectra and literature FTIR data indicates that the effective polarizability remains approximately constant across the investigated frequency range. Under these conditions, the PiFM signal is dominated by photo-absorption mostly reflecting the imaginary part of the sample's dielectric function ($Q(z) \propto \varepsilon''$) [244]. This relationship enables simpler chemical identification, as the spectroscopic contrast correlates with the material's intrinsic vibrational modes. The theoretical framework and mathematical derivations supporting this interpretation are provided in the Chapter 2.

Conclusion

In conclusion, we showed that PiFM is capable of detecting and mapping surface functional groups on pristine $Ti_3C_2T_x$ and pristine $Ti_3C_{1.5}N_{0.5}T_x$. Futhermore, siloxane compounds are detected on the corresponding aged MXene surfaces with nanoscale precision. The detected Si—C and Si-O-Si vibrational modes confirm the presence of siloxane species uniformly distributed across MXene flakes, highlighting their high reactivity due to surface –OH terminations. In contrast, conventional techniques (Raman, FTIR, and EDS) did not reveal any evidence of siloxane contamination on the same sample. This illustrates the superior sensitivity and spatial resolution of PiFM, making it uniquely capable of detecting nanoscale contaminants that are otherwise invisible to bulk or traditional surface characterization methods. Additionally, the Al_2O_3 substrate remained chemically inert, pointing out the selective nature of siloxane adsorption on MXenes. The sources of contamination likely include laboratory environments (e.g., handling tools, solvents, or ambient siloxanes) or could also arise from storage environment. These findings emphasize the importance of contamination control in experimental workflows involving MXenes, particularly for applications where surface chemistry is crucial, such as in electrochemical energy storage, catalysis, or sensing. These findings emphasize the importance of contamination control in experimental workflows involving MXenes. While this chapter has provided critical insights into MXene surface chemistry and contamination detection at the nanoscale, the identified siloxane-MXene interactions also present intriguing opportunities for practical applications. Building on these fundamental findings, the following chapter explores how MXenes can be integrated into functional sensing platforms using surface plasmon resonance (SPR) technology. Chapter 5 demonstrates the real-time monitoring of MXene thin-film deposition processes and investigates the detection capabilities for (3-Aminopropyl)triethoxysilane

(APTES), directly applying the surface chemistry insights gained from our PiFM analysis.

Chapter 5

Application of MXene for sensing using Surface Plasmon Resonance

5.1 MXene thin-film deposition monitored by SPR 123

5.1.1 Current Methods for MXene Film Fabrication 123

5.1.2 Microfluidic-Assisted Deposition of MXene Films Monitored by SPR 124

5.1.3 MXene film deposition via controlled sedimentation 126

5.1.4 Determination of the dielectric constant of MXene 131

5.2 (3-Aminopropyl)triethoxysilane detection using MXene 134

Surface Plasmon Resonance (SPR) has emerged as a powerful optical sensing technique with remarkable sensitivity for detecting changes at metal-dielectric interfaces [245]. Since its first demonstration for biosensing applications in the early 1980s [246], SPR has revolutionized label-free, real-time detection across fields ranging from biochemistry and pharmaceutical research to environmental monitoring and food safety [247]. The fundamental principle of SPR relies on the collective oscillation of free electrons (plasmons) at the interface between a metal film and a dielectric medium when excited by incident light under specific conditions (incidence angle and wavelength) [248].

The Kretschmann configuration, which couples incident light with surface plasmons on a thin metal film using attenuated total reflection through a prism [249], and the Otto configuration, in which a tiny gap separates the prism from the metal surface [250], are the two main configurations that have been established for SPR excitation. Due to its advantages in practical implementation and increased sensitivity for sensing applications, the Kretschmann arrangement has become widely used [251].

Fundamental approach of surface plasmon

Surface plasmons are collective oscillations of the free electron gas at the metal-dielectric interface, which propagate as surface waves along this boundary [252]. These surface plasmon polaritons (SPPs) represent coupled excitations of electromagnetic waves and electron density oscillations. For a single metal-dielectric inter-

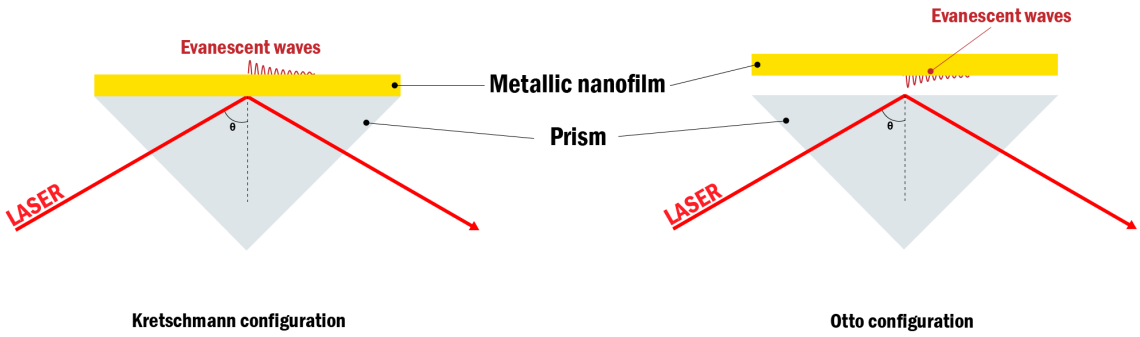

Figure 5.1: Schematic showing Kretschmann and Otto SPR configurations.

face, the SPP is characterized by a parallel wavevector component k_{sp} (or propagation constant) given by:

$$k_{sp} = \frac{\omega}{c}\sqrt{\frac{\varepsilon_m \varepsilon_d}{\varepsilon_m + \varepsilon_d}} = k_d\sqrt{\frac{\varepsilon_m}{\varepsilon_m + \varepsilon_d}} \tag{5.1}$$

where ω is the angular frequency, c is the speed of light, ε_m is the dielectric constant of the metal which is mostly negative and ε_d is the real and positive dielectric constant of the probed medium[253]. Since ε_m and ε_d have opposite real parts, the propagation constant of the SPP along the surface k_{sp} typically exceeds the value of the free space wavevector in the dielectric k_d.

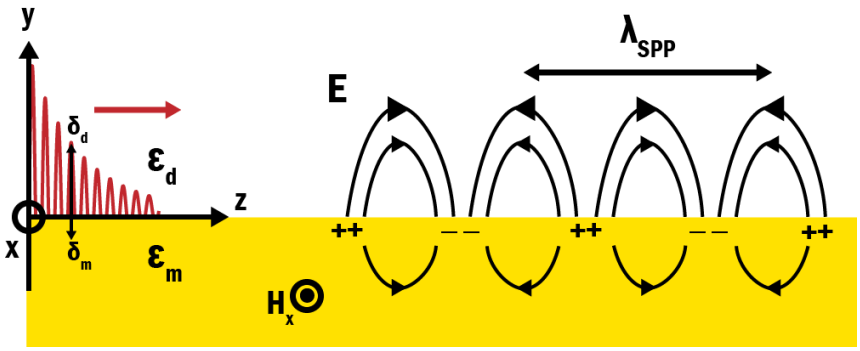

Figure 5.2: Illustration of surface plasmon wave propagation at a metal-dielectric interface. Left: Exponential decay of the electromagnetic field into both the dielectric medium (δ_d) and the metal (δ_m), with respective dielectric constants ε_d and ε_m. Right: Distribution of the electromagnetic field components showing the electric field (E) loops and magnetic field (H_x) perpendicular to the propagation direction. The wavelength of the surface plasmon polariton (λ_{SPP}) is indicated above.

As a result of the momentum mismatch between the radiation optical wave and surface plasmons, surface plasmons cannot be excited by direct excitation. The Kretschmann configuration overcomes this limitation by using a third medium: a high refractive index prism (glass or quartz) used to increase the momentum of incident photons, enabling SPP excitation when the in-plane component of the photon wavevector matches the SPP wavevector at the metal-dielectric interface [254]. This resonance condition occurs near a specific incident angle (so-called SPR angle, or Kretschmann angle, usually expressed in °), resulting in a characteristic dip in the reflected light intensity.

More precisely, in the Kretschmann configuration, a thin metal film (typically 40–50 nm of gold in the visible range) is sandwiched between two dielectrics—the prism and the analyte medium—forming a three-layer system. For sufficiently thin films, the SPPs at the two interfaces couple, giving rise to either a symmetric mode (in-phase coupling) or an antisymmetric mode (out-of-phase coupling). In both cases, the field inside the metal results from the superposition of contributions from both interfaces [255]. In the Kretschmann setup, the prism has a higher refractive index than the analyte. The antisymmetric mode, which exhibits a smaller k_{sp}, becomes leaky: it radiates within the prism. This leaky nature allows the mode to be efficiently excited by incident radiation from the prism.

As mentioned before, the optimal coupling occurs at the Kretschmann angle, above the critical angle defined by the refractive indices of prism and the dielectric. The field intensity $I(z)$ of the evanescent wave generated in the analyte is expressed as a function of distance z from the interface:

$$I(z) = I(0)e^{-z/d_p} \tag{5.2}$$

where d_p is the penetration depth, given by:

$$d_p = \frac{\lambda}{4\pi}\left(n_p^2 \sin^2\theta - n_d^2\right)^{-1/2} \tag{5.3}$$

with λ the wavelength of incident light, n_p the refractive index of the prism, θ the incident angle, and n_d the refractive index of the dielectric medium [256]. In our configuration, $d_p = 83.2\ nm$ ($n_p = 1.54$, $n_d = 1.33$, $\theta = 65$, $\lambda = 680$ nm).

The evanescent field couples with surface plasmons at the resonance condition, which makes the SPR phenomenon highly sensitive to changes in the refractive index within this penetration depth. This high sensitivity forms the foundation for SPR sensing applications, enabling detection of molecular binding events and structural changes at the interface [257].

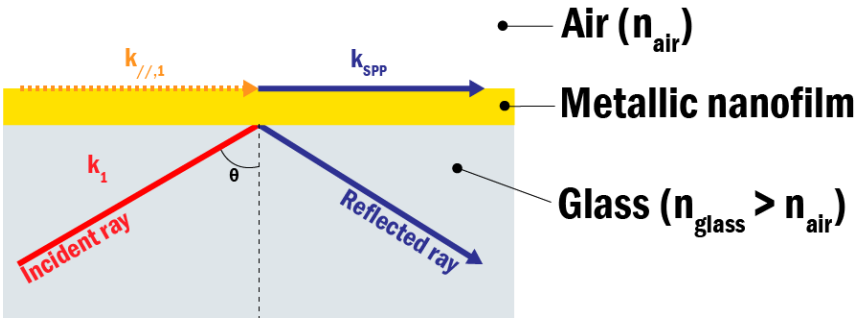

Figure 5.3: Schematic representation of Surface Plasmon Resonance excitation in the Kretschmann configuration. An incident light beam (k_1) at angle θ_1 passes through a high refractive index prism ($n_{glass} > n_{air}$). When the parallel component of the incident wavevector ($k_{//,1}$) matches the surface plasmon propagation constant (k_{SPP}) at the metal-air interface, resonance occurs, resulting in a characteristic dip in the reflected light intensity.

Phase-Sensitive SPR detection

Conventional SPR systems primarily monitor intensity or amplitude ($I \propto A^2$) changes in the reflected light, measuring either the resonance angle shift or the reflectivity change at a fixed angle [258]. Beyond this approach, phase-sensitive SPR measurement has emerged as a powerful technique offering significant advantages for ultrasensitive detection [259].

When light interacts with surface plasmons near the resonance condition, it undergoes not only amplitude attenuation but also a sharp phase shift. This phase change occurs over a narrower angular range compared to amplitude variations, providing enhanced measurement sensitivity [260]. The relationship between phase shift ϕ and incident angle θ near resonance can be approximated by:

$$\phi(\theta) \approx \phi_0 + \frac{\pi}{2} - \arctan\left(\frac{\theta - \theta_{SPR}}{\Gamma/2}\right) \tag{5.4}$$

where ϕ_0 is a constant phase term, θ_{SPR} is the resonance angle, and Γ is the angular width of the resonance [261].

In this project, we use the IPSOLAB compact SPR system from Phase Lab Instrument, which integrates amplitude and phase detection capabilities (Figure 5.6) [262]. This system utilizes interferometric techniques to achieve simultaneous monitoring of both amplitude and phase changes with high stability and resolution. Phase detection techniques can achieve detection limits 2-3 orders of magnitude better than amplitude-based approaches for the same experimental setup [263]. This notable enhancement results from the phase changes' intrinsically sharper responsiveness to changes in refractive index as well as the diminished impact of background noise and intensity fluctuations [264].

The phase information provides additional data to amplitude measurements, which enables a higher sensitivity and a better comprehension of the binding events [30]. As shown experimentally, when the refractive index of the sensing medium changes, the phase shift exhibits a much steeper dependence on the incident angle than the corresponding intensity change, particularly near the resonance condition. This steeper transition translates directly into improved signal-to-noise ratio and lower detection limits for subtle biomolecular interactions [259].

Gold is the predominant metal for SPR applications due to its favorable optical properties, excellent chemical stability, and biocompatibility [265]. However, various alternative metals have been investigated for specialized SPR sensing applications, each of them offer unique advantages for specific detection scenarios. For instance, silver films exhibit sharper resonance peaks and higher sensitivity than gold, which leads to a lower detection limits, but their high susceptibility to oxidation has limited widespread adoption [266]. Copper is also another alternative to gold with good SPR performance, particularly when protected by appropriate surface modifications or overlayers such as MXene to prevent oxidation [267]. As demonstrated by Wu et al., copper-based SPR sensors coated with 9 layers of $Ti_3C_2T_x$ MXene can achieve sensitivity enhancements of up to 33.6%, making them economically attractive options for certain applications [267].

The strategic selection of plasmonic metals must balance considerations of sensitivity, stability, cost, and specific analyte requirements. While gold remains the standard choice for most biosensing applications, the integration of alternative met-

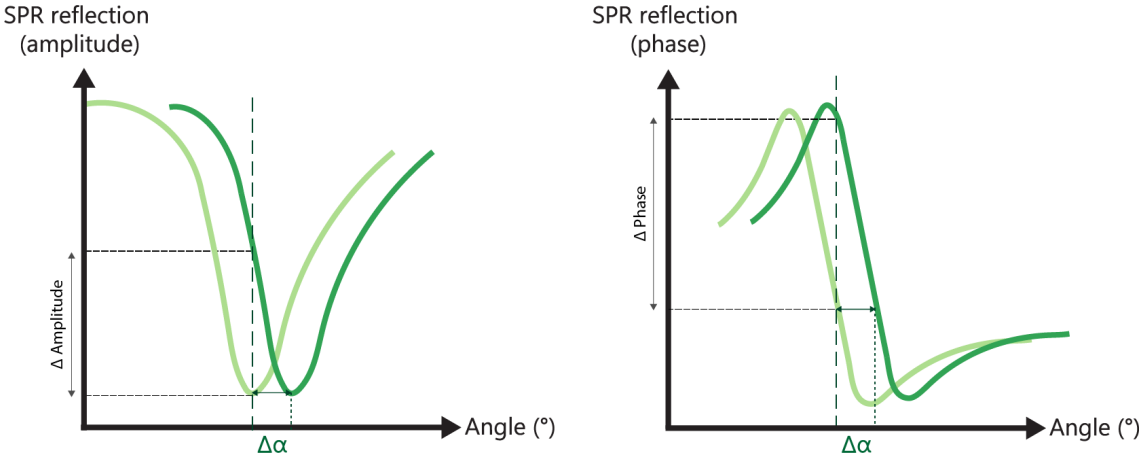

Figure 5.4: Comparison between amplitude and phase responses in SPR sensing. Left: Reflectivity (amplitude) curves showing the characteristic resonance dip shift ($\Delta\alpha$) in response to a change in the refractive index at the sensing interface. Right: Corresponding phase response curves for the same refractive index change, demonstrating the steeper transition in phase compared to amplitude. The same angular shift ($\Delta\alpha$) produces a more pronounced change in the phase signal than in the amplitude signal.

als with protective layers such as MXene opens promising pathways for specialized and economically viable SPR sensing platforms.

2D materials for enhanced SPR

In order to improve SPR performance, recent developments in materials science have concentrated on combining two-dimensional (2D) materials with gold sheets [268]. Remarkable gains in sensitivity, detection limits, and selectivity have been shown when atomically thin 2D materials with plasmonic structures are integrated [269]. 2D materials such as graphene [270], transition metal dichalcogenides [271], and black phosphorus [272] have shown promising results when coupled into SPR sensing systems. These 2D materials introduce unique electronic and optical properties that can significantly modify the plasmonic behavior at the interface [32].

MXenes are one of the new 2D materials that has generated a lot of interest for SPR applications [110]. MXenes combine several properties such as a high metallic conductivity, hydrophilicity, and surface functionality that distinguishes them from other 2D materials [273]. Based on previous publication, adding MXene layers to gold films can improve SPR sensitivity via a number of processes, such as surface plasmon coupling effects, enhanced adsorption sites, and electron transfer processes [274].

The surface chemistry of MXenes is composed of surface terminations (–O, –OH, and –F) which can bind to target analyte, enabling selective detection capabilities [275]. According to earlier studies that examined the effects of various surface terminations on SPR detection response, it has been shown that $Ti_3C_2F_2$ offers the best sensitivity and detection accuracy [276].

The tunable surface chemistry of MXenes has two advantages for SPR applications: First, the coupling with the gold substrate is made possible by their high

electrical conductivity, which also improves the plasmonic resonance and sensitivity of the detection. Second, their versatile surface terminations facilitate selective functionalization for targeting specific analytes. This dual capability of MXenes to both enhance plasmonic response and provide active sensing sites represents a major advantage.

In this chapter, we study the integration of $Ti_3C_2T_x$ MXene with SPR technology through two approaches. In Section 5.1, we investigate the deposition process of MXene thin films monitored in real-time using SPR, providing insights into the film formation. Additionally, we enhance the SPR sensitivity by decreasing the amplitude at the SPR angle. Section 5.2 demonstrates the practical application of MXene-enhanced SPR system for the detection of (3-Aminopropyl)triethoxysilane (APTES). Both of these studies show the potential of MXenes in SPR sensing technology toward higher sensitivity and improved selectivity.

5.1 MXene thin-film deposition monitored by SPR

The fabrication of MXene films, whether on substrates or as free-standing membranes, is a crucial process for the preparation of MXene-based materials for various applications. However, producing homogeneous, ultrathin, and uniform MXene films remains challenging due to the intrinsic morphological characteristics of MXene flakes and their complex colloidal behavior in solution [111].

5.1.1 Current Methods for MXene Film Fabrication

There are several methods for creating MXene films, and each has its own benefits and drawbacks. Spin-coating is one of the most used techniques, it is based on the deposition of the colloidal solution containing the delaminated MXene flakes onto a substrate spinning it at a high speed, resulting in the formation of a film through centrifugal forces. Even though this technique is easy to set up, it is difficult to precisely control the film thickness, the homogeneity, and the surface coverage remains challenging. Spin-coated MXene films often exhibit "coffee ring" effects and uneven thickness distributions that can compromise device performance in sensing applications [277].

Spray-coating offers an alternative approach, in which MXene colloidal solution is aerosolized onto the surface of a substrate [278]. This technique enables coating of large and irregular surfaces but suffers from significant operator dependency, as spray parameters, distance, and angle significantly influence the resulting film properties. Hu et al. demonstrated that spray-coated MXene films exhibit variable thickness and often require multiple application cycles to achieve complete substrate coverage [279].

The doctor blade technique, also known as blade coating or knife coating, allows to have a good control over the film thickness but it produces only thick films (>1 μm), making it less suitable for applications requiring ultrathin coatings [280]. To do so, a high concentrated colloidal solution of MXene is spread directly onto a substrate.

Dip coating is another technique where a substrate is immersed in a MXene colloidal solution and withdrawn. The withdrawn step is critical and dictate the

film quality. MXene flakes remain on the substrate by capillary forces, and evaporation mechanisms [281]. Although dip coating enables uniform coverage of complex geometries, it is dfficult to control the thickness and it usually require multiple cycles to achieve desired properties.

Other emerging methods exist, such as the layer-by-layer assembly [282], the Langmuir-Blodgett deposition [283], the vacuum filtration followed by transfer [284], and the inkjet printing [285]. Each of these techniques has specific advantages, but they also present unique difficulties in terms of reproducibility, scalability, and accurate control over the characteristics.

5.1.2 Microfluidic-Assisted Deposition of MXene Films Monitored by SPR

In this section, we work on a new approach of a MXene thin film fabrication on a gold substrate using a microfluidic system coupled with Surface Plasmon Resonance (SPR). This hybrid method offers a real-time monitoring of the 2D film formation, which is a critical step for the fabrication of SPR sensor chip.

The deposition using the microfluidic system allows to control many parameters such as the flow, the concentration of the colloidal solution and the SPR probes the film formation in real-time. By manipulating these parameters, we achieve controlled deposition of $Ti_3C_2T_x$ MXene onto gold-coated SPR sensing chip.

The technique that we propose aims to address several limitations of conventional deposition techniques by offering a precise control of the thickness, a high reproducibility by controlling the flow rate and a reduction in material consumption compared to conventional methods. Furthermore, the proposed technique allows real-time quality assessment during the deposition process. The resulting MXene films exhibit a high uniformity across the sensing surface, as confirmed by scanning electron microscopy (SEM) analysis.

Materials and methods

SPR Chip Preparation

A gold thin film (43 nm thickness) was deposited onto a HBAK3 glass prism using physical vapor deposition (Plassys MEB 400) with a chromium adhesion layer (2 nm) to ensure strong adhesion between the glass substrate and the gold film. Prior to deposition, the prism surface was subjected to rigorous cleaning by sequential sonication in Neutracon, acetone, isopropanol, and deionized water for 10 minutes each.

To facilitate MXene adhesion, the gold surface was functionalized with a self-assembled monolayer (SAM) of 11-mercaptoundecanoic acid (MUA, Sigma-Aldrich, 95% purity). The functionalization was performed by immersing the gold-coated prism in a 5 mM ethanolic solution of MUA for 24 hours at room temperature. Following SAM formation, the prism was thoroughly rinsed with ethanol and deionized water to remove any non-specifically bound MUA molecules. To maximize the density of negatively charged carboxylate groups (COO^-) at the surface, the functionalized prism was subsequently immersed in 0.05 M NaOH solution for 5 minutes.

This critical activation step deprotonates the terminal carboxylic acid groups, enhancing the negative surface charge density and creating an optimal electrostatic environment for subsequent polyelectrolyte adsorption [286]. After activation, the prism was rinsed with DI water and integrated into the microfluidic system.

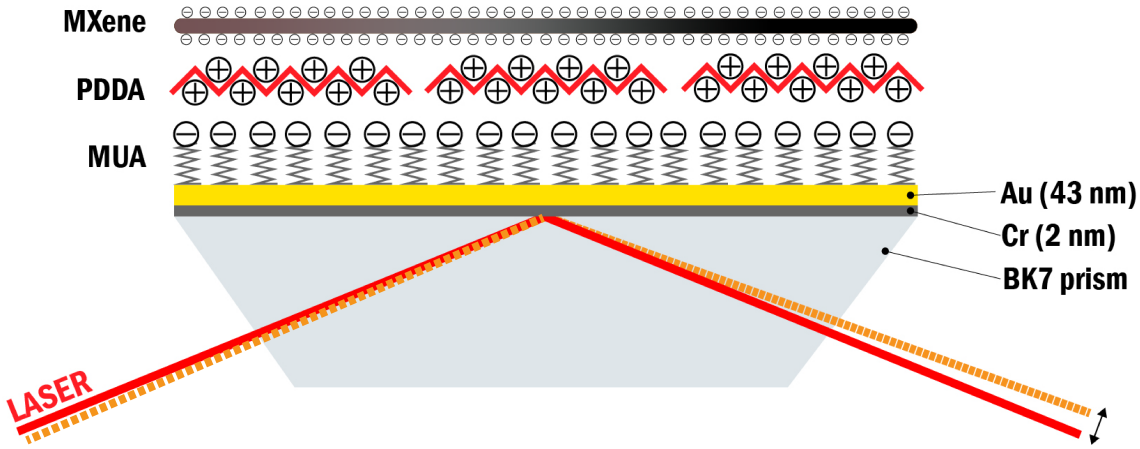

Figure 5.5: Schematic illustration of the multilayer system employed for MXene film fabrication. The initial surface functionalization with 11-mercaptoundecanoic acid (MUA) on the gold surface (43 nm) with chromium adhesion layer is performed by soaking method. Positively charged PDDA polymer and MXene layers are formed by microfluidic.

MXene Synthesis and Colloidal Solution Preparation

$Ti_3C_2T_x$ MXene colloïdal solution has been prepared similarly as described in Chapter 1.

The concentration of the final colloidal solution was adjusted to 1.0 mg/mL based on dry weight measurements. The colloidal stability was assessed through visual inspection and stability tests over several days, with no significant sedimentation observed, indicating good dispersion characteristics.

SPR Setup and Microfluidic Integration

SPR measurements were conducted using an IPSO lab system (PhaseLab Instrument) equipped with dual channels: one serving as a reference channel to account for bulk refractive index changes and instrumental drift, and the other as the analysis channel for monitoring MXene deposition. The system employs a 680 nm laser source with a sensitivity down to 10^{-6} refractive index units (RIU).

A custom microfluidic flow cell was fabricated using double-sided tape with a channel height of 100 μm, a width of 1 mm, and a length of 15 mm. A programmable syringe pump was used to control the fluid delivery.

Layer-by-Layer Assembly and MXene Deposition

Prior to MXene deposition, a layer of poly(diallyldimethylammonium chloride) (PDDA, Mw = 100,000, Sigma-Aldrich) was deposited to create a positively charged surface that would electrostatically attract the negatively charged MXene sheets.

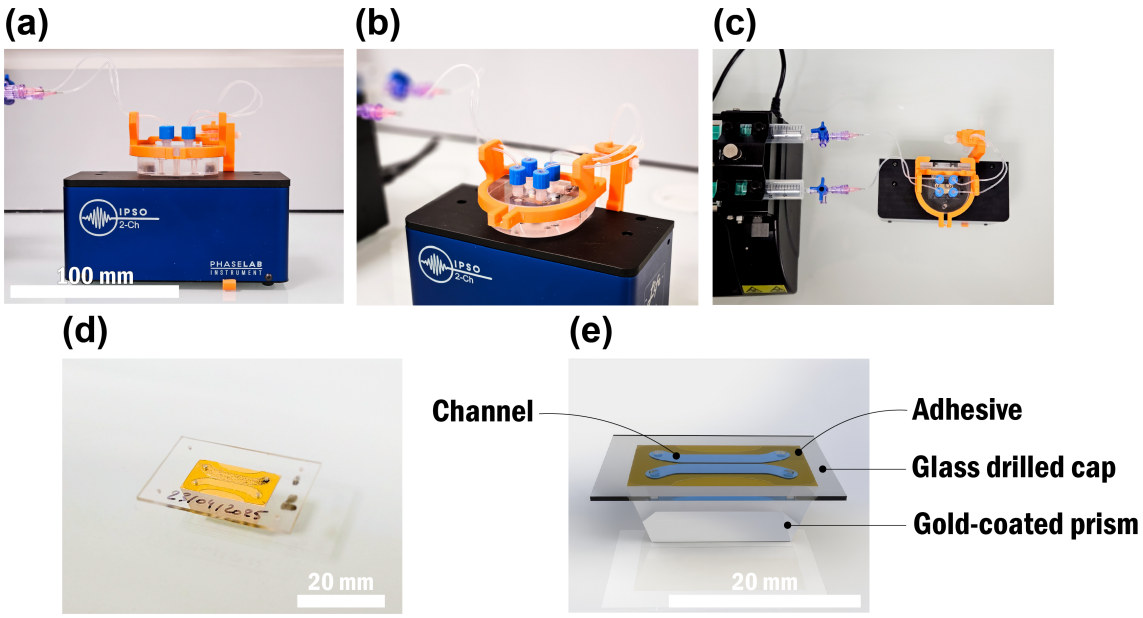

Figure 5.6: Experimental setup for microfluidic-assisted MXene film deposition with real-time SPR monitoring. (a) Front view of the IPSOLab SPR system integrated with the microfluidic setup. (b) Close-up view of the microfluidic system. (c) Top view of the complete system showing the syringedrivers, microfluidic cell mounted on the prism, and solution reservoirs. (d) 2-channel gold-coated microfluidic chip. (e) Schematic decomposition of a microfluidic cell showing the glass drilled cap, channel dimensions, adhesive layer, and gold-coated prism.

PDDA solution (0.1 mg/L in 0.5 M NaCl) was injected into the microfluidic channel at a flow rate of 50 μL/min for 10 minutes, followed by a washing step with deionized water at 50 μL/min for 5 minutes to remove any excess polyelectrolyte. For MXene deposition, the colloidal solution was initially introduced into the microfluidic channel at 50 μL/min until the channel was completely filled (approx. 3 min). The flow was then stopped, allowing the MXene flakes to naturally sediment and assemble onto the PDDA-modified gold surface under static conditions. This sedimentation process was continued for 150 min while continuously monitoring the SPR signal. Following deposition, the system was gently flushed with deionized water at a flow rate of 50 μL/min.

Results and discussion

5.1.3 MXene film deposition via controlled sedimentation

Initial experiments showed that it is important to have precise thickness control MXene film formation for optimal SPR performance. The microfluidic flow was stopped after filling the channel with MXene colloidal solution (about 3 min), allowing natural sedimentation to proceed under static conditions. Angular SPR scans were performed at 3-minute intervals throughout the deposition process to monitor film evolution in real-time.

The phase and amplitude responses from this deposition technique are presented in Figure 5.8. Both phase and amplitude measurements indicate a continuous in-

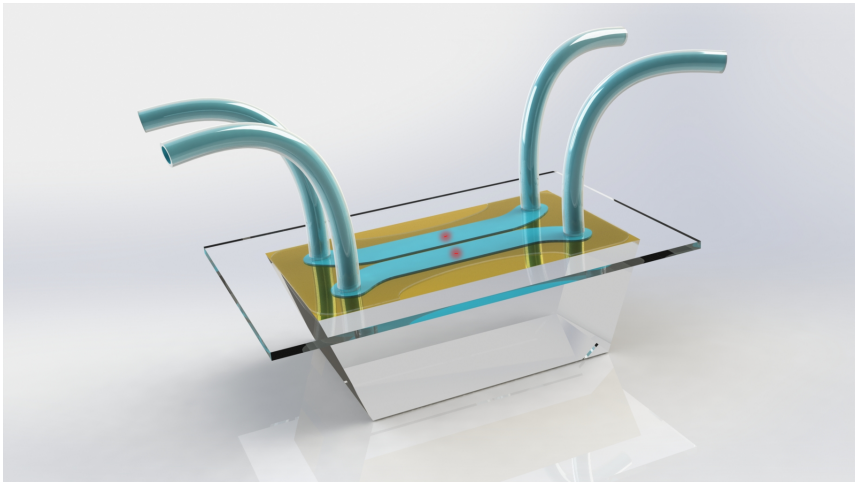

Figure 5.7: Three-dimensional visualization of the microfluidic cell used for MXene film deposition and SPR monitoring. The glass prism is covered with a thin gold layer (< 50 nm). Blue microfluidic channels are sealed against the gold surface, with inlet and outlet tubes.

crease in SPR performance during the 90 minute observation period. The amplitude response (right panel) shows a gradual deepening of the resonance dip from more or less 0.20 to 0.16, with a slight shift of resonance angle. The phase response (right panel) shows a gradual steepening of the transition slope with no orientation inversion, indicating the film thickness is still inside the optimal enhancement window.

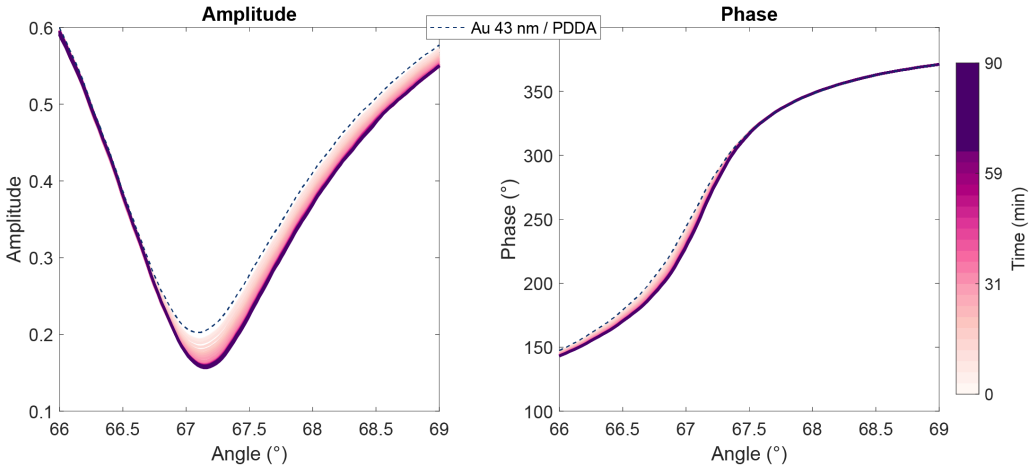

Figure 5.8: SPR angular scans showing amplitude (left) and phase (right) responses during optimized MXene film deposition via controlled sedimentation. The dashed blue curves represent the reference state (Au 43 nm with PDDA monolayer), while the color-coded curves illustrate the temporal evolution of the MXene film formation over approximately 90 minutes.

SEM observation (Figure 5.9) confirms the higher coverage of the gold layer by the MXene flakes compared to the first method. The uniform $Ti_3C_2T_x$ layer exhibits approximately 10 nm thickness with near-complete surface coverage (measurement details are available in the Appendix).

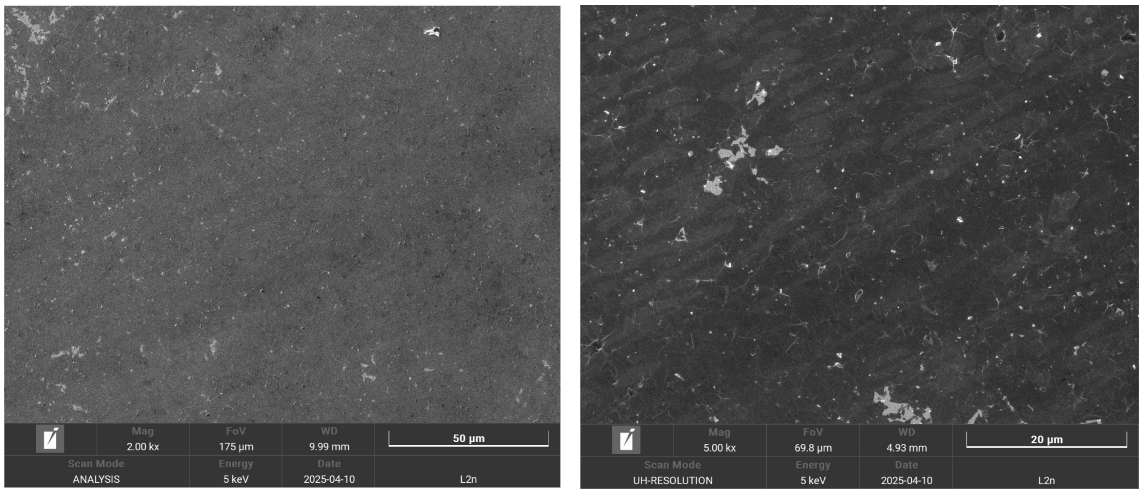

Figure 5.9: SEM pictures of $Ti_3C_2T_x$ MXene nanosheets covering the gold surface of SPR prism at different magnifications (left: 2.00 kx, right: 5.00 kx).

Kinetics of MXene Film Formation. Key SPR parameters during MXene film deposition under static conditions are illustrated in Figure 5.10. The square marker curve represents the resonance angle shift, and the the triangle marker curve represents the minimum amplitude value at resonance. We find that resonance angle shifted sharply from 67.10° to 67.125° during initial phase (0-40 minutes), indicating rapid accumulation of MXene sheets on the surface. The amplitude decreases sharply from 0.19 to 0.165, suggesting better plasmonic coupling efficiency. Following the initial growth phase, the system enters a more stable regime characterized by two different behaviors namely the resonance angle stays constant with minor variations between 67.14° and 67.15° and the amplitude decreases gradually but very slowly reaching 0.157 after 60 min. Such biphasic behavior may represent a transition from rapid adsorption to slower consolidation phase during which MXene flakes may be reoriented and packed closer without increasing film thickness significantly. The kinetic profile provides information necessary for process optimization, indicating that deposition time of about 80-90 minutes is sufficient for near-optimal film properties, and that longer deposition times are not very useful.

Comparing the phase shift shown in Figure 5.11 with the minimum angular shift shown in Figure 5.10 demonstrates the advantages of phase-based SPR detection in terms of measurement precision and data quality.

The angular shift measurements (square markers in Figure 5.10) exhibit considerable scatter and discontinuous behavior, particularly evident in the initial 20 minutes where the data points show irregular jumps and lack smooth progression. This behavior is in sharp contrast to the smooth, continuous curve of the phase measurements (Figure 5.11), with a well-defined exponential decay profile throughout the measurement period.

Several factors contribute to the superior quality of phase measurements. First, the resonance angle minimum determination requires finding the lowest point of the reflectance curve, which is sensitive to noise and small fluctuations in the optical system. Even with high-resolution interpolation using 1000 data points, the angular minimum determination is sensitive to instrumental drift and thermal variations that can shift the reflectance curve. In contrast, phase measurements at a fixed angle are a more stable reference point since they directly monitor the optical phase

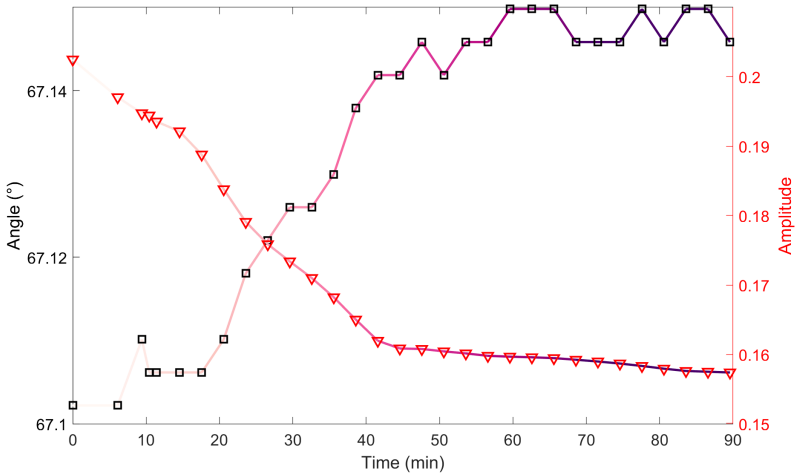

Figure 5.10: Key SPR parameters change over time during MXene film formation by controlled sedimentation. The square marker curve (left axis) shows the minimum SPR amplitude resonance angle shift and the triangle marker curve (right axis) shows the minimum reflectivity value at resonance. In the initial phase (0-40 minutes), rapid MXene accumulation is indicated by a sharp change in resonance angle from 67.10° to 67.13° and in minimum amplitude from 0.19 to 0.165. After this initial growth phase of $>$ 40 minutes, the resonance angle remains with minor fluctuations around 67.15° and the amplitude decreases gradually to 0.157 after 90 minutes. Such biphasic kinetic profile suggests that optimal film properties are achieved after about 40 minutes of deposition.

change without the need for curve fitting or minimum-finding algorithms.

In addition, the signal to noise ratio is much better in the phase measurements. Amplitude measurements show fluctuations that propagate into angles, whereas the phase signal is stable with little scatter around the fitted curve. Such improved precision becomes useful for quantitative kinetic analysis, which requires high-quality low-noise data for rate constants and binding parameters determination.

Smooth exponential behavior in phase measurements suggests that they better reflect the underlying physical processes at the sensor surface, while discontinuous angular measurements may introduce artifacts that misinterpret the kinetic mechanisms.

Another set of experiments has been performed with the aim of reaching the optimal coupling (lowest amplitude). To do that, MXene colloidal solution is injected similarly as described before, but here, the gold layer is slightly thicker (approximately 2 nm thicker). In Figure 5.12(a), the amplitude shows initial and dynamic scans with the optimal coupling (orange line). The amplitude line is sharp and reaches a value close to 0 (0.002), which indicates an optimized coupling. This optimal SPR coupling is reached after less than 10 minutes and after that, we observe a slight degradation of the resonance (shift to higher resonance angle and increase of the amplitude). The phase in Figure 5.12(b) gives information on the transition from optimal to sub-optimal: after the first three scans, the phase curve shape flips.

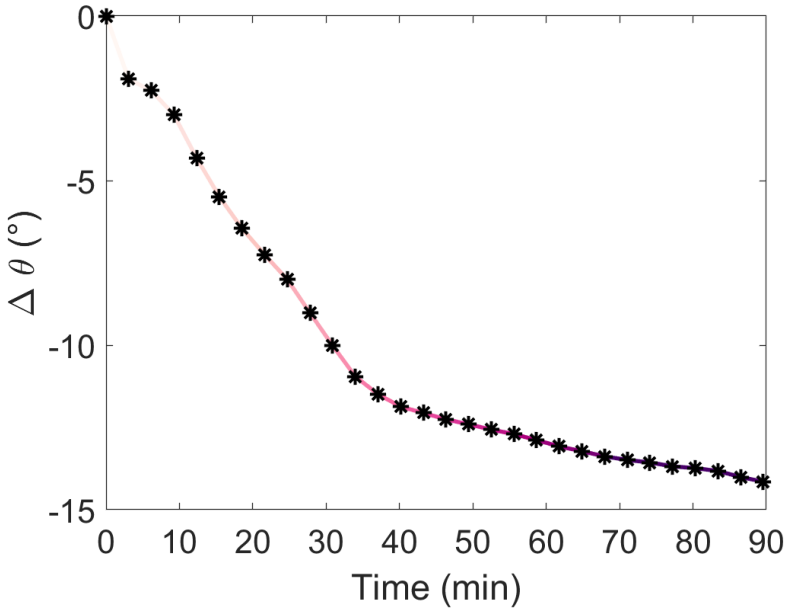

Figure 5.11: Time evolution of phase shift during MXene film formation via controlled sedimentation at 67.1°.

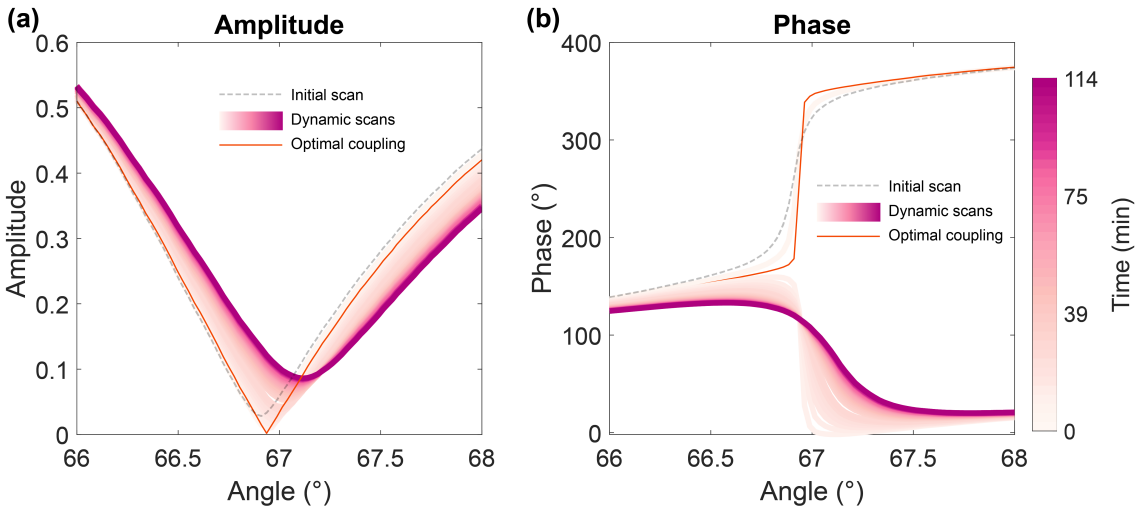

Figure 5.12: SPR angular scans showing amplitude (left) and phase (right) responses during optimized MXene film deposition via controlled sedimentation. The dashed curve represents the reference state, while the color-coded curves illustrate the temporal evolution of the MXene film formation. The orange curve is the optimal resonance coupling.

5.1.4 Determination of the dielectric constant of MXene

The determination of the dielectric function of a 2D material is challenging because the material is not homogeneous in terms of chemical composition, leading to anisotropic optical properties that are further complicated by sample fabrication effects. Conventional tools for determining the dielectric function of materials typically require smooth surfaces to fit the data properly and yield reliable results. We initially attempted to measure the refractive index using a Woolam ellipsometer, but the results we obtained differed from those reported in the literature. Several factors can strongly influence these results, including the fitting model used, sample preparation parameters such as the substrate choice, layer thickness, and deposition method.

From SPR measurements, thickness characterization, and multilayer modeling, it is possible to extract the dielectric function at a single wavelength. In this section, we aim to determine the dielectric constant at 680 nm, corresponding to the wavelength of the laser used in the SPR setup. To achieve this, we first measure the refractive index of the MXene layer using the ellipsometer and the resulting values were used as baseline parameters to fit both amplitude and phase responses through analytical simulations, allowing us to deduce the actual dielectric constant of the system. To do that, we first matched the amplitude and resonance angle of the gold layer by adjusting the thickness parameter in our model leading to a thickness of 43.15 nm. For the MXene layer, the measured thickness is 10 nm, as determined by profilometry. Knowing the thickness and the optical response (amplitude and resonance angle), we can determine ε' and ε'' values that best match the experimental data using a multilayer optical model. The theoretical SPR response is calculated using Fresnel equations for multilayer systems. For a three-layer configuration (air/MXene/gold/substrate), the total reflection coefficient is determined by the recursive application of Fresnel coefficients at each interface. The amplitude and phase of the reflected light are given by:

$$r_{\text{total}} = \frac{r_{01} + r_{12}e^{2i\beta_1} + r_{23}e^{2i(\beta_1+\beta_2)} + r_{01}r_{12}r_{23}e^{2i\beta_2}}{1 + r_{01}r_{12}e^{2i\beta_1} + r_{01}r_{23}e^{2i(\beta_1+\beta_2)} + r_{12}r_{23}e^{2i\beta_2}} \tag{5.5}$$

where r_{ij} are the Fresnel reflection coefficients at each interface, and $\beta_j = \frac{2\pi}{\lambda} n_j d_j \cos\theta_j$ represents the phase accumulated in each layer.

Table 5.1 shows the different parameters used to fit the experimental data:

Table 5.1: Parameters used for the multilayer optical model fit

	Material	ϵ'	ϵ"	**Thickness (nm)**
1	Water	1.77145	0	NaN
2	Constant	1.8	0.03	8
3	rough	16.6413	2.44951	0.1
4	Au	−14.8689	1.06216	43.15
5	Cr	−5.38055	30.5223	2
6	HBAK3	2.38191	0	NaN

The dielectric constants are systematically varied until the calculated SPR curves match the experimental amplitude and resonance angle. Through this iterative

fitting process, we found that:

$$\varepsilon' = 1.8 \quad \text{and} \quad \varepsilon'' = 0.03 \tag{5.6}$$

provide the best fit to our experimental results.

The corresponding refractive index n and extinction coefficient k, calculated using the relations $n = \sqrt{(\varepsilon' + |\varepsilon|)/2}$ and $k = \sqrt{(-\varepsilon' + |\varepsilon|)/2}$ where $|\varepsilon| = \sqrt{\varepsilon'^2 + \varepsilon''^2}$, are:

$$n = 1.3417 \quad \text{and} \quad k = 0.0112 \tag{5.7}$$

We can note that the calculated dielectric function of the MXene layer is close to that of water. This can be explained by the intercalation of water between the sheets. Indeed, the deposition method is carried out in an aqueous medium and the SPR system does not allow for a deep drying step (high temperature under an inert atmosphere).

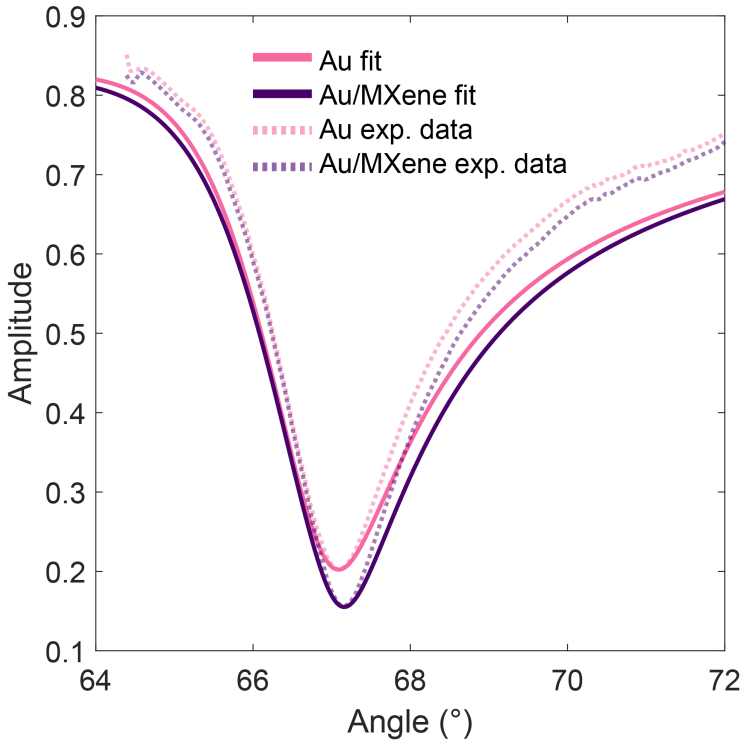

Figure 5.13: Surface plasmon resonance simulated amplitude signal for a 43.3 nm gold layer (pink solid line) and a 43.3 nm gold layer with an additional 10 nm $Ti_3C_2T_x$ MXene layer (purple solid line) compared to the experimental data (dashed lines). The simulated response is calculated using a multilayer model that determines the reflectivity of a multilayer system as a function of incident angle and wavelength.

These values differ from the refractive indices measured by other methods. For example, using Variable Angle Spectroscopic Ellipsometry (VASE) measurements, we obtained wavelength-dependent optical constants across the visible and near-infrared range (300-1600 nm). Figure 5.14 shows the experimental data (Psi and Delta at three angles: 60°, 65°, and 70°) along with the fitted model.

The fitting procedure employed a multi-layer optical model comprising the BK7 substrate, thin metallic layers (Cr/Au), and the $Ti_3C_2T_x$ film with a thickness of 10.00 nm (more details are available in the Appendix). Although the fitted model

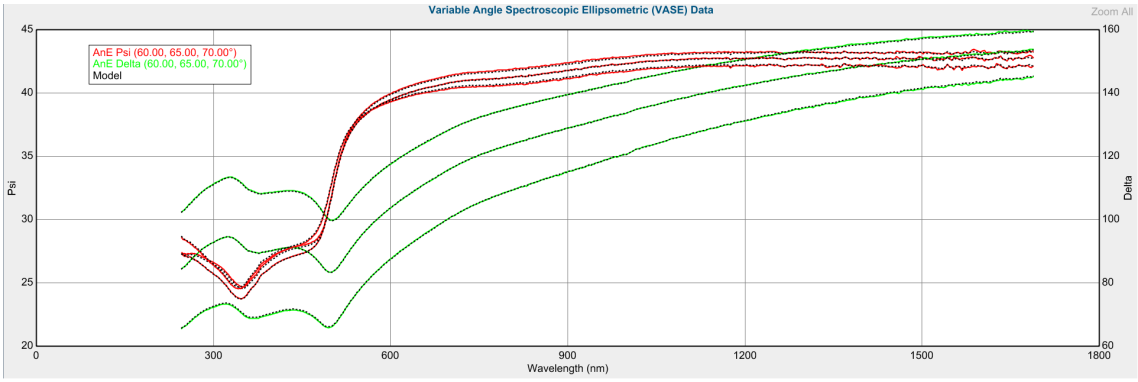

Figure 5.14: Variable Angle Spectroscopic Ellipsometry (VASE) data for $Ti_3C_2T_x$ on a 43.3 nm gold layer (SPR prism). The experimental data (Psi in red, Delta in green) measured at three incident angles (60°, 65°, 70°), with the fitted model represented by black dotted lines. The model consists of a three-layer structure: BK7 substrate, a 0.29 nm Cr adhesion layer, a 40.11 nm Au layer, and a 10 nm thick $Ti_3C_2T_x$ top layer.

shows excellent agreement with the experimental data, as indicated by the low Mean Squared Error (MSE = 2.516), the extracted optical constants are inconsistent with both literature values and those determined by SPR measurements. At 680 nm, this VASE analysis yielded $n = 2.2285 + 1.8306i$ for $Ti_3C_2T_x$, which significantly deviates from expected values. This discrepancy suggests that despite the good quality of fit, the optical model may not adequately capture the complex optical behavior of $Ti_3C_2T_x$ in this multilayer configuration, possibly due to interface effects, surface roughness, or the inherent anisotropy of the MXene material. However, a key advantage of ellipsometry over SPR is its ability to provide comprehensive wavelength-dependent optical constants over a broad spectral range, enabling a more complete characterization of the material's optical properties across the visible and near-infrared regions.

Conclusion

This study reports on the successful microfluidic-controlled MXene film fabrication under real time SPR monitoring, which gives unprecedented insight into deposition dynamics and optimization of $Ti_3C_2T_x$ films for sensing applications. Our comparative analysis between continuous flow and controlled sedimentation approaches reveals a critical balance between deposition rate and film quality, where the sedimentation method permits the precise control of film thickness within the optimal enhancement regime. Time-resolved SPR measurements revealed a biphasic growth pattern with initial rapid adsorption (0-40 minutes) and consolidation phase ($>$ 45 minutes) providing valuable guidance for process optimization. Deepening resonance minima and enhanced phase sensitivity with no orientation inversion demonstrate the good functional coating capability of MXene for SPR sensing platforms. This microfluidic-SPR integrated approach advances fundamental knowledge on MXene film formation mechanisms and provides a platform for development of high-performance MXene-enhanced SPR sensors with tailored surface properties for targeted sensing applications.

5.2 (3-Aminopropyl)triethoxysilane detection using MXene

Because of their unique surface chemistry [287, 288], two-dimensional MXene materials are promising platforms for chemical and biochemical sensing applications. Abundant functional groups and in particular hydroxyl (-OH) terminations on MXene surfaces constitute reactive sites for selective molecular interactions [209, 210]. In this section, we exploit this distinctive surface reactivity to develop a novel sensing approach for siloxane-containing molecules, specifically (3-Aminopropyl)triethoxysilane (APTES).

Recent investigations by photo-induced force microscopy (PiFM) revealed that MXene surfaces are easily contaminated with spontaneous siloxane by environmental exposure, more information can be found in Chapter 4. The hydroxyl-terminated basal planes of MXene flakes readily undergo dehydration condensation reactions with silanol (Si-OH) groups, forming stable Ti-O-Si linkages [289, 290]. This chemical affinity was initially discovered as an unintended contamination phenomenon and now provides a target for targeted molecular detection.

Based on that, we have designed an SPR sensing system that leverages the gold-MXene hybrid interface to monitor the kinetics of siloxane binding in real-time [267]. By incorporating $Ti_3C_2T_x$ MXene as the active sensing layer on gold-coated SPR chips, we create a platform that combines the exceptional surface chemistry of MXenes with the high sensitivity of phase-sensitive SPR detection [259, 263].

APTES, a widely used aminosilane coupling agent, serves as our model analyte due to its well-characterized siloxane functionality and significant importance in various bioconjugation and surface modification applications [291, 292]. When exposed to the MXene surface, APTES molecules can undergo condensation reactions with surface hydroxyl groups, resulting in detectable changes in the local refractive index at the sensing interface [290, 293].

Herein we report binding kinetics, sensitivity limits and selectivity of our MXene-enhanced SPR platform for APTES detection. Systematic characterization of sensor response under different conditions reveals key mechanisms underlying siloxane-MXene interactions and demonstrates its utility for real-time monitoring of siloxane compounds. The results provide valuable insights into both the practical applications of MXene-based sensors and the fundamental surface chemistry of these emerging two-dimensional materials.

Materials and methods

MXene Film Preparation

$Ti_3C_2T_x$ MXene films were deposited onto gold-coated SPR sensors using the controlled sedimentation approach via microfluidics, as described in the previous section. This methodology was selected based on our findings that the sedimentation technique produces more uniform MXene films with optimal thickness for SPR sensing applications, avoiding the over-accumulation issues observed with continuous flow deposition. The deposition was monitored in real-time using SPR to ensure reproducible film formation with consistent thickness and coverage.

APTES solution preparation and experimental design

Solutions of (3-Aminopropyl)triethoxysilane (APTES, 99%, Sigma-Aldrich) were prepared at four different concentrations: 10^{-9}, 10^{-6}, 10^{-3}, and 10^{-1} mol/L. The solvent system consisted of 95% ethanol and 5% deionized water (v/v). This specific solvent composition was selected for several crucial reasons. The predominant ethanol component (95%) ensures complete dissolution of APTES, which exhibits limited solubility in pure water, while preventing rapid self-condensation reactions that would occur in aqueous environments [294]. Simultaneously, the small water fraction (5%) provides the minimal hydrolysis conditions necessary to activate the ethoxy groups of APTES, converting them to reactive silanol (Si-OH) groups that can subsequently undergo condensation reactions with the hydroxyl-terminated MXene surface [242, 291].

This optimized ethanol/water ratio represents a balance between two competing requirements: sufficient hydrolysis of APTES to enable surface binding, while limiting the self-condensation reactions that would form oligomeric siloxane networks in solution before reaching the sensing surface. Previous studies have demonstrated that this solvent composition promotes controlled monolayer formation of APTES on hydroxylated surfaces [295].

SPR Measurement and Data Analysis

Real-time monitoring of APTES binding to the MXene-functionalized surface was performed using a PhaseLab SPR instrument. Solutions were injected into the microfluidic cell at a controlled flow rate of 50 μL/min, allowing for real-time observation of binding kinetics. Between each APTES concentration, the cell was thoroughly rinsed with the ethanol/water solvent mixture to remove any non-specifically bound molecules.

Both amplitude and phase angular scans were collected before and after exposure to each APTES concentration. Additionally, continuous sensorgrams were recorded throughout the experiments to monitor the time-dependent binding process. Raw sensorgram data, which records the time evolution of the resonance angle, provides direct information about binding events at the sensor surface. These data were subsequently converted to refractive index units (RIU) using calibration curves established with solutions of known refractive indices.

The conversion to RIU offers several significant analytical advantages [251, 257]. First, it enables quantitative comparison between different experimental runs by normalizing the instrument-specific response factors. Second, RIU values facilitate direct correlation between the measured signal and the surface mass density of bound analytes through the application of the de Feijter equation:

$$\Gamma = \frac{d \cdot (n - n_0)}{dn/dc} \tag{5.8}$$

where Γ is the surface mass density, d is the effective thickness of the adsorbed layer, n is the refractive index of the layer, n_0 is the refractive index of the bulk solution, and dn/dc is the refractive index increment of the analyte [296]. This enables quantitative determination of the amount of APTES molecules bound to the MXene surface. Furthermore, the RIU representation allows for comparison with

results from different SPR instruments and experimental configurations, enhancing the reproducibility and transferability of our findings.

The binding kinetics were analyzed by fitting the RIU sensorgrams to appropriate kinetic models, including pseudo-first-order and pseudo-second-order models, to determine rate constants and binding capacities, providing mechanistic insights into the APTES-MXene interaction process.

Results and discussion

Refractive index variation

The concentration-dependent optical response of the MXene-enhanced SPR sensor to APTES binding is shown by systematic angular scans showing amplitude and phase shifts over the concentration range from 10^{-9}M to 10^{-1}M, with ethanol (95%) as solvent control (Figure 5.15).

Amplitude measurements in the left panel reveal typical SPR resonance curves with minima around 70.7° after the complete APTES adsorption. A sharp rightward shift of the resonance angle with increasing APTES concentration is observed, indicating an increase in the effective refractive index at the sensing interface. This progressive shift follows the expected concentration-dependent trend, where each higher concentration leads to a larger angular displacement. The resonance depth also changes systematically with concentration, reflecting changes in optical coupling efficiency as APTES molecules accumulate on the MXene surface.

The right panel phase measurements are more sensitive than amplitude detection with steeper transitions and stronger concentration-dependent shifts. The phase curves show resonance crossings at similar angular positions as the amplitude minima, but greatly enhanced slope characteristics that amplify small refractive index changes due to molecular binding events. Such a dual parameter detection approach confirms the binding of APTES with high detection sensitivity and measurement confidence.

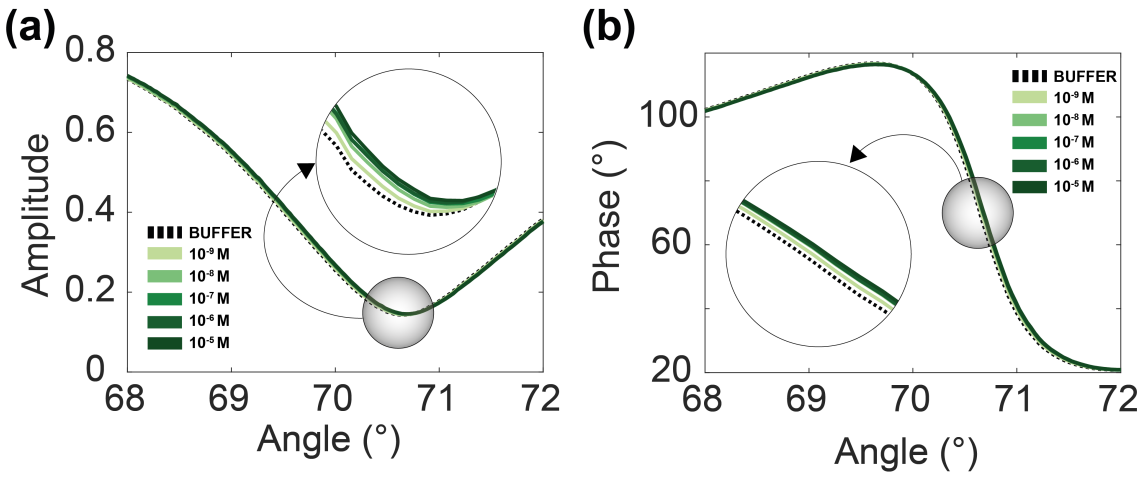

Figure 5.15: Amplitude (a) and phase (b) angular scans demonstrating APTES surface functionalization on MXene at various concentrations following rinsing treatment.

Figure 5.16(a) shows a 160-minute real-time binding experiment based on differential SPR detection, where the MXene-coated sensing channel is referenced against a bare gold control channel. The experimental protocol involves sequential injection of increasing APTES concentrations (from 10^{-9} M to 10^{-5} M) with buffer wash cycles to remove excess molecules that did not bind to the surface.

A key to interpreting the sensorgram data is the distinction between bulk and surface-bound molecular contributions to the SPR signal. During the analyte injection phases, the observed increase in ΔmRIU reflects both bulk refractive index changes due to APTES molecules in solution and any surface binding that may occur simultaneously. However, the true extent of molecular grafting to the MXene surface can only be assessed by analyzing signal changes after rinsing, when unbound molecules and solvent are removed. The difference in ΔmRIU between the pre-injection baseline and the post-rinse plateau reflects the refractive index modification caused by APTES molecules that have formed covalent bonds with the MXene surface.

The first concentration exposure (10^{-9} M) shows fast binding kinetics, and the signal reaches approximately 0.17 mRIU during injection. The subsequent buffer wash crucially removes excess solution-phase molecules while maintaining the elevated signal level, confirming irreversible covalent binding of APTES silanol groups to MXene surface hydroxyl terminations via Ti–O–Si condensation chemistry.

The 10^{-8} M concentration phase shows another fast binding event with a signal reaching 0.23 mRIU. Similar to the previous injection, the rinsing step does not bring the signal back to baseline, which indicates that covalent binding also occurs. For higher concentrations (10^{-6} M and 10^{-5} M), the differential line shows no variation, indicating that the behavior in the analyzed channel is similar to the reference channel.

Figure 5.16(b) represents the refractive index variation of the analyzed channel (green dotted line) and the reference channel (black solid line). On the reference channel, after the rinsing step, the signal returns to the initial RIU values. This indicates that APTES does not bind to the reference channel (Au/MUA/PDDA). Indeed, the top layer of the chip is composed of PDDA, which is a positively charged polyelectrolyte, and APTES contains NH_3^+ groups. Both species are positively charged, resulting in electrostatic repulsion that prevents any electrostatic interaction.

On the other hand, the analyzed curve (dashed green curve) highlights the covalent binding between APTES and the –OH groups on the MXene surface, as described in Chapter 4. These systematic buffer wash cycles constitute critical control phases that validate the APTES–MXene interactions. The absence of signal decay during buffer exposure eliminates concerns about non-specific adsorption artifacts and confirms stable Ti–O–Si linkages. Using the differential measurement approach, bulk refractive index contributions and non-specific binding effects are eliminated, and the sustained positive ΔmRIU signals indicate preferential attachment to the MXene-functionalized surface over bare gold.

This experimental design exploits MXene surface chemistry for selective siloxane detection. The combination of real-time kinetic monitoring and angular response analysis characterizes the binding mechanism, while the distinction between bulk and surface-bound contributions allows precise quantification of molecular grafting events. The irreversible binding behavior, concentration-dependent response, and

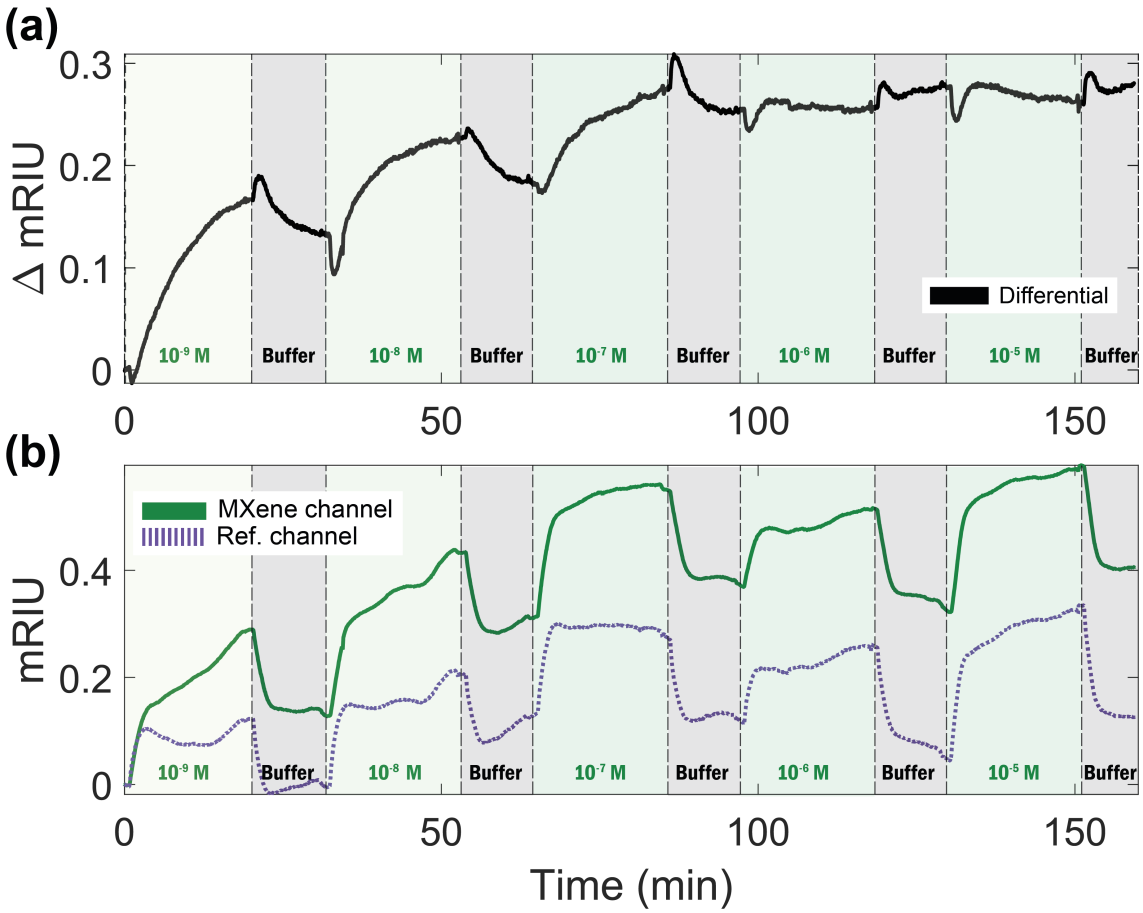

Figure 5.16: Sensorgram of the APTES deposition on $Ti_3C_2T_x$ layer expressed in refractive index unit over the time. Green areas refer to the association of APTES molecules while the grey areas corresponds to the dissociation performed by running the buffer solution. (a) The differential signal (Ch1(MXene) - Ch2(Reference) and (b) the signal of each channel (Ch1: MXene channel in dotted green and Ch2: Reference channel is the solid black line).

MXene-enhanced selectivity observed herein validate this approach for targeted detection of siloxane-containing molecules, which is of interest for monitoring surface modification processes and bioconjugation applications.

Conclusion

In this section, we used microfluidic-SPR technique coupled with $Ti_3C_2T_x$ MXene to fabricate a highly homogeneous MXene thin film with a thickness of 10 nm on a gold substrate. This approach allowed us to enhance the SPR system resonance, achieving optimal coupling conditions with minimal amplitude values. Furthermore, the dielectric constant of the material was analytically determined. Additionally, we investigated the adsorption behavior of (3-Aminopropyl)triethoxysilane (APTES) on $Ti_3C_2T_x$ MXene surfaces. The chemical binding between APTES and the MXene occurs within minutes, providing supporting information for the results presented in Chapter 4. The SPR-based detection demonstrates sensitivity down to nanomolar concentrations of APTES.

General conclusion

This thesis provides a comprehensive understanding of the infrared optical properties of MXenes through a multi-scale approach, ranging from optical characterization to emerging technological applications. The results presented in the three result chapters bring new knowledges on MXene optical properties and demonstrate their potential for technological applications across multiple domains.

Chapter 1 aims to establish the context for understanding MXenes within the broader landscape of 2D materials science. The systematic examination of established 2D materials—graphene, TMDs, black phosphorus, and hBN—reveals a rich diversity of properties. MXenes represent a paradigm shift in this landscape, introducing materials that uniquely combine metallic conductivity with surface chemistry tunability—characteristics largely absent in conventional 2D materials. This positions MXenes as complementary rather than alternative to existing 2D systems, opening applications requiring both high conductivity and chemical reactivity.

Analyzing synthesis methods raises an important issue regarding relationship between chemical etching conditions and material properties. Unlike mechanical exfoliation for van der Waals materials, selective etching for MXene synthesis permits the termination of engineering in other 2D systems. This foundation highlights knowledge gaps, namely the poor understanding of structure-property relationships in the infrared region and the need for nanoscale characterization techniques. These gaps justify the systematic multi-scale investigation of MXene optical properties that constitutes the core of this thesis, in which advanced characterization approaches will reveal relationships between composition, surface chemistry and optical response.

Chapter 2 described the theoretical and experimental foundations for multi-scale optical characterization by linking fundamental light-matter interactions with advanced near-field microscopy techniques. Comprehensive treatment of infrared spectroscopy principles ranging from molecular vibrations to crystalline phonons laid the conceptual basis for optical phenomena in 2D materials. Atomic force microscopy principles, scattering-type scanning near-field optical microscopy (s-SNOM), and photo-induced force microscopy (PiFM) were described and thus formed the methodological toolkit for nanoscale optical investigation. The complementary character of s-SNOM and PiFM on semiconductor reference systems was described in Chapter 2.

Chapter 3 demonstrated that the carbon-to-nitrogen ratio in $Ti_3C_{(2-y)}N_yT_x$ MXenes constitutes a powerful control parameter for modulating their infrared optical properties. This investigation revealed a good correlation between composition and IR performance, which suggests a good direction for optical property engineering. Carbon-rich compositions ($Ti_3C_2T_x$) have extremely low emissivity (0.06) and are thus suitable for IR shielding applications and reflective coatings. In turn, progressive nitrogen incorporation increases emissivity to 0.65 for Ti_3CNT_x, allowing

thermal management and IR sensing applications.

These results provide theoretical as well as experimental foundations for MXene materials with tunable optical response. The systematic variation of lattice parameters with increasing nitrogen content, confirmed by X-ray diffraction analysis, provides structural insights related to optical property changes. The temperature-dependent emissivity behavior, in particular, the near-linear increase in compositions containing moderate nitrogen content, is in good agreement with our extended Hagen-Rubens model including electron-phonon interactions and changes in electrical conductivity. This knowledge base allows predictive design of MXene compositions targeting infrared properties.

Additionally, the second section of the chapter demonstrates the application of infrared spectroscopy for in-situ studies of MXene-based electrochemical cells. This innovative approach leverages the infrared optical properties characterized throughout this thesis to monitor electrochemical processes in real-time. The ability to probe structural and chemical changes occurring at MXene electrodes during electrochemical cycling represents a significant advancement in understanding the mechanisms governing MXene performance in energy storage applications.

Chapter 4 represents a step forward in MXene characterization as Photo-induced Force Microscopy (PiFM) was demonstrated to be very sensitive to surface chemistry at the nanoscale. In this way, surface functional groups were detected and mapped on pristine MXenes and siloxane contaminants were identified on exposed surfaces with nanometer spatial resolution. Notably, PiFM revealed selective adsorption phenomena of siloxane compounds on MXenes that were not detected by conventional characterization techniques such as Raman Spectroscopy, FTIR, and EDS. Vibrational modes detected Si–C and Si-O-Si confirmed that the siloxane species are uniformly distributed over MXene flakes and are highly reactive due to surface-OH terminations. This finding indicates how high-resolution characterization methods are essential for understanding surface-environment interactions.

The investigation extended to Nb_2CT_x MXenes, where PiFM showed higher sensitivity in detecting oxidation signatures even in single/few-layered flakes with thicknesses as low as 15 nm. The characteristic peaks around 950–980 cm^{-1} associated with niobium oxide formation were clearly identified, showcasing the technique's capability to probe nanoscale chemical transformations. These results show that PiFM is a powerful tool for investigating 2D material surface chemistry and open new perspectives for controlled and targeted functionalization of MXene surfaces.

Chapter 5 demonstrated the transition from optical properties to practical applications by developing detection platforms based on Surface Plasmon Resonance (SPR) coupled with MXenes. Highly homogeneous MXene thin films (10 nm thickness) were prepared on gold substrates for analytical determination of the dielectric constant as well as investigation of APTES adsorption behavior.

This approach showed remarkable detection sensitivity down to nanomolar concentrations confirming the suitability of MXenes for advanced molecular detection applications. Results confirm and extend basic insights on siloxane-MXene interactions derived from the PiFM model, bringing understanding in line with practical applications. Their live monitoring capabilities and fast chemical binding kinetics (in minutes) demonstrate the real-world application of MXene-based sensors.

The microfluidic-SPR technique coupling with $Ti_3C_2T_x$ MXenes represents a significant advancement in sensor platform development, providing both high sen-

sitivity and selectivity for organosilane detection. The analytical determination of dielectric properties through this approach contributes valuable data for the optical modeling and design of MXene-based devices. As a future perspective, it would be particularly interesting to perform APTES detection using SPR in air rather than in aqueous solution. Such measurements would more closely replicate the conditions employed in Chapter 4 with PiFM characterization, enabling a direct comparison between the two techniques and providing complementary insights into gas-phase versus liquid-phase silane-MXene interactions.

This research opens promising development axes that warrant further investigation. For instance, extending the compositional engineering approach to other MXene systems (notably vanadium, niobium, and molybdenum carbides and nitrides) could reveal even more diverse optical properties. The systematic investigation of terminal group influence on optical properties constitutes a promising research direction, where PiFM emerges as a powerful tool to probe and characterize surface modifications of MXenes at the nanoscale. This capability to directly monitor surface chemistry changes could provide crucial insights into the structure-property relationships governing MXene optical behavior. The integration of MXenes into multiplexed detection systems, exploiting their selective reactivity and compatibility with microfabrication technologies, constitutes a promising avenue for developing advanced detection platforms. The possibility of controlled functionalization of MXene surfaces, demonstrated in this thesis, opens perspectives for specific and selective sensors capable of distinguishing between closely related molecular species. The techniques and approaches developed in this thesis are transferable to other 2D material systems, increasing their scientific and technological impact. Integrating multi-scale characterization approaches, from bulk optical measurements to nanoscale surface chemistry mapping, could provide new knowledge.

Appendix A

Chapter 3: Fabrication and characterization details

Samples fabrication and characterization methods

Synthesis of MAX Phases and MXenes

Ti (Alfa Aesar, -325 mesh, 99.5%), Al (Alfa Aesar, -325 mesh, 99.5%), AlN (Fisher Scientific, -325 mesh, N 32.0% min), TiN (Thermo Scientific, -325 mesh, 99.5%), and C (graphite, Alfa Aesar, -325 mesh, 99%) powders were used for MAX synthesis.

MAX phase	Precursors	Atomic ratio	Sintering conditions
Ti_3AlC_2	TiC:Al:Ti	2:2.2:1.25	1400°C, 2h
$Ti_3AlC_{1.75}N_{0.25}$	Ti:AlN:C	3:1:2	1400°C, 2h
$Ti_3AlC_{1.5}N_{0.5}$	Ti:AlN:C	3:1:1.5	1400°C, 2h
Ti_3AlCN	Ti:AlN:C	3:1:1	1400°C, 2h

Table A.1: Synthesis conditions of MAX phases

For $Ti_3C_yN_{(2-y)}T_x$ (y = 0, 0.25, 0.5, and 1), Ti, Al, AlN, and C were mixed in a M/A/X molar ratio specified in Table 1. Fifty grams of each powder mixture and 100 g of 5 mm YSZ milling balls were added to polypropylene bottles. The powders were ball-milled for 16 h, followed by passivation (allowing powders to settle and then exposing them to air overnight). The passivated powders were added into alumina crucibles and annealed in a high-temperature tube furnace (Carbolite Gero). The tube was purged with ultra-high purity Ar at 200 sccm for 1 h before heating. The furnace ramping was set at 3 °C/min to reach 1400 °C, and sintering was held for 2 h. The lightly sintered block was then crushed with a mortar and pestle. The powders were stirred with concentrated HCl (Fisher Scientific, 38 wt.%) overnight to dissolve the intermetallic impurities and then washed with deionized water by vacuum-assisted filtration. The obtained powders were dried overnight under vacuum at room temperature and sieved using a stainless-steel mesh to <38 μm. $Ti_3C_2T_x$ was produced following the same procedure with TiC, Al, and Ti precursors with an M/A/X molar ratio of 2:2.2:1.25.

MXenes were synthesized following the procedure described in Chapter 1. The four MXenes with different C/N ratios were prepared using an identical procedure.

Characterization

The 10-degree specular reflectance of MXene films was measured using a Fourier Transform Infrared (FTIR) spectrometer (Invenio-X, Bruker) equipped with a reflectance accessory (10Spec, Pike Technologies). A gold-coated mirror served as the reference. Thermal emissivity was assessed using the same FTIR instrument. An emission adapter (A540, Bruker) was employed for sample heating, while a soot layer served as the black body reference. Transmission FTIR spectroscopy was used to analyze the chemical bonding of MXene. Initially, the MXene colloidal solution was dried, ground, and then mixed with KBr powder to make a pellet using a hydraulic press (1 mg of MXene for 200 mg of KBr). Subsequently, the IR collimated beam was passed through this pellet at a normal incidence. X-ray diffraction (XRD) patterns were acquired on freeze-dried MXene powders using Cu ($\lambda = 1.54$ Å) anticathode at 40 kV (Bruker D8 Advance). Reflection-mode Raman spectra were collected using a Horiba Labram Raman microscope using a 63x objective and 1800 line/mm grating. For MXenes, a 633 nm laser wavelength was used with a 60 s acquisition time and 0.12 mW laser power. The spectra were normalized between 0 and 1. The morphology of MXene-coated films was examined using a 3D laser scanning confocal microscope (Keyence, VK-X1000), and a scanning electron microscope (FEG SU8030, Hitachi). The electric properties of MXene samples were evaluated using a four-point probe (JandelTM).

Computational details[1]

Density functional theory (DFT) calculations were performed Vienna Ab initio Simulation Package (VASP) [297, 298] to study the impact of the carbon-to-nitrogen ratio on the optical response of $Ti_3C_{(2-y)}N_yT_x$ MXenes. The exchange-correlation interactions were treated using the generalized gradient approximation (GGA) with the Perdew-Burke-Ernzerhof (PBE) functional [299]. The projector augmented wave (PAW) method [300] was used to describe the core–valence electron interactions, and a plane-wave kinetic energy cutoff of 450 eV was applied. To account for long-range dispersion forces, the DFT-D3 correction [301] scheme developed by Grimme was included. Structural optimizations were performed using a $5\times5\times1$ Monkhorst-Pack k-point mesh [302] with convergence achieved when atomic forces were under 0.01 eV/Å. The total-energy difference between two successive self-consistent steps was less than 10^{-5} eV. To eliminate spurious interactions between periodic images, a vacuum spacing of 15 Å was introduced along the z-direction. Following structural optimization, a denser k-point mesh of $9\times9\times1$ was used to compute the frequency-dependent complex dielectric function $\varepsilon(\omega) = \varepsilon_1(\omega) + i\varepsilon_2(\omega)$. The reflectance at normal incidence was calculated from the real and imaginary parts of the dielectric function. To enable comparison with experimental IR spectra extending beyond the DFT-calculated range ($\sim$7 μm), the reflectance data were linearly extrapolated up to 25 μm based on the long-wavelength dielectric behavior.

[1]DFT calculations have been performed by B. Moses Abraham, Drexel University.

Chapter 4: Fabrication and characterization details

Synthesis of MXenes

MAX phase precursors Ti_3AlC_2 and $Ti_3AlC_{1.5}N_{0.5}$ were provided by A.J. Drexel Nanomaterials Institute. Both MXenes were synthesized by selective etching of their corresponding MAX phases using hydrochloric acid (38 wt.% aq. Thermo Fisher Scientific), and hydrofluoric acid (51 wt.% aq. Thermo Fisher Scientific). After etching, the material was repeatedly washed with deionized water until reaching a neutral pH. The resulting sediment was then delaminated with lithium chloride (LiCl, 99% anhydrous, Thermo Fisher Scientific, -20 mesh) to obtain a colloidal solution of single-layered MXenes [82].

Characterization

X-ray diffraction (XRD) Measurements. XRD was performed using Cu (λ = 1.54 Å) anticathode at 40 kV (Bruker D4 Endeavor). The $Ti_3C_{1.5}N_{0.5}T_x$ was freezed-dried and the powder has been analyzed.

Scanning electron microscopy (SEM) and energy dispersive X-ray spectroscopy (EDS) Measurements. SEM analysis was performed on a Hitachi FEG SU8030 with an accelerating voltage of 5 to 10 kV and a working distance of 4 mm for imaging. For element mapping, the acceleration voltage was set at 5 kV at a working distance of 15 mm. The sample was deposited on an Al_2O_3 substrate via spin-coating.

Photo-induced Force microscopy (PiFM). The local infrared response was investigated with near-field IR microscopy using Vista One from Molecular Vista Inc. The photo-induced mechanical force is produced by a power-modulated quantum cascade laser (5.3 – 13 μm) from Block Engineering, focused at the tip apex using a parabolic mirror (NA=0.9). The signal is detected through the mechanical oscillation of the AFM tip generated by periodic light excitation at the tip apex. Platinum-coated silicon cantilevers were employed, and the system operated in the "sideband" (heterodyne) mode via detecting the photo-induced oscillation signal at the first mechanical tip frequency (f_1) while the laser is modulated at $f_m = f_2 - f_1$ where f_2 represents the first and second mechanical resonance frequencies of the cantilever [146]. Samples were deposited on an Al_2O_3 substrate via spin-coating.

Raman measurements. Micro-Raman analysis was carried out using LabRAM HR Evolution instrument from Horiba Scientific, with a laser excitation at 633 nm and a X50 objective. The sample was deposited on an Al_2O_3 substrate via spin-coating.

Fourier transform infrared (FTIR) measurements. Reflection measurements were done using a micro-FTIR from Frontier Perkin-Elmer with a spectral resolution of 4 cm^{-1}, ranging from 700 to 4000 cm^{-1}, and 10 scans. The sample was deposited on an Al_2O_3 substrate via spin-coating.

Siloxane compounds deposition

Silicon wafers were subjected to a multi-step surface functionalization procedure to enable controlled APTES grafting. Initially, the wafer surfaces were thoroughly

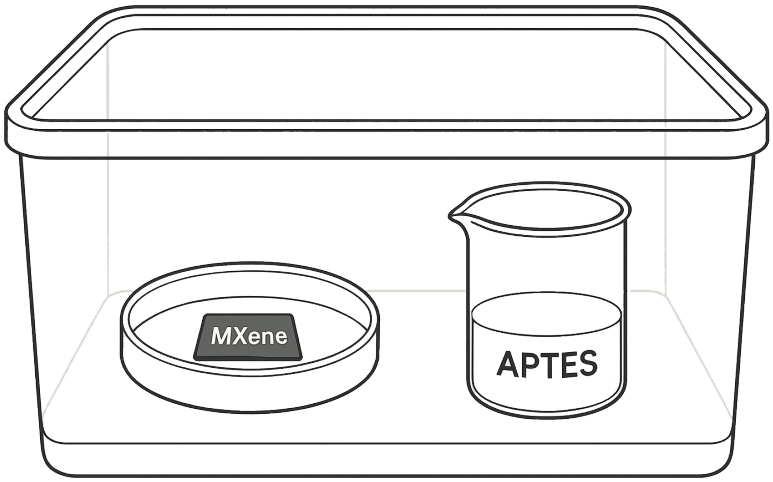

Figure A.1: Schematic of MXene exposure setup: A pristine MXene sample deposited on an alumina substrate is placed inside a sealed chamber together with a glass beaker containing a small volume of neat APTES. The closed environment ensures vapor-phase exposure of the MXene surface to APTES under atmospheric pressure and ambient air.

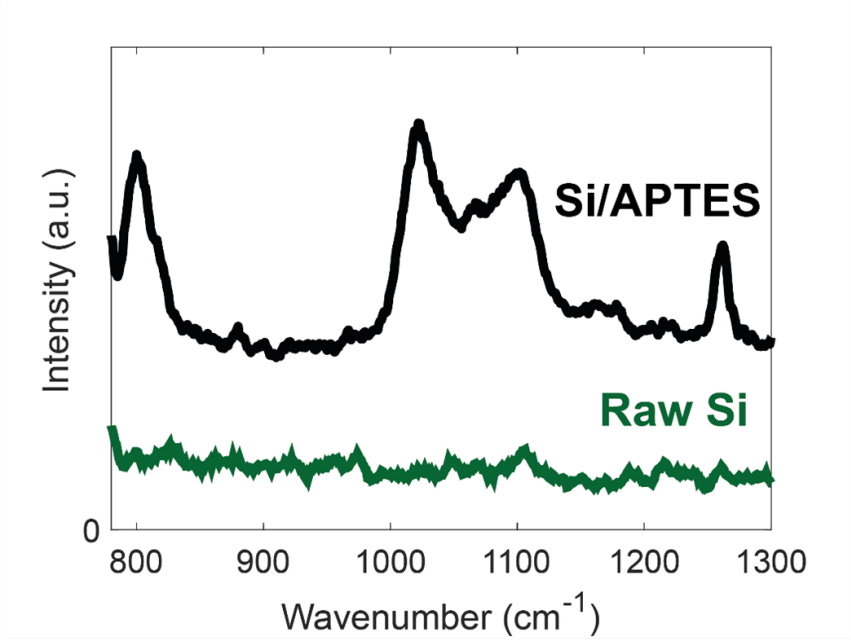

Figure A.2: PiFM spectra of undoped silicon wafer raw (green curve) and after APTES gas functionalization (black curve). Si/APTES spectrum exhibits four characteristic peaks of siloxane compounds.

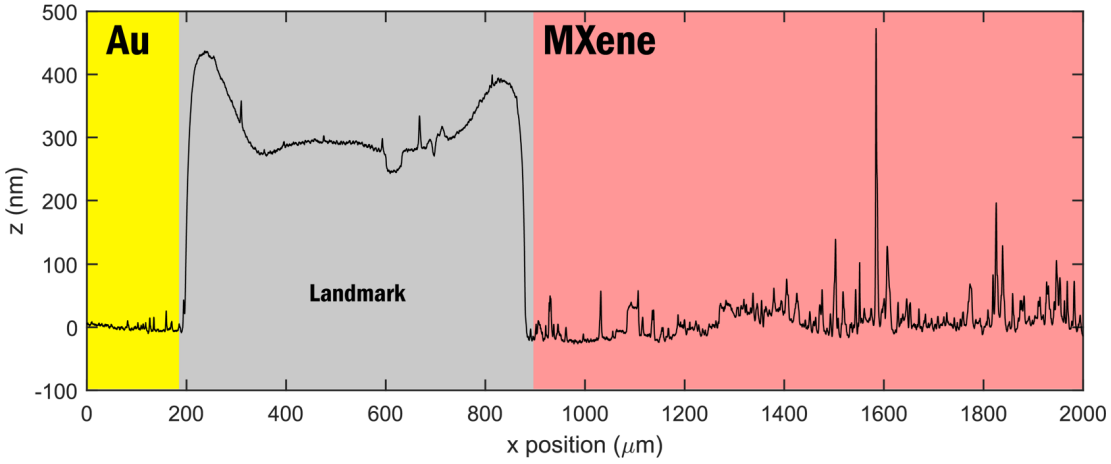

Figure A.3: Profilometric measurement showing an average thickness of 10 nm over 5 measurements.

cleaned using standard semiconductor cleaning protocols to remove organic contaminants and native oxide layers. The cleaned substrates were then exposed to ozone treatment for 10 minutes to maximize surface hydroxyl (-OH) group density, creating reactive sites essential for silane coupling reactions. For APTES functionalization, the hydroxylated silicon wafers were placed in a vacuum desiccator alongside a small volume of neat APTES solution. The system was evacuated under vacuum conditions for 24 hours at room temperature, allowing vapor-phase APTES molecules to react with surface hydroxyl groups through condensation reactions. This vapor-phase approach ensures uniform monolayer formation while minimizing multilayer deposition that can occur in solution-based methods. Following the functionalization period, samples were removed from the vacuum chamber and immediately rinsed with absolute ethanol to eliminate physisorbed APTES molecules and reaction byproducts. The substrates were then dried under nitrogen flow. This controlled functionalization protocol provides a well-defined reference system for validating APTES spectral signatures observed on MXene surfaces, enabling direct comparison between intentional functionalization and environmental contamination processes.

Chapter 5: Application of MXene for sensing using SPR

Characterization of Deposited MXene Films

A Bruker DektakXT stylus profilometer with a 2 μm radius stylus tip and a 1 mg contact force was used to measure the thickness of the deposited MXene. Multiple measurements have been made at different locations across the sample to assess thickness uniformity.

The MXene films' surface morphology, coverage, and homogeneity were examined using scanning electron microscopy (TESCAN MIRA) with an accelerating voltage of 5 kV. The SEM analysis provided information on the orientation of MXene flakes,

the presence of any aggregates, and the completeness of surface coverage under different deposition conditions.

The optical constants of $Ti_3C_2T_x$ at 680 nm (n = 2.22853, k = 1.83062) were determined experimentally using spectroscopic ellipsometry (J.A. Woollam M-2000, USA) on a reference MXene film deposited on a BK7 glass microscope slide. The ellipsometric measurements were performed at multiple angles of incidence (55°, 65°, and 75°) over the spectral range of 400-1000 nm. A wavelength-by-wavelength fitting method was used, which allowed to determine the complex refractive index at each wavelength. In our case, this method is particularly appropriate for novel 2D materials like MXene, where the optical behavior may not follow conventional dispersion relations typically applied to bulk materials [303]. The resulting values were used as baseline parameters to fit both amplitude and phase responses through analytical simulations, allowing us to deduce the actual dielectric constant of the system.

Bibliography

[1] K. S. Novoselov, A. K. Geim, S. V. Morozov, D. Jiang, Y. Zhang, S. V. Dubonos, I. V. Grigorieva, and A. A. Firsov, "Electric Field Effect in Atomically Thin Carbon Films," *Science*, vol. 306, pp. 666–669, Oct. 2004.

[2] G. Cassabois, "Hexagonal boron nitride is an indirect bandgap semiconductor," *NATURE PHOTONICS*, 2016.

[3] K. F. Mak, C. Lee, J. Hone, J. Shan, and T. F. Heinz, "Atomically Thin MoS2: A New Direct-Gap Semiconductor," *PHYSICAL REVIEW LETTERS*, 2010.

[4] L. Li, "Black phosphorus field-effect transistors," *NATURE NANOTECHNOLOGY*, 2014.

[5] A. Gupta, "Recent development in 2D materials beyond graphene," *Progress in Materials Science*, 2015.

[6] G. R. Bhimanapati, Z. Lin, V. Meunier, Y. Jung, J. Cha, S. Das, D. Xiao, Y. Son, M. S. Strano, V. R. Cooper, L. Liang, S. G. Louie, E. Ringe, W. Zhou, S. S. Kim, R. R. Naik, B. G. Sumpter, H. Terrones, F. Xia, Y. Wang, J. Zhu, D. Akinwande, N. Alem, J. A. Schuller, R. E. Schaak, M. Terrones, and J. A. Robinson, "Recent Advances in Two-Dimensional Materials beyond Graphene," vol. 9, no. 12, 2015.

[7] M. Naguib, M. Kurtoglu, V. Presser, J. Lu, J. Niu, M. Heon, L. Hultman, Y. Gogotsi, and M. W. Barsoum, "TwoDimensional Nanocrystals Produced by Exfoliation of Ti3AlC2," *Adv. Mater.*, vol. 23, pp. 4248–4253, Oct. 2011.

[8] B. Anasori, *2D Metal Carbides and Nitrides (MXenes): Structure, Properties and Applications*. Cham: Springer International Publishing AG, 2019.

[9] N. Mounet, "Two-dimensional materials from high-throughput computational exfoliation of experimentally known compounds," *Nature Nanotechnology*, 2018.

[10] S. Haastrup, M. Strange, M. Pandey, T. Deilmann, P. S. Schmidt, N. F. Hinsche, M. N. Gjerding, D. Torelli, P. M. Larsen, A. C. Riis-Jensen, J. Gath, K. W. Jacobsen, J. Jørgen Mortensen, T. Olsen, and K. S. Thygesen, "The computational 2d materials database: high-throughput modeling and discovery of atomically thin crystals," *2D Materials*, vol. 5, p. 042002, sep 2018.

[11] A. Molle, "Buckled two-dimensional Xene sheets," *NATURE MATERIALS*.

[12] F. Zhang and L. Qi, "Recent progress in self-supported metal oxide nanoarray electrodes for advanced lithium-ion batteries," *Advanced Science*, vol. 3, no. 9, p. 1600049, 2016.

[13] P. Ares, J. J. Palacios, G. Abellán, J. Gómez-Herrero, and F. Zamora, "Recent Progress on Antimonene: A New Bidimensional Material," *Adv. Mater.*, 2017.

[14] G. Wang, J. Chang, W. Tang, W. Xie, and Y. S. Ang, "2D materials and heterostructures for photocatalytic water-splitting: a theoretical perspective," *Appl. Phys.*, 2022.

[15] H. Liu, A. T. Neal, Z. Zhu, Z. Luo, and X. Xu, "Phosphorene: An Unexplored 2D Semiconductor with a High Hole Mobility," vol. 8, no. 4, 2014.

[16] A. J. Mannix, "Borophene as a prototype for synthetic 2D materials development," *Nature Nanotechnology*, vol. 13, 2018.

[17] M. Knoll and E. Ruska, "Das Elektronenmikroskop,"

[18] D. W. Pohl and W. Denk, "Optical stethoscopy: Image recording with resolution .1/20," 1984.

[19] A. Dazzi, R. Prazeres, F. Glotin, and J. M. Ortega, "Local infrared microspectroscopy with subwavelength spatial resolution with an atomic force microscope tip used as a photothermal sensor,"

[20] I. Rajapaksa, K. Uenal, and H. K. Wickramasinghe, "Image force microscopy of molecular resonance: A microscope principle," *Appl. Phys. Lett.*, 2014.

[21] J. Jahng, *Photo-induced Force Microscopy and Spectroscopy at Space and Time Limits*. PhD thesis, UC Irvine, 2016. Retrieved from https://escholarship.org/uc/item/6zz957n5.

[22] Z. Dai, L. Liu, and Z. Zhang, "Strain Engineering of 2D Materials: Issues and Opportunities at the Interface," *Adv. Mater.*, 2019.

[23] B. Anasori, "The global expansion of MXenes," *D Materials*, 2023.

[24] J. K. El-Demellawi, S. Lopatin, J. Yin, O. F. Mohammed, and H. N. Alshareef, "Tunable Multipolar Surface Plasmons in 2D Ti3C2Tx MXene Flakes," *ACS Nano*, vol. 12, pp. 8485–8493, Aug. 2018.

[25] V. Mauchamp, M. Bugnet, E. P. Bellido, G. A. Botton, P. Moreau, D. Magne, M. Naguib, T. Cabioc'h, and M. W. Barsoum, "Enhanced and tunable surface plasmons in two-dimensional Ti3C2 stacks: Electronic structure versus boundary effects," *PHYSICAL REVIEW B*, 2014.

[26] D. Zhang, D. Shah, A. Boltasseva, and Y. Gogotsi, "MXenes for Photonics," *ACS Photonics*, vol. 9, pp. 1108–1116, Apr. 2022.

[27] Q. Ma, G. Ren, K. Xu, and J. Z. Ou, "Tunable optical properties of 2d materials and their applications," *Advanced Optical Materials*, vol. 9, no. 2, p. 2001313, 2021.

[28] Y. Fang, Y. Ge, C. Wang, and H. Zhang, "Mid-infrared photonics using 2d materials: Status and challenges," *Laser & Photonics Reviews*, vol. 14, no. 1, p. 1900098, 2020.

[29] X. Zeng, C. Wan, Z. Zhao, D. Huang, Z. Wang, X. Cheng, and T. Jiang, "Nonlinear optics of two-dimensional heterostructures," *Frontiers of Physics*, vol. 19, no. 3, p. 33301, 2024.

[30] Y. Wang, W. Knoll, and J. Dostalek, "Bacterial pathogen surface plasmon resonance biosensor advanced by long range surface plasmons and magnetic nanoparticle assays," *Analytical Chemistry*, vol. 84, no. 19, pp. 8345–8350, 2012.

[31] K. S. Novoselov, V. I. Fal'ko, L. Colombo, P. R. Gellert, M. G. Schwab, and K. Kim, "A roadmap for graphene," *Nature*, vol. 490, no. 7419, pp. 192–200, 2012.

[32] F. Xia, H. Wang, D. Xiao, M. Dubey, and A. Ramasubramaniam, "Two-dimensional material nanophotonics," *Nature Photonics*, vol. 8, no. 12, pp. 899–907, 2014.

[33] A. K. Geim and I. V. Grigorieva, "Van der waals heterostructures," *Nature*, vol. 499, no. 7459, pp. 419–425, 2013.

[34] K. S. Novoselov, A. K. Geim, S. V. Morozov, D. Jiang, Y. Zhang, S. V. Dubonos, I. V. Grigorieva, and A. A. Firsov, "Electric field effect in atomically thin carbon films," *Science*, vol. 306, no. 5696, pp. 666–669, 2004.

[35] A. K. Geim and K. S. Novoselov, "The rise of graphene," *Nature Materials*, vol. 6, no. 3, pp. 183–191, 2007.

[36] R. R. Nair, P. Blake, A. N. Grigorenko, K. S. Novoselov, T. J. Booth, T. Stauber, N. M. Peres, and A. K. Geim, "Fine structure constant defines visual transparency of graphene," *Science*, vol. 320, no. 5881, pp. 1308–1308, 2008.

[37] A. N. Grigorenko, M. Polini, and K. S. Novoselov, "Graphene plasmonics," *Nature Photonics*, vol. 6, no. 11, pp. 749–758, 2012.

[38] F. Wang, Y. Zhang, C. Tian, C. Girit, A. Zettl, M. Crommie, and Y. R. Shen, "Gate-variable optical transitions in graphene," *Science*, vol. 320, no. 5873, pp. 206–209, 2008.

[39] M. Liu, X. Yin, E. Ulin-Avila, B. Geng, T. Zentgraf, L. Ju, F. Wang, and X. Zhang, "A graphene-based broadband optical modulator," *Nature*, vol. 474, no. 7349, pp. 64–67, 2011.

[40] Q. Bao, H. Zhang, Y. Wang, Z. Ni, Y. Yan, Z. X. Shen, K. P. Loh, and D. Tang, "Atomic-layer graphene as a saturable absorber for ultrafast pulsed lasers," *Advanced Functional Materials*, vol. 19, no. 19, pp. 3077–3083, 2009.

[41] F. Xia, T. Mueller, Y.-m. Lin, A. Valdes-Garcia, and P. Avouris, "Ultrafast graphene photodetector," *Nature Nanotechnology*, vol. 4, no. 12, pp. 839–843, 2009.

[42] H. Yan, T. Low, W. Zhu, Y. Wu, M. Freitag, X. Li, F. Guinea, P. Avouris, and F. Xia, "Tunable infrared plasmonic devices using graphene/insulator stacks," *Nature Nanotechnology*, vol. 8, no. 9, pp. 630–633, 2013.

[43] J. Wilson and A. Yoffe, "The transition metal dichalcogenides discussion and interpretation of the observed optical, electrical and structural properties," *Advances in Physics*, vol. 18, no. 73, pp. 193–335, 1969.

[44] G. Eda, H. Yamaguchi, D. Voiry, T. Fujita, M. Chen, and M. Chhowalla, "Photoluminescence from chemically exfoliated mos2," *Nano letters*, vol. 11, no. 12, pp. 5111–5116, 2011.

[45] K. F. Mak, C. Lee, J. Hone, J. Shan, and T. F. Heinz, "Atomically thin mos2: a new direct-gap semiconductor," *Physical review letters*, vol. 105, no. 13, p. 136805, 2010.

[46] A. Splendiani, L. Sun, Y. Zhang, T. Li, J. Kim, C.-Y. Chim, G. Galli, and F. Wang, "Emerging photoluminescence in monolayer mos2," *Nano letters*, vol. 10, no. 4, pp. 1271–1275, 2010.

[47] Y. Sun, D. Wang, and Z. Shuai, "Indirect-to-direct band gap crossover in few-layer transition metal dichalcogenides: a theoretical prediction," *The Journal of Physical Chemistry C*, vol. 120, no. 38, pp. 21866–21870, 2016.

[48] A. Chernikov, T. C. Berkelbach, H. M. Hill, A. Rigosi, Y. Li, O. B. Aslan, D. R. Reichman, M. S. Hybertsen, and T. F. Heinz, "Exciton binding energy and nonhydrogenic rydberg series in monolayer ws2," *Physical review letters*, vol. 113, no. 7, p. 076802, 2014.

[49] M. Bernardi, M. Palummo, and J. C. Grossman, "Extraordinary sunlight absorption and one nanometer thick photovoltaics using two-dimensional monolayer materials," *Nano letters*, vol. 13, no. 8, pp. 3664–3670, 2013.

[50] D. Xiao, G.-B. Liu, W. Feng, X. Xu, and W. Yao, "Coupled spin and valley physics in monolayers of mos2 and other group-vi dichalcogenides," *Physical review letters*, vol. 108, no. 19, p. 196802, 2012.

[51] J. R. Schaibley, H. Yu, G. Clark, P. Rivera, J. S. Ross, K. L. Seyler, W. Yao, and X. Xu, "Valleytronics in 2d materials," *Nature Reviews Materials*, vol. 1, no. 11, pp. 1–15, 2016.

[52] H. J. Conley, B. Wang, J. I. Ziegler, R. F. Haglund Jr, S. T. Pantelides, and K. I. Bolotin, "Bandgap engineering of strained monolayer and bilayer mos2," *Nano letters*, vol. 13, no. 8, pp. 3626–3630, 2013.

[53] A. Raja, A. Chaves, J. Yu, G. Arefe, H. M. Hill, A. F. Rigosi, T. C. Berkelbach, P. Nagler, C. Schüller, T. Korn, *et al.*, "Coulomb engineering of the bandgap and excitons in two-dimensional materials," *Nature communications*, vol. 8, no. 1, pp. 1–7, 2017.

[54] K. F. Mak, K. He, J. Shan, and T. F. Heinz, "Control of valley polarization in monolayer mos2 by optical helicity," *Nature nanotechnology*, vol. 7, no. 8, pp. 494–498, 2012.

[55] P. Rivera, J. R. Schaibley, A. M. Jones, J. S. Ross, S. Wu, G. Aivazian, P. Klement, K. Seyler, G. Clark, N. J. Ghimire, *et al.*, "Observation of long-lived interlayer excitons in monolayer mose2–wse2 heterostructures," *Nature communications*, vol. 6, no. 1, pp. 1–6, 2015.

[56] T. Mueller and E. Malic, "Exciton physics and device application of two-dimensional transition metal dichalcogenide semiconductors," *npj 2D Materials and Applications*, vol. 2, no. 1, pp. 1–12, 2018.

[57] V. Tran, R. Soklaski, Y. Liang, and L. Yang, "Layer-controlled band gap and anisotropic excitons in few-layer black phosphorus," *Phys. Rev. B*, vol. 89, p. 235319, 2014.

[58] X. Wang, A. M. Jones, K. L. Seyler, V. Tran, Y. Jia, H. Zhao, H. Wang, L. Yang, X. Xu, and F. Xia, "Highly anisotropic and robust excitons in monolayer black phosphorus," *Nat. Nanotechnol.*, vol. 10, pp. 517–521, 2015.

[59] J. Qiao, X. Kong, Z.-X. Hu, F. Yang, and W. Ji, "High-mobility transport anisotropy and linear dichroism in few-layer black phosphorus," *Nat. Commun.*, vol. 5, p. 4475, 2014.

[60] C. Chen, N. Youngblood, R. Peng, D. Yoo, D. A. Mohr, T. W. Johnson, S.-H. Oh, and M. Li, "Widely tunable black phosphorus mid-infrared photodetector," *Nano Lett.*, vol. 17, pp. 985–991, 2017.

[61] Q. Guo, A. Pospischil, M. Bhuiyan, H. Jiang, H. Tian, D. Farmer, B. Deng, C. Li, S.-J. Han, H. Wang, Q. Xia, T.-P. Ma, T. Mueller, and F. Xia, "Black phosphorus mid-infrared photodetectors with high gain," *Nano Lett.*, vol. 16, pp. 4648–4655, 2016.

[62] Z. Qin, G. Xie, C. Zhao, S. Wen, P. Yuan, and L. Qian, "Black phosphorus as saturable absorber for the q-switched er:zblan fiber laser at 2.8 μm," *Opt. Express*, vol. 23, pp. 24713–24718, 2015.

[63] Z. Qin, G. Xie, C. Zhao, S. Zhang, P. Yuan, and L. Qian, "Black phosphorus q-switched and mode-locked mid-infrared er:zblan fiber laser at 3.5 μm wavelength," *Opt. Lett.*, vol. 41, pp. 56–59, 2016.

[64] S. Deckoff-Jones, H. Lin, D. Kita, H. Zheng, D. Li, W. Zhang, and J. Hu, "Chalcogenide glass waveguide-integrated black phosphorus mid-infrared photodetector," *J. Opt.*, vol. 20, p. 044004, 2018.

[65] K. Watanabe, T. Taniguchi, and H. Kanda, "Direct-bandgap properties and evidence for ultraviolet lasing of hexagonal boron nitride single crystal," *Nat. Mater.*, vol. 3, pp. 404–409, 2004.

[66] J. D. Caldwell, A. V. Kretinin, Y. Chen, V. Giannini, M. M. Fogler, Y. Francescato, C. T. Ellis, J. G. Tischler, C. R. Woods, A. J. Giles,

M. Hong, K. Watanabe, T. Taniguchi, S. A. Maier, and K. S. Novoselov, "Sub-diffractional volume-confined polaritons in the natural hyperbolic material hexagonal boron nitride," *Nat. Commun.*, vol. 5, p. 5221, 2014.

[67] A. Woessner, M. B. Lundeberg, Y. Gao, A. Principi, P. Alonso-González, M. Carrega, K. Watanabe, T. Taniguchi, G. Vignale, M. Polini, J. Hone, R. Hillenbrand, and F. H. L. Koppens, "Electrical 2π phase control of infrared light in a 350-nm footprint using graphene plasmons," *Nat. Mater.*, vol. 16, pp. 809–813, 2017.

[68] Z. Zheng, N. Xu, S. L. Oscurato, M. Tamagnone, F. Sun, Y. Jiang, Y. Ke, J. Chen, W. Huang, W. L. Wilson, A. Ambrosio, S. Deng, and H. Chen, "Phonon polaritons in twisted double-layers of hyperbolic van der waals crystals," *Nano Lett.*, vol. 20, pp. 5301–5308, 2020.

[69] P. Li, M. Lewin, A. V. Kretinin, J. D. Caldwell, K. S. Novoselov, T. Taniguchi, K. Watanabe, F. Gaussmann, and T. Taubner, "Infrared hyperbolic metasurface based on nanostructured van der waals materials," *Science*, vol. 359, pp. 892–896, 2018.

[70] X. Xiao, H. Wang, P. Urbankowski, and Y. Gogotsi, "Topochemical synthesis of 2D materials," *Chem. Soc. Rev.*, vol. 47, no. 23, pp. 8744–8765, 2018.

[71] A. Lipatov, A. Goad, M. J. Loes, N. S. Vorobeva, J. Abourahma, Y. Gogotsi, and A. Sinitskii, "High electrical conductivity and breakdown current density of individual monolayer Ti3C2T MXene flakes," *Matter*, vol. 4, pp. 1413–1427, Apr. 2021.

[72] B. Anasori, M. R. Lukatskaya, and Y. Gogotsi, "2D metal carbides and nitrides (MXenes) for energy storage," *Nature Reviews Materials*.

[73] M. Han, C. E. Shuck, R. Rakhmanov, D. Parchment, B. Anasori, C. M. Koo, G. Friedman, and Y. Gogotsi, "Beyond $Ti_3C_2T_x$: MXenes for Electromagnetic Interference Shielding," *ACS Nano*, vol. 14, pp. 5008–5016, Apr. 2020.

[74] R. Rakhmanov, C. E. Shuck, J. Al Hourani, S. Ippolito, Y. Gogotsi, and G. Friedman, "Ultrathin MXene film interaction with electromagnetic radiation in the microwave range," *Applied Physics Letters*, vol. 123, no. 20, p. 204105, 2023.

[75] A. Sinha, Dhanjai, H. Zhao, Y. Huang, X. Lu, J. Chen, and R. Jain, "MXene: An emerging material for sensing and biosensing," *TrAC Trends in Analytical Chemistry*, vol. 105, pp. 424–435, Aug. 2018.

[76] M. T. Hossaın, M. R. Repon, M. A. Shahid, A. Ali, and T. Islam, "Progress, Prospects and Challenges of MXene Integrated Optoelectronics Devices," *ChemElectroChem*, vol. 11, p. e202400008, Apr. 2024.

[77] M. Dahlqvist, M. W. Barsoum, and J. Rosen, "MAX phases – Past, present, and future," *Materials Today*, vol. 72, pp. 1–24, Jan. 2024.

[78] S. Z. Butler, S. M. Hollen, L. Cao, Y. Cui, J. A. Gupta, H. R. Gutiérrez, T. F. Heinz, S. S. Hong, J. Huang, A. F. Ismach, E. Johnston-Halperin, M. Kuno, V. V. Plashnitsa, R. D. Robinson, R. S. Ruoff, S. Salahuddin, J. Shan, L. Shi, M. G. Spencer, M. Terrones, W. Windl, and J. E. Goldberger, "Progress, Challenges, and Opportunities in Two-Dimensional Materials Beyond Graphene," *ACS Nano*, vol. 7, pp. 2898–2926, Apr. 2013.

[79] A. K. Geim and I. V. Grigorieva, "Van der Waals heterostructures," *Nature*, vol. 499, pp. 419–425, July 2013.

[80] Q. H. Wang, K. Kalantar-Zadeh, A. Kis, J. N. Coleman, and M. S. Strano, "Electronics and optoelectronics of two-dimensional transition metal dichalcogenides," *Nature Nanotech*, vol. 7, pp. 699–712, Nov. 2012.

[81] M. A. Hope, A. C. Forse, K. J. Griffith, M. R. Lukatskaya, M. Ghidiu, Y. Gogotsi, and C. P. Grey, "NMR reveals the surface functionalisation of Ti_3 C_2 MXene," *Phys. Chem. Chem. Phys.*, vol. 18, no. 7, pp. 5099–5102, 2016.

[82] M. Downes, C. E. Shuck, B. McBride, J. Busa, and Y. Gogotsi, "Comprehensive synthesis of Ti3C2Tx from MAX phase to MXene," *Nat Protoc*, vol. 19, pp. 1807–1834, June 2024.

[83] O. Mashtalir, M. Naguib, B. Dyatkin, Y. Gogotsi, and M. W. Barsoum, "Kinetics of aluminum extraction from Ti3AlC2 in hydrofluoric acid," *Materials Chemistry and Physics*, vol. 139, pp. 147–152, Apr. 2013.

[84] E. S. Muckley, M. Naguib, H.-W. Wang, L. Vlcek, N. C. Osti, R. L. Sacci, X. Sang, R. R. Unocic, Y. Xie, M. Tyagi, E. Mamontov, K. L. Page, P. R. C. Kent, J. Nanda, and I. N. Ivanov, "Multimodality of Structural, Electrical, and Gravimetric Responses of Intercalated MXenes to Water," *ACS Nano*, vol. 11, pp. 11118–11126, Nov. 2017.

[85] M. Naguib, O. Mashtalir, J. Carle, V. Presser, J. Lu, L. Hultman, Y. Gogotsi, and M. W. Barsoum, "Two-Dimensional Transition Metal Carbides," *ACS Nano*, vol. 6, pp. 1322–1331, Feb. 2012.

[86] J. Halim, S. Kota, M. R. Lukatskaya, M. Naguib, M. Zhao, E. J. Moon, J. Pitock, J. Nanda, S. J. May, Y. Gogotsi, and M. W. Barsoum, "Synthesis and Characterization of 2D Molybdenum Carbide (MXene)," *Adv Funct Materials*, vol. 26, pp. 3118–3127, May 2016.

[87] S. P. Surwade, S. N. Smirnov, I. V. Vlassiouk, R. R. Unocic, G. M. Veith, S. Dai, and S. M. Mahurin, "Water desalination using nanoporous single-layer graphene," *Nature Nanotech*, vol. 10, pp. 459–464, May 2015.

[88] C. E. Ren, K. B. Hatzell, M. Alhabeb, Z. Ling, K. A. Mahmoud, and Y. Gogotsi, "Charge- and Size-Selective Ion Sieving Through Ti_3 C_2 T_x MXene Membranes," *J. Phys. Chem. Lett.*, vol. 6, pp. 4026–4031, Oct. 2015.

[89] G. R. Berdiyorov, "Effect of surface functionalization on the electronic transport properties of Ti_3 C_2 MXene," *EPL*, vol. 111, p. 67002, Sept. 2015.

[90] S. Nosé, "A molecular dynamics method for simulations in the canonical ensemble," *Molecular Physics*, vol. 52, pp. 255–268, June 1984.

[91] P. Srivastava, A. Mishra, H. Mizuseki, K.-R. Lee, and A. K. Singh, "Mechanistic Insight into the Chemical Exfoliation and Functionalization of Ti_3 C_2 MXene," *ACS Appl. Mater. Interfaces*, vol. 8, pp. 24256–24264, Sept. 2016.

[92] B. Anasori, C. Shi, E. J. Moon, Y. Xie, C. A. Voigt, P. R. C. Kent, S. J. May, S. J. L. Billinge, M. W. Barsoum, and Y. Gogotsi, "Control of electronic properties of 2D carbides (MXenes) by manipulating their transition metal layers," *Nanoscale Horiz.*, vol. 1, no. 3, pp. 227–234, 2016.

[93] C. Shi, M. Beidaghi, M. Naguib, O. Mashtalir, Y. Gogotsi, and S. J. Billinge, "Structure of Nanocrystalline Ti 3 C 2 MXene Using Atomic Pair Distribution Function," *Phys. Rev. Lett.*, vol. 112, p. 125501, Mar. 2014.

[94] M. A. Hope, A. C. Forse, K. J. Griffith, M. R. Lukatskaya, M. Ghidiu, Y. Gogotsi, and C. P. Grey, "Nmr reveals the surface functionalization of ti3c2 mxene," *Physical Chemistry Chemical Physics*, vol. 18, no. 7, pp. 5099–5102, 2016.

[95] D. Magne, V. Mauchamp, S. Célérier, P. Chartier, and T. Cabioc'h, "Spectroscopic evidence in the visible-ultraviolet energy range of surface functionalization sites in the multilayer Ti 3 C 2 MXene," *Phys. Rev. B*, vol. 91, p. 201409, May 2015.

[96] M. Tang, J. Li, Y. Wang, W. Han, S. Xu, M. Lu, W. Zhang, and H. Li, "Surface Terminations of MXene: Synthesis, Characterization, and Properties," *Symmetry*, vol. 14, p. 2232, Oct. 2022.

[97] L. H. Karlsson, J. Birch, J. Halim, M. W. Barsoum, and P. O. Persson, "Atomically Resolved Structural and Chemical Investigation of Single MXene Sheets," *Nano Lett.*, vol. 15, pp. 4955–4960, Aug. 2015.

[98] M. Alhabeb, K. Maleski, B. Anasori, P. Lelyukh, L. Clark, S. Sin, and Y. Gogotsi, "Guidelines for Synthesis and Processing of Two-Dimensional Titanium Carbide (Ti_3 C_2 T_x MXene)," *Chem. Mater.*, vol. 29, pp. 7633–7644, Sept. 2017.

[99] Y. Gogotsi and B. Anasori, "The Rise of MXenes," *ACS Nano*, vol. 13, pp. 8491–8494, Aug. 2019.

[100] A. Sarycheva and Y. Gogotsi, "Raman Spectroscopy Analysis of the Structure and Surface Chemistry of Ti_3 C_2 T_x MXene," *Chem. Mater.*, vol. 32, pp. 3480–3488, Apr. 2020.

[101] P. P. Michałowski, M. Anayee, T. S. Mathis, S. Kozdra, A. Wójcik, K. Hantanasirisakul, I. Jóźwik, A. Piątkowska, M. Możdżonek, A. Malinowska, R. Diduszko, E. Wierzbicka, and Y. Gogotsi, "Oxycarbide MXenes and MAX phases identification using monoatomic layer-by-layer analysis with ultralow-energy secondary-ion mass spectrometry," *Nature Nanotechnology*, vol. 17, no. 11, pp. 1192–1197, 2022.

[102] M. R. Shcherbakov, E. O. Potma, Y. Sugawara, D. Nowak, M. Stepanova, P. R. Davies, J. Davies-Jones, and H. K. Wickramasinghe, "Photo-induced force microscopy," *Nature Reviews Methods Primers*, vol. 5, p. 34, may 2025.

[103] Y. Ibrahim, A. Mohamed, A. M. Abdelgawad, K. Eid, A. M. Abdullah, and A. Elzatahry, "The Recent Advances in the Mechanical Properties of Self-Standing Two-Dimensional MXene-Based Nanostructures: Deep Insights into the Supercapacitor," *Nanomaterials*, vol. 10, p. 1916, Sept. 2020.

[104] K. Maleski, C. E. Shuck, A. T. Fafarman, and Y. Gogotsi, "The Broad Chromatic Range of Two-Dimensional Transition Metal Carbides," *Advanced Optical Materials*, vol. 9, p. 2001563, Feb. 2021.

[105] K. Chaudhuri, M. Alhabeb, Z. Wang, V. M. Shalaev, Y. Gogotsi, and A. Boltasseva, "Highly Broadband Absorber Using Plasmonic Titanium Carbide (MXene)," *ACS Photonics*, vol. 5, pp. 1115–1122, Mar. 2018.

[106] A. Sarycheva, T. Makaryan, K. Maleski, E. Satheeshkumar, A. Melikyan, H. Minassian, M. Yoshimura, and Y. Gogotsi, "Two-Dimensional Titanium Carbide (MXene) as Surface-Enhanced Raman Scattering Substrate," *J. Phys. Chem. C*, vol. 121, pp. 19983–19988, Sept. 2017.

[107] L. Wu, Q. You, Y. Shan, S. Gan, Y. Zhao, X. Dai, and Y. Xiang, "Few-layer Ti3C2Tx MXene: A promising surface plasmon resonance biosensing material to enhance the sensitivity," *Sensors and Actuators B: Chemical*, vol. 277, pp. 210–215, 2018.

[108] L. Hasanah, R. Mutia, C. Wulandari, B. Mulyanti, S. K. Sahari, R. E. Pawinanto, and A. A. Hamzah, "Investigating the effect of surface termination and thickness of MXene on the detection response of the SPR sensor using FDTD simulation," *Results in Optics*, vol. 12, p. 100438, 2023.

[109] X. Li, M. Fang, W. Wang, S. Guo, W. Liu, H. Liu, and X. Wang, "Graphene heat dissipation film for thermal management of hot spot in electronic device," *Journal of Materials Science: Materials in Electronics*, vol. 27, no. 7, pp. 7715–7721, 2016.

[110] B. Anasori, M. R. Lukatskaya, and Y. Gogotsi, "2d metal carbides and nitrides (mxenes) for energy storage," *Nature Reviews Materials*, vol. 2, no. 2, pp. 1–17, 2017.

[111] M. Alhabeb, K. Maleski, B. Anasori, P. Lelyukh, L. Clark, S. Sin, and Y. Gogotsi, "Guidelines for synthesis and processing of two-dimensional titanium carbide ($ti_3c_2t_x$ mxene)," *Chemistry of Materials*, vol. 29, no. 18, pp. 7633–7644, 2017.

[112] H. Gunzler and H.-U. Gremlich, *IR Spectroscopy: An Introduction*. Weinheim: Wiley-VCH, 1994.

[113] T. Parker, D. Zhang, D. Bugallo, K. Shevchuk, M. Downes, G. Valurouthu, A. Inman, B. Chacon, T. Zhang, C. E. Shuck, Y.-J. Hu, and Y. Gogotsi, "Fourier-Transform Infrared Spectral Library of MXenes," *Chem. Mater.*, vol. 36, pp. 8437–8446, Sept. 2024.

[114] K. Shevchuk, A. Sarycheva, C. E. Shuck, and Y. Gogotsi, "Raman Spectroscopy Characterization of 2D Carbide and Carbonitride MXenes," *Chem. Mater.*, vol. 35, pp. 8239–8247, Oct. 2023.

[115] K. Shevchuk, A. Sarycheva, and Y. Gogotsi, "Evaluation of two-dimensional transition-metal carbides and carbonitrides (MXenes) for SERS substrates," *MRS Bulletin*, vol. 47, pp. 545–554, June 2022.

[116] K. Shevchuk, *Raman spectroscopy of MXenes beyond $Ti_3C_2T_x$: characterization and applications*. PhD thesis, Drexel University, Philadelphia, Pennsylvania, 2025.

[117] A. Sarycheva and Y. Gogotsi, "Raman spectroscopy analysis of the structure and surface chemistry of $ti_3c_2t_x$ mxene," *Chemistry of Materials*, vol. 32, no. 8, pp. 3480–3488, 2020.

[118] R. García, "Dynamic atomic force microscopy methods," *Surface Science Reports*, vol. 47, pp. 197–301, Sept. 2002.

[119] G. Meyer and N. M. Amer, "Erratum: Novel optical approach to atomic force microscopy [Appl. Phys. Lett. **5 3** , 1045 (1988)]," *Applied Physics Letters*, vol. 53, pp. 2400–2402, Dec. 1988.

[120] Q. Zhong, D. Inniss, K. Kjoller, and V. B. Elings, "Fractured polymer/silica fiber surface studied by tapping mode atomic force microscopy," *Surface Science Letters*, vol. 290, no. 1-2, pp. L688–L692, 1993.

[121] E. Synge, "XXXVIII. *A suggested method for extending microscopic resolution into the ultra-microscopic region*," *The London, Edinburgh, and Dublin Philosophical Magazine and Journal of Science*, vol. 6, pp. 356–362, Aug. 1928.

[122] B. Knoll and F. Keilmann, "Enhanced dielectric contrast in scattering-type scanning near-field optical microscopy," *Optics Communications*, vol. 182, pp. 321–328, Aug. 2000.

[123] R. Hillenbrand, T. Taubner, and F. Keilmann, "Phonon-enhanced light–matter interaction at the nanometre scale," *Nature*, vol. 418, pp. 159–162, July 2002.

[124] F. Keilmann, "Surface-polariton propagation for scanning near-field optical microscopy application," *Journal of Microscopy*, vol. 194, pp. 567–570, May 1999.

[125] X. Chen, D. Hu, R. Mescall, G. You, D. N. Basov, Q. Dai, and M. Liu, "Modern Scattering-Type Scanning Near-Field Optical Microscopy for Advanced Material Research," *Advanced Materials*, vol. 31, p. 1804774, June 2019.

[126] Zurich Instruments, "Principles of lock-in detection and the state of the art," white paper, Zurich Instruments, Zurich, Switzerland, April 2023. Last update: April 2023.

[127] X. G. Xu, L. Gilburd, and G. C. Walker, "Phase stabilized homodyne of infrared scattering type scanning near-field optical microscopy," *Applied Physics Letters*, vol. 105, p. 263104, Dec. 2014.

[128] L. Gomez, R. Bachelot, A. Bouhelier, G. P. Wiederrecht, S.-h. Chang, S. K. Gray, F. Hua, S. Jeon, J. A. Rogers, M. E. Castro, S. Blaize, I. Stefanon, G. Lerondel, and P. Royer, "Apertureless scanning near-field optical microscopy: a comparison between homodyne and heterodyne approaches," *J. Opt. Soc. Am. B*, vol. 23, p. 823, May 2006.

[129] J. E. Hall, G. P. Wiederrecht, S. K. Gray, S.-H. Chang, S. Jeon, J. A. Rogers, R. Bachelot, and P. Royer, "Heterodyne apertureless near-field scanning optical microscopy on periodic gold nanowells," *Opt. Express*, vol. 15, no. 7, p. 4098, 2007.

[130] I. Stefanon, S. Blaize, A. Bruyant, S. Aubert, G. Lerondel, R. Bachelot, and P. Royer, "Heterodyne detection of guided waves using a scattering-type Scanning Near-Field Optical Microscope," *Opt. Express*, vol. 13, no. 14, p. 5553, 2005.

[131] N. Ocelic, A. Huber, and R. Hillenbrand, "Pseudoheterodyne detection for background-free near-field spectroscopy," *Applied Physics Letters*, vol. 89, p. 101124, Sept. 2006.

[132] C. Moreno, J. Alda, E. Kinzel, and G. Boreman, "Phase imaging and detection in pseudo-heterodyne scattering scanning near-field optical microscopy measurements," *Appl. Opt.*, vol. 56, p. 1037, Feb. 2017.

[133] D. E. Tranca, C. Stoichita, R. Hristu, S. G. Stanciu, and G. A. Stanciu, "A study on the image contrast of pseudo-heterodyned scattering scanning near-field optical microscopy," *Opt. Express*, vol. 22, p. 1687, Jan. 2014.

[134] A. Bruyant, J. Vaillant, T.-H. Wu, Y. Zhu, Y. Huang, and A. Al Mohtar, "Interferometry Using Generalized Lock-in Amplifier (G-LIA): A Versatile Approach for Phase-Sensitive Sensing and Imaging," in *Optical Interferometry* (A. A. Banishev, M. Bhowmick, and J. Wang, eds.), InTech, Feb. 2017.

[135] A. A. Sifat, J. Jahng, and E. O. Potma, "Photo-induced force microscopy (PiFM) – principles and implementations," *Chem. Soc. Rev.*, vol. 51, no. 11, pp. 4208–4222, 2022.

[136] J. A. Davies-Jones and P. R. Davies, "Photo-induced force microscopy: chemical spectroscopy beyond the diffraction limit," *Materials Chemistry Frontiers*, vol. 6, no. 12, pp. 1552–1573, 2022.

[137] F. T. Ladani and E. O. Potma, "Dyadic green's function formalism for photoinduced forces in tip-sample nanojunctions," *Phys. Rev. B*, vol. 95, p. 205440, May 2017.

[138] L. Novotny and B. Hecht, *Principles of nano-optics*. Cambridge: Cambridge University Press, 2nd ed., 2012.

[139] K.-T. Wu, Y. El-Helou, E. Usureau, E. Vuillermet, M. Kazan, M. Lazar, G. Gautier, W.-Y. Woon, and A. Bruyant, "Infrared photoinduced force near-field spectroscopy of silicon carbide," *Applied Surface Science*, vol. 684, p. 161798, 2025. Received 6 June 2024; Received in revised form 11 November 2024; Accepted 12 November 2024; Available online 20 November 2024.

[140] A. A. Govyadinov, I. Amenabar, F. Huth, P. S. Carney, and R. Hillenbrand, "Quantitative Measurement of Local Infrared Absorption and Dielectric Function with Tip-Enhanced Near-Field Microscopy," *J. Phys. Chem. Lett.*, vol. 4, pp. 1526–1531, May 2013.

[141] J. Jahng, E. O. Potma, and E. S. Lee, "Nanoscale spectroscopic origins of photoinduced tip–sample force in the midinfrared," *Proceedings of the National Academy of Sciences*, vol. 116, no. 52, pp. 26359–26366, 2019.

[142] J. Li, J. Jahng, X. Ma, J. Liang, X. Zhang, Q. Min, X.-L. Wang, S. Chen, E. S. Lee, and X.-H. Xia, "Surface-phonon-polariton-enhanced photoinduced dipole force for nanoscale infrared imaging," *National Science Review*, vol. 11, no. 5, p. nwae101, 2024.

[143] J. Jahng, E. O. Potma, and E. S. Lee, "Tip-enhanced thermal expansion force for nanoscale chemical imaging and spectroscopy in photoinduced force microscopy," *Analytical Chemistry*, vol. 90, no. 18, pp. 11054–11061, 2018.

[144] D. Nowak, W. Morrison, H. K. Wickramasinghe, J. Jahng, E. Potma, L. Wan, R. Ruiz, T. R. Albrecht, K. Schmidt, J. Frommer, D. P. Sanders, and S. Park, "Nanoscale chemical imaging by photoinduced force microscopy," *Sci. Adv.*, vol. 2, p. e1501571, Mar. 2016.

[145] J. A. Davies-Jones and P. R. Davies, "Photo induced force microscopy: chemical spectroscopy beyond the diffraction limit," *Mater. Chem. Front.*, vol. 6, no. 12, pp. 1552–1573, 2022.

[146] R. A. Murdick, W. Morrison, D. Nowak, T. R. Albrecht, J. Jahng, and S. Park, "Photoinduced force microscopy: A technique for hyperspectral nanochemical mapping," *Jpn. J. Appl. Phys.*, vol. 56, p. 08LA04, Aug. 2017.

[147] S. Patabendigedara, D. Nowak, M. J. B. Nancarrow, and S. M. Clark, "Determining the water content of nominally anhydrous minerals at the nanometre scale," *Review of Scientific Instruments*, vol. 92, p. 023103, Feb 2021.

[148] Y. E. Helou, *Thermal Investigation of Silicon Carbide Based on Infrared Photo-induced Force Microscopy*. Thèse de doctorat, Université de Technologie de Troyes, Troyes, France, December 2024. Spécialité : Matériaux, Mécanique, Optique et Nanotechnologie.

[149] L. Pauling, *The nature of the chemical bond and the structure of molecules and crystals: An introduction to modern structural chemistry*. Ithaca, New York: Cornell University Press, 3rd ed., 1989.

[150] L. Gao, H. Chen, A. V. Kuklin, S. Wageh, A. A. Al-Ghamdi, H. Ågren, and H. Zhang, "Optical properties of few-layer Ti_3CN MXene: From experimental observations to theoretical calculations," *ACS Nano*, vol. 16, no. 2, pp. 3059–3069, 2022.

[151] A. D. Handoko, S. N. Steinmann, and Z. W. Seh, "Theory-guided materials design: two-dimensional MXenes in electro- and photocatalysis," *Nanoscale Horizons*, vol. 4, no. 4, pp. 809–827, 2019.

[152] M. Han, D. Zhang, A. Singh, T. Hryhorchuk, C. Eugene Shuck, T. Zhang, L. Bi, B. McBride, V. B. Shenoy, and Y. Gogotsi, "Versatility of infrared properties of MXenes," *Materials Today*, vol. 64, pp. 31–39, Apr. 2023.

[153] A. Iqbal, F. Shahzad, K. Hantanasirisakul, M.-K. Kim, J. Kwon, J. Hong, H. Kim, D. Kim, Y. Gogotsi, and C. M. Koo, "Anomalous absorption of electromagnetic waves by 2D transition metal carbonitride Ti3CNTx (MXene)," 2020.

[154] T. Zhang, C. E. Shuck, K. Shevchuk, M. Anayee, and Y. Gogotsi, "Synthesis of Three Families of Titanium Carbonitride MXenes," *J. Am. Chem. Soc.*, vol. 145, pp. 22374–22383, Oct. 2023.

[155] Y. Zhang, L. Wang, N. Zhang, and Z. Zhou, "MXene printing and patterned coating for device applications," *Advanced Materials*, vol. 32, no. 21, p. 1908486, 2020.

[156] M. Magnuson, M. Mattesini, S. Li, C. Höglund, M. Beckers, L. Hultman, and O. Eriksson, "Bonding mechanism in the nitrides Ti 2 Al N and TiN: An experimental and theoretical investigation," *Phys. Rev. B*, vol. 76, p. 195127, Nov. 2007.

[157] M. Khazaei, M. Arai, T. Sasaki, C. Chung, N. S. Venkataramanan, M. Estili, Y. Sakka, and Y. Kawazoe, "Novel Electronic and Magnetic Properties of Two-Dimensional Transition Metal Carbides and Nitrides," *Adv Funct Materials*, vol. 23, pp. 2185–2192, May 2013.

[158] M. Naguib, M. Kurtoglu, V. Presser, J. Lu, J. Niu, M. Heon, L. Hultman, Y. Gogotsi, and M. W. Barsoum, "Two-Dimensional Nanocrystals Produced by Exfoliation of Ti3AlC2," *Advanced Materials*, vol. 23, no. 37, pp. 4248–4253, 2011. _eprint: https://onlinelibrary.wiley.com/doi/pdf/10.1002/adma.201102306.

[159] A. R. Denton and N. W. Ashcroft, "Vegard's law," *Phys. Rev. A*, vol. 43, pp. 3161–3164, Mar. 1991.

[160] T. Hu, J. Wang, H. Zhang, Z. Li, M. Hu, and X. Wang, "Vibrational properties of Ti_3C_2 and $Ti_3C_2T_2$ (T = O, F, OH) monosheets by first-principles calculations: a comparative study," *Phys. Chem. Chem. Phys.*, vol. 17, no. 15, pp. 9997–10003, 2015.

[161] G. Gouadec and P. Colomban, "Raman Spectroscopy of nanomaterials: How spectra relate to disorder, particle size and mechanical properties," *Progress in Crystal Growth and Characterization of Materials*, vol. 53, pp. 1–56, Mar. 2007.

[162] E. Hecht, *Optics*. Boston: Pearson Education, Inc, 5 edition. global edition ed., 2017.

[163] M. Born and E. Wolf, *Principles of optics: electromagnetic theory of propagation, interference and diffraction of light*. Cambridge New York: Cambridge university press, 7th (expanded) ed ed., 1999.

[164] E. D. Palik, *Handbook of optical constants of solids*. Orlando San Diego New York: Academic press, 1985.

[165] H. Günzler and H.-U. Gremlich, *IR spectroscopy: an introduction*. Weinheim: Wiley-VCH, 2002.

[166] M. Magnuson, M. Mattesini, S. Li, C. Höglund, M. Beckers, L. Hultman, and O. Eriksson, "Bonding mechanism in the nitrides Ti2AlN and TiN: An experimental and theoretical investigation," *Physical Review B*, vol. 76, no. 19, p. 195127, 2007.

[167] P. Drude, "Zur Elektronentheorie der Metalle," *Annalen der Physik*, vol. 306, pp. 566–613, Jan. 1900.

[168] L. Pauling, *The nature of the chemical bond and the structure of molecules and crystals: an introduction to modern structural chemistry*. The George Fisher Baker non-resident lectureship in chemistry at Cornell university, Ithaca New York: Cornell university press, 3rd ed ed., 1989.

[169] C. F. Bohren and D. R. Huffman, *Absorption and scattering of light by small particles*. A Wiley-Interscience publication, New York: Wiley-CH Verlag GmbH & Co KGaA, 2004.

[170] M. A. Salim, "Effect of thickness on the optical properties of ZnO thin films prepared by pulsed laser deposition technique (PLD)," *IJP*, vol. 15, pp. 114–121, Jan. 2019.

[171] J. R. Howell, M. P. Mengüç, and K. Daun, *Thermal radiation: an introduction*. Boca Raton, FL: CRC Press, first edition ed., 2023.

[172] H. Watanabe, J. Ishii, H. Wakabayashi, T. Kumano, and L. Hanssen, "Spectral Emissivity Measurements," in *Experimental Methods in the Physical Sciences*, vol. 46, pp. 333–366, Elsevier, 2014.

[173] N. Liu, Q. Li, H. Wan, L. Chang, H. Wang, J. Fang, T. Ding, Q. Wen, L. Zhou, and X. Xiao, "High-temperature stability in air of Ti3C2Tx MXene-based composite with extracted bentonite," *Nat Commun*, vol. 13, p. 5551, Sept. 2022.

[174] X. Qin, P. Zhang, S. Wang, Y. Du, Y. Zhang, and Z. Sun, "The influence of N content on structure, phase stability, elastic and electronic properties in $Ti_3AlC_{2x}N_x$ ($x = 0$–2)," *Physica Status Solidi (b)*, vol. 254, p. 1700009, July 2017.

[175] S. M. Sze and K. K. Ng, *Physics of semiconductor devices*. Wiley-Interscience online books, Hoboken, N.J: Wiley-Interscience, 3. ed ed., 2007.

[176] M. F. Modest, *Radiative heat transfer*. New York: Academic Press, 3d edition ed., 2013.

[177] M. Khazaei, M. Arai, T. Sasaki, C.-Y. Chung, N. S. Venkataramanan, M. Estili, Y. Sakka, and Y. Kawazoe, "Novel electronic and magnetic properties of two-dimensional transition metal carbides and nitrides," *Advanced Functional Materials*, vol. 23, no. 17, pp. 2185–2192, 2013.

[178] X. Qin, P. Zhang, S. Wang, Y. Du, Y. Zhang, and Z. Sun, "The influence of N content on structure, phase stability, elastic and electronic properties in $Ti_3AlC_{2-x}N_x$ (x = 0–2)," *Physica Status Solidi B*, vol. 254, no. 7, p. 1700009, 2017.

[179] J. R. Howell, M. P. Mengüç, and K. Daun, *Thermal radiation: An introduction*. Boca Raton, FL: CRC Press, 1st ed., 2023.

[180] M. F. Modest, *Radiative heat transfer*. New York: Academic Press, 3rd ed., 2013.

[181] T. Ohsaka, F. Izumi, and Y. Fujiki, "Raman spectrum of anatase, tio_2," *Journal of Raman Spectroscopy*, vol. 7, no. 6, pp. 321–324, 1978.

[182] U. Diebold, "The surface science of titanium dioxide," *Surface Science Reports*, vol. 48, no. 5-8, pp. 53–229, 2003.

[183] A. D. Rakić, A. B. Djurišić, J. M. Elazar, and M. L. Majewski, "Optical properties of metallic films for vertical-cavity optoelectronic devices," *Applied optics*, vol. 37, no. 22, pp. 5271–5283, 1998.

[184] M. Li, J. Lu, K. Chen, A. Razavieh, F. Cheng, J. Steilmann, H. Zhang, Z. Liu, Z. Shi, *et al.*, "Mxene chemistry, electrochemistry and energy storage applications," *Nature Reviews Chemistry*, vol. 6, no. 11, pp. 389–404, 2022.

[185] B. Anasori, M. R. Lukatskaya, and Y. Gogotsi, "2d metal carbides and nitrides (mxenes) for energy storage," *Nature Reviews Materials*, vol. 2, no. 2, p. 16098, 2017.

[186] M. R. Lukatskaya, O. Mashtalir, C. E. Ren, Y. Dall'Agnese, P. Rozier, P. L. Taberna, M. Naguib, P. Simon, M. W. Barsoum, and Y. Gogotsi, "Cation intercalation and high volumetric capacitance of two-dimensional titanium carbide," *Science*, vol. 341, no. 6153, pp. 1502–1505, 2013.

[187] M. Ghidiu, M. R. Lukatskaya, M.-Q. Zhao, Y. Gogotsi, and M. W. Barsoum, "Conductive two-dimensional titanium carbide 'clay' with high volumetric capacitance," *Nature*, vol. 516, no. 7529, pp. 78–81, 2014.

[188] P. Simon and Y. Gogotsi, "Perspectives for electrochemical capacitors and related devices," *Nature Materials*, vol. 19, no. 11, pp. 1151–1163, 2020.

[189] S.-M. Bak, E. Hu, Y. Zhou, X. Yu, S. D. Senanayake, S.-J. Cho, K.-B. Kim, K. Y. Chung, X.-Q. Yang, and K.-W. Nam, "Structural changes and thermal stability of charged $lini_xmn_yco_zo_2$ cathode materials studied by combined in situ time-resolved xrd and mass spectroscopy," *ACS Applied Materials & Interfaces*, vol. 6, no. 24, pp. 22594–22601, 2014.

[190] V. Augustyn, J. Come, M. A. Lowe, J. W. Kim, P.-L. Taberna, S. H. Tolbert, H. D. Abruna, P. Simon, and B. Dunn, "High-rate electrochemical energy storage through li+ intercalation pseudocapacitance," *Nature Materials*, vol. 12, no. 6, pp. 518–522, 2013.

[191] Z. Lin, P. Rozier, B. Duployer, P.-L. Taberna, B. Anasori, Y. Gogotsi, and P. Simon, "Capacitance of ti3c2tx mxene in ionic liquid electrolyte," *Journal of Power Sources*, vol. 326, no. 9, pp. 575–579, 2016.

[192] J. T. Lang, D. Kulkarni, C. W. Foster, Y. Huang, M. A. Sepe, S. Shimpalee, D. Y. Parkinson, and I. V. Zenyuk, "X-ray tomography applied to electrochemical devices and electrocatalysis," *Chemical Reviews*, vol. 123, no. 16, pp. 9880–9914, 2023.

[193] M. R. Lukatskaya, B. Dunn, and Y. Gogotsi, "Probing the mechanism of high capacitance in 2d titanium carbide using in situ x-ray absorption spectroscopy," *Advanced Energy Materials*, vol. 5, no. 12, p. 1500589, 2015.

[194] M. Lounasvuori, T. Zhang, Y. Gogotsi, and T. Petit, "Tuning the microenvironment of water confined in ti3c2tx mxene by cation intercalation," *The Journal of Physical Chemistry C*, vol. 128, no. 7, pp. 2803–2813, 2024.

[195] A. Sarycheva and Y. Gogotsi, "Raman spectroscopy analysis of the structure and surface chemistry of ti3c2tx mxene," *Chemistry of Materials*, vol. 32, no. 8, pp. 3480–3488, 2020.

[196] O. Mashtalir, M. Naguib, V. N. Mochalin, Y. Dall'Agnese, M. Heon, M. W. Barsoum, and Y. Gogotsi, "Intercalation and delamination of layered carbides and carbonitrides," *Nature Communications*, vol. 4, no. 1, p. 1716, 2013.

[197] T. Parker, Y. Zhang, K. Shevchuk, T. Zhang, V. Khokhar, Y.-H. Kim, G. Kadagishvili, D. Bugallo, M. Tanwar, B. Davis, *et al.*, "In situ raman and fourier transform infrared spectroscopy studies of mxene–electrolyte interfaces," *ACS Nano*, vol. 19, pp. 22228–22239, 2025.

[198] P. Thongnopkun and S. Ekgasit, "Ftir spectra of faceted diamonds and diamond simulants," *Diamond and Related Materials*, vol. 14, no. 10, pp. 1592–1599, 2005.

[199] A. V. Iogansen, "Direct proportionality of the hydrogen bonding energy and the intensification of the stretching (xh) vibration in infrared spectra," *Spectrochimica Acta Part A: Molecular and Biomolecular Spectroscopy*, vol. 55, no. 7-8, pp. 1585–1612, 1999.

[200] A. Novak, "Hydrogen bonding in solids correlation of spectroscopic and crystallographic data," in *Large Molecules*, (Berlin, Heidelberg), pp. 177–216, Springer Berlin Heidelberg, 1974.

[201] D. A. Schmidt and K. Miki, "Structural correlations in liquid water: A new interpretation of ir spectroscopy," *The Journal of Physical Chemistry A*, vol. 111, no. 40, pp. 10119–10122, 2007.

[202] J. Come, Y. Xie, M. Naguib, S. Jesse, S. V. Kalinin, Y. Gogotsi, P. R. Kent, and N. Balke, "Nanoscale elastic changes in 2d $ti_3c_2t_x$ (mxene) pseudocapacitive electrodes," *Advanced Energy Materials*, vol. 6, no. 9, p. 1502290, 2016.

[203] J. K. El-Demellawi, S. Lopatin, J. Yin, O. F. Mohammed, and H. N. Alshareef, "Plasmonics of two-dimensional titanium carbide mxenes," *Chemical Communications*, vol. 54, no. 32, pp. 4045–4048, 2018.

[204] J. Rieger, A. Ghosh, J. L. Spellberg, C. Raab, A. Mohan, P. P. Joshi, and S. B. King, "Imaging and simulation of surface plasmon polaritons on layered 2d mxenes," *Science Advances*, vol. 11, p. eads3689, 2025.

[205] J. Chen, M. Badioli, P. Alonso-González, S. Thongrattanasiri, F. Huth, J. Osmond, M. Spasenović, A. Centeno, A. Pesquera, P. Godignon, *et al.*, "Optical nano-imaging of gate-tunable graphene plasmons," *Nature*, vol. 487, no. 7405, pp. 77–81, 2012.

[206] Z. Fei, A. S. Rodin, G. O. Andreev, W. Bao, A. S. McLeod, M. Wagner, L. M. Zhang, Z. Zhao, M. Thiemens, G. Dominguez, *et al.*, "Gate-tuning of graphene plasmons revealed by infrared nano-imaging," *Nature*, vol. 487, no. 7405, pp. 82–85, 2012.

[207] I. Amenabar, S. Poly, W. Nuansing, E. H. Hubrich, A. A. Govyadinov, F. Huth, R. Krutokhvostov, L. Zhang, M. Knez, J. Heberle, A. M. Bittner, and R. Hillenbrand, "Structural analysis and mapping of individual protein complexes by infrared nanospectroscopy," *Nature Communications*, vol. 4, no. 1, p. 2890, 2013.

[208] F. Keilmann and R. Hillenbrand, "Near-field microscopy by elastic light scattering from a tip," *Philosophical Transactions of the Royal Society A: Mathematical, Physical and Engineering Sciences*, vol. 362, no. 1817, pp. 787–805, 2004.

[209] P. O. r. Persson, "Mxene surface chemistry," in *2D Metal Carbides and Nitrides (MXenes): Structure, Properties and Applications* (B. Anasori and Y. Gogotsi, eds.), pp. 125–136, Cham: Springer International Publishing, 2019.

[210] M. A. Hope, A. C. Forse, K. J. Griffith, M. R. Lukatskaya, M. Ghidiu, Y. Gogotsi, and C. P. Grey, "Nmr reveals the surface functionalisation of ti_3c_2 mxene," *Physical Chemistry Chemical Physics*, vol. 18, no. 7, pp. 5099–5102, 2016.

[211] M. Zhao, W. Seddon, T. Bullions, L. Wang, and M. J. Green, "Improving oxidation stability of 2d mxenes: synthesis, storage media, and conditions," *Nano Convergence*, vol. 8, no. 1, pp. 1–26, 2021.

[212] J. Halim, M. R. Lukatskaya, K. M. Cook, J. Lu, C. R. Smith, L.-Å. Näslund, S. J. May, L. Hultman, Y. Gogotsi, P. Eklund, *et al.*, "X-ray photoelectron spectroscopy of select multi-layered transition metal carbides (mxenes)," *Applied Surface Science*, vol. 362, pp. 406–417, 2016.

[213] T. Su, R. Peng, Z. D. Hood, M. Naguib, I. N. Ivanov, J. K. Keum, Z. Qin, Z. Guo, and Z. Wu, "One-step synthesis of $nb_2o_5/c/nb_2c$ (mxene) composites and their use as photocatalysts for hydrogen evolution," *ChemSusChem*, vol. 11, no. 4, pp. 688–699, 2018.

[214] H. Cheng and W. Zhao, "Regulating the Nb_2C nanosheets with different degrees of oxidation in water lubricated sliding toward an excellent tribological performance," *Friction*, vol. 10, no. 3, pp. 398–410, 2022.

[215] T. Su, R. Peng, Z. D. Hood, M. Naguib, I. N. Ivanov, J. K. Keum, Z. Qin, Z. Guo, and Z. Wu, "One-step synthesis of Nb_2O_5/c/Nb_2C (MXene) composites and their use as photocatalysts for hydrogen evolution," *ChemSusChem*, vol. 11, no. 4, pp. 688–699, 2018.

[216] Z. U. Din Babar, J. Fatheema, N. Arif, M. S. Anwar, S. Gul, M. Iqbal, and S. Rizwan, "Magnetic phase transition from paramagnetic in Nb_2AlC-MAX to superconductivity-like diamagnetic in Nb_2C-MXene: An experimental and computational analysis," *RSC Advances*, vol. 10, no. 43, pp. 25669–25678, 2020.

[217] A. C. Ferrari and J. Robertson, "Interpretation of raman spectra of disordered and amorphous carbon," *Physical Review B*, vol. 61, no. 20, pp. 14095–14107, 2000.

[218] Sigma-Aldrich, "Ir spectrum table & chart." https://www.sigmaaldrich.com/technical-documents/articles/biology/ir-spectrum-table.html. Accessed: 2024-01-15.

[219] G. Li, S. Lian, J. Wang, G. Xie, N. Zhang, and X. Xie, "Surface chemistry engineering and the applications of MXenes," *Journal of Materiomics*, vol. 9, pp. 1160–1184, Nov. 2023.

[220] Y. Liu, H. Xiao, and W. A. Goddard, "Schottky-Barrier-Free Contacts with Two-Dimensional Semiconductors by Surface-Engineered MXenes," *J. Am. Chem. Soc.*, vol. 138, pp. 15853–15856, Dec. 2016.

[221] C. Si, J. Zhou, and Z. Sun, "Half-Metallic Ferromagnetism and Surface Functionalization-Induced Metal–Insulator Transition in Graphene-like Two-Dimensional Cr_2 C Crystals," *ACS Appl. Mater. Interfaces*, vol. 7, pp. 17510–17515, Aug. 2015.

[222] V. Kamysbayev, A. S. Filatov, H. Hu, X. Rui, F. Lagunas, D. Wang, R. F. Klie, and D. V. Talapin, "Covalent surface modifications and superconductivity of two-dimensional metal carbide MXenes," *Science*, vol. 369, pp. 979–983, Aug. 2020.

[223] K. Kim, T. Parker, B. M. Abraham, T. Zhang, A. Bruyant, J. Mallet, and Y. Gogotsi, "The c/n ratio as a lever for infrared properties tuning in carbonitride mxenes," *Materials Today Physics*, vol. 58, p. 101860, 2025.

[224] D. Capela, A. Alves, V. Homem, and L. Santos, "From the shop to the drain — Volatile methylsiloxanes in cosmetics and personal care products," *Environment International*, vol. 92-93, pp. 50–62, July 2016.

[225] K. Kumari, A. Singh, and D. Marathe, "Cyclic volatile methyl siloxanes (D4, D5, and D6) as the emerging pollutants in environment: environmental distribution, fate, and toxicological assessments," *Environ Sci Pollut Res*, vol. 31, pp. 38681–38709, Feb. 2023.

[226] E. Gallego, P. Teixidor, F. Roca, and J. Perales, "Levels of volatile methyl siloxanes in outdoor air," in *Volatile Methylsiloxanes in the Environment*, vol. 89 of *The Handbook of Environmental Chemistry*, Cham: Springer, 2018.

[227] M. Shen, Y. Zhang, Y. Tian, and G. Zeng, "Recent advances in research on cyclic volatile methylsiloxanes in sediment, soil and biosolid: a review," *Chemistry and Ecology*, vol. 34, no. 7, pp. 675–695, 2018.

[228] J. Ji, L. Zhao, Y. Shen, S. Liu, and Y. Zhang, "Covalent stabilization and functionalization of MXene via silylation reactions with improved surface properties," *FlatChem*, vol. 17, p. 100128, Sept. 2019.

[229] T. Yousaf, A. Areeb, M. Murtaza, A. Munir, Y. Khan, and A. Waseem, "Silane-Grafted MXene (Ti_3 C_2 T_x) Membranes for Enhanced Water Purification Performance," *ACS Omega*, vol. 7, pp. 19502–19512, June 2022.

[230] H. Riazi, M. Anayee, K. Hantanasirisakul, A. A. Shamsabadi, B. Anasori, Y. Gogotsi, and M. Soroush, "Surface Modification of a MXene by an Aminosilane Coupling Agent," *Adv Materials Inter*, vol. 7, p. 1902008, Mar. 2020.

[231] K. Kim, C. Pérez De La Vega, Y. El Helou, E. Vuillermet, K.-T. Wu, J. Mallet, and A. Bruyant, "Far-field and near-field spectroscopic characterization of Nb2CTx MXene," in *2D Photonic Materials and Devices VII* (A. Majumdar, C. M. Torres, and H. Deng, eds.), (San Francisco, United States), p. 33, SPIE, Mar. 2024.

[232] A. Jorio, E. H. M. Ferreira, M. V. O. Moutinho, F. Stavale, C. A. Achete, and R. B. Capaz, "Measuring disorder in graphene with the G and D bands," *Physica Status Solidi (b)*, vol. 247, pp. 2980–2982, Dec. 2010.

[233] D. Liu, T. Li, W. Sun, W. Zhou, and G. Zhang, "Magnetic ti3c2 mxene nanomaterials for doxorubicin adsorption from aqueous solutions: Kinetic, isotherms, and thermodynamic studies," *ACS Omega*, vol. 7, pp. 31945–31953, Sept. 2022.

[234] T. Cygan, J. Wozniak, M. Petrus, A. Lachowski, W. Pawlak, B. Adamczyk-Cieślak, A. Jastrzębska, A. Rozmysłowska-Wojciechowska, T. Wojciechowski, W. Ziemkowska, and A. Olszyna, "Microstructure and mechanical properties of alumina composites with addition of structurally modified 2d ti3c2 (mxene) phase," *Materials*, vol. 14, no. 4, 2021.

[235] R. M. Silverstein, F. X. Webster, and D. J. Kiemle, *Spectrometric identification of organic compounds*. New York: John Wiley & Sons, 7th ed., 2005.

[236] D. Liu, T. Li, W. Sun, W. Zhou, and G. Zhang, "Magnetic Ti_3 C_2 MXene Nanomaterials for Doxorubicin Adsorption from Aqueous Solutions: Kinetic, Isotherms, and Thermodynamic Studies," *ACS Omega*, vol. 7, pp. 31945–31953, Sept. 2022.

[237] J. A. Davies-Jones and P. R. Davies, "Photo induced force microscopy: chemical spectroscopy beyond the diffraction limit," *Mater. Chem. Front.*, vol. 6, pp. 1552–1573, 2022.

[238] N. Takano, T. Fukuda, and K. Ono, "Analysis of Structures of Oligomeric Siloxanes from Dimethoxydimethylsilane under Heat Treatment by FT-IR," *Polym J*, vol. 33, pp. 469–474, June 2001.

[239] S. Wachholz, F. Keidel, U. Just, H. Geissler, and K. Käppler, "Analysis of a mixture of linear and cyclic siloxanes by cryo-gas chromatography-fourier transform infrared spectroscopy and gas chromatography-mass spectrometry," *Journal of Chromatography A*, vol. 693, no. 1, pp. 89–99, 1995. First received 18 July 1994; revised manuscript received 1 November 1994; accepted 11 November 1994.

[240] Y. Sato, R. Hayami, and T. Gunji, "Characterization of NMR, IR, and Raman spectra for siloxanes and silsesquioxanes: a mini review," *J Sol-Gel Sci Technol*, vol. 104, pp. 36–52, Oct. 2022.

[241] F. D. Osterholtz and E. R. Pohl, "Kinetics of the hydrolysis and condensation of organofunctional alkoxysilanes: a review," *Journal of Adhesion Science and Technology*, vol. 6, no. 1, pp. 127–149, 1992.

[242] B. Arkles, "Hydrophobicity, hydrophilicity and silanes," *Paint and Coatings Industry*, vol. 22, no. 10, pp. 114–135, 2006.

[243] M. Sypabekova, A. Hagemann, D. Rho, and S. Kim, "Review: 3-aminopropyltriethoxysilane (aptes) deposition methods on oxide surfaces in solution and vapor phases for biosensing applications," *Biosensors*, vol. 13, p. 36, dec 2022. Review article on APTES deposition methods for biosensing applications.

[244] K.-T. Wu, Y. El-Helou, E. Usureau, E. Vuillermet, M. Kazan, M. Lazar, G. Gautier, W.-Y. Woon, and A. Bruyant, "Infrared photoinduced force near-field spectroscopy of silicon carbide," *Applied Surface Science*, vol. 684, p. 161798, Mar. 2025.

[245] J. Homola, S. S. Yee, and G. Gauglitz, "Surface plasmon resonance sensors: review," *Sensors and Actuators B: Chemical*, vol. 54, no. 1-2, pp. 3–15, 1999.

[246] B. Liedberg, C. Nylander, and I. Lunström, "Surface plasmon resonance for gas detection and biosensing," *Sensors and Actuators*, vol. 4, pp. 299–304, 1983.

[247] M. A. Cooper, "Optical biosensors in drug discovery," *Nature Reviews Drug Discovery*, vol. 1, no. 7, pp. 515–528, 2002.

[248] H. Raether, *Surface plasmons on smooth and rough surfaces and on gratings*. Springer, 1988.

[249] E. Kretschmann and H. Raether, "Radiative decay of non-radiative surface plasmons excited by light," *Zeitschrift für Naturforschung A*, vol. 23, no. 12, pp. 2135–2136, 1968.

[250] A. Otto, "Excitation of nonradiative surface plasma waves in silver by the method of frustrated total reflection," *Zeitschrift für Physik A Hadrons and nuclei*, vol. 216, no. 4, pp. 398–410, 1968.

[251] J. Homola, "Surface plasmon resonance sensors for detection of chemical and biological species," *Chemical Reviews*, vol. 108, no. 2, pp. 462–493, 2008.

[252] S. A. Maier, *Plasmonics: fundamentals and applications*. Springer Science & Business Media, 2007.

[253] J. M. Pitarke, V. M. Silkin, E. V. Chulkov, and P. M. Echenique, "Theory of surface plasmons and surface-plasmon polaritons," *Reports on Progress in Physics*, vol. 70, no. 1, p. 1, 2007.

[254] W. Knoll, "Interfaces and thin films as seen by bound electromagnetic waves," *Annual Review of Physical Chemistry*, vol. 49, no. 1, pp. 569–638, 1998.

[255] S. Ekgasit, C. Thammacharoen, and W. Knoll, "Surface plasmon resonance spectroscopy based on evanescent field treatment," *Analytical Chemistry*, vol. 71, no. 10, pp. 1952–1958, 1999.

[256] R. B. Schasfoort and A. J. Tudos, eds., *Handbook of surface plasmon resonance*. Royal Society of Chemistry, 2017.

[257] M. Piliarik and J. Homola, "Surface plasmon resonance (spr) sensors: approaching their limits?," *Optics Express*, vol. 17, no. 19, pp. 16505–16517, 2009.

[258] J. Homola, "Present and future of surface plasmon resonance biosensors," *Analytical and Bioanalytical Chemistry*, vol. 377, no. 3, pp. 528–539, 2003.

[259] A. V. Kabashin, S. Patskovsky, and A. N. Grigorenko, "Phase and amplitude sensitivities in surface plasmon resonance bio and chemical sensing," *Optics Express*, vol. 17, no. 23, pp. 21191–21204, 2009.

[260] S. G. Nelson, K. S. Johnston, and S. S. Yee, "High sensitivity surface plasmon resonance sensor based on phase detection," *Sensors and Actuators B: Chemical*, vol. 35, no. 1-3, pp. 187–191, 1996.

[261] A. V. Kabashin and P. I. Nikitin, "Surface plasmon resonance interferometer for bio-and chemical-sensors," *Optics Communications*, vol. 150, no. 1-6, pp. 5–8, 1998.

[262] PhaseLab Instrument, "High-resolution phase-sensitive spr systems for advanced research applications," technical documentation, 2023.

[263] Y. H. Huang, H. P. Ho, S. K. Kong, and A. V. Kabashin, "Phase-sensitive surface plasmon resonance biosensors: methodology, instrumentation and applications," *Annalen der Physik*, vol. 524, no. 11, pp. 637–662, 2012.

[264] S. Shen, T. Liu, and J. Guo, "Optical phase-shift detection of surface plasmon resonance," *Applied Optics*, vol. 37, no. 10, pp. 1747–1751, 2013.

[265] E. Hutter and J. H. Fendler, "Exploitation of localized surface plasmon resonance," *Advanced Materials*, vol. 16, no. 19, pp. 1685–1706, 2004.

[266] A. K. Sharma, R. Jha, and B. D. Gupta, "Fiber-optic sensors based on surface plasmon resonance: a comprehensive review," *IEEE Sensors Journal*, vol. 7, no. 8, pp. 1118–1129, 2007.

[267] X. Wu, B. Han, H. Zhang, and X. Xie, "Surfaces of mxenes: structures and functionalities," *Nano-Micro Letters*, vol. 10, no. 3, p. 48, 2018.

[268] S. Zeng, S. Hu, J. Xia, T. Anderson, X. Q. Dinh, X. M. Meng, *et al.*, "Graphene–mos2 hybrid nanostructures enhanced surface plasmon resonance biosensors," *Sensors and Actuators B: Chemical*, vol. 207, pp. 801–810, 2018.

[269] Q. Ouyang, S. Zeng, L. Jiang, L. Hong, G. Xu, X. Q. Dinh, *et al.*, "Sensitivity enhancement of transition metal dichalcogenides/silicon nanostructure-based surface plasmon resonance biosensor," *Scientific Reports*, vol. 6, p. 28190, 2016.

[270] L. Wu, H. S. Chu, W. S. Koh, and E. P. Li, "Highly sensitive graphene biosensors based on surface plasmon resonance," *Optics Express*, vol. 18, no. 14, pp. 14395–14400, 2017.

[271] S. Zeng, D. Baillargeat, H. P. Ho, and K. T. Yong, "Nanomaterials enhanced surface plasmon resonance for biological and chemical sensing applications," *Chemical Society Reviews*, vol. 43, no. 10, pp. 3426–3452, 2016.

[272] G. Qiu, S. P. Ng, and C. M. L. Wu, "Bimetallic au–ag alloy nanoislands for highly sensitive localized surface plasmon resonance biosensing," *Sensors and Actuators B: Chemical*, vol. 265, pp. 459–467, 2018.

[273] M. Naguib, V. N. Mochalin, M. W. Barsoum, and Y. Gogotsi, "25th anniversary article: Mxenes: a new family of two-dimensional materials," *Advanced Materials*, vol. 26, no. 7, pp. 992–1005, 2014.

[274] Y. Lei, D. Butler, M. C. Lucking, F. Zhang, T. Xia, K. Fujisawa, *et al.*, "Single-atom doping of mos2 with manganese enables ultrasensitive detection of dopamine: experimental and computational approach," *Science Advances*, vol. 5, no. 7, p. eaax4961, 2019.

[275] F. Shahzad, M. Alhabeb, C. B. Hatter, B. Anasori, S. Man Hong, C. M. Koo, and Y. Gogotsi, "Electromagnetic interference shielding with 2d transition metal carbides (mxenes)," *Science*, vol. 353, no. 6304, pp. 1137–1140, 2016.

[276] L. Hasanah, R. Mutia, C. Wulandari, B. Mulyanti, S. K. Sahari, R. E. Pawinanto, and A. A. Hamzah, "Investigating the effect of surface termination and thickness of mxene on the detection response of the spr sensor using fdtd simulation," *Results in Optics*, vol. 12, p. 100438, 2023.

[277] C. J. Zhang, B. Anasori, A. Seral-Ascaso, S. H. Park, N. McEvoy, A. Shmeliov, G. S. Duesberg, J. N. Coleman, Y. Gogotsi, and V. Nicolosi, "Transparent, flexible, and conductive 2d titanium carbide (mxene) films with high volumetric capacitance," *Advanced Materials*, vol. 32, p. 1901372, May 2020.

[278] A. D. Dillon, M. J. Ghidiu, A. L. Krick, J. Griggs, S. J. May, Y. Gogotsi, M. W. Barsoum, and A. T. Fafarman, "Highly conductive optical quality

solution-processed films of 2d titanium carbide," *Advanced Functional Materials*, vol. 26, no. 23, pp. 4162–4168, 2016.

[279] M. Hu, Z. Li, H. Zhang, T. Hu, C. Zhang, Z. Wu, X. Wang, and P. Hu, "Self-assembled $ti_3c_2t_x$ mxene film with high gravimetric capacitance," *Chemical Communications*, vol. 51, no. 70, pp. 13531–13533, 2015.

[280] S. A. Shah, T. Habib, H. Gao, P. Gao, W. Sun, M. J. Green, and M. Radovic, "Template-free 3d titanium carbide ($ti_3c_2t_x$) mxene particles crumpled by capillary forces," *Chemical Communications*, vol. 53, no. 2, pp. 400–403, 2017.

[281] Z. Ling, C. E. Ren, M. Q. Zhao, J. Yang, J. M. Giammarco, J. Qiu, M. W. Barsoum, and Y. Gogotsi, "Flexible and conductive mxene films and nanocomposites with high capacitance," *Proceedings of the National Academy of Sciences*, vol. 111, no. 47, pp. 16676–16681, 2014.

[282] X. Wang, T. S. Mathis, K. Li, Z. Lin, L. Vlcek, T. Torita, N. C. Osti, C. Hatter, P. Urbankowski, A. Sarycheva, M. Tyagi, E. Mamontov, P. Simon, and Y. Gogotsi, "Influences from solvents on charge storage in titanium carbide mxenes," *Nature Energy*, vol. 4, no. 3, pp. 241–248, 2019.

[283] B. Xu, M. Zhu, W. Zhang, X. Zhen, Z. Pei, Q. Xue, C. Zhi, and P. Shi, "Ultrathin mxene-micropattern-based field-effect transistor for probing neural activity," *Advanced Materials*, vol. 28, no. 17, pp. 3333–3339, 2016.

[284] K. Maleski, V. N. Mochalin, and Y. Gogotsi, "Dispersions of two-dimensional titanium carbide mxene in organic solvents," *Chemistry of Materials*, vol. 29, no. 4, pp. 1632–1640, 2017.

[285] W. Yang, J. Yang, J. J. Byun, F. P. Moissinac, J. Xu, S. J. Haigh, M. Domingos, M. A. Bissett, R. A. W. Dryfe, and S. Barg, "3d printing of freestanding mxene architectures for current-collector-free supercapacitors," *Advanced Materials*, vol. 31, no. 37, p. 1902725, 2019.

[286] H. Wang, S. Chen, L. Li, and S. Jiang, "Improved method for the preparation of carboxylic acid and amine terminated self-assembled monolayers of alkanethiolates," *Langmuir*, vol. 21, no. 7, pp. 2633–2636, 2005.

[287] A. Sinha, Dhanjai, H. Zhao, Y. Huang, X. Lu, J. Chen, and R. Jain, "Mxene: An emerging material for sensing and biosensing," *TrAC Trends in Analytical Chemistry*, vol. 105, pp. 424–435, 2018.

[288] M. Anayee, N. Kurra, M. Alhabeb, M. Seredych, M. N. Hedhili, A.-H. Emwas, H. N. Alshareef, B. Anasori, and Y. Gogotsi, "Role of acid mixtures etching on the surface chemistry and sodium ion storage in $ti_3c_2t_x$ mxene," *Chemical Communications*, vol. 56, pp. 6090–6093, 2020.

[289] J. Ji, L. Zhao, Y. Shen, S. Liu, and Y. Zhang, "Covalent stabilization and functionalization of mxene via silylation reactions with improved surface properties," *FlatChem*, vol. 17, p. 100128, 2019.

[290] H. Riazi, M. Anayee, K. Hantanasirisakul, A. A. Shamsabadi, B. Anasori, Y. Gogotsi, and M. Soroush, "Surface modification of a mxene by an aminosilane coupling agent," *Advanced Materials Interfaces*, vol. 7, no. 5, p. 1902008, 2020.

[291] Y. Liu, Y. Li, X.-M. Li, and T. He, "Kinetics of (3-aminopropyl)triethoxylsilane (aptes) silanization of superparamagnetic iron oxide nanoparticles," *Langmuir*, vol. 29, no. 49, pp. 15275–15282, 2013.

[292] J. Zhu, J. Gao, J. Li, J. Zhao, Z. Ahmad, and D. Li, "Improving the dispersibility of 2d mxene in organic solvents through a simple and general silane-functionalization approach," *ACS Applied Nano Materials*, vol. 3, no. 8, pp. 8537–8547, 2020.

[293] T. Yousaf, A. Areeb, M. Murtaza, A. Munir, Y. Khan, and A. Waseem, "Silane-grafted mxene ($ti_3c_2t_x$) membranes for enhanced water purification performance," *ACS Omega*, vol. 7, no. 25, pp. 19502–19512, 2022.

[294] J. A. Howarter and J. P. Youngblood, "Optimization of silica silanization by 3-aminopropyltriethoxysilane," *Langmuir*, vol. 22, no. 26, pp. 11142–11147, 2006.

[295] R. G. Acres, A. V. Ellis, J. Alvino, C. E. Lenahan, D. A. Khodakov, G. F. Metha, and G. G. Andersson, "Molecular structure of 3-aminopropyltriethoxysilane layers formed on silanol-terminated silicon surfaces," *The Journal of Physical Chemistry C*, vol. 116, no. 10, pp. 6289–6297, 2012.

[296] J. A. De Feijter, J. Benjamins, and F. A. Veer, "Ellipsometry as a tool to study the adsorption behavior of synthetic and biopolymers at the air-water interface," *Biopolymers*, vol. 17, no. 7, pp. 1759–1772, 1978.

[297] G. Kresse and J. Furthmüller, "Efficiency of ab-initio total energy calculations for metals and semiconductors using a plane-wave basis set," *Computational Materials Science*, vol. 6, pp. 15–50, 1996.

[298] G. Kresse and J. Furthmüller, "Efficient iterative schemes for ab initio total-energy calculations using a plane-wave basis set," *Physical Review B*, vol. 54, pp. 11169–11186, 1996.

[299] J. P. Perdew, K. Burke, and M. Ernzerhof, "Generalized gradient approximation made simple," *Physical Review Letters*, vol. 77, pp. 3865–3868, 1996.

[300] P. E. Blöchl, "Projector augmented-wave method," *Physical Review B*, vol. 50, pp. 17953–17979, 1994.

[301] S. Grimme, S. Ehrlich, and L. Goerigk, "Effect of the damping function in dispersion corrected density functional theory," *Journal of Computational Chemistry*, vol. 32, pp. 1456–1465, 2011.

[302] H. J. Monkhorst and J. D. Pack, "Special points for Brillouin-zone integrations," *Physical Review B*, vol. 13, pp. 5188–5192, 1976.

[303] M. Losurdo, K. Hingerl, P. Prunici, and G. Bruno, "Ellipsometry at the nanoscale," *Thin Solid Films*, vol. 518, no. 5, pp. 1382–1388, 2009.

Synthèse et nanospectroscopie infrarouge de matériaux MXenes, application à la détection de composés siloxanes

RÉSUMÉ FRANÇAIS

Table des matières

Introduction **177**

1 État de l'art sur les matériaux 2D et les MXenes **184**
1.1 Brève revue des matériaux bidimensionnels en optique 184
1.2 L'émergence des carbures et nitrures de métaux de transition en 2D . 184

2 Aspects fondamentaux de la spectroscopie IR pour les MXenes **188**
2.1 Fondamentaux de la spectroscopie IR 188
2.2 La nanospectroscopie par sonde locale 188

3 Caractérisation infrarouge en champ lointain des MXenes : études de la composition chimique et de l'interface électrochimique **191**
3.1 Influence du rapport carbone/azote dans le MXène $Ti_3C_yN_{(2-y)}T_x$ sur les propriétés infrarouges 191
3.1.1 Réflectance IR 192
3.1.2 Émission IR 192
3.1.3 Calculs de théorie fonctionnelle de la densité 194
3.2 Sondage infrarouge in situ des intercalations ioniques dans le MXene $Ti_3C_2T_x$ 195
3.2.1 Montage de cellule électrochimique sur cristal FTIR-ATR . . . 195
3.2.2 Résultats et Discussion 195

4 Propriétés optiques en champ proche des MXenes par nanoscopie IR **198**
4.1 Terminaisons de surface des MXenes 198
4.2 Analyse de l'oxydation et des défauts carbonés sur le Nb_2CT_x 200
4.3 Cartographie des contaminants à base de siloxane sur les MXenes . . 200

5 Application du MXene à la détection par résonance plasmonique de surface **205**
5.1 Dépôt de film mince MXene surveillé par SPR 206
5.2 Détection de (3-Aminopropyl)triethoxysilane utilisant le MXene . . . 208

Conclusion générale **211**

Bibliographie **214**

Introduction

La découverte du graphène en 2004 par Novoselov et Geim [1] a marqué un moment important dans la science des matériaux, inaugurant l'ère des matériaux bidimensionnels (2D). Cette avancée révolutionnaire, reconnue par le prix Nobel de physique en 2010, a démontré que les matériaux atomiquement minces pouvaient non seulement exister dans des conditions stables, mais aussi présenter des propriétés extraordinaires différentes de leurs homologues massifs. Depuis cette découverte fondamentale, le monde des matériaux 2D s'est développé de manière exponentielle, englobant d'autres types de matériaux 2D. Au-delà du graphène, avec sa mobilité électronique remarquable dépassant 200 000 $cm^2/V{\cdot}s$ et sa résistance mécanique exceptionnelle, d'autres matériaux 2D ont émergé avec des propriétés complémentaires. Le nitrure de bore hexagonal (hBN), présente d'excellentes propriétés diélectriques avec une large bande interdite de 5,9 eV et une conductivité thermique remarquable, ce qui en fait un substrat idéal et une couche isolante pour les hétérostructures 2D [2]. Les dichalcogénures de métaux de transition (TMD) tels que le MoS_2, le WS_2 et le WSe_2 possèdent des bandes interdites directes sous leur forme monocouche, permettant des interactions lumière-matière efficaces et des applications en optoélectronique [3]. Le phosphore noir (BP) présente des propriétés électroniques et optiques hautement anisotropes avec une bande interdite dépendante de l'épaisseur allant de 0,3 à 2,0 eV, comblant l'écart entre le graphène et les TMD [4]. Ces matériaux offrent une riche palette de caractéristiques électroniques, optiques, mécaniques et chimiques uniques [5, 6].

Les récentes avancées en simulation de la science des matériaux, notamment grâce à l'intégration de l'intelligence artificielle, a considérablement accéléré la prédiction théorique de nouveaux matériaux 2D. Les bases de données actuelles suggèrent l'existence potentielle de plus de 6 000 matériaux 2D théoriquement stables, représentant une énorme base inexploité de matériaux aux propriétés potentiellement transformatrices [7, 8]. Ce paysage théorique en expansion inclut les Xènes (silicène, germanène, stannène), qui présentent des états non triviaux et des bandes interdites ajustables [9] ; les oxydes métalliques 2D (par exemple V_2O_5) avec des propriétés électrochimiques exceptionnelles pour les applications de stockage d'énergie [10] ; et les matériaux 2D monoélémentaires émergents comme l'antimonène et le bismuthène avec des performances thermoélectriques prometteuses [11]. Cependant, la réalisation expérimentale de ces structures théoriquement prédites reste difficile, avec environ 100 matériaux 2D distincts synthétisés et caractérisés avec succès à ce jour [12]. Cette disparité entre les prédictions théoriques et les réalisations expérimentales souligne l'importance des techniques de synthèse avancées et des méthodologies de caractérisation précises.

La caractérisation des matériaux 2D présente des défis uniques qui les distinguent des matériaux massifs conventionnels. Leur nature atomiquement mince, compre-

nant souvent seulement quelques couches atomiques, nécessite des techniques de caractérisation avec une sensibilité et une résolution spatiale exceptionnelles. De plus, de nombreux matériaux 2D présentent des propriétés anisotropes, avec des comportements différents perpendiculairement et parallèlement à leurs plans basaux. Par exemple, les TMD du groupe VI affichent des conductivités thermiques dans le plan environ 100 fois supérieures à leurs valeurs hors plan [13], tandis que les MXenes démontrent une anisotropie significative dans leurs réponses électriques et optiques en raison de leur conductivité métallique dans le plan contrastant avec un comportement de type semi-conducteur entre les couches [14]. Les hydroxydes doubles lamellaires (LDH) présentent une chimie d'intercalation unique qui varie substantiellement entre les régions de surface et inter-couches. Même au sein de la même famille, les propriétés peuvent varier dramatiquement — les polymorphes de borophène affichent un comportement métallique, semi-conducteur ou supraconducteur selon leur arrangement atomique précis [15]. Ces propriétés distinctives rendent les méthodes de caractérisation traditionnelles inadéquates, nécessitant des approches spécialisées capables de sonder les propriétés à l'échelle nanométrique.

De plus, la physique gouvernant les phénomènes à l'échelle nanométrique s'éloigne des comportements macroscopiques, les effets de confinement quantique et les rapports surface-volume accrus modifiant fondamentalement les propriétés des matériaux. Par conséquent, le développement de nouvelles techniques de caractérisation spécifiquement adaptées à l'analyse nanoscopique est devenu un axe de recherche critique. L'évolution de techniques telles que la microscopie électronique à balayage (MEB), développée au début des années 1930 par Knoll et Ruska [16], a révolutionné notre capacité à visualiser les échantillons conducteurs avec une résolution nanométrique. Cette évolution s'est poursuivie avec l'émergence des techniques de microscopie en champ proche, qui ont dépassé la limite de diffraction traditionnelle des investigations optiques. La microscopie optique en champ proche (SNOM), pionnière de Pohl *et al.* dans les années 1980 [17], a marqué un changement de paradigme en exploitant les ondes évanescentes pour atteindre une résolution spatiale sub-longueur d'onde. En positionnant une ouverture ou une pointe nanoscopique dans la région de champ proche d'un échantillon (typiquement $<$50 nm), le SNOM a permis l'imagerie optique et la spectroscopie avec une résolution environ un ordre de grandeur au-delà de la limite de diffraction. Le développement ultérieur de la spectroscopie infrarouge basée sur la microscopie à force atomique (AFM-IR), introduite par Dazzi *et al.* au début des années 2000 [18], a encore amélioré nos capacités en détectant l'expansion photo-thermique des échantillons illuminés par le rayonnement infrarouge, fournissant ainsi une cartographie topographique et chimique simultanée à résolution nanoscopique. Cette technique exploite le mode contact de l'AFM pour transduire l'expansion thermique induite par l'absorption infrarouge en déflexions du cantilever, offrant des aperçus sans précédent sur les compositions moléculaires à l'échelle nanométrique.

Plus récemment, la microscopie à force photo-induite (PiFM), développée par Rajapaksa *et al.* [19] et affinée par Jahng *et al.* [20], a repoussé les limites de la spectroscopie en champ proche en mesurant directement les interactions dipôle-dipôle entre la pointe et l'échantillon lors de l'illumination infrarouge. Opérant en mode non-contact, le PiFM détecte la force de gradient résultant de l'interaction entre les dipôles optiquement induits dans la pointe et l'échantillon, fournissant une sensibilité exceptionnelle à la chimie de surface avec une résolution spatiale

approchant 10 nm. Ces avancées en microscopies à sonde locale ont considérablement élargi notre capacité à interroger les propriétés fondamentales des matériaux 2D avec une résolution spatiale et chimique sans précédent [21], permettant des investigations détaillées de phénomènes localisés qui resteraient autrement inaccessibles par les approches conventionnelles de champ lointain.

Parmi la famille croissante des matériaux 2D, les MXenes ont émergé comme une classe de matériaux particulièrement prometteuse avec un potentiel exceptionnel pour diverses applications technologiques. Découverts pour la première fois en 2011 par Naguib *et al.* à l'Université Drexel [22], les MXenes représentent une famille de carbures, nitrures et carbonitrures de métaux de transition 2D avec la formule générale $M_{n+1}X_nT_x$, où M désigne un métal de transition (par exemple, Ti, V, Nb, Mo), X représente le carbone et/ou l'azote, et T_x indique les terminaisons de surface (par exemple, -OH, -O, -F) [14]. Ces matériaux ont attiré une attention considérable en raison de leur combinaison remarquable de conductivité métallique, d'hydrophilie et de robustesse mécanique, les positionnant comme candidats prometteurs pour des applications allant du stockage d'énergie et du blindage contre les interférences électromagnétiques à la purification de l'eau et aux applications biomédicales [14].

Les recherches récentes de l'Université Drexel ont souligné l'intérêt mondial sans précédent pour les MXenes, avec le nombre de publications et de brevets liés à ces matériaux augmentant exponentiellement depuis leur découverte [23]. Selon Anasori *et al.*, cette augmentation de l'activité de recherche reflète la versatilité extraordinaire des MXenes dans de multiples domaines technologiques, avec un accent particulier sur leur potentiel pour les dispositifs de stockage d'énergie de nouvelle génération, le blindage contre les interférences électromagnétiques et les applications de détection avancées.

Un aspect particulièrement fascinant des MXenes réside dans leurs propriétés optiques exceptionnelles et leur comportement plasmonique. Les résultats d'El-Demellawi *et al.* ont démontré que les feuillets de MXene $Ti_3C_2T_x$ présentent des plasmons de surface multipolaires accordables qui peuvent être contrôlés systématiquement en faisant varier les dimensions latérales et l'épaisseur des feuillets [24]. Cette découverte positionne les MXenes comme des candidats hautement prometteurs pour les dispositifs plasmoniques de nouvelle génération, avec des applications potentielles en biodétection, photocatalyse et technologies optoélectroniques. De plus, les investigations théoriques de Mauchamp *et al.* ont révélé que la structure électronique et les propriétés diélectriques des MXenes peuvent être modulées avec précision grâce à l'ingénierie compositionnelle et la fonctionnalisation de surface, offrant des opportunités sans précédent pour adapter leur réponse optique sur une large gamme spectrale [25].

Malgré ces découvertes prometteuses et le corpus de recherche en croissance rapide sur les MXenes, la caractérisation optique de ces matériaux reste relativement limitée, particulièrement dans la région spectrale infrarouge. Ce domaine spectral est d'une importance primordiale car il englobe les fréquences vibrationnelles de la plupart des groupes fonctionnels organiques et fournit des aperçus cruciaux sur la chimie de surface et les configurations structurelles des MXenes [14]. Les propriétés optiques des MXenes dans la région infrarouge sont particulièrement pertinentes pour les applications en détection, photonique et optoélectronique, où l'interaction entre le rayonnement électromagnétique et les propriétés des matériaux détermine fondamentalement les performances des dispositifs [26].

Cette thèse de doctorat vise à combler cette lacune de connaissances en étudiant les propriétés optiques des MXenes, avec un focus spécifique sur leur comportement dans la région spectrale infrarouge. La recherche présentée ici adopte une approche multifacette, englobant trois domaines principaux d'investigation :

Premièrement, nous visons à aborder la synthèse des MXenes à partir de leurs phases MAX correspondantes, détaillant les protocoles rigoureux établis pour obtenir des feuillets de MXene de haute qualité. Elle discute la fabrication de différents types d'échantillons selon leurs applications spécifiques, à travers différentes techniques. Nous soulignons l'importance de la caractérisation structurelle pour assurer la reproductibilité des propriétés des matériaux, essentielle pour une caractérisation optique fiable.

Deuxièmement, nous conduisons une caractérisation optique complète en champ lointain des échantillons de MXene utilisant des techniques spectroscopiques conventionnelles, incluant la spectroscopie infrarouge à transformée de Fourier (FTIR), la spectroscopie Raman et la spectroscopie ultraviolet-visible. Bien que ces investigations révèlent des aperçus précieux sur la réponse optique collective des ensembles de MXenes, la résolution spatiale limitée par la diffraction des techniques de champ lointain émerge comme une limitation significative pour sonder les phénomènes localisés et les hétérogénéités aux échelles de longueur pertinentes.

Finalement, pour surmonter ces contraintes de résolution spatiale, la troisième phase de notre recherche emploie des techniques avancées de nanoscopie en champ proche, spécifiquement la microscopie à force photo-induite (PiFM). Cette approche de pointe permet une cartographie topographique et spectroscopique simultanée avec une résolution spatiale nanométrique, contournant la limite de diffraction qui contraint les méthodologies optiques conventionnelles. En implémentant cette technique, nous obtenons des aperçus sans précédent sur les propriétés optiques localisées des MXenes à l'échelle nanométrique, élucidant les relations structure-propriétés qui restent inaccessibles par les approches de caractérisation traditionnelles.

À travers ce programme de recherche complet, nous visons à établir une compréhension fondamentale des propriétés optiques infrarouges des MXenes, comblant l'écart entre leur structure moléculaire et leur comportement macroscopique. Les résultats présentés dans cette thèse contribuent non seulement à la connaissance scientifique fondamentale de cette classe émergente de matériaux 2D, mais fournissent également des aperçus critiques pour leur intégration rationnelle dans des applications technologiques avancées, particulièrement dans les domaines où leurs propriétés optiques jouent un rôle déterminant.

Organisation de la thèse

En plus de l'introduction générale, cette thèse se compose de cinq chapitres et est structurée comme suit :

Le chapitre 1 fournit une revue de littérature détaillée des matériaux 2D, avec un accent particulier sur la synthèse, la structure et les propriétés optiques des MXenes. Commençant par le développement historique des matériaux bidimensionnels depuis la découverte du graphène jusqu'à nos jours, il retrace l'évolution de ce domaine en expansion rapide. Le chapitre se concentre ensuite sur les MXenes comme classe émergente de matériaux avec un potentiel significatif pour les applications optiques, introduisant leur structure fondamentale comme carbures et nitrures

de métaux de transition 2D. Il explore en détail les précurseurs de phase MAX dont les MXenes sont dérivés, les diverses méthodologies de synthèse employées pour leur production, et comment ces approches de synthèse influencent directement les caractéristiques structurelles. Une attention particulière est accordée à la chimie de surface des MXenes, soulignant le rôle critique des terminaisons de surface (T_x) dans la détermination des propriétés des matériaux et du potentiel d'application. La section finale examine la compréhension actuelle des propriétés optiques des MXenes, avec un focus particulier sur leur comportement plasmonique, leur réponse infrarouge et leur potentiel pour les applications en détection optique, blindage électromagnétique et dispositifs optoélectroniques.

Le chapitre 2 présente les fondements théoriques et les approches méthodologiques pour l'étude multi-échelle des MXenes, incluant les principes fondamentaux des interactions lumière-matière et les fondements des techniques de microscopie en champ proche. Ce chapitre développe le cadre conceptuel requis pour comprendre les phénomènes optiques dans les matériaux 2D à travers différentes échelles de longueur. Il explore comment le rayonnement électromagnétique interagit avec les couches atomiquement minces, avec un focus sur la région spectrale infrarouge où la plupart des groupes fonctionnels organiques présentent des signatures vibrationnelles distinctives. Le chapitre introduit les limitations des techniques conventionnelles limitées par la diffraction et plonge dans les fondements théoriques de la microscopie en champ proche. Un accent particulier est mis sur la microscopie à force photo-induite (PiFM), élucidant le modèle d'interaction dipôle-dipôle, l'origine des forces photo-induites et les mécanismes physiques permettant la cartographie chimique nanoscopique avec cette technique. À travers des modèles théoriques et des considérations expérimentales, ce chapitre construit le fondement méthodologique pour l'approche de caractérisation multi-échelle employée tout au long de la thèse.

La deuxième section développe la spectroscopie infrarouge en tant que sonde in-situ pour l'investigation des processus électrochimiques dans les électrodes à base de MXene $Ti_3C_2T_x$. Grâce à la spectroscopie infrarouge à transformée de Fourier en réflexion totale atténuée (ATR-FTIR), ces travaux permettent de suivre en temps réel l'intercalation des ions Li^+ en détectant le déplacement des molécules d'eau présentes entre les feuillets du MXene. Une cellule électrochimique potentiostatique sur mesure, intégrée à un cristal ATR en diamant, permet la surveillance en temps réel des modes de vibration au cours des cycles de charge-décharge, offrant ainsi un aperçu direct des mécanismes d'intercalation et des modifications structurales dans l'espace interfeuillet du MXene.

Le chapitre 3 étudie l'influence du rapport carbone-azote dans le MXene $Ti_3C_{(2-y)}N_yT_x$ sur les propriétés infrarouges, révélant comment l'ajustement compositionnel peut moduler la réponse optique à travers le spectre infrarouge. Basé sur une expérimentation systématique avec des MXenes de rapports C/N variables (y = 0, 0,25, 0,5 et 1), ce chapitre démontre que le rapport carbone-azote sert de levier pour ajuster les propriétés optiques infrarouges. À travers une caractérisation complète utilisant la diffraction des rayons X, la spectroscopie Raman et la spectroscopie infrarouge à transformée de Fourier, il révèle comment l'incorporation d'azote modifie systématiquement la structure cristalline, changeant les paramètres de réseau tout en préservant l'architecture fondamentale du MXene. Le chapitre présente une analyse détaillée des mesures de réflectance infrarouge, montrant qu'un contenu plus élevé en carbone améliore la réflectance IR, tandis qu'un contenu accru en azote

élève l'émissivité. Il explore également le comportement d'émissivité dépendant de la température de ces matériaux et corrèle les résultats expérimentaux avec les calculs de théorie fonctionnelle de la densité pour élucider les mécanismes fondamentaux responsables des variations observées des propriétés optiques. Cette investigation établit une stratégie claire pour concevoir la réponse infrarouge des MXenes de carbonitrure de titane à travers un contrôle compositionnel précis.

Le chapitre 4 se concentre sur la reconnaissance des terminaisons chimiques de surface et la modification de surface des MXenes 2D utilisant la nanoscopie IR, démontrant les capacités du PiFM à identifier à la fois les groupes fonctionnels de surface natifs et les contaminants environnementaux à l'échelle nanométrique. Ce chapitre exploite la spécificité chimique et la résolution spatiale de la microscopie à force photo-induite pour étudier la chimie de surface à des échelles sans précédent. Il révèle les groupes fonctionnels de surface présents sur les MXenes pristines $Ti_3C_2T_x$, $Ti_3C_{1.5}N_{0.5}T_x$ et V_2CT_x, identifiant les liaisons chimiques caractéristiques telles que C=C, C–H, C–O et C–F liées aux groupes terminaux. Le chapitre étudie également le MXene Nb_2CT_x à travers des techniques spectroscopiques complémentaires de champ lointain et de champ proche, avec un accent particulier sur la capacité du PiFM à détecter les phénomènes d'oxydation nanoscopiques. Cette analyse révèle des caractéristiques d'absorption distinctives dans la gamme 770–1860 cm^{-1}, notamment les pics caractéristiques autour de 950–980 cm^{-1} associés à la formation d'oxyde de niobium. Remarquablement, le PiFM démontre une sensibilité accrue dans la détection de ces signatures d'oxydation même dans les feuillets de MXene mono/peu-couches avec des épaisseurs aussi faibles que 15 nm, soulignant la sensibilité à l'échelle nanométrique. De plus, le chapitre démontre la capacité du PiFM à détecter et cartographier la contamination à base de siloxane sur les feuillets de MXene vieillis, identifiant spécifiquement les liaisons Si–C et Si–O–Si distribuées uniformément sur la surface, qui restent indétectables par les techniques spectroscopiques conventionnelles. Le chapitre explore les mécanismes de réaction entre les terminaisons hydroxyle du MXene et les composés siloxanes, fournissant des aperçus sur les processus de modification de surface et soulignant la liaison préférentielle aux sites de surface plutôt qu'aux bords. À travers une analyse comparative avec les méthodes spectroscopiques conventionnelles, il établit le PiFM comme outil essentiel pour étudier la chimie de surface nanoscopique dans les matériaux 2D, avec des implications profondes pour comprendre les interactions environnementales et développer des approches stratégiques pour la fonctionnalisation de surface.

Le chapitre 5 explore l'application des MXenes pour la détection utilisant la résonance plasmonique de surface, se concentrant spécifiquement sur les processus de dépôt de films minces et les capacités de détection moléculaire. Ce chapitre fait la transition de la caractérisation fondamentale aux applications pratiques, démontrant l'intégration des MXenes dans des plateformes de détection fonctionnelles. La première section étudie le monitoring en temps réel du dépôt de films minces de MXene utilisant la technique de résonance plasmonique de surface, fournissant des aperçus sur la dynamique de formation des films, le contrôle de l'épaisseur et l'uniformité de la couverture de surface. La seconde section explore la détection du (3-Aminopropyl)triéthoxysilane (APTES) utilisant des capteurs SPR basés sur les MXenes, exploitant les aperçus de chimie de surface obtenus des chapitres précédents, particulièrement les interactions siloxane-MXene identifiées par l'analyse PiFM. Cette investigation établit une preuve de concept pour les applications

des MXenes en détection chimique et démontre comment les propriétés de surface uniques de ces matériaux 2D peuvent être exploitées pour détecter des composés moléculaires spécifiques, ouvrant des voies pour développer des technologies de détection avancées basées sur les plateformes MXene.

Cette progression de recherche — de la synthèse fondamentale à la caractérisation optique en champ lointain et finalement aux investigations nanoscopiques en champ proche — établit une image complète des propriétés infrarouges des MXenes et démontre leur potentiel pour les applications technologiques en détection et au-delà. La thèse fait avancer à la fois la compréhension fondamentale de la chimie de surface des MXenes et les propriétés optiques tout en fournissant des aperçus pratiques pour leur implémentation dans des technologies optiques avancées.

Chapitre 1

État de l'art sur les matériaux 2D et les MXenes

1.1 Brève revue des matériaux bidimensionnels en optique

Depuis la découverte du graphène en 2004, les matériaux bidimensionnels (2D), notamment les dichalcogénures de métaux de transition (TMD), le phosphore noir (BP) et le nitrure de bore hexagonal (hBN), ont révolutionné la science des matériaux grâce à leurs propriétés optiques uniques. La transition du vrac au 2D introduit des effets de confinement quantique, des bandes interdites dépendant de la couche et des réponses optiques non linéaires considérablement améliorées en raison de l'épaisseur à l'échelle atomique.

Ces matériaux couvrent l'ensemble du spectre électronique, du graphène semi-métallique au hBN à large bande interdite (6 eV), offrant ainsi une boîte à outils complète pour la conception de dispositifs optiques. Les hétérostructures de Van der Waals permettent une ingénierie des propriétés sans précédent, sans contraintes d'adaptation au réseau.

L'avantage principal des matériaux 2D réside dans leur capacité exceptionnelle à être accordés par des stimuli externes : le gating électrique module la conductivité optique, la déformation mécanique permet d'accorder la bande interdite et les champs magnétiques induisent des effets de polarisation de la vallée, offrant ainsi de nouveaux degrés de liberté pour la manipulation de la lumière.

1.2 L'émergence des carbures et nitrures de métaux de transition en 2D

Les MXenes sont une famille de carbures et nitrures bidimensionnels de métaux de transition découverts en 2011[22], le premier matériau synthétisé étant $Ti_3C_2T_x$. Ils suivent la formule générale $M_{n+1}X_nT_x$, où M est un métal de transition précoce, X est le carbone ou l'azote, T représente les terminaisons de surface (=O, -F, -OH), et $n = 1 - 4$.

Les MXenes sont principalement synthétisés par gravure sélective de couches d'aluminium à partir de précurseurs en phase MAX, à l'aide de solutions d'acides

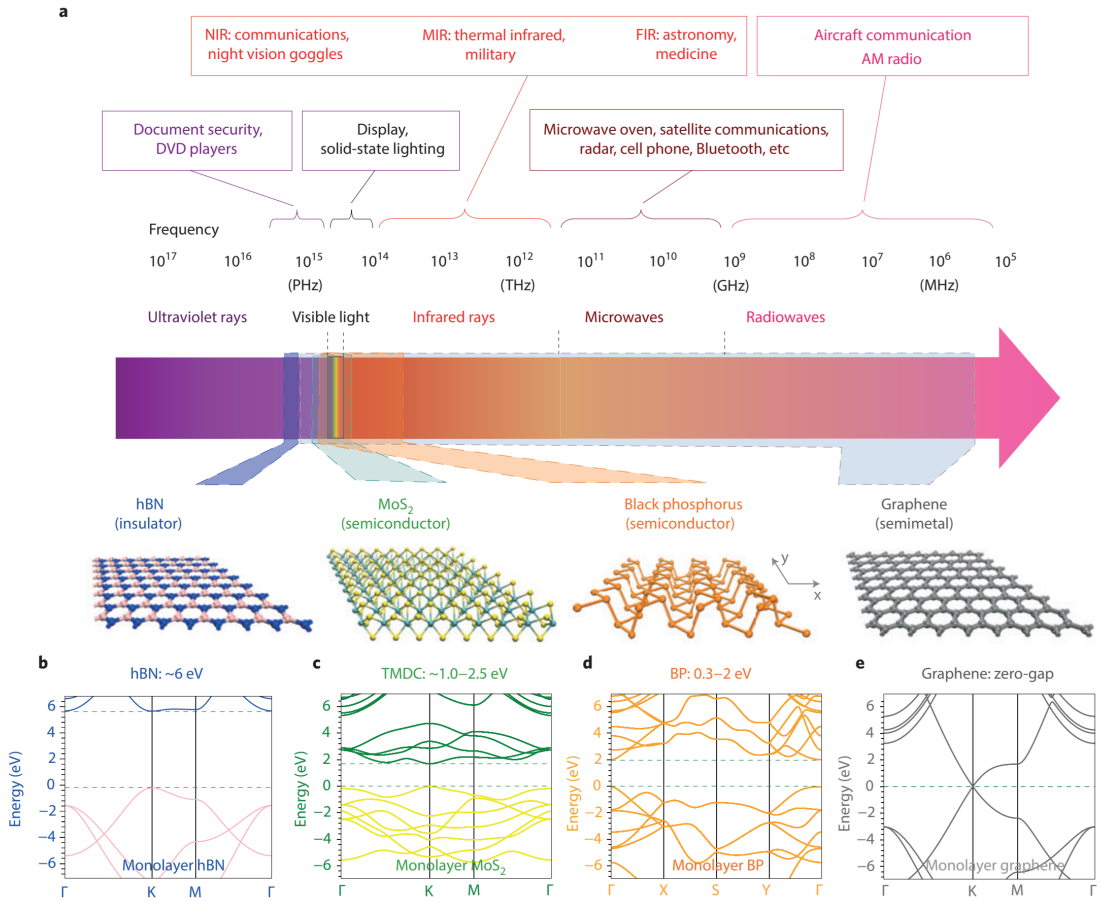

Figure 1.1 Matériaux 2D couvrant une large gamme spectrale. (a) Spectre électromagnétique. Les applications qui utilisent les différentes gammes spectrales sont présentées dans la partie supérieure du panneau. NIR, MIR et FIR indiquent respectivement l'infrarouge proche, moyen et lointain. Les structures atomiques de hBN, MoS_2, BP et graphène sont montrées dans la partie inférieure du panneau, de gauche à droite. Les directions cristallines (x et y) du BP anisotrope sont indiquées. Les gammes spectrales possibles couvertes par différents matériaux sont indiquées par des polygones colorés. (b–e) Structures de bandes du hBN monocouche (b), MoS_2 (c), BP (d) et graphène (e). Extrait de [27].

contenant de l'acide fluorhydrique et de l'acide chlorhydrique [14, 28]. Contrairement aux matériaux 2D conventionnels maintenus ensemble par des forces de van der Waals, les phases MAX ont des liaisons chimiques fortes entre les couches, ce qui rend l'exfoliation mécanique impossible et nécessite des méthodes de gravure chimique.

Avec plus de 50 combinaisons expérimentales possibles, les MXenes présentent diverses propriétés, notamment l'hydrophilie, une conductivité électrique élevée et des résonances plasmoniques [24]. Ces caractéristiques les destinent à diverses applications, notamment le stockage de l'énergie [29], le blindage contre les interférences électromagnétiques [30, 31], les capteurs [32], l'optoélectronique [33] et les applications biomédicales [14]. Leur polyvalence permet de les fabriquer sous différentes formes, depuis les encres jusqu'aux films minces et aux composites polymères.

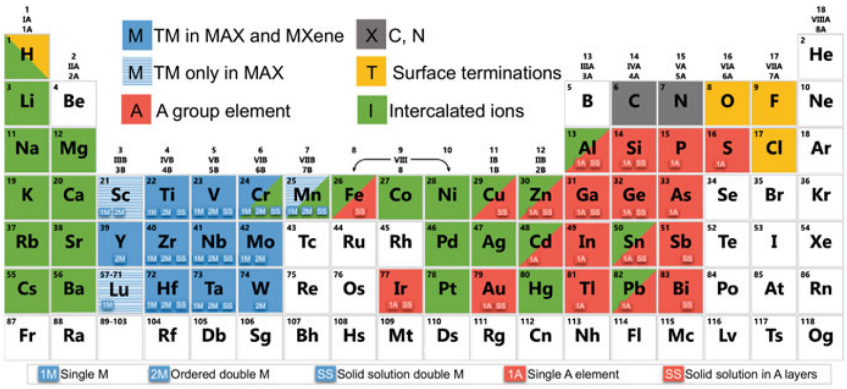

Figure 1.2 Tableau périodique représentant les éléments dans les phases MAX et les MXenes, et les terminaisons de surface [14].

Les MXenes sont synthétisés par attaque chimique spécifique des atomes de la couche A des précurseurs de la phase MAX à l'aide de solutions d'acide fluorhydrique. La synthèse dépend de nombreux paramètres, notamment la composition de l'agent de gravure, la concentration, la température, la nature du métal de transition, et la taille des particules du précurseur, qui influencent directement les propriétés structurelles et chimiques du matériau final.

Le processus de gravure élimine sélectivement les éléments A tout en préservant la structure 2D, mais peut introduire des défauts structurels tels que des nanopores. Le processus est contrôlé par diffraction des rayons X en suivant les changements de la constante de réseau c, qui est sensible à l'intercalation d'ions, aux molécules d'eau et aux conditions de séchage.

Les surfaces de MXene se terminent naturellement par des espèces issues du processus de gravure, représentées par la formule $M_{n+1}X_nT_x$, où T désigne les groupes de terminaison (principalement -F, -OH, =O). Au cours de la gravure HF du Ti_3AlC_2, les ions fluorure se lient aux atomes A et M, la couche A est éliminée sous forme d'AlF_3, et les surfaces M exposées sont terminées de manière prédominante par des ions fluorure.

Les techniques de caractérisation avancées révèlent une chimie de surface complexe où l'oxygène et le fluor constituent la majorité des sites de surface (>95%), les groupes hydroxyles occupant une fraction minime [34]. La chimie de surface est dynamique, les groupes hydroxyles pouvant se recombiner pour former de l'eau et de l'oxygène atomique. Les MXenes sont très réactifs dans les conditions ambiantes

et subissent une oxydation rapide lorsqu'ils sont exposés à l'air, ce qui souligne l'importance des environnements contrôlés pour préserver leurs propriétés.

Les MXenes font preuve d'une polyvalence exceptionnelle dans de multiples applications technologiques, notamment les systèmes plasmoniques, les plates-formes de biodétection et le blindage contre les interférences électromagnétiques (EMI). Leur combinaison unique de propriétés plasmoniques et d'une excellente conductivité électrique en fait des matériaux essentiels pour les futurs systèmes de détection, de conversion d'énergie et de protection électronique.

L'analyse complète des MXenes révèle leur potentiel exceptionnel en tant que matériaux 2D dotés de propriétés optiques et plasmoniques distinctives. Cependant, l'exploitation complète de ces caractéristiques nécessite une compréhension approfondie de leur comportement optique dans l'infrarouge, en particulier en tenant compte de l'influence critique des terminaisons de surface sur leurs propriétés physicochimiques.

Cette thèse étudie les propriétés optiques des MXenes, en particulier leur réponse spectrale dans l'infrarouge. Le travail établira les aspects fondamentaux de la spectroscopie infrarouge pour la caractérisation des MXenes, fournissant des cadres théoriques pour comprendre les interactions lumière-matière dans ces systèmes 2D complexes. Des techniques avancées de microscopie en champ proche seront explorées pour permettre une investigation optique à l'échelle nanométrique au-delà de la limite de diffraction, facilitant ainsi des études de caractérisation complètes.

La poursuite des recherches sur la modification des surfaces et l'optimisation des matériaux devrait permettre de découvrir d'autres applications en optoélectronique, dans les systèmes de sécurité et dans les technologies de communication à haute fréquence, ce qui élargira encore l'importance technologique des MXenes.

Chapitre 2

Aspects fondamentaux de la spectroscopie IR pour les MXenes

2.1 Fondamentaux de la spectroscopie IR

La spectroscopie est l'étude de l'interaction entre la lumière et d'autres formes de rayonnement et la matière. Ce domaine analyse le rayonnement électromagnétique en fonction de la longueur d'onde ou de la fréquence afin d'obtenir des informations sur la matière analysée. L'analyse spectroscopique a joué un rôle fondamental dans le développement de théories physiques clés, notamment la mécanique quantique, la relativité générale et l'électrodynamique quantique.

La spectroscopie peut être classée en différentes méthodes en fonction du type de rayonnement utilisé : rayonnement électromagnétique, particules, ondes acoustiques et analyse mécanique dynamique. Ce travail se concentre spécifiquement sur l'interaction entre le rayonnement électromagnétique et la matière, avec un accent particulier sur les ondes électromagnétiques infrarouges.

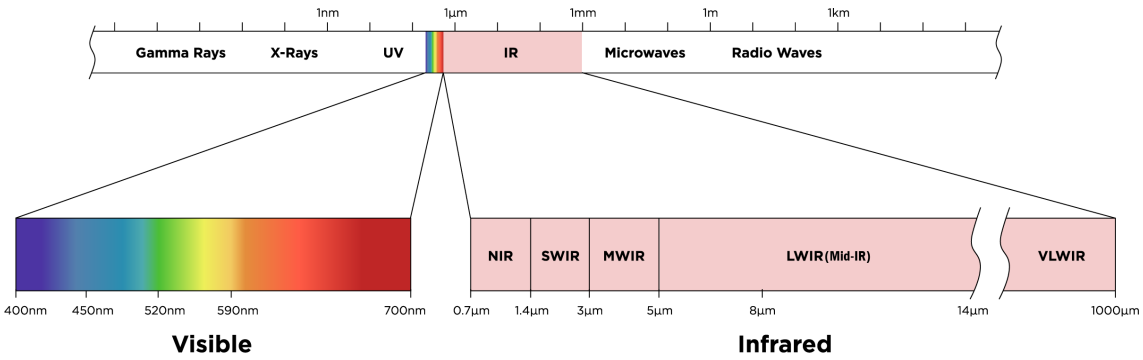

Figure 2.1 Spectre électromagnétique combinant toutes les fréquences du rayonnement électromagnétique. Dans ce travail, nous avons principalement concentré notre attention sur l'infrarouge à grandes longueurs d'onde (LWIR), également appelé région infrarouge moyen (Mid-IR).

2.2 La nanospectroscopie par sonde locale

La microscopie à sonde à balayage (SPM) a révolutionné la caractérisation des matériaux à l'échelle nanométrique grâce à l'imagerie haute résolution et l'analyse

de surface. Les principales techniques SPM comprennent la microscopie à force atomique (AFM), la microscopie optique en champ proche de diffusion (s-SNOM), et la microscopie à force photo-induite (PiFM), chacune exploitant les interactions sonde-échantillon pour extraire des informations nanométriques complémentaires.

Ces techniques ont émergé pour répondre à la limite de diffraction de la microscopie optique conventionnelle, qui restreint la résolution spatiale à environ $d = \frac{\lambda}{2n \sin \theta}$ (centaines de nanomètres pour la lumière visible/infrarouge). Cette limitation dépasse largement les dimensions caractéristiques des nanostructures, nécessitant des méthodes de caractérisation avancées.

L'AFM sert de technique fondamentale, fournissant des informations topographiques et mécaniques précises grâce à la détection des forces sonde-surface. Le s-SNOM s'appuie sur l'AFM en intégrant l'excitation optique, où la pointe AFM métallique agit comme une nanoantenne, confinant la lumière à des dimensions sub-longueur d'onde et diffusant les interactions de champ proche en rayonnement de champ lointain détectable. Cela permet l'imagerie optique nanométrique et l'accès aux propriétés diélectriques locales.

Le PiFM avance ces capacités en couplant la sensibilité mécanique de l'AFM avec les forces optiques localisées issues des interactions lumière-matière. Cette approche hybride permet la cartographie directe des signatures chimiques et des propriétés optiques avec une résolution spatiale au niveau de l'AFM tout en conservant la spécificité moléculaire de la spectroscopie infrarouge et Raman.

Ces techniques complémentaires représentent l'évolution de la caractérisation AFM purement mécanique vers l'imagerie optique et chimique avancée, formant un cadre complet pour l'investigation nanométrique en microélectronique, nanophotonique et science des matériaux.

La microscopie à force photo-induite (PiFM) est une technique de nanoscopie à sonde à balayage basée sur la microscopie à force atomique. Cette technique combine l'information topographique à l'échelle nanométrique en mesurant la force d'interaction entre une pointe nanoscopique et la surface d'un échantillon, ainsi que l'information spectroscopique utilisant un laser d'excitation modulé et accordable qui induit une interaction optique entre la pointe et l'échantillon. La nature accordable du laser permet de réaliser des spectres sur une large gamme spectrale, produisant des signaux similaires aux spectres d'absorption conventionnels mais avec une résolution spatiale nanométrique.

Le PiFM fait partie d'une grande famille de SPM nano-spectroscopiques, incluant la microscopie optique en champ proche de diffusion (s-SNOM) et la spectroscopie Raman exaltée par pointe. Le PiFM détecte l'interaction lumière-matière à travers la vibration mécanique du cantilever, tandis que le s-SNOM détecte la lumière diffusée par l'apex de la pointe en champ lointain.

Le PiFM fonctionne en mode tapping, où la pointe est excitée par un élément piézoélectrique pour créer une oscillation du cantilever avec une petite amplitude (typiquement 1 à 2 nm). Pour les mesures topographiques, le cantilever oscille à la seconde résonance mécanique ($f_2 \simeq 1.6$ MHz), tandis que pour le signal de force photo-induite, le cantilever est accordé sur sa première résonance mécanique ($f_1 \simeq 250$ kHz).

Le système Vista One de Molecular Vista inclut également un module s-SNOM. Au lieu de détecter l'oscillation mécanique du cantilever induite par le laser infrarouge, la lumière diffusée par l'apex de la pointe est collectée par un miroir parabo-

lique et envoyée vers un détecteur (typiquement MCT refroidi à l'azote liquide). Un module interférométrique à deux bras permet les schémas de détection homodyne et hétérodyne.

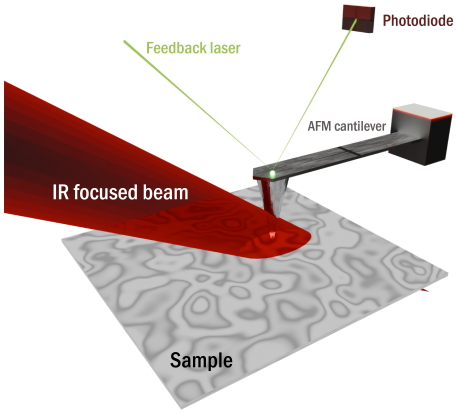

Figure 2.2 Schéma du système PiFM et modes de détection. En mode de détection *directe*, la topographie est acquise à la seconde résonance mécanique du cantilever f_2 et la force photo-induite est mesurée à la première résonance mécanique f_1. Cependant, en mode de détection *bande latérale*, la force photo-induite est détectée par $f_m = |f_2 \pm f_1|$.

Chapitre 3

Caractérisation infrarouge en champ lointain des MXenes : études de la composition chimique et de l'interface électrochimique

3.1 L'influence du rapport carbone/azote dans le MXène $Ti_3C_yN_{(2-y)}T_x$ sur les propriétés infrarouges [1]

Les MXenes carbonitrures de titane ont attiré une attention considérable en raison de leurs propriétés exceptionnelles incluant une stabilité chimique remarquable, une conductivité électrique élevée, des voies de production rentables, et une chimie de surface accordable. La différence fondamentale entre les atomes de carbone et d'azote réside dans leurs valeurs d'électronégativité, l'azote présentant une électronégativité plus élevée que le carbone. Cette différence résulte en des liaisons Ti–N plus fortes comparées aux liaisons Ti–C, conduisant à des modifications distinctes des propriétés physiques, électroniques et optiques du matériau.

Cette section étudie les propriétés optiques infrarouges des MXenes carbonitrures de titane avec des rapports carbone-azote systématiquement variés dans la gamme de longueurs d'onde 1-25 μm. La sélection de quatre rapports carbone-azote spécifiques (y=0, 0.25, 0.5 et 1) a été stratégiquement conçue pour couvrir la gamme compositionnelle complète du carbure pur au contenu égal carbone-azote.

Résultats et discussion

Les échantillons MXene ont été préparés en utilisant deux méthodes distinctes : dépôt par pulvérisation et dépôt par étalement (Figure 3.1). L'analyse par diffraction des rayons X (DRX) des $Ti_3C_{(2-y)}N_yT_x$ avec des rapports C/N variables a révélé des modifications structurales. Le paramètre de maille c diminue linéairement avec

1. Une version abrégée de ce chapitre a été publiée dans *Materials Today Physics*, The C/N ratio as a lever for infrared properties tuning in carbonitride MXenes, Materials Today Physics, Volume 58, October 2025, 101860, https://doi.org/10.1016/j.mtphys.2025.101860

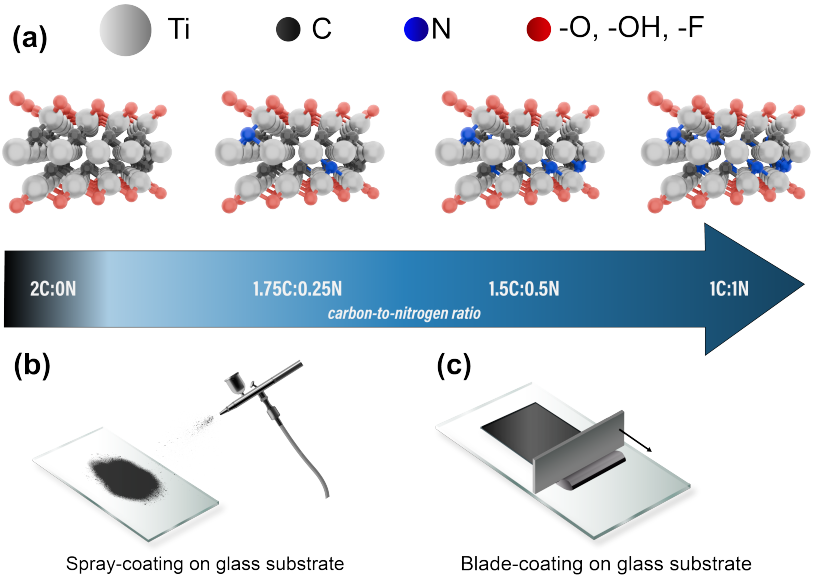

Figure 3.1 (a) Modèles 3D des carbonitrures de titane et leurs rapports C/N correspondants. (b) Technique de dépôt par pulvérisation de MXene. (c) Technique de dépôt par lame de MXene.

l'augmentation du contenu en azote, suivant la loi de Vegard, allant de 18.72 Å pour Ti_3AlC_2 (y = 0) à 18.44 Å pour Ti_3AlCN (y = 1).

3.1.1 Réflectance IR

Les spectres de réflectance des dépôts MXene à température ambiante ont été mesurés de 1 à 25 μm (Figure 3.2). Les mesures révèlent que la réflectance globale augmente systématiquement avec l'augmentation du contenu en carbone dans la structure MXene. Pour le $Ti_3C_2T_x$ MXene (y=0), la réflectance intégrée $\bar{R}$ égale 23.45, représentant 93.8% de la réflectance théorique maximale, comparée à 15.85 (63.4%) pour le Ti_3CNT_x (y=1).

Dans la région proche infrarouge (NIR), la faible réflectance observée peut être attribuée à l'absorption d'énergie par les électrons libres, comportement caractéristique des matériaux métalliques. Les propriétés intrinsèques des atomes de carbone et d'azote influencent significativement ce comportement.

3.1.2 Émission IR

Les mesures d'émissivité spectrale de 5 à 25 μm pour les quatre MXenes déposés par pulvérisation à 200°C (Figure 3.3(a)) révèlent que l'émissivité globale augmente systématiquement avec l'augmentation du contenu en azote. La composition pure (y=0) présente l'émissivité la plus faible (0.05), tandis que le MXene contenant le plus d'azote (y=1) montre l'émissivité la plus élevée (0.65).

Pour l'échantillon $Ti_3C_{1.75}N_{0.25}$, nous observons une augmentation presque linéaire de l'émissivité avec l'augmentation de la température (Figure 3.3(b-c)). Ce comportement dépendant de la température peut être analysé à travers un cadre théorique intégré combinant plusieurs phénomènes physiques basés sur une relation étendue de Hagen-Rubens.

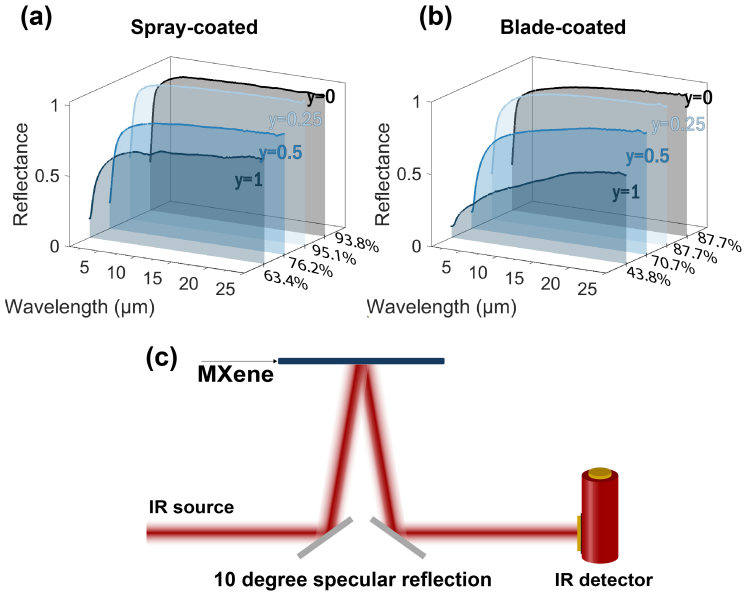

Figure 3.2 Spectres de réflectance expérimentaux des MXenes (a) revêtus par pulvérisation et (b) revêtus par lame avec des rapports C/N variables. (c) Schéma du montage de mesure de réflectance.

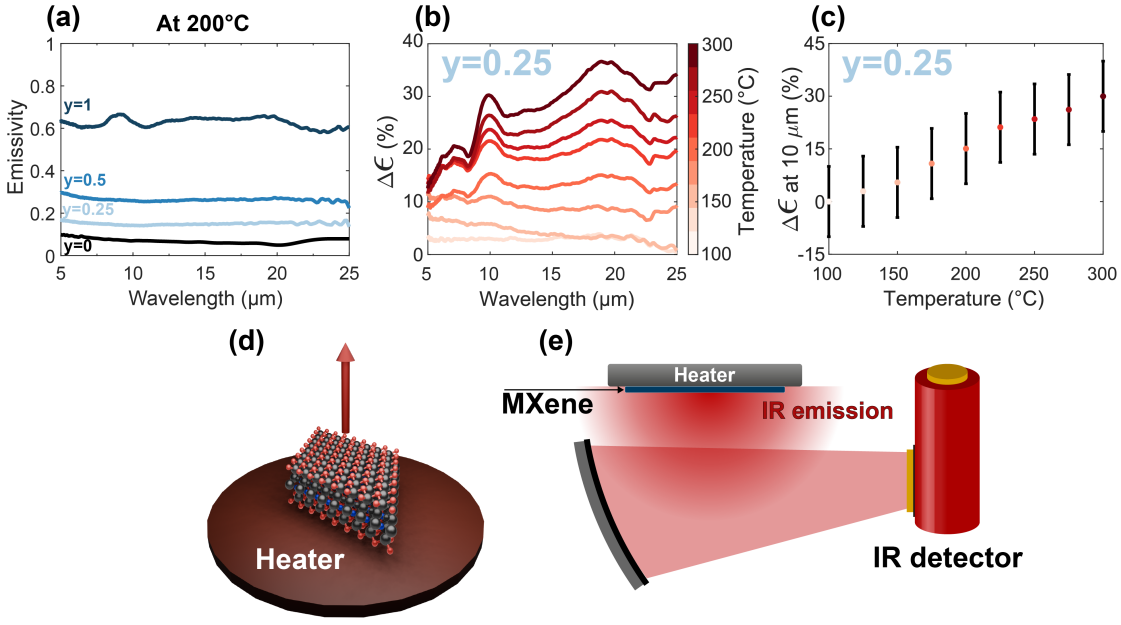

Figure 3.3 (a) Émissivité à 200°C des $Ti_3C_{(2-y)}N_yT_x$ (y=0, 0.25, 0.5 et 1). (b) Spectres d'émissivité du $Ti_3C_{1.75}N_{0.25}T_x$ revêtu par pulvérisation à des températures allant de 100 à 300°C et (c) variation de l'émissivité à 10 μm en fonction de la température. (d) Représentation schématique de l'émission IR des films MXene. (e) Schéma du montage de mesure d'émission thermique.

3.1.3 Calculs de théorie fonctionnelle de la densité

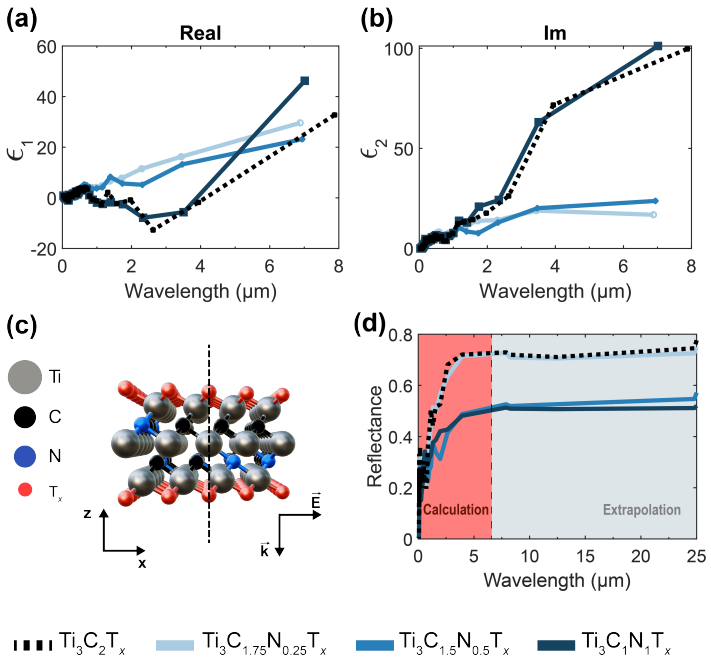

Figure 3.4 Parties réelle (a) et imaginaire (b) de la fonction diélectrique calculée. (c) Schéma de structure de couche 2D de $Ti_3C_{(2-y)}N_yT_x$, montrant la direction du vecteur d'onde k le long de la direction z et la composante électrique de la lumière orientée dans le plan x-y. (d) Spectres de réflectance calculés de $Ti_3C_{(2-y)}N_yT_x$. La ligne pointillée sépare les données calculées et extrapolées.

Les effets du rapport carbone-azote sur les propriétés optiques des MXenes $Ti_3C_{(2-y)}N_yT_x$ ont été étudiés théoriquement en utilisant la théorie fonctionnelle de la densité (DFT). Les calculs ont été effectués en utilisant le Vienna Ab initio Simulation Package (VASP) avec l'approximation du gradient généralisé (GGA). Les calculs ont été effectués par B. Moses Abraham, Drexel University.

Les parties réelle (ε_1) et imaginaire (ε_2) calculées de la fonction diélectrique sont présentées dans les Figures 3.4(a) et (b). Dans la région infrarouge moyen (2–4 μm), $Ti_3C_2T_x$ présente des valeurs ε_1 fortement négatives, reflétant son caractère métallique. Avec l'augmentation du contenu en azote, ε_1 se déplace vers des valeurs positives, indiquant une transition vers un comportement diélectrique.

La Figure 3.4(d) montre que $Ti_3C_2T_x$ a la réflectance IR la plus élevée en raison de son comportement métallique, tandis que Ti_3CNT_x a la réflectance la plus faible, ce qui est cohérent avec les résultats expérimentaux.

Conclusion

Cette étude montre la modulation réussi des propriétés infrarouges (IR) dans les MXenes carbonitrures de titane $Ti_3C_{(2-y)}N_yT_x$ grâce au contrôle précis de leur rapport carbone-azote. Les résultats établissent une stratégie claire pour l'ingénierie de la réponse IR des MXenes carbonitrures de titane, soulignant leur potentiel comme matériaux accordables et multifonctionnels pour les technologies optoélectroniques et optiques de nouvelle génération.

Le contenu en carbone plus élevé améliore la réflectance IR, rendant ces compositions prometteuses pour le blindage IR et les revêtements réfléchissants, avec $Ti_3C_2T_x$ présentant une émissivité exceptionnellement faible de 0.06. En revanche, l'augmentation du contenu en azote conduit à une émissivité plus élevée, atteignant 0.65 pour Ti_3CNT_x, exploitable dans les applications de gestion thermique et de détection IR.

3.2 Sondage infrarouge in situ des intercalations ioniques dans le MXene $Ti_3C_2T_x$

Les MXenes, notamment le $Ti_3C_2T_x$, sont des matériaux bidimensionnels prometteurs pour le stockage d'énergie grâce à leur conductivité élevée et leur capacité d'intercalation ionique. Cependant, la compréhension des mécanismes électrochimiques dynamiques reste limitée par les techniques de caractérisation existantes, principalement ex-situ ou nécessitant des installations synchrotron.

Ce travail propose l'utilisation de la spectroscopie ATR-FTIR comme sonde in-situ pour étudier en temps réel l'intercalation de Li^+ dans les électrodes $Ti_3C_2T_x$. En suivant l'évolution des bandes vibrationnelles de l'eau lors du déplacement des molécules d'eau par les ions lithium dans l'espace intercouche, cette approche révèle les mécanismes d'intercalation et les processus électrochimiques. Le montage expérimental intègre une cellule électrochimique avec un cristal ATR diamant pour monitorer les modes vibrationnels pendant le cyclage galvanostatique.

3.2.1 Montage de cellule électrochimique sur cristal FTIR-ATR

Une cellule électrochimique sur mesure a été conçue pour les mesures ATR-FTIR in situ. La configuration à deux électrodes comprend une électrode de travail MXene $Ti_3C_2T_x$ de 15 μm d'épaisseur déposée directement sur un substrat de cristal ATR diamant, couplée à une contre-électrode en graphite. Les électrodes sont en contact via un séparateur Cellguard imbibé d'un électrolyte aqueux LiCl 1 M, choisi pour sa conductivité ionique élevée et sa compatibilité avec la chimie de surface du MXene. Un courant constant appliqué entre les électrodes pilote le processus d'intercalation/désintercalation du lithium, permettant le suivi en temps réel par spectroscopie ATR-FTIR.

3.2.2 Résultats et Discussion

L'évolution des spectres ATR-FTIR durant la polarisation cathodique (0 V à -1.2 V) révèle des modifications systématiques reflétant l'intercalation de Li^+ dans la structure MXene. La région O-H (2500-4000 cm^{-1}) montre une diminution progressive de l'intensité durant la charge, corrélée au déplacement des molécules d'eau par les ions Li^+ entrants. Le processus de décharge présente une récupération complète des caractéristiques spectrales initiales, confirmant la réversibilité du mécanisme d'intercalation.

La déconvolution spectrale résout quatre populations d'eau distinctes : molécules d'eau fortement liées (3159 cm^{-1}), modérément liées (3298 cm^{-1}), faiblement liées

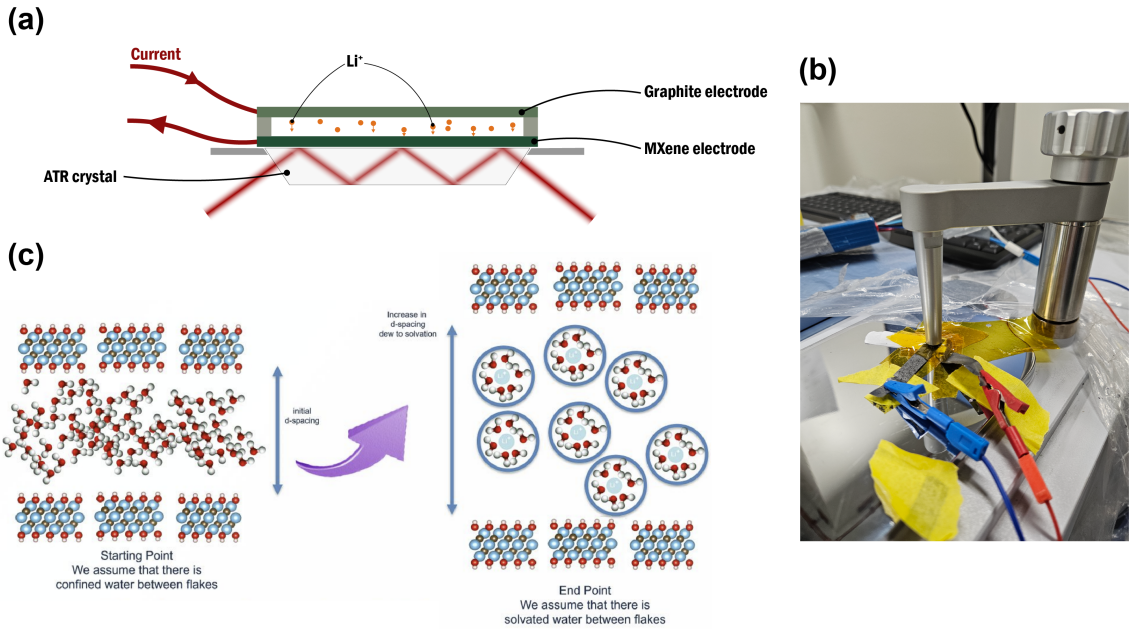

Figure 3.5 Concept de surveillance électrochimique des MXenes. (a) Représentation schématique de la cellule électrochimique utilisée pour la spectroscopie ATR-FTIR in situ. La cellule est constituée d'une électrode de travail en MXène $Ti_3C_2T_x$ (épaisseur d'environ 15 μm) déposée sur un cristal ATR, et d'une contre-électrode en graphite. Les ions Li^+ (sphères oranges) sont représentés s'intercalant dans la structure du MXène pendant le cyclage électrochimique. (b) Montage de la cellule ATR-FTIR. (c) Comparaison entre OH-confiné et OH-solvaté pour $Ti_3C_2T_x$ dans LiCl, schéma extrait de [35].

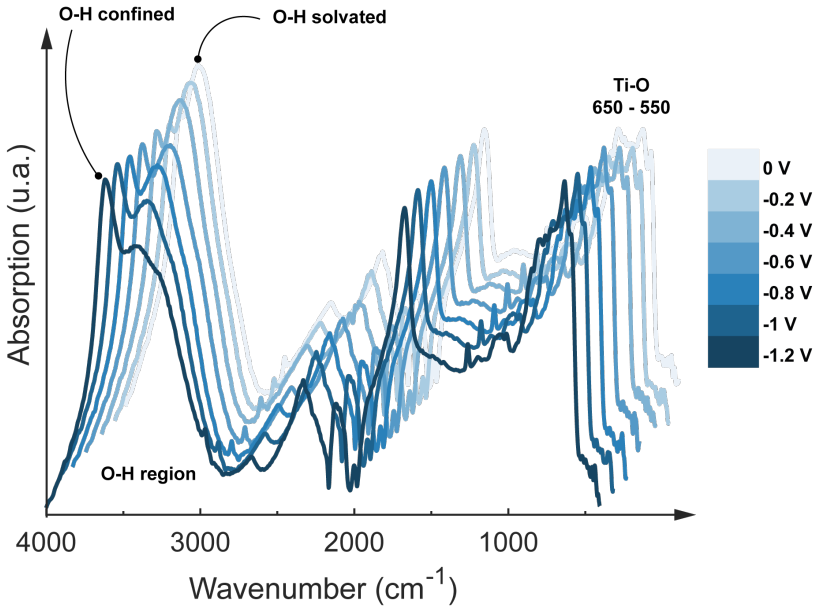

Figure 3.6 Evolution of ATR-FTIR spectra of $Ti_3C_2T_x$ MXene electrode as a function of applied potential from 0 V to -1.2 V during Li^+ intercalation in 1 M LiCl aqueous electrolyte.

(3411 cm^{-1}), et groupes OH libres (3591 cm^{-1}). Ces assignations correspondent aux différents environnements de liaison hydrogène dans l'espace intercouche du MXene.

Ces investigations préliminaires ont été validées et étendues par l'équipe de Drexel University, démontrant l'applicabilité de la méthodologie ATR-FTIR sur différents systèmes d'électrolytes et types de cations. L'approche ouvre des perspectives pour la caractérisation par microscopie à force photo-induite (PiFM), combinant résolution spatiale AFM et spécificité chimique infrarouge pour cartographier les propriétés à l'échelle nanométrique.

Chapitre 4

Propriétés optiques en champ proche des MXenes par nanoscopie IR

Le chapitre précédent a exploré comment la variation systématique du rapport carbone-azote dans les MXenes carbonitrures de titane ($Ti_3C_{(2-y)}N_yT_x$) impacte significativement leurs propriétés infrarouges. Cependant, la chimie de surface joue un rôle crucial dans l'ingénierie des propriétés : le type et la distribution des groupes fonctionnels terminaux (T_x). Ces terminaisons de surface induites par gravure contiennent habituellement des groupes oxygène, hydroxyle et fluorure, critiques pour les comportements électroniques, optiques et chimiques des MXenes.

Les méthodes spectroscopiques conventionnelles telles que la spectroscopie FTIR et la spectroscopie Raman fournissent des informations sur la chimie de surface des MXenes mais sont spatialement limitées. Ce chapitre aborde ces défis en utilisant des techniques avancées de nanoscopie infrarouge en champ proche pour la cartographie chimique avec une résolution spatiale nanométrique.

4.1 Terminaisons de surface des MXenes

La chimie de surface des MXenes est d'un intérêt particulier car elle affecte les propriétés dans plusieurs domaines, incluant la conductivité électrique, la réactivité chimique et le comportement optique. Le type et la distribution des terminaisons de surface (–OH, –O, –F, –Cl) influencent la structure électronique, la fonction de travail et la stabilité chimique de ces matériaux bidimensionnels.

La microscopie à force photo-induite (PiFM) représente un avancement significatif dans ce domaine, offrant une résolution spatiale inégalée (5-10 nm) combinée avec une spécificité chimique grâce à la spectroscopie infrarouge. L'analyse PiFM de $Ti_3C_2T_x$ et V_2CT_x pristines (Figure 4.1) révèle des signatures PiFM claires autour de la région 1000-1200 cm^{-1} pour les terminaisons de surface contenant oxygène et fluor. L'uniformité spatiale des signaux PiFM à travers les mon-feuillets indique une chimie de surface homogène, cohérente avec les conditions de gravure uniformes utilisées pendant la synthèse.

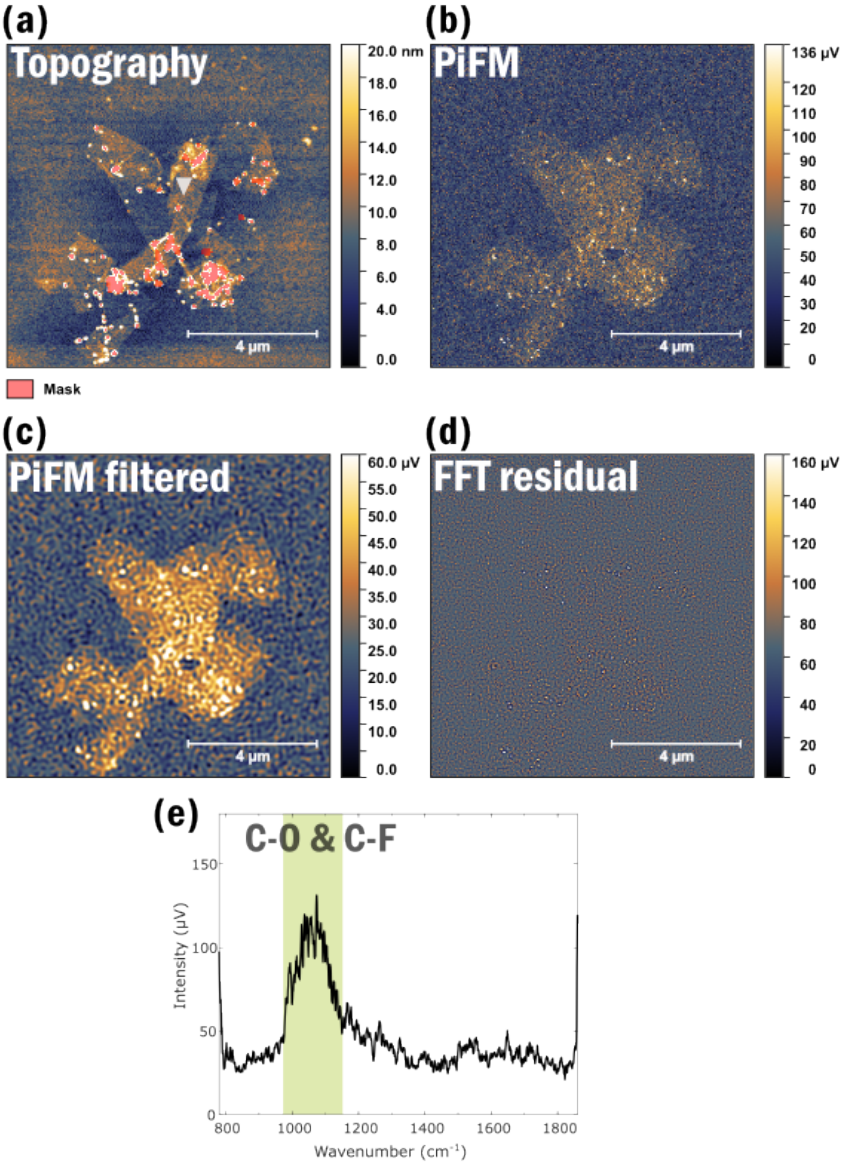

Figure 4.1 feuillet unique de $Ti_3C_2T_x$ pristine sondé par PiFM montrant les liaisons liées aux terminaisons de surface. (a) topographie du MXene. (b) image spectrale PiFM brute à 1067 cm^{-1}. (c) image PiFM filtrée 2D FFT à 1067 cm^{-1}. (d) image résiduelle après filtrage. (e) spectre PiFM moyenné acquis au point blanc montré sur la topographie.

4.2 Analyse de l'oxydation et des défauts carbonés sur le Nb_2CT_x

Le MXene carbure de niobium (Nb_2CT_x) présente une tendance à s'oxyder dans des conditions ambiantes [36, 37]. L'objectif de cette étude est de caractériser la distribution des espèces d'oxyde de niobium dérivées de Nb_2CT_x par une approche spectroscopique multi-échelle.

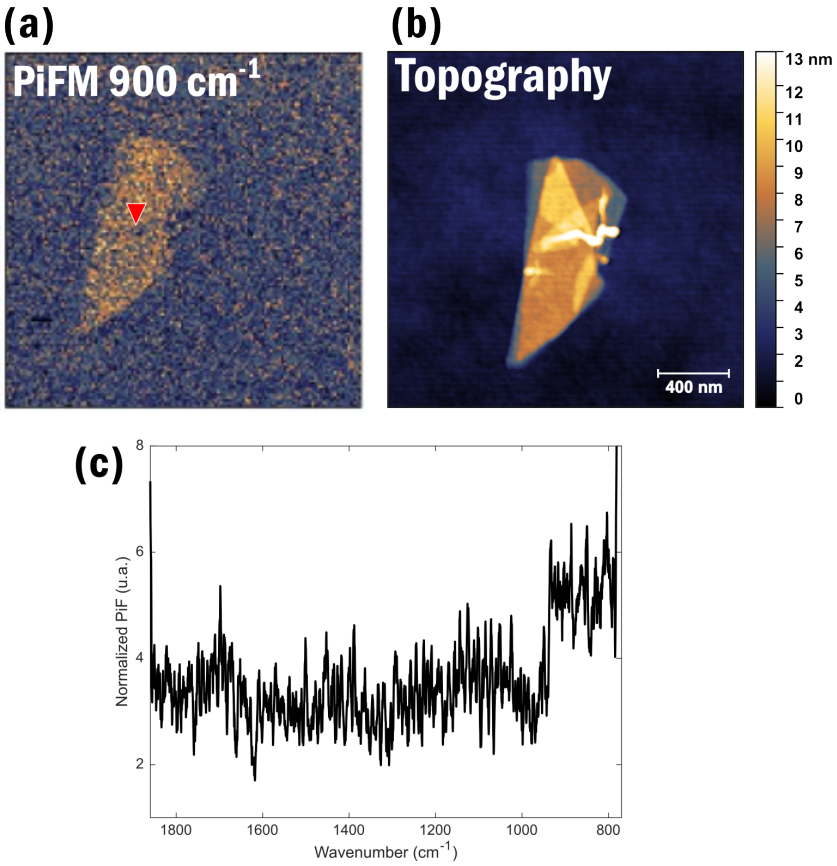

Figure 4.2 Caractérisation PiFM de Nb_2CT_x : (a) image spectrale acquise à 900 cm^{-1}, (b) topographie correspondante, montrant une épaisseur d'environ 6 nm, indiquant un empilement de 2 à 3 feuillets uniques. (c) spectre PiFM acquis au point triangle rouge montré sur la topographie.

L'analyse PiFM du Nb_2CT_x (Figure 4.2) révèle des pics à 1640 cm^{-1} et 1490 cm^{-1} attribués respectivement aux liaisons C=C et à la contamination organique ou à la dégradation des feuillets. Une bande d'absorption substantielle en dessous de 1000 cm^{-1} est liée à l'oxydation du MXene.

4.3 Cartographie des contaminants à base de siloxane sur les MXenes

Les composés siloxanes sont des contaminants ubiquitaires caractérisés par des liaisons répétitives silicium-oxygène (Si–O–Si) et sont présents dans les produits industriels et de consommation. Les MXenes, présentant des terminaisons de surface

hautement réactives (groupes –OH), sont particulièrement susceptibles aux interactions avec les groupes Si–OH présents dans les espèces siloxanes.

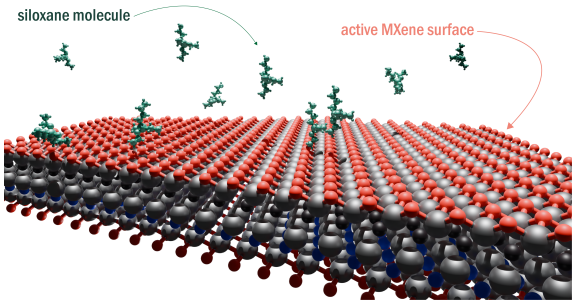

Figure 4.3 Illustration schématique d'un MXene monocouche avec sa surface active et des composés siloxanes. La structure MXene montre l'arrangement en couches caractéristique avec les terminaisons de surface (sphères rouges représentant les atomes d'oxygène), tandis que les molécules de siloxane (structures vertes) sont représentées interagissant avec les sites de surface actifs du MXene.

Propriétés infrarouges en champ lointain

Les techniques de spectroscopie vibrationnelle, incluant la spectroscopie Raman et FTIR, ont été employées pour caractériser l'échantillon $Ti_3C_{1.5}N_{0.5}T_x$ fabriqué et exposé à un environnement contenant des siloxanes.

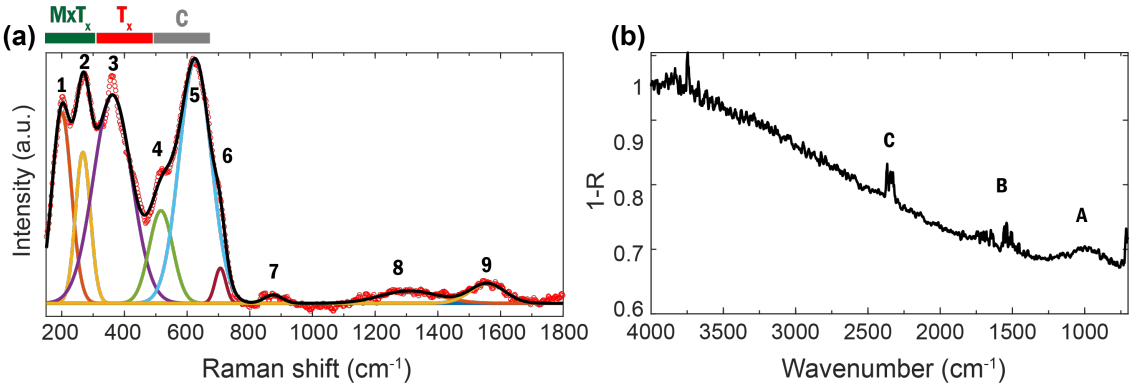

Figure 4.4 Spectroscopie vibrationnelle des feuillets MXene $Ti_3C_{1.5}N_{0.5}T_x$ vieillis montrant les groupes de terminaison de surface et les caractéristiques structurales. (a) Spectre Raman expérimental des feuillets $Ti_3C_{1.5}N_{0.5}T_x$ vieillis (100 nm d'épaisseur) déposés sur substrat Al_2O_3. (b) Spectre infrarouge à transformée de Fourier (FTIR) mesuré en mode réflectance du même échantillon normalisé par rapport au fond Al_2O_3, présenté comme (1 – Réflectance) versus nombre d'onde.

L'analyse Raman (Figure 4.4(a)) montre des pics caractéristiques : pic à 200 cm^{-1} attribué à la vibration symétrique A_{1g}Ti–C, pic à 350 cm^{-1} correspondant à la vibration E_g(O), et pic à 520 cm^{-1} correspondant à la vibration A_{1g}(OH) des groupes -OH. La spectroscopie FTIR (Figure 4.4(b)) identifie trois caractéristiques d'absorption distinctes à 1000, 1535 et 2345 cm^{-1}. Cependant, aucune des deux techniques ne montrent la présence d'adsorption de composés siloxanes sur les feuillets de MXene.

Pour compléter notre analyse, nous utilisons la nanoscopie IR.

Propriétés infrarouges locales

La microscopie infrarouge en champ proche, spécifiquement la microscopie à force photo-induite (PiFM), a été employée pour étudier la présence de composé siloxanes sur la surface des feuillets MXene mono- et quelques-couches.

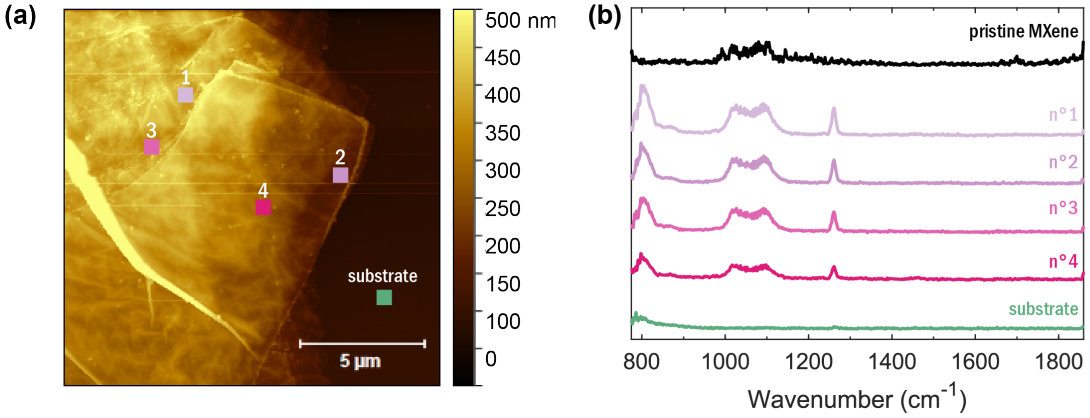

Figure 4.5 Analyse par microscopie à force photo-induite (PiFM) révélant la contamination par siloxane sur les surfaces MXene $Ti_3C_{1.5}N_{0.5}T_x$ vieillies. (a) Topographie AFM des feuillets $Ti_3C_{1.5}N_{0.5}T_x$ vieillis montrant les emplacements de mesure. (b) Spectres PiFM comparatifs acquis par pas de 1 cm^{-1} avec 30 s de temps d'acquisition par point. Le spectre $Ti_3C_{1.5}N_{0.5}T_x$ pristine (courbe noire) présente une bande caractéristique de 1000–1100 cm^{-1} attribuée aux terminaisons de surface MXene natives (liaisons C–O et C–F). Les spectres $Ti_3C_{1.5}N_{0.5}T_x$ vieillis montrent des signatures spectrales cohérentes avec quatre pics distincts liés au siloxane.

le $Ti_3C_{1.5}N_{0.5}T_x$ pristine a été étudié pour référence, le spectre PiFM (Figure 4.5) présente une bande caractéristique de 1000 à 1100 cm^{-1}, associée aux liaisons C–O et C–F. Les résultats sont similaires à ceux du $Ti_3C_2T_x$ pristine, présentés dans la Figure 4.1.

Les feuillets $Ti_3C_{1.5}N_{0.5}T_x$ vieillis présentent une signature spectrale nettement différente, avec quatre pics distincts distribués uniformément à travers la surface du feuillet. Les pics à 820 cm^{-1} et 1260 cm^{-1} sont attribués aux vibrations d'étirement Si–C, tandis que ceux à 1020 cm^{-1} et 1100 cm^{-1} correspondent aux vibrations d'étirement Si–O–Si.

La comparaison avec le spectre FTIR de référence du dimethoxydimethylsilane oligomère (Figure 4.6, courbe noire) confirme l'identification du siloxane, montrant une excellente correspondance entre les spectres de référence et expérimentaux.

Cartographie spectrale

Les images spectrales PiFM acquises à quatre nombres d'onde distincts (Figure 4.7) fournissent des informations sur la distribution spatiale des liaisons chimiques spécifiques à travers les feuillets $Ti_3C_{1.5}N_{0.5}T_x$ vieillis. Ces cartes spectrales révèlent la présence de liaisons chimiques liées au siloxane distribuées uniformément à travers la surface MXene. Tous les signaux liés au siloxane sont uniformément distribués à travers la surface du feuillet MXene, confirmant une contamination homogène.

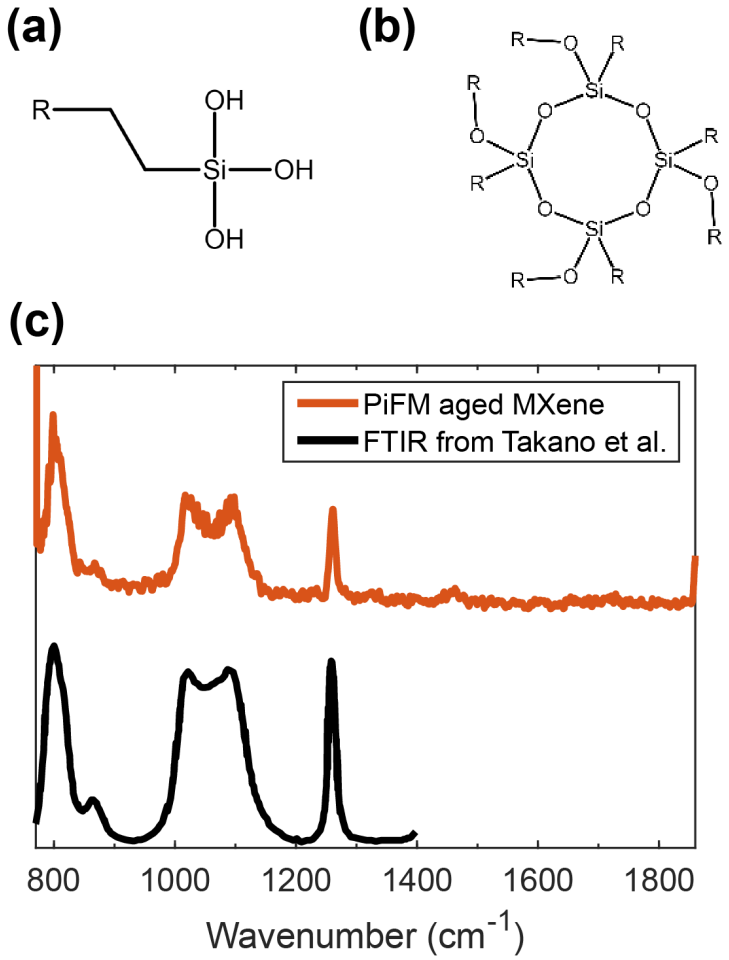

Figure 4.6 Identification des groupes fonctionnels siloxane et validation structurale montrant (a) configuration Si–O–Si linéaire et (b) arrangement Si–O–Si cyclique. (c) Spectroscopie infrarouge comparative validant l'identification du siloxane. Le spectre FTIR de référence de l'oligomère diméthoxydimethylsilane (ligne noire) présente quatre pics d'absorption caractéristiques à 800, 1020, 1090, et 1260 cm^{-1} correspondant aux différentes vibrations siloxanes. Le spectre PiFM du MXene $Ti_3C_{1.5}N_{0.5}T_x$ vieilli (ligne orange) montre des positions et motifs de pics remarquablement similaires, confirmant la présence de composés siloxanes sur la surface MXene.

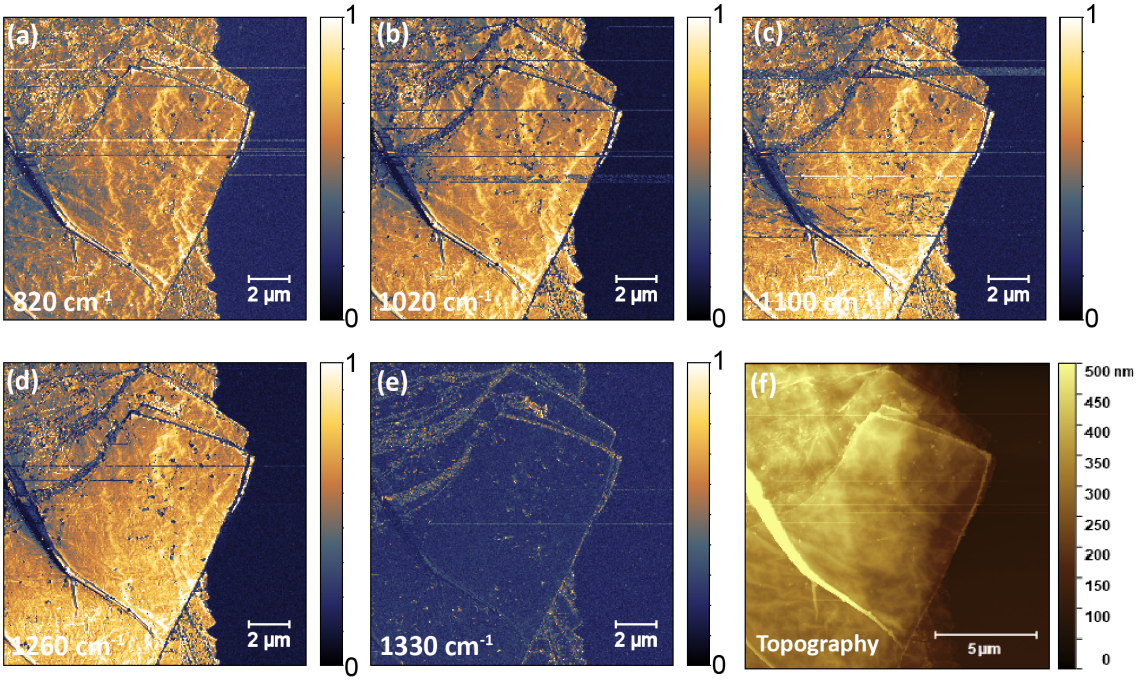

Figure 4.7 Cartographie de la distribution spatiale de la contamination par siloxane sur les feuillets MXene $Ti_3C_{1.5}N_{0.5}T_x$ vieillis utilisant l'imagerie spectrale PiFM. (a) 820 cm^{-1} (étirement Si–C), (b) 1020 cm^{-1} (étirement Si–O–Si), (c) 1100 cm^{-1} (étirement Si–O–Si), et (d) 1260 cm^{-1} (étirement Si–C). (e) Mesure de contrôle à 1330 cm^{-1} montrant un signal négligeable. (f) Topographie AFM acquise simultanément montrant la morphologie du feuillet.

Conclusion

Nous avons démontré que le PiFM est capable de détecter et cartographier les groupes fonctionnels de surface sur les $Ti_3C_2T_x$ et $Ti_3C_{1.5}N_{0.5}T_x$ pristines. De plus, les composés siloxanes adsorbés sont détectés sur les surfaces MXene vieillies correspondantes avec une précision nanométrique. Les modes vibrationnels Si–C et Si-O-Si détectés confirment la présence d'espèces siloxanes uniformément distribuées à travers les feuillets MXene, soulignant leur haute réactivité due aux terminaisons de surface –OH.

En contraste, les techniques de caractérisation conventionnelles telles que la spectroscopie Raman et la spectroscopie FTIR n'ont révélé aucune évidence de contamination par siloxane sur le même échantillon. Ceci souligne la sensibilité supérieure et la résolution spatiale du PiFM, le rendant uniquement capable de détecter des contaminants nanométriques autrement invisibles aux méthodes de caractérisation en volume ou de surface traditionnelles.

Chapitre 5

Application du MXene à la détection par résonance plasmonique de surface

La résonance plasmonique de surface (SPR) est devenue une technique de détection optique puissante avec une sensibilité remarquable pour détecter les changements aux interfaces métal-diélectrique [38]. Depuis sa première démonstration pour les applications de biodétection au début des années 1980 [39], la SPR a révolutionné la détection sans marquage et en temps réel dans des domaines allant de la biochimie et de la recherche pharmaceutique à la surveillance environnementale et à la sécurité alimentaire [40].

Approche fondamentale du plasmon de surface

Les plasmons de surface sont des oscillations collectives de la densité de gaz d'électrons libres à l'interface métal-diélectrique, qui se propagent comme des ondes de surface le long de cette frontière. Ces polaritons plasmoniques de surface (SPP) représentent des excitations couplées d'ondes électromagnétiques et d'oscillations de densité électronique, caractérisées par un vecteur d'onde k_{sp} donné par :

$$k_{sp} = \frac{\omega}{c}\sqrt{\frac{\varepsilon_m \varepsilon_d}{\varepsilon_m + \varepsilon_d}} \tag{5.1}$$

où ω est la fréquence angulaire, c est la vitesse de la lumière, et ε_m et ε_d sont les constantes diélectriques du métal et du milieu diélectrique, respectivement.

Les plasmons de surface ne peuvent pas être excités par excitation directe en raison du désaccord de moment entre les photons et les plasmons de surface. La configuration de Kretschmann [41] surmonte cette limitation en utilisant un prisme d'indice de réfraction élevé pour augmenter le moment des photons incidents, permettant l'excitation SPP lorsque la composante dans le plan du vecteur d'onde du photon correspond au vecteur d'onde SPP à l'interface métal-diélectrique.

Matériaux 2D pour la SPR améliorée

Afin d'améliorer les performances SPR, les développements récents en science des matériaux se sont concentrés sur la combinaison de matériaux bidimensionnels (2D) avec des couches d'or. Des gains remarquables en sensibilité, limites de détection et

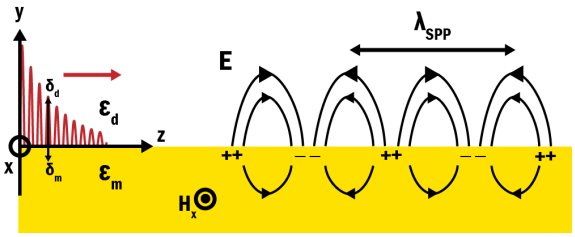

Figure 5.1 Illustration de la propagation d'onde plasmonique de surface à une interface métal-diélectrique. Gauche : Décroissance exponentielle du champ électromagnétique dans le milieu diélectrique (δ_d) et le métal (δ_m), avec les constantes diélectriques respectives ε_d et ε_m. Droite : Distribution des composantes du champ électromagnétique montrant les boucles de champ électrique (E) et le champ magnétique (H_x) perpendiculaire à la direction de propagation. La longueur d'onde du polariton plasmonique de surface (λ_{SPP}) est indiquée au-dessus.

sélectivité ont été démontrés lorsque des matériaux 2D atomiquement minces sont intégrés avec des structures plasmoniques.

Les MXenes sont l'un des nouveaux matériaux 2D qui a généré beaucoup d'intérêt pour les applications SPR. Les MXenes combinent plusieurs propriétés telles qu'une conductivité métallique élevée, l'hydrophilie et la fonctionnalité de surface qui les distinguent des autres matériaux 2D. La chimie de surface accordable des MXenes présente deux avantages pour les applications SPR : premièrement, leur conductivité électrique élevée facilite le couplage avec le substrat d'or, ce qui améliore également la résonance plasmonique et la sensibilité de détection. Deuxièmement, leurs terminaisons de surface polyvalentes facilitent la fonctionnalisation sélective pour cibler des analytes spécifiques.

5.1 Dépôt de film mince MXene surveillé par SPR

La fabrication de films MXene, que ce soit sur des substrats ou comme membranes libres, est un processus crucial pour la préparation de matériaux à base de MXene pour diverses applications. Cependant, produire des films MXene homogènes, ultra-minces et uniformes reste difficile en raison des caractéristiques morphologiques intrinsèques des flocons MXene et de leur comportement colloïdal complexe en solution.

Dans cette section, nous travaillons sur une nouvelle approche de fabrication de film mince MXene sur un substrat d'or utilisant un système microfluidique couplé avec la résonance plasmonique de surface (SPR). Cette méthode hybride offre une surveillance en temps réel de la formation du film 2D, qui est une étape critique pour la fabrication de puces de capteur SPR.

Le dépôt utilisant le système microfluidique permet de contrôler de nombreux paramètres tels que le débit, la concentration de la solution colloïdale et la SPR sonde la formation du film en temps réel. En manipulant ces paramètres, nous obtenons un dépôt contrôlé de MXene $Ti_3C_2T_x$ sur une puce de détection SPR revêtue d'or.

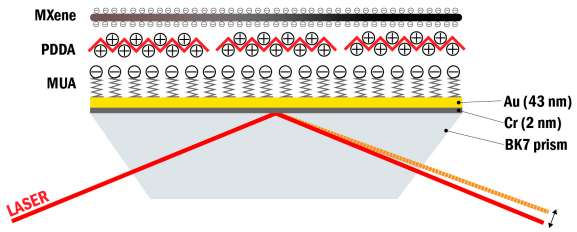

Figure 5.2 Illustration schématique du système multicouche employé pour la fabrication de film MXene. La fonctionnalisation de surface initiale avec l'acide 11-mercaptoundécanoïque (MUA) sur la surface d'or (43 nm) avec couche d'adhésion chrome est réalisée par méthode de trempage. Les couches de polymère PDDA chargé positivement et de MXene sont formées par microfluidique.

Analyse de la réponse SPR pendant la formation du film MXene

L'optimisation du dépôt de film MXene via sédimentation contrôlée a montré que les expériences initiales ont souligné l'importance d'un contrôle précis de l'épaisseur pour la formation de film MXene pour des performances SPR optimales. Le flux microfluidique a été arrêté après remplissage du canal avec la solution colloïdale MXene (environ 3 min), permettant à la sédimentation naturelle de procéder dans des conditions statiques.

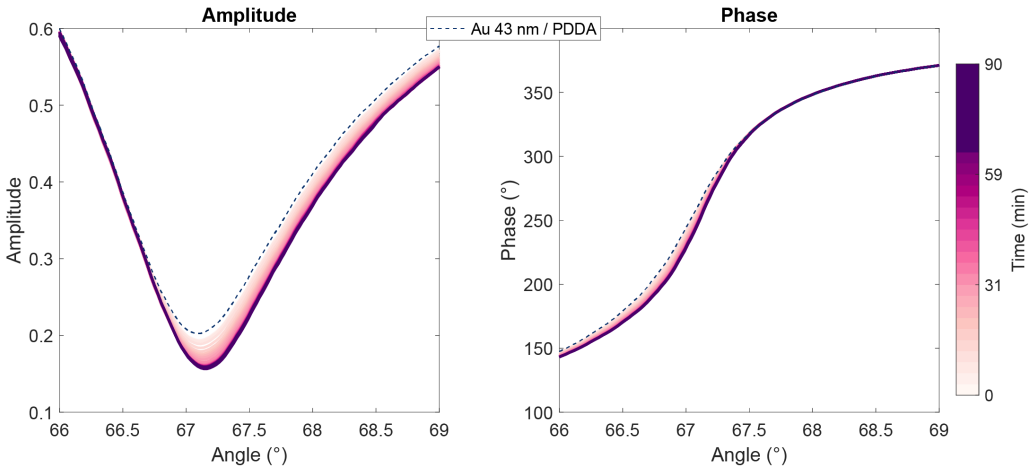

Figure 5.3 Balayages angulaires SPR montrant les réponses d'amplitude (gauche) et de phase (droite) pendant le dépôt de film MXene optimisé via sédimentation contrôlée. Les courbes bleues en pointillés représentent l'état de référence (Au 43 nm avec monocouche PDDA), tandis que les courbes codées par couleur illustrent l'évolution temporelle de la formation du film MXene sur environ 90 minutes. Le balayage d'amplitude révèle un approfondissement progressif du minimum de résonance de 0,20 à 0,16 et un léger décalage vers des angles plus élevés, indiquant une croissance contrôlée dans le régime d'épaisseur optimal. La réponse de phase montre un raidissement graduel de la pente de transition tout en maintenant la même orientation que l'état de référence, confirmant que le processus de dépôt préserve avec succès le régime d'amélioration sans dépasser le seuil d'épaisseur critique qui déclencherait une dégradation de résonance.

Les réponses de phase et d'amplitude de cette technique de dépôt optimisée sont présentées dans la Figure 5.3. Contrairement à nos observations précédentes,

les mesures de phase et d'amplitude indiquent une amélioration continue des performances SPR pendant la période d'observation de 90 minutes. La réponse d'amplitude (panneau gauche) montre un approfondissement graduel du creux de résonance de 0,20 à 0,16, avec un léger décalage de l'angle de résonance. La réponse de phase (panneau droit) montre un raidissement graduel de la pente de transition sans inversion d'orientation, indiquant que l'épaisseur du film est toujours dans la fenêtre d'amélioration optimale.

Ces résultats confirment que la sédimentation contrôlée permet une meilleure régulation des propriétés du film MXene que le dépôt par flux continu. En excluant les forces de cisaillement du flux continu, l'approche de sédimentation permet aux feuillets MXene de s'assembler plus lentement sur la surface au lieu de rapidement comme dans nos premières expériences.

5.2 Détection de (3-Aminopropyl)triethoxysilane utilisant le MXene

En raison de leur chimie de surface unique, les matériaux MXenes sont des matériaux prometteurs pour les applications de détection chimique et biochimique. Les groupes fonctionnels abondants et en particulier les terminaisons hydroxyle (–OH) sur les surfaces MXene constituent des sites réactifs pour les interactions moléculaires sélectives.

Dans cette section, nous exploitons cette réactivité de surface distinctive pour développer une approche de détection nouvelle pour les molécules contenant du siloxane, spécifiquement le (3-Aminopropyl)triethoxysilane (APTES). Basé sur cela, nous avons conçu un système de détection SPR qui exploite l'interface hybride or-MXene pour surveiller la cinétique de liaison siloxane en temps réel.

La réponse optique SPR en fonction de la concentration d'APTES est montrée par des balayages angulaires systématiques montrant les variation d'amplitude et de phase sur la gamme de concentration de 10^{-9}M à 10^{-5}M (Figure 5.4). Les mesures d'amplitude révèlent des courbes de résonance SPR typiques avec des minima autour de 70,7° après l'adsorption complète d'APTES. Un décalage net vers la droite de l'angle de résonance avec l'augmentation de la concentration APTES est observé, indiquant une augmentation de l'indice de réfraction effectif à l'interface de détection.

L'expérience de liaison en temps réel sur 160 minutes utilise la détection SPR différentielle, où le canal fonctionnalisé MXene est référencé contre un canal de contrôle or nu. Le protocole implique l'injection séquentielle de concentrations croissantes d'APTES (10^{-9} à 10^{-5} M) avec des cycles de lavage tampon.

L'interprétation des données distingue les contributions moléculaires en solution et liées à la surface. Pendant l'injection, l'augmentation de ΔmRIU reflète à la fois les changements d'indice de réfraction en volume et la liaison de surface. Cependant, le véritable greffage moléculaire ne peut être évalué qu'après rinçage, lorsque les molécules non liées sont éliminées.

Les premières expositions (10^{-9} et 10^{-8} M) montrent une cinétique de liaison rapide avec des signaux atteignant 0,17 et 0,23 mRIU respectivement. Le lavage tampon maintient le signal élevé, confirmant la liaison covalente irréversible des groupes silanol d'APTES aux terminaisons hydroxyle du MXene via la chimie de

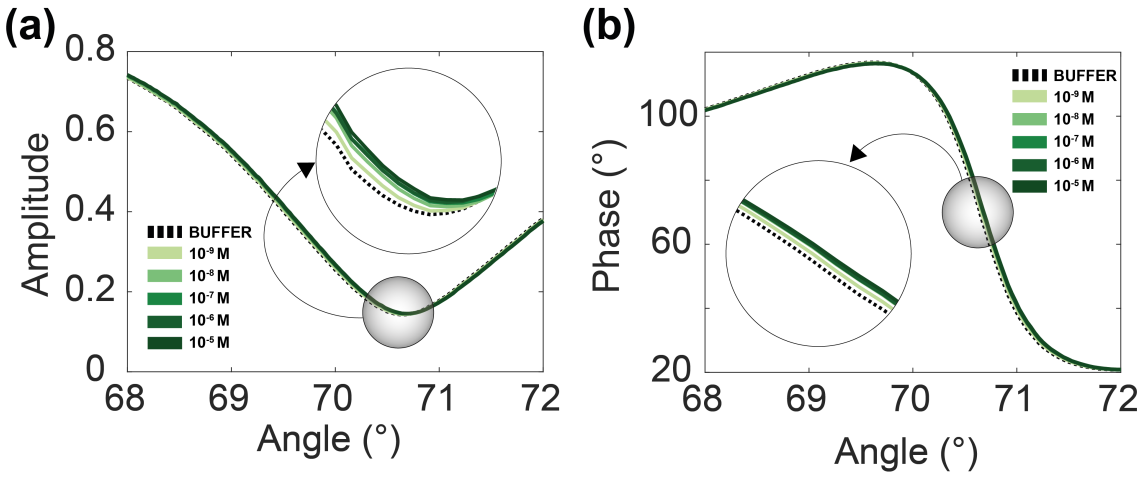

Figure 5.4 Balayages angulaires d'amplitude (a) et de phase (b) démontrant la fonctionnalisation de surface APTES sur MXene à différentes concentrations après rinçage.

condensation Ti–O–Si. Pour les concentrations supérieures, aucune variation n'est observée.

Le canal de référence (Au/MUA/PDDA) ne montre aucune liaison d'APTES en raison de la répulsion électrostatique entre les charges positives. Cette approche différentielle élimine les contributions d'indice de réfraction en volume et valide la sélectivité de la surface MXene pour la détection de molécules contenant des siloxanes.

Conclusion

Cette section a démontré l'utilisation de la technique SPR microfluidique couplée au MXene $Ti_3C_2T_x$ pour fabriquer un film mince hautement homogène de 10 nm d'épaisseur sur substrat d'or. Cette approche a permis d'améliorer la résonance du système SPR, atteignant des conditions de couplage optimales avec des valeurs d'amplitude minimales. La constante diélectrique du matériau a été déterminée analytiquement.

L'étude du comportement d'adsorption de l'(3-Aminopropyl)triéthoxysilane (APTES) sur les surfaces MXene $Ti_3C_2T_x$ révèle une liaison chimique se produisant en quelques minutes, corroborant les résultats du Chapitre 4. La détection basée sur SPR démontre une sensibilité jusqu'aux concentrations nanomolaires d'APTES, validant l'efficacité de cette approche pour la caractérisation des interactions moléculaires avec les surfaces MXene.

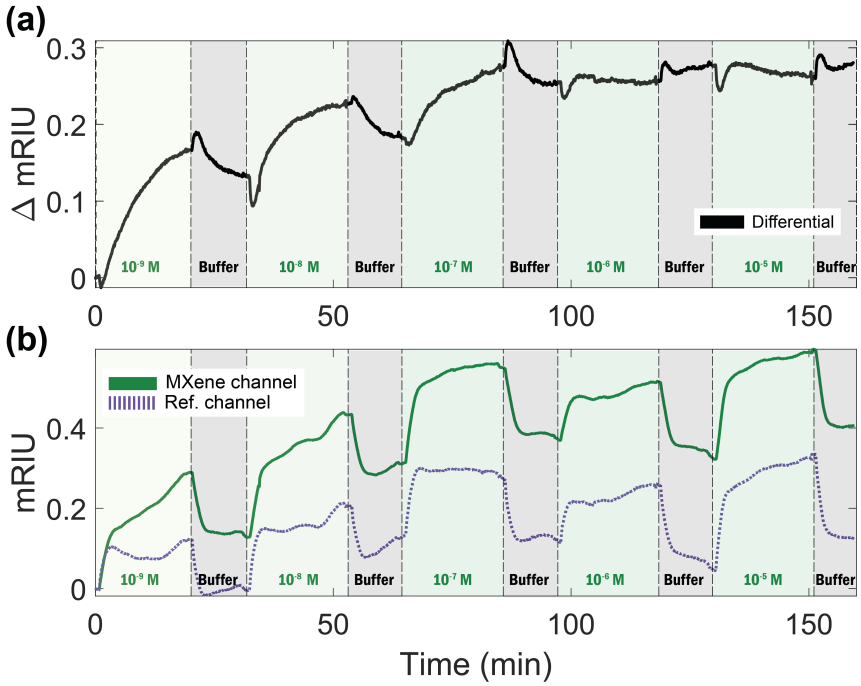

Figure 5.5 Sensogramme du dépôt d'APTES sur la couche $Ti_3C_2T_x$ exprimé en unité d'indice de réfraction au fil du temps. Les zones vertes correspondent à l'association des molécules d'APTES, tandis que les zones grises correspondent à la dissociation effectuée par l'écoulement de la solution tampon. (a) Le signal différentiel (Ch1(MXene) - Ch2(Référence) et (b) le signal de chaque canal (Ch1 : canal MXene en vert pointillé et Ch2 : canal de référence en ligne noire continue).

Conclusion générale

Cette thèse fournit une compréhension des propriétés optiques infrarouges des MXenes à travers une approche multi-échelle, allant de la caractérisation optique aux applications technologiques émergentes. Les résultats présentés dans les trois chapitres de résultats apportent de nouvelles connaissances sur les propriétés optiques des MXenes et démontrent leur potentiel pour des applications technologiques dans de multiples domaines.

Chapitre 1 vise à établir le contexte pour comprendre les MXenes dans le paysage plus large de la science des matériaux 2D. La présentation systématique des matériaux 2D établis—graphène, TMDs, phosphore noir et hBN—révèle une riche diversité de propriétés. Les MXenes représentent un changement de paradigme dans ce paysage, introduisant des matériaux qui combinent de manière unique une conductivité métallique avec une chimie de surface ajustable—des caractéristiques largement absentes dans les matériaux 2D conventionnels. Cela positionne les MXenes comme complémentaires plutôt qu'alternatifs aux systèmes 2D existants, ouvrant des applications nécessitant à la fois une conductivité élevée et une réactivité chimique.

L'analyse des méthodes de synthèse soulève une question importante concernant la relation entre les conditions de gravure chimique et les propriétés des matériaux. Contrairement à l'exfoliation mécanique pour les matériaux de van der Waals, la gravure sélective pour la synthèse de MXenes permet l'ingénierie des terminaisons dans d'autres systèmes 2D. Cette base met en évidence des lacunes de connaissance, notamment la faible compréhension des relations structure-propriétés dans la région infrarouge et le besoin de techniques de caractérisation à l'échelle nanométrique. Ces lacunes justifient l'investigation systématique multi-échelle des propriétés optiques des MXenes qui constitue le cœur de cette thèse, dans laquelle des approches de caractérisation avancées révéleront les relations entre composition, chimie de surface et réponse optique.

Chapitre 2 décrit les fondements théoriques et expérimentaux pour la caractérisation optique multi-échelle en reliant les interactions fondamentales lumière-matière avec les techniques avancées de microscopie en champ proche. Le traitement complet des principes de la spectroscopie infrarouge, allant des vibrations moléculaires aux phonons cristallins, a posé les bases conceptuelles pour les phénomènes optiques dans les matériaux 2D. Les principes de la microscopie à force atomique, de la microscopie optique en champ proche à diffusion (s-SNOM) et de la microscopie à force photo-induite (PiFM) ont été décrits et ont ainsi formé la boîte à outils méthodologique pour l'investigation optique à l'échelle nanométrique. Le caractère complémentaire du s-SNOM et du PiFM sur des systèmes semi-conducteurs de référence a été décrit dans le chapitre 2.

Chapitre 3 a démontré que le rapport carbone/azote dans les MXenes

$Ti_3C_{(2-y)}N_yT_x$ constitue un paramètre de contrôle puissant pour moduler leurs propriétés optiques infrarouges. Cette investigation a révélé une bonne corrélation entre la composition et les performances IR, ce qui suggère une direction prometteuse pour l'ingénierie des propriétés optiques. Les compositions riches en carbone ($Ti_3C_2T_x$) présentent une émissivité extrêmement faible (0,06) et sont donc adaptées aux applications de blindage IR et de revêtements réfléchissants. À l'inverse, l'incorporation progressive d'azote augmente l'émissivité jusqu'à 0,65 pour Ti_3CNT_x, permettant des applications de gestion thermique et de détection IR.

Ces résultats fournissent des fondements théoriques et expérimentaux pour des matériaux MXenes avec une réponse optique ajustable. La variation systématique des paramètres de maille avec l'augmentation de la teneur en azote, confirmée par l'analyse par diffraction des rayons X, fournit des informations structurales liées aux changements de propriétés optiques. Le comportement de l'émissivité en fonction de la température, en particulier l'augmentation quasi-linéaire dans les compositions contenant une teneur modérée en azote, est en bon accord avec notre modèle de Hagen-Rubens étendu incluant les interactions électron-phonon et les changements de conductivité électrique. Cette base de connaissances permet la conception prédictive de compositions de MXenes ciblant des propriétés infrarouges spécifiques.

De plus, la deuxième section du chapitre démontre l'application de la spectroscopie infrarouge pour des études in-situ de cellules électrochimiques à base de MXenes. Cette approche innovante exploite les propriétés optiques infrarouges caractérisées tout au long de cette thèse pour surveiller les processus électrochimiques en temps réel. La capacité à sonder les changements structuraux et chimiques se produisant au niveau des électrodes de MXenes pendant le cyclage électrochimique représente une avancée significative dans la compréhension des mécanismes régissant les performances des MXenes dans les applications de stockage d'énergie.

Chapitre 4 représente une avancée dans la caractérisation des MXenes car la microscopie à force photo-induite (PiFM) s'est révélée très sensible à la chimie de surface à l'échelle nanométrique. Ainsi, les groupes fonctionnels de surface ont été détectés et cartographiés sur des MXenes vierges et des contaminants siloxanes ont été identifiés sur les surfaces exposées avec une résolution spatiale nanométrique. Notamment, la PiFM a révélé des phénomènes d'adsorption sélective de composés siloxanes sur les MXenes qui n'ont pas été détectés par les techniques de caractérisation conventionnelles telles que la spectroscopie Raman, la FTIR et l'EDS. Les modes vibrationnels détectés Si–C et Si-O-Si ont confirmé que les espèces siloxanes sont uniformément réparties sur les flocons de MXenes et sont hautement réactives en raison des terminaisons de surface –OH. Cette découverte indique à quel point les méthodes de caractérisation à haute résolution sont essentielles pour comprendre les interactions surface-environnement.

L'investigation s'est étendue aux MXenes Nb_2CT_x, où la PiFM a montré une sensibilité plus élevée dans la détection des signatures d'oxydation même dans des flocons mono/multi-couches avec des épaisseurs aussi faibles que 15 nm. Les pics caractéristiques autour de 950–980 cm^{-1} associés à la formation d'oxyde de niobium ont été clairement identifiés, démontrant la capacité de la technique à sonder les transformations chimiques à l'échelle nanométrique. Ces résultats montrent que la PiFM est un outil puissant pour investiguer la chimie de surface des matériaux 2D et ouvrent de nouvelles perspectives pour une fonctionnalisation contrôlée et ciblée des surfaces de MXenes.

Chapitre 5 a démontré la transition des propriétés optiques vers les applications pratiques en développant des plateformes de détection basées sur la résonance plasmonique de surface (SPR) couplée aux MXenes. Des films minces de MXenes hautement homogènes (épaisseur de 10 nm) ont été préparés sur des substrats d'or pour la détermination analytique de la constante diélectrique ainsi que pour l'investigation du comportement d'adsorption de l'APTES.

Cette approche a montré une sensibilité de détection remarquable jusqu'à des concentrations nanomolaires, confirmant l'aptitude des MXenes pour des applications avancées de détection moléculaire. Les résultats confirment et étendent les connaissances de base sur les interactions siloxane-MXene dérivées du modèle PiFM, alignant la compréhension avec les applications pratiques. Leurs capacités de surveillance en temps réel et leur cinétique de liaison chimique rapide (en quelques minutes) démontrent l'application concrète des capteurs à base de MXenes.

Le couplage de la technique microfluidique-SPR avec les MXenes $Ti_3C_2T_x$ représente une avancée significative dans le développement de plateformes de capteurs, offrant à la fois une sensibilité et une sélectivité élevées pour la détection d'organosilanes. La détermination analytique des propriétés diélectriques par cette approche contribue à des données précieuses pour la modélisation optique et la conception de dispositifs à base de MXenes. Comme perspective future, il serait particulièrement intéressant d'effectuer la détection de l'APTES en utilisant la SPR dans l'air plutôt qu'en solution aqueuse. De telles mesures reproduiraient plus fidèlement les conditions employées dans le chapitre 4 avec la caractérisation PiFM, permettant une comparaison directe entre les deux techniques et fournissant des informations complémentaires sur les interactions silane-MXene en phase gazeuse par rapport à la phase liquide.

Cette recherche ouvre des axes de développement prometteurs qui méritent une investigation plus approfondie. Par exemple, l'extension de l'approche d'ingénierie compositionnelle à d'autres systèmes de MXenes (notamment les carbures et nitrures de vanadium, niobium et molybdène) pourrait révéler des propriétés optiques encore plus diverses. L'investigation systématique de l'influence des groupes terminaux sur les propriétés optiques constitue une direction de recherche prometteuse, où la PiFM émerge comme un outil puissant pour sonder et caractériser les modifications de surface des MXenes à l'échelle nanométrique. Cette capacité à surveiller directement les changements de chimie de surface pourrait fournir des informations cruciales sur les relations structure-propriétés régissant le comportement optique des MXenes. L'intégration des MXenes dans des systèmes de détection multiplexés, exploitant leur réactivité sélective et leur compatibilité avec les technologies de microfabrication, constitue une voie prometteuse pour développer des plateformes de détection avancées. La possibilité de fonctionnalisation contrôlée des surfaces de MXenes, démontrée dans cette thèse, ouvre des perspectives pour des capteurs spécifiques et sélectifs capables de distinguer entre des espèces moléculaires étroitement apparentées. Les techniques et approches développées dans cette thèse sont transférables à d'autres systèmes de matériaux 2D, augmentant leur impact scientifique et technologique. L'intégration d'approches de caractérisation multi-échelles, allant des mesures optiques macroscopiques à la cartographie de la chimie de surface à l'échelle nanométrique, pourrait fournir de nouvelles connaissances.

Bibliographie

[1] K. S. Novoselov, A. K. Geim, S. V. Morozov, D. Jiang, Y. Zhang, S. V. Dubonos, I. V. Grigorieva, and A. A. Firsov, "Electric Field Effect in Atomically Thin Carbon Films," *Science*, vol. 306, pp. 666–669, Oct. 2004.

[2] G. Cassabois, "Hexagonal boron nitride is an indirect bandgap semiconductor," *NATURE PHOTONICS*, 2016.

[3] K. F. Mak, C. Lee, J. Hone, J. Shan, and T. F. Heinz, "Atomically Thin MoS2 : A New Direct-Gap Semiconductor," *PHYSICAL REVIEW LETTERS*, 2010.

[4] L. Li, "Black phosphorus field-effect transistors," *NATURE NANOTECHNOLOGY*, 2014.

[5] A. Gupta, "Recent development in 2D materials beyond graphene," *Progress in Materials Science*, 2015.

[6] G. R. Bhimanapati, Z. Lin, V. Meunier, Y. Jung, J. Cha, S. Das, D. Xiao, Y. Son, M. S. Strano, V. R. Cooper, L. Liang, S. G. Louie, E. Ringe, W. Zhou, S. S. Kim, R. R. Naik, B. G. Sumpter, H. Terrones, F. Xia, Y. Wang, J. Zhu, D. Akinwande, N. Alem, J. A. Schuller, R. E. Schaak, M. Terrones, and J. A. Robinson, "Recent Advances in Two-Dimensional Materials beyond Graphene," vol. 9, no. 12, 2015.

[7] N. Mounet, "Two-dimensional materials from high-throughput computational exfoliation of experimentally known compounds," *Nature Nanotechnology*, 2018.

[8] S. Haastrup, M. Strange, M. Pandey, T. Deilmann, P. S. Schmidt, N. F. Hinsche, M. N. Gjerding, D. Torelli, P. M. Larsen, A. C. Riis-Jensen, J. Gath, K. W. Jacobsen, J. Jørgen Mortensen, T. Olsen, and K. S. Thygesen, "The computational 2d materials database : high-throughput modeling and discovery of atomically thin crystals," *2D Materials*, vol. 5, p. 042002, sep 2018.

[9] A. Molle, "Buckled two-dimensional Xene sheets," *NATURE MATERIALS*.

[10] F. Zhang and L. Qi, "Recent progress in self-supported metal oxide nanoarray electrodes for advanced lithium-ion batteries," *Advanced Science*, vol. 3, no. 9, p. 1600049, 2016.

[11] P. Ares, J. J. Palacios, G. Abellán, J. Gómez-Herrero, and F. Zamora, "Recent Progress on Antimonene : A New Bidimensional Material," *Adv. Mater.*, 2017.

[12] G. Wang, J. Chang, W. Tang, W. Xie, and Y. S. Ang, "2D materials and heterostructures for photocatalytic water-splitting : a theoretical perspective," *Appl. Phys.*, 2022.

[13] H. Liu, A. T. Neal, Z. Zhu, Z. Luo, and X. Xu, "Phosphorene : An Unexplored 2D Semiconductor with a High Hole Mobility," vol. 8, no. 4, 2014.

[14] B. Anasori, *2D Metal Carbides and Nitrides (MXenes) : Structure, Properties and Applications*. Cham : Springer International Publishing AG, 2019.

[15] A. J. Mannix, "Borophene as a prototype for synthetic 2D materials development," *Nature Nanotechnology*, vol. 13, 2018.

[16] M. Knoll and E. Ruska, "Das Elektronenmikroskop,"

[17] D. W. Pohl and W. Denk, "Optical stethoscopy : Image recording with resolution .1/20," 1984.

[18] A. Dazzi, R. Prazeres, F. Glotin, and J. M. Ortega, "Local infrared microspectroscopy with subwavelength spatial resolution with an atomic force microscope tip used as a photothermal sensor,"

[19] I. Rajapaksa, K. Uenal, and H. K. Wickramasinghe, "Image force microscopy of molecular resonance : A microscope principle," *Appl. Phys. Lett.*, 2014.

[20] J. Jahng, *Photo-induced Force Microscopy and Spectroscopy at Space and Time Limits*. PhD thesis, UC Irvine, 2016. Retrieved from https ://escholarship.org/uc/item/6zz957n5.

[21] Z. Dai, L. Liu, and Z. Zhang, "Strain Engineering of 2D Materials : Issues and Opportunities at the Interface," *Adv. Mater.*, 2019.

[22] M. Naguib, M. Kurtoglu, V. Presser, J. Lu, J. Niu, M. Heon, L. Hultman, Y. Gogotsi, and M. W. Barsoum, "TwoDimensional Nanocrystals Produced by Exfoliation of Ti3AlC2," *Adv. Mater.*, vol. 23, pp. 4248–4253, Oct. 2011.

[23] B. Anasori, "The global expansion of MXenes," *D Materials*, 2023.

[24] J. K. El-Demellawi, S. Lopatin, J. Yin, O. F. Mohammed, and H. N. Alshareef, "Tunable Multipolar Surface Plasmons in 2D Ti3C2Tx MXene Flakes," *ACS Nano*, vol. 12, pp. 8485–8493, Aug. 2018.

[25] V. Mauchamp, M. Bugnet, E. P. Bellido, G. A. Botton, P. Moreau, D. Magne, M. Naguib, T. Cabioc'h, and M. W. Barsoum, "Enhanced and tunable surface plasmons in two-dimensional Ti3C2 stacks : Electronic structure versus boundary effects," *PHYSICAL REVIEW B*, 2014.

[26] D. Zhang, D. Shah, A. Boltasseva, and Y. Gogotsi, "MXenes for Photonics," *ACS Photonics*, vol. 9, pp. 1108–1116, Apr. 2022.

[27] F. Xia, H. Wang, D. Xiao, M. Dubey, and A. Ramasubramaniam, "Two-dimensional material nanophotonics," *Nature Photonics*, vol. 8, no. 12, pp. 899–907, 2014.

[28] X. Xiao, H. Wang, P. Urbankowski, and Y. Gogotsi, "Topochemical synthesis of 2D materials," *Chem. Soc. Rev.*, vol. 47, no. 23, pp. 8744–8765, 2018.

[29] B. Anasori, M. R. Lukatskaya, and Y. Gogotsi, "2D metal carbides and nitrides (MXenes) for energy storage," *Nature Reviews Materials*.

[30] M. Han, C. E. Shuck, R. Rakhmanov, D. Parchment, B. Anasori, C. M. Koo, G. Friedman, and Y. Gogotsi, "Beyond $Ti_3 C_2 T_x$: MXenes for Electromagnetic Interference Shielding," *ACS Nano*, vol. 14, pp. 5008–5016, Apr. 2020.

[31] R. Rakhmanov, C. E. Shuck, J. Al Hourani, S. Ippolito, Y. Gogotsi, and G. Friedman, "Ultrathin MXene film interaction with electromagnetic radiation in the microwave range," *Applied Physics Letters*, vol. 123, no. 20, p. 204105, 2023.

[32] A. Sinha, Dhanjai, H. Zhao, Y. Huang, X. Lu, J. Chen, and R. Jain, "MXene : An emerging material for sensing and biosensing," *TrAC Trends in Analytical Chemistry*, vol. 105, pp. 424–435, Aug. 2018.

[33] M. T. Hossain, M. R. Repon, M. A. Shahid, A. Ali, and T. Islam, "Progress, Prospects and Challenges of MXene Integrated Optoelectronics Devices," *ChemElectroChem*, vol. 11, p. e202400008, Apr. 2024.

[34] M. A. Hope, A. C. Forse, K. J. Griffith, M. R. Lukatskaya, M. Ghidiu, Y. Gogotsi, and C. P. Grey, "NMR reveals the surface functionalisation of $Ti_3 C_2$ MXene," *Phys. Chem. Chem. Phys.*, vol. 18, no. 7, pp. 5099–5102, 2016.

[35] T. Parker, Y. Zhang, K. Shevchuk, T. Zhang, V. Khokhar, Y.-H. Kim, G. Kadagishvili, D. Bugallo, M. Tanwar, B. Davis, *et al.*, "In situ raman and fourier transform infrared spectroscopy studies of mxene–electrolyte interfaces," *ACS Nano*, vol. 19, pp. 22228–22239, 2025.

[36] M. Zhao, W. Seddon, T. Bullions, L. Wang, and M. J. Green, "Improving oxidation stability of 2d mxenes : synthesis, storage media, and conditions," *Nano Convergence*, vol. 8, no. 1, pp. 1–26, 2021.

[37] J. Halim, M. R. Lukatskaya, K. M. Cook, J. Lu, C. R. Smith, L.-Å. Näslund, S. J. May, L. Hultman, Y. Gogotsi, P. Eklund, *et al.*, "X-ray photoelectron spectroscopy of select multi-layered transition metal carbides (mxenes)," *Applied Surface Science*, vol. 362, pp. 406–417, 2016.

[38] J. Homola, S. S. Yee, and G. Gauglitz, "Surface plasmon resonance sensors : review," *Sensors and Actuators B : Chemical*, vol. 54, no. 1-2, pp. 3–15, 1999.

[39] B. Liedberg, C. Nylander, and I. Lunström, "Surface plasmon resonance for gas detection and biosensing," *Sensors and Actuators*, vol. 4, pp. 299–304, 1983.

[40] M. A. Cooper, "Optical biosensors in drug discovery," *Nature Reviews Drug Discovery*, vol. 1, no. 7, pp. 515–528, 2002.

[41] E. Kretschmann and H. Raether, "Radiative decay of non-radiative surface plasmons excited by light," *Zeitschrift für Naturforschung A*, vol. 23, no. 12, pp. 2135–2136, 1968.

Synthèse et nanospectroscopie infrarouge de matériaux MXenes, application à la détection de composés siloxanes

Cette thèse étudie les propriétés optiques infrarouges des MXenes par le biais d'une caractérisation à plusieurs échelles, établit des relations structure-propriété fondamentales et présente des applications pratiques. Le chapitre 1 décrit les matériaux bidimensionnels, positionnant les MXenes comme de nouveaux carbures et nitrures de métaux de transition 2D avec une conductivité métallique élevée et une chimie de surface accordable. Le chapitre 2 développe les bases théoriques de la caractérisation optique multi-échelle et introduit des techniques avancées de microscopie en champ proche comme la microscopie optique en champ proche à balayage de type diffusion (s-SNOM) et la microscopie à force photo-induite (PiFM) pour l'investigation à l'échelle nanométrique au-delà des limites de la diffraction. Le chapitre 3 démontre le contrôle systématique des propriétés infrarouges par l'ingénierie de la composition, révélant que le rapport carbone/azote dans les MXenes $Ti_3C_{(2-y)}N_yT_x$ permet une modulation de la réflectance et de l'émissivité. Les compositions riches en carbone présentent des capacités exceptionnelles de blindage IR, tandis que l'incorporation d'azote augmente pour les applications de gestion thermique. De plus, l'étude infrarouge in-situ des intercalations ioniques dans le MXene $Ti_3C_2T_x$ montre des réponses optiques dynamiques pendant les processus électrochimiques, fournissant des informations sur les modifications structurales en temps réel et les mécanismes de transfert de charge. La PiFM est utilisée dans le chapitre 4 pour la caractérisation de la chimie des surfaces à l'échelle nanométrique, mettant en évidence des terminaisons de surface natives et une contamination par le siloxane non détectée par méthode conventionnelle. L'étude est étendue à la détection de l'oxydation du Nb_2CT_x et à la liaison préférentielle du siloxane aux plans basaux composés de terminaison hydroxyle. Dans le Chapitre 5, nous appliquons les MXenes aux plateformes de détection par Résonance Plasmonique de Surface. Le MXene $Ti_3C_2T_x$ améliore le couplage SPR et permet la détection du (3-aminopropyl)triéthoxysilane (APTES).} L'approche de caractérisation optique multi-échelle développée met en lumière les performances et la versatilité de cette famille émergente de matériaux 2D.

MXene - Spectroscopie infrarouge - Matériaux 2D - Nanoscopie - Chimie de surface - Contamination par les siloxanes

Synthesis and infrared nanospectroscopy of MXene materials, application to the detection of siloxane compounds

This thesis investigates the infrared optical properties of MXenes through multiscale characterization, establishes fundamental structure property relationships, and shows practical applications. Chapter 1 describes two-dimensional materials, positioning MXenes as novel 2D transition metal carbides and nitrides with high metallic conductivity and tunable surface chemistry. Chapter 2 develops theoretical foundations for multi-scale optical characterization and introduces advanced near-field microscopy techniques like scattering-type scanning near-field optical microscopy (s-SNOM) and photo-induced force microscopy (PiFM) for nanoscale investigation beyond diffraction limits. Chapter 3 demonstrates systematic control of infrared properties through compositional engineering, revealing that carbon-to-nitrogen ratio in $Ti_3C_{(2-y)}N_yT_x$ MXenes enables precise tuning of reflectance and emissivity. Carbon-rich compositions exhibit exceptional IR shielding capabilities, while nitrogen incorporation increases emissivity for thermal management applications. Additionally, infrared in-situ probing of ion intercalations in $Ti_3C_2T_x$ MXene reveals dynamic optical responses during electrochemical processes, providing insights into real-time structural modifications and charge transfer mechanisms. PiFM is employed in Chapter 4 for nanoscale surface chemistry characterization, showcasing native surface terminations and undetected siloxane contamination. Its investigation is extended to Nb_2CT_x oxidation detection and siloxane-preferential binding to hydroxyl-terminated basal planes. In Chapter 5, we apply MXene to Surface Plasmon Resonance sensing platforms. $Ti_3C_2T_x$ MXene enhances the SPR coupling and enables the detection of (3-aminopropyl)triethoxysilane (APTES). The developed multiscale optical characterization approach highlights the performance and versatility of this emerging family of 2D materials.

MXene – Infrared spectroscopy – 2D materials - Nanoscopy – Surface chemistry – Siloxane contamination

Discipline : PHYSIQUE

Spécialité : Sciences des matériaux, Surfaces et Interfaces

Université de Reims Champagne-Ardenne

L2n - CNRS UMR 7076

12 Rue Marie Curie – CS 42060 – 10004 Troyes